

# Application and System Design of Elastomer Based Optofluidic Lenses

by

Nickolaos Savidis

---

A Dissertation Submitted to the Faculty of the

COLLEGE OF OPTICAL SCIENCES

In Partial Fulfillment of the Requirements

For the Degree of

DOCTOR OF PHILOSOPHY

In the Graduate College

THE UNIVERSITY OF ARIZONA

2012

Copyright © Nickolaos Savidis 2012

THE UNIVERSITY OF ARIZONA  
GRADUATE COLLEGE

As members of the Dissertation Committee, we certify that we have read the dissertation

Prepared by Nickolaos Savidis

Entitled Application and System Design of Elastomer Based Optofluidic Lenses

And recommend that it be accepted as fulfilling the dissertation requirement for the

Degree of Doctor of Philosophy

\_\_\_\_\_ Date: 10/11/2012

James Schwiegerling

\_\_\_\_\_ Date: 10/11/2012

Nasser Peyghambarian

\_\_\_\_\_ Date: 10/11/2012

Gholam Peyman

Final approval and acceptance of this dissertation is contingent upon the candidate's submission of the final copies of the dissertation to the Graduate College.

I hereby certify that I have read this dissertation prepared under my direction and recommend that it be accepted as fulfilling the dissertation requirement.

---

Date: 10/11/2012

Dissertation Director: James Schwiegerling

## STATEMENT BY AUTHOR

This dissertation has been submitted in partial fulfillment of requirements for an advanced degree at the University of Arizona and is deposited in the University Library to be made available to borrowers under rules of the Library.

Brief quotations from this dissertation are allowable without special permission, provided that accurate acknowledgment of source is made. Requests for permission for extended quotation from or reproduction of this manuscript in whole or in part may be granted by the head of the major department or the Dean of the Graduate College when in his or her judgment the proposed use of the material is in the interests of scholarship. In all other instances, however, permission must be obtained from the copyright holder.

SIGNED: Nickolaos Savidis

## ACKNOWLEDGEMENTS

I would like to thank my advisor, Prof. Jim Schwiegerling, Prof. Nasser Peyghambarian and Prof. Gholam Peyman for their guidance and support for this research, and the friendship and understanding they have shown through the progress of our research

## DEDICATION

*To my family who have always offered support.*

## TABLE OF CONTENTS

LIST OF FIGURES .....	11
LIST OF TABLES .....	16
ABSTRACT .....	17
1.0 INTRODUCTION .....	19
1.1 History of Optofluidic Lenses .....	19
1.2 Optofluidic Lenses .....	21
1.3 Surface Profile Control of Pressure Actuated Fluidic Lenses .....	22
1.3.1 Shell Surface Profile .....	23
1.3.2 Spherical Surface Profile .....	24
1.3.3 Cylindrical Surface Profile .....	25
2.0 HUMAN VISUAL SYSTEM .....	28
2.1 Eye's Anatomy .....	28
2.2 Eye's Optical Properties .....	29
2.4 Spatial Acuity .....	32
3.0 ABERRATIONS AND ABBERATION CORRECTION .....	34
3.1 Circularly Symmetric Optical Systems and the Wavefront .....	34
3.1.1 Defocus Aberration .....	36
3.1.2 Chromatic Aberration .....	37
3.1.3 Astigmatism Aberration .....	39
3.1.4 Spherical Aberration .....	40
3.2 Asymmetric Optical Systems, Zernike Fitting, and Ocular Aberrations .....	41
3.2.1 Zernike Polynomials .....	41
3.2.2 Zernike Fitting and Ocular Aberrations .....	42
3.2.3 Factors Causing Ocular Aberrations .....	45

## TABLE OF CONTENTS- Continued

3.2.4 Measuring Ocular Aberrations and Optical Measuring Devices .....	46
3.2.5 Light Source of Shack-Hartmann Wavefront Sensor .....	49
3.2.6 Tradeoffs of the Shack-Hartmann Wavefront Sensor.....	49
4.0 SPHERICAL FLUIDIC LENSES AND NON-MECHANICAL ZOOM .....	52
4.1 Theory of Spherical Fluidic Lenses .....	53
4.2 Fabrication of Elastomer Membrane .....	55
4.3 Spherical Fluidic Lens One.....	56
4.4 Spherical Fluidic Lens Two .....	59
4.5 Zoom Lenses .....	60
4.6 Theory: Variable Power Zoom System.....	61
4.7 Experiment: Zoom System Verification .....	64
4.8 Limitations of Fluidic Zoom System .....	67
5.0 FLUIDIC ACHROMAT .....	69
5.1 Achromat One: Diffractive / Refractive Hybrid .....	70
5.1.2 Liquid Crystal Diffractive Lens .....	72
5.1.3 Fluidic Refractive Lens.....	73
5.1.4 Test Methods and Results of the Hybrid Diffractive/Refractive Achromat .....	75
5.2 Continuous Variable Achromat Fluidic Lens .....	89
5.2.1 Variable Focal Length Achromat Design .....	90
5.2.2 Testing Methods for Continuous Variable Focal Length Achromat .....	93
6.0 WAVEFRONT CORRECTION OF THE FLUIDIC PHOROPTER AND FLUIDIC AUTO-PHOROPTER .....	101
6.1 Fluidic Phoropter .....	104
6.1.1 Wavefront Analysis of Defocus and Astigmatism Lenses .....	104
6.1.2 Wavefront Analysis of Fluidic Phoropter .....	107
6.2 Wavefront Analysis of the Fluidic Auto-Phoropter.....	111

## TABLE OF CONTENTS- Continued

7.0 FLUIDIC AUTO-PHOROPTER PROTOTYPE ONE: SYSTEM DESIGN .....	113
7.1 Design of Fluidic Auto-Phoropter Prototype One .....	114
7.1.1 Fluidic Auto-Phoropter Prototype One: Light Path from Source to Fluidic Phoropter.....	115
7.1.2 Fluidic Auto-Phoropter Prototype One: Light Path from Fluidic Phoropter through the Eye Model.....	118
7.1.2.1 Fluid Selection for Fluidic Phoropter .....	119
7.1.2.2 Test Results with Fluidic Phoropter.....	123
7.1.3 Fluidic Auto-Phoropter Prototype One: Light Path Through Keplerian Telescope .....	128
7.1.4 Fluidic Auto-Phoropter Prototype One: Light Path from Keplerian Telescope to Shack - Hartmann Wavefront Sensor .....	131
7.2 Fluidic Auto-Phoropter Prototype One: Alignment for Monocular Setup .....	133
7.3 Fluidic Auto-Phoropter Prototype One: Binocular Alignment and Inter-Pupillary Distance .....	135
8.0 FLUIDIC AUTO-PHOROPTER PROTOTYPE ONE: MODELING .....	141
8.1 Lens Design Model of Dynamic Range of Auto-Phoropter .....	141
8.2 Illumination Model of Dynamic Range of Fluidic Auto-Phoropter .....	148
9.0 FLUIDIC AUTO-PHOROPTER PROTOTYPE ONE: TESTING .....	158
9.1 Testing Approach: Measurements of Model Eye .....	159
9.2 Testing Approach: Measuring Fluidic Phoropter .....	166
9.2.1 Defocus Lens Filled with DI Water Fluid Volume Tested with Fluidic Auto-Phoropter set for 3 mm and 6 mm Stop Sizes.....	169
9.2.2 Defocus Lens Filled with BK-7 Oil # 3 Tested with Fluidic Auto-Phoropter for 3 mm and 6 mm Stop Sizes.....	174
9.2.3 Astigmatism Lens Filled with DI Water and Fluidic Auto-Phoropter set at a 3 mm Stop Size .....	179
9.3 Nulling Error with the Fluidic Auto-Phoropter: Fluidic Phoropter Cancels Model Eye Error .....	191
9.4 Limits of the Optical Design.....	192

## TABLE OF CONTENTS- Continued

10.0 FLUIDIC AUTO-PHROPTER: OFF-AXIS OPTICAL DESIGNS .....	198
10.1 Fluidic Auto-Phoropter with Traditional Off-Axis Optics .....	199
10.1.1 Design Setup of Fluidic Auto-Phoropter Prototype Two .....	201
10.1.2 Modeling and Testing of Fluidic Auto-Phoropter Prototype Two.....	203
10.2 Nulling Error with Prototype Two Fluidic Auto-Phoropter .....	206
10.3 Limits of Optical Design.....	208
11.0 FLUIDIC AUTO-PHOROPTERS: OFF-AXIS OPTICAL DESIGNS WITH HOLOGRAPHIC OPTICAL ELEMENTS .....	215
11.1 Holography and Holographic Lenses.....	217
11.2 Design of Fluidic Holographic Auto-Phoropter with Holographic Optical Elements as Lenses .....	219
11.3 Modeling of Fluidic Holographic Auto-Phoropter Prototype One .....	220
11.4 Design and Setup of the Fluidic Holographic Auto-Phoropter.....	222
11.5 Testing of Fluidic Holographic Auto-Phoropter.....	224
11.6 Nulling Error with Fluidic Holographic Auto-Phoropter .....	228
11.7 Limits of Holographic Optical Design.....	230
12.0 CONCLUSION AND FUTURE WORK .....	234
12.1 Wavefront Comparison of Freely Supported Edge vs. Clamped Edge Designs....	235
12.2 Improving Fluidic Zoom with a Redesigned Terrestrial Keplerian Telescope.....	236
12.3 Progression of Fluidic Achromat .....	237
12.4 Progression of the Fluidic Auto-Phoropter Systems.....	237
12.5 Progression of Fluidic Holographic Auto-Phoropter .....	240
12.6 Mobile Holographic Fluidic Auto-Phoropter.....	243
REFERENCES .....	247

## LIST OF FIGURES

Figure 1-1: Shell Membrane .....	23
Figure 1-2: Spherical Membrane .....	24
Figure 2-1: Eye Profile.....	28
Figure 2-2: The Arizona Eye Model .....	30
Figure 2-3: Optical and Visual Axis .....	31
Figure 2-4: Visual Acuity .....	33
Figure 3-1: Optical Coordinate System .....	35
Figure 3-2: Defocus Aberration.....	37
Figure 3-3: Chromatic Aberration of the Marginal Ray .....	38
Figure 3-4: Chromatic Aberration of the Chief Ray .....	39
Figure 3-5: Astigmatism Aberration.....	40
Figure 3-6: Spherical Aberration .....	41
Figure 3-7: Shack-Hartmann Wavefront Sensing.....	47
Figure 3-8: Shack-Hartmann Spot Displacement .....	48
Figure 3-9: Shack-Hartmann Dynamic Range vs. Sensitivity .....	50
Figure 4-1: Fluidic Lens 1.....	56
Figure 4-2: Zoom Control of Fluidic Lens 1 .....	58
Figure 4-3: Fluidic Lens 2.....	59
Figure 4-4: Zoom Control of Fluidic Lens 2 .....	60
Figure 4-5: Zoom System .....	62
Figure 4-6: Zoom System Setup .....	64
Figure 4-7: Zoom Magnification of Letter Chart.....	65
Figure 4-8: Experimental vs. Theoretical Zoom Magnifying Power.....	66
Figure 5-1: Diffractive / Refractive Hybrid Design.....	71
Figure 5-2: Achromat Test Setup.....	79

## LIST OF FIGURES - Continued

Figure 5-3: Diffractive Spot's Per Wavelength .....	84
Figure 5-4: Fluidic Achromat Focal Length .....	85
Figure 5-5: Discrete Diffractive / Refractive Focal Length Achromat Results .....	88
Figure 5-6: Dual Fluidic Achromatic Lens Design.....	91
Figure 5-7: Dual Chamber Fluidic Achromat.....	92
Figure 5-8: Coupled Single Chamber Achromatic Design .....	92
Figure 5-9: Dual Achromat Testing Design.....	93
Figure 5-10: ZEMAX Model of a 80 mm Focal Length Achromat Design .....	96
Figure 5-11: ZEMAX Model of a 400 mm Focal Length Achromat Design .....	96
Figure 5-12: ZEMAX Model of a - 100 mm Focal Length Achromat Design.....	99
Figure 5-13: ZEMAX Model of a - 60 mm Focal Length Achromat Design.....	99
Figure 6-1: Fluidic Phoropter Compared to Standard Phoropter.....	103
Figure 6-2: Wavefront Measurement of Defocus Lens .....	105
Figure 6-3: Wavefront Measurement of Astigmatism Lens .....	107
Figure 6-4: Fluidic Phoropter Orientation .....	108
Figure 7-1: Targets at Multiple Planes for Focusing Through Fluidic Auto-Phoropter .	113
Figure 7-2: Layout of Optofluidic Auto-Phoropter Prototype One .....	115
Figure 7-3: Specifications of Fiber Coupled SLD .....	116
Figure 7-4: Circuit Used to Drive the SLD's.....	117
Figure 7-5: Defocus Lens Power Profile .....	124
Figure 7-6: Double Astigmatic Fluidic Lens Power Profile .....	125
Figure 7-7: Imaging Results of Model Eye through Fluidic Phoropter .....	126
Figure 7-8: Modeling Myopia and Hyperopia.....	127
Figure 7-9: Design of Optofluidic Auto-Phoropter Prototype One .....	128
Figure 7-10: Folding Mirror Analysis.....	131
Figure 7-11: Line of Sight of User.....	132

## LIST OF FIGURES - Continued

Figure 7-12: Alignment of Monocular Fluidic Auto-Phoropter Prototype One .....	133
Figure 7-13: Base Setup of the Binocular Fluidic Auto-Phoropter .....	137
Figure 7-14: Machined Adapters for Inter-pupillary Distance of Binocular Fluidic Auto-Phoropter .....	138
Figure 7-15: Spots of Alignment Beam at 15 Feet Away of Binocular Fluidic Auto-Phoropter.....	140
Figure 7-16: User Position in a Fully Aligned Binocular Fluidic Auto-Phoropter.....	140
Figure 8-1: ZEMAX Layout of Monocular Setup of Auto-Phoropter.....	142
Figure 8-2: Model of Image Plane of Shack-Hartmann Wavefront Sensor in ZEMAX	144
Figure 8-3: Dynamic Range Limits of Auto-Phoropter .....	148
Figure 8-4: FRED Model of Binocular Fluidic Auto-Phoropter .....	149
Figure 8-5: Model of Image Plane of Shack-Hartmann Wavefront Sensor in FRED ....	150
Figure 8-6: Power Range of Defocus Lens of Fluidic Phoropter .....	151
Figure 8-7: Power Variation of Defocus Fluidic Lens in FRED of Fluidic Auto-Phoropter.....	154
Figure 8-8: Defocus Lens Power Variation and Effects on Fluidic Auto-Phoropter.....	155
Figure 8-9: Astigmatism Lens One Power Variation and Effects on Fluidic Auto-Phoropter.....	156
Figure 8-10: Astigmatism Lens Two Power Variation and Effects on Fluidic Auto-Phoropter.....	157
Figure 8-11: Defocus and Astigmatism Lens Two Power Variation and Effects on Fluidic Auto-Phoropter .....	157
Figure 9-1: Step 2: Testing Auto-Phoropter with Eye Model .....	160
Figure 9-2: Unfolded Eye Model.....	161
Figure 9-3: Model Eye Power vs. Defocus Wavefront Relative to Pupil Size .....	165
Figure 9-4: Defocus Measurements through our Auto-Phoropter System .....	166
Figure 9-5: Step 3: Testing Auto-Phoropter with Fluidic Phoropter .....	167
Figure 9-6: Wavefront Measurements with DI water and 3 mm Stop for Defocus Lens	171
Figure 9-7: Wavefront Measurements with DI water and 6 mm Stop for Defocus Lens	172

## LIST OF FIGURES - Continued

Figure 9-8: Refraction Terms with DI Water and 3 mm Stop for Defocus Lens .....	173
Figure 9-9: Refraction Terms with DI Water and 6 mm Stop for Defocus Lens .....	174
Figure 9-10: Wavefront Measurements with BK-7 Oil and 3 mm Stop for Defocus Lens.....	176
Figure 9-11: Wavefront Measurements with BK-7 Oil and 6 mm Stop for Defocus Lens.....	177
Figure 9-12: Refractive Terms with BK-7 Oil and 3 mm Stop for Defocus Lens.....	178
Figure 9-13: Refractive Terms with BK-7 Oil and 6 mm Stop for Defocus Lens.....	178
Figure 9-14: Fluidic Valve Control System.....	180
Figure 9-15: Fluidic Phoropter Combination.....	181
Figure 9-16: Wavefront Measurements with DI Water and 3 mm Stop for Astigmatism Lens One .....	182
Figure 9-17: Wavefront Measurements with DI Water and 3 mm Stop for Astigmatism Lens Two .....	183
Figure 9-18: Axis Term for Astigmatism Lens One with DI Water and 3 mm Stop for Fluidic Auto- Phoropter .....	185
Figure 9-19: Axis Term for Astigmatism Lens Two with DI Water and 3 mm Stop for Fluidic Auto- Phoropter .....	186
Figure 9-20: Cylinder and Sphere Term for Astigmatism Lens One with DI Water and 3 mm Stop for Fluidic Auto-Phoropter .....	187
Figure 9-21: Cylinder and Sphere Term for Astigmatism Lens Two with DI Water and 3 mm Stop for Fluidic Auto-Phoropter .....	188
Figure 9-22: Astigmatic Mapping of Auto-Phoropter System .....	191
Figure 9-23: Nulled Defocus Error with Eye Model at 1 D and -1 D Defocus of Fluidic Phoropter .....	192
Figure 9-24: Line of Sight Limit of Fluidic Auto-Phoropter.....	195
Figure 9-25: Line of Sight Limit of Off-Axis Fluidic Auto- Phoropter .....	196
Figure 10-1: Fluidic Auto-Phoropter Prototype Two .....	200
Figure 10-2: Testing Fluidic Auto-Phoropter Prototype Two .....	202
Figure 10-3: Mobile Fluidic Auto-Phoropter Prototype Two .....	203

## LIST OF FIGURES - Continued

Figure 10-4: Comparing Wavefront Error of Prototypes One and Two Relative to Defocus Power of the Model Eye .....	205
Figure 10-5: Wavefront Error of Prototype Two Relative to Defocus Power of the Model Eye .....	206
Figure 10-6: Nulling Power Error with Fluidic Auto-Phoropter Prototype Two .....	207
Figure 10-7: Nulling Power Observed for Fluidic Auto-Phoropter Prototype Two from Shack-Hartmann Wavefront Sensor.....	208
Figure 10-8: Modified Fluidic Auto-Phoropter Prototype Two .....	211
Figure 10-9: Fluidic Auto-Phoropter Prototype Three .....	213
Figure 10-10: Image of Fluidic Auto-Phoropter Prototype Three .....	214
Figure 11-1: Fluidic Holographic Auto-Phoropter .....	220
Figure 11-2: Fluidic Holographic Auto-Phoropter ZEMAX Model.....	221
Figure 11-3: Fluidic Holographic Auto-Phoropter Power Range.....	222
Figure 11-4: Testing Fluidic Holographic Auto-Phoropter .....	224
Figure 11-5: Comparing Wavefront Error of Prototypes Two and HOE Designs Relative Defocus Power of the Model Eye.....	226
Figure 11-6: Wavefront Error of Prototype Two Relative to Defocus Power of the Model Eye .....	228
Figure 11-7: Nulling Power Error with Holographic Fluidic Auto-Phoropter .....	229
Figure 11-8: Image Plane of Holographic Fluidic Auto-Phoropter .....	230
Figure 11-9: Polarization Controlled Holographic Fluidic Auto-Phoropter Design .....	232
Figure 12-1: Terrestrial Keplerian Telescope in Zoom System.....	237
Figure 12-2: Advanced Holographic Fluidic Auto-Phoropter with Pupil Imaging .....	242
Figure 12-3: 4F Advanced Holographic Fluidic Auto-Phoropter with Pupil Imaging...	243
Figure 12-4: Binocular Advanced 4F Holographic Fluidic Auto-Phoropter without Pupil Imaging.....	245
Figure 12-5: Mobile Binocular Helmet with Two Advanced 4F Holographic Fluidic Auto-Phoropter Designs.....	246

## LIST OF TABLES

Table 3-1: Ocular Aberrations .....	44
Table 4-1: Zoom Magnification.....	66
Table 5-1: Achromat Lookup Table .....	76
Table 5-2: Diffractive Lens A.....	83
Table 5-3: Diffractive Lens B .....	84
Table 5-4: Analysis of Fluidic Lens Radius of Curvature .....	94
Table 5-5: Radius of Curvature for Achromitization of Two Fluids .....	98
Table 7-1: Fluid Compatibility with Auto-Phoropter Material.....	121
Table 7-2: Fluid Optical and Chemical Properties .....	121
Table 8-1: Power Shift of Auto-Phoropter System Due to Variation in Corneal Radii .	146
Table 8-2: Empirical Measurements of Defocus Lens and Radii of Curvature.....	152
Table 9-1: Results of Auto-Phoropter with Eye Model .....	163

## ABSTRACT

Adaptive optic technology has revolutionized real time correction of wavefront aberrations. Optofluidic based applied optic devices have offered an opportunity to produce flexible refractive lenses in the correction of wavefronts. Fluidic lenses have superiority relative to their solid lens counterparts in their capabilities of producing tunable optical systems, that when synchronized, can produce real time variable systems with no moving parts. We have developed optofluidic fluidic lenses for applications of applied optical devices, as well as ophthalmic optic devices. The first half of this dissertation discusses the production of fluidic lenses as optical devices. In addition, the design and testing of various fluidic systems made with these components are evaluated. We begin with the creation of spherical or defocus singlet fluidic lenses. We then produced zoom optical systems with no moving parts by synchronizing combinations of these fluidic spherical lenses. The variable power zoom system incorporates two singlet fluidic lenses that are synchronized. The coupled device has no moving parts and has produced a magnification range of 0.1 x to 10 x or a 20 x magnification range. The chapter after fluidic zoom technology focuses on producing achromatic lens designs. We offer an analysis of a hybrid diffractive and refractive achromat that offers discrete achromatized variable focal lengths. In addition, we offer a design of a fully optofluidic based achromatic lens. By synchronizing the two membrane surfaces of the fluidic achromat we develop a design for a fluidic achromatic lens.

The second half of this dissertation discusses the production of optofluidic technology in ophthalmic applications. We begin with an introduction to an optofluidic phoropter system. A fluidic phoropter is designed through the combination of a defocus lens with two cylindrical fluidic lenses that are orientated  $45^\circ$  relative to each other. Here we discuss the designs of the

fluidic cylindrical lens coupled with a previously discussed defocus singlet lens. We then couple this optofluidic phoropter with relay optics and Shack-Hartmann wavefront sensing technology to produce an auto-phoropter device. The auto-phoropter system combines a refractometer designed Shack-Hartmann wavefront sensor with the compact refractive fluidic lens phoropter. This combination allows for the identification and control of ophthalmic cylinder, cylinder axis, as well as refractive error. The closed loop system of the fluidic phoropter with refractometer enables for the creation of our see-through auto-phoropter system. The design and testing of several generations of transmissive see-through auto-phoropter devices are presented in this section.

## 1.0 INTRODUCTION

The field of optofluidics was initially coined in the 1980's through developments in the field of micro-electronics [1, 2]. At the time, massive technological breakthroughs in nanotechnology brought micro-electronics into the field of optics. Fast and small fluid controlled mechanisms made on-chip optical devices realizable. Currently, optofluidics has progressed to encapsulate all optical devices which apply fluid or fluid control, where fluid encapsulates liquids and gases [3]. With this broad definition, optofluidics has been found in the fields of imaging, medical devices, bioengineering, metrology, display technologies, data storage and optical communication.

Due to the diversity of optofluidics, the field can be categorized in a couple of broadly engulfing sub-fields. There has been an evolution of optofluidics in two primary directions: 1) Photonics and 2) Applied Optics. Optofluidic based photonic devices have found application in sensing, switching, waveguides, tweezing, plasmonics, resonators, photonic crystals, material research, amongst other branches. Optofluidic based applied optic devices have found application in imaging, lenses, microlenses, plasmonics, and material research.

Optofluidic technologies have grown across a wide variety of fields due to their ease in producing highly controlled, wide dynamic range, high resolution, and smooth interfacing capabilities. We have found that these advantages offered by optofluidic lenses relative to solid lenses are desirable. Our primary focus of this dissertation is on the development of optofluidic lenses and their applications in system devices. We will describe the optofluidic lenses developed and the devices we applied towards imaging, medical devices, and bioengineering.

### 1.1 History of Optofluidic Lenses

The origins of fluid controlled optical devices have a longer history in the field of lenses. In the late 18<sup>th</sup> century Robert Blair achieved aberration correction by trapping fluid in two glass pieces. The control mechanism was to alter the concentration of fluid which enabled the device to then alter the index of refraction. In turn these static lenses were capable of correcting aberration through fluid volume control. This optofluidic device is the first documented fluid based optical lens [4].

The first optofluidic lens with a flexible surface was invented in the late 19<sup>th</sup> century through, to the author's knowledge, the oldest patent filed on the subject matter [5]. The patent, which was filed in 1890 and accepted in 1893, offered a pressure controlled mechanism to alter the curvature of a refracting or reflecting surface. This lens was described to offer transmission in radiant energy on both sides of the lens. Each side of the lens was composed of elastic material such as elastic plates or membranes.

Optofluidic lenses in the field of ophthalmic optics progressed further in 1918 with the proposition of fluid based spectacles [6]. This patent was focused on producing multifocal lenses by altering the amount of fluid in a central chamber. Screws on the side of the glasses would be adjusted to alter the amount of transmissive fluid in the line of sight of the user. These glasses were proposed to correct for defocus through the control of the focal power of the optofluidic lenses. Two decades later a patent was filed in 1938 and accepted in 1942 to produce a variable cylinder fluidic lens to correct for astigmatism [7]. This optofluidic lens was proposed to have a flat transparent side and a flexible membrane side. Cylinder was produced by bending the transmissive membrane in one direction. A relatively stiff material was required to flex the membrane in one dimension, limiting this proposed design.

A modern pressure actuated optofluidic lens was proposed in a patent filed in 1941 from Bausch and Lomb [8]. The motivation was to correct for spherical aberration and also for chromatic aberration. Fluid inserted into one or more chambers were placed between a transparent elastic diaphragm and a rigid transparent surface. Pressure actuation deformed the surface membrane into a continuous shape that corrected for spherical aberration. Multiple fluid chambers with varying index of refraction allowed for the creation of chromatically corrected optofluidic lenses. This proposed patent focused on the properties of the fluids. In addition to the transparency of the material, they suggested control on the index of refraction and fluid reactivity to system mechanisms. This lens structure is still a major approach utilized today in membrane actuated optofluidic lenses.

## **1.2 Optofluidic Lenses**

The patent from B&L in 1941 was an introduction to the modern pressure controlled optofluidic lenses built with widely tunable membranes. Progress in the field continued into the 1980's in both theory and design [9, 10, 11]. As is in the early B & L patent, large aperture fluidic lenses are composed of a rigid chamber with an elastic polymer based wall. The polymer wall flexes as pressure is applied into the chamber.

There are two types of optofluidic lens: liquid lenses and pneumatic lenses [3]. Liquid based optofluidic lenses contain fluid within the rigid structure, where the fluid is either a liquid or a gas. Here is where the author's definition slight differs with a more commonly used term in the field. We call optofluidic liquid lenses fluidic lenses rather than liquid lenses for a fundamental reason. The designed lenses pressure mechanism is applicable to either a gas or liquid. The term liquid lens implies a limitation to this optofluidic technology and neglects the

possibility of gas-based optofluidic lenses. For this reason we select to call fluid chamber optofluidic lenses fluidic lenses from here forth.

The functionality of the fluidic lenses has a flexible surface. The polymer membrane deforms to compensate for a pressure differential as fluid is injected or withdrawn within the active chamber. Pneumatic based optofluidic lenses do not contain any fluid and are based on varying the polymer shape to produce focusing power [12]. Both optofluidic lenses operate through the application of pressure on an elastomer surface.

The difference in controlling optical power lies in the approach of producing power variation. Optical power tuning in pneumatic optofluidic lenses is achieved through optical pathlength variation across the elastomer's clear aperture, as the lens is one continuous elastomer material. In fluidic lenses, optical power tuning is achieved by controlling the bending profile of the elastomer membrane, which is microns thick, and the index variation between the contained fluid and material external to the lens. When the elastomer membrane is thin it is observed as negligible, allowing for the fluidic lens power to be modeled directly by the indexes stated above and the surface curvature. The fluidic lens can produce a wide range of powers as certain elastomers offer high flexibility but often times do not produce large clear apertures. One can increase clear apertures of fluidic lenses through control of the surface profile.

### **1.3 Surface Profile Control of Pressure Actuated Fluidic Lenses**

Pressure actuated fluidic lenses produce a bending to the thin elastomer membrane. As we know, index variation and surface curvature defines the power control of the fluidic lens. Through the control of the opto-mechanical structure of the optofluidic element, we are able to produce various spherical and cylindrical lenses by controlling the surface profile of the

membranes. We first begin with the surface profile characterization of an optofluidic lens that produces a circularly symmetric optical element and then that of a cylinder lens. In this section we will characterize the geometric representations of the surface profiles. There are two approaches in characterizing the geometry of a circularly designed flexed membrane surface: that of a shell geometry [13, 14] or that of a sphere geometry [15, 16].

### 1.3.1 Shell Surface Profile

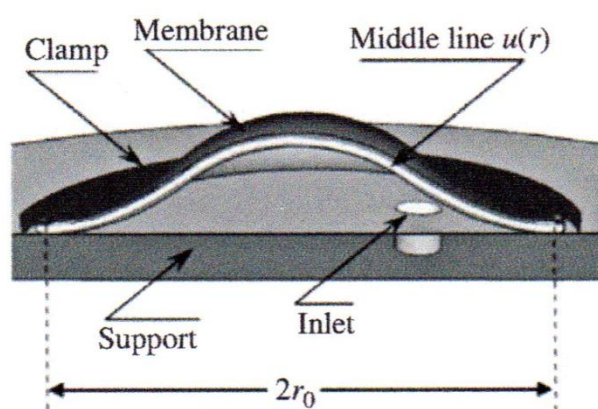


Figure 1-1 **Shell Membrane:** This is a typical membrane where the clear aperture applies the entire active area of the membrane with multiple radii of curvature. [3]

Shell geometry is a fair representation of an optofluidic liquid lens that actively applies the majority of the elastomer surface in the clear aperture of the optical element. If  $r_0$  is the semi-diameter of the clear aperture as is observed from Figure 1-1, there is a variation in the radius of curvature of the membrane as one progresses from the central active area to the peripheral active area. The periphery is clamped down to maintain a chamber structure. This causes the curvature  $u(r)$  to vary along the surface profile. It is desirable to develop an optomechanical design that produces one continuous surface profile. Hence, we would be able to define a continuous radius of curvature and model the optofluidic liquid lenses with a single continuous radius of curvature from a single geometry.

### 1.3.2 Spherical Surface Profile

There are two approaches used to design a liquid lens where we can estimate the surface profile with a spherical geometry. One approach is to control the clear aperture area of the lens. If one were to apply just the central active area of the optofluidic liquid lens as the clear aperture, it would be observed as approximately a continuous spherical surface. The periphery will still have a radius that is discontinuous, but relative to the active clear aperture area, the device observes a continuous radius of curvature. A second approach in producing an optofluidic liquid lens with a spherical geometry is to design the opto-mechanics of the structure so the lenses would be tightly suspended on the periphery, similar to a drum. By creating a drum suspension there is continuous pressure surrounding the periphery of the clear aperture through the center. We have applied both approaches in the development of our two spherical fluidic lenses that are modeled by this spherical geometry.

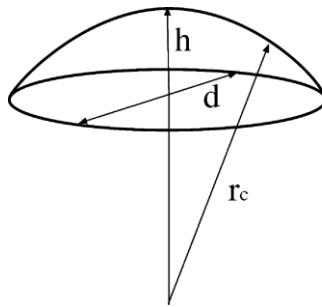


Figure 1-2 **Spherical Membrane:** This is a typical membrane where the clear aperture applies the active area of the membrane with a single continuous radius of curvature [16].

Figure 1-2 defines a spherical membrane with a diameter  $d$ , a sag  $h$ , and a radius of curvature  $r_c$ . We are capable of extracting the radius of curvature of the spherical surface through the simple relationship of knowing the optical power  $\phi$  of the optofluidic liquid lens [16].

$$r_c = \frac{n_{fluid} - n_{external}}{\phi}$$

The index of refraction of the fluid  $n_{\text{fluid}}$  and the external surroundings  $n_{\text{external}}$  must be known. One can measure the focal location and optical power of the lens. One can derive the sag of the fluidic lens from information of the radius of curvature and diameter of the clear aperture.

$$h = r_c \pm \sqrt{r_c^2 - d^2/4}$$

We were able to determine the sag and radius of curvature of the volume from the structure of the fluidic lens and the power at the focal position. The determination of the amount of fluidic volume required to alter the curvature of the lens is further expanded from the top two equations [16]. Fluidic volume (V) is determined by

$$V = \pi h^2 \frac{(3r_c - h)}{3}$$

From the equation of optical power of an interfacing surface and the assumption of a spherically symmetric surface, we were able to map the correlation of the radius of curvature, sag, change in fluid volume and optical power produced by any fluidic lens.

### 1.3.3 Cylindrical Surface Profile

A cylindrical profile is achievable by destroying the circular symmetry of the fluidic lens. The fluidic lens must be developed through a rectangular suspension with reflective mirror

symmetry. This is achievable by opto-mechanically designing the optofluidic liquid lens so that the membrane has a rectangular frame. The active area of the cylinder lens is designed such that the restrained rectangular frame is much larger than the clear aperture of the liquid lens.

Through the examination of the freely constrained beam deflection we are able to map this cylindrical surface profile [17]. The relative length of the long side and short side of the rectangular frame define the performance of the cylindrical profile. We are able to replicate that of a freely constrained beam when constraining the frame so that the longer side is significantly longer than the shorter side. Beam deflection for a freely constrained surface profile is mapped by [18]:

$$d(x) = \delta - \frac{q}{2EI} \left[ \frac{l^2 x^2}{2} - \frac{x^4}{12} - \frac{1}{5} c^2 x^2 + \left( 1 + \frac{1}{2} \nu \right) c^2 x^2 \right]$$

1-4

Where  $\delta$  is the displacement at the center of the beam,  $q$  is the pressure,  $E$  is the Young's Modulus,  $I$  is the shape factor, which depends on the cross sectional profile of the beam,  $l$  is the length,  $c$  is the thickness, and  $\nu$  is the Poisson ratio. This produces a cross sectional profile that is effectively a  $x^2$  term and a  $x^4$  term. This term is similar to the circular lens cross sectional profile.

We can achieve control of larger deflections where the curvature becomes more parabolic by properly modeling the rectangular restraints. The separation between the edge restraints defines the mirror symmetry. If we analyze the cross sectional profile from the long side of the frame to the opposite side of the frame, across the short side of the rectangle, we see that the highest magnitude of deflection is at the center and is zero at the edges. The clear aperture,

however, is located at the center of the rectangular frame. The clear aperture is designed as a  $360^\circ$  window that does not reach the edge of the frame. Therefore, at no period of inserting or withdrawing fluid is the deflection magnitude zero unless there is zero power variation in the clear aperture region.

The size of the clear aperture relative to the rectangular frame allows for the cylindrical profile to be achieved. If we define the shortest side from the center to the edge as our zero point, we can rotate in the clear aperture by  $45^\circ$  to the edge of the rectangular frame. The short side by our starting point has the highest slope as the magnitude of the deflection monotonically decreases from the center across our horizontal profile. As we rotate towards the edge of the rectangular frame our curvature lowers until we hit that  $45^\circ$  angle. At this  $45^\circ$  location we have hit the lowest curvature as it is the longest distance from the center of the membrane to the corner of the frame. By limiting the active area of the membrane to the central portion of the constraint, we are able to treat the four corners as single low curvatures to the edges. Edge effects that produce higher order aberrations are negligible as their effects are not observed in the central active area of the fluidic lenses clear aperture. Depending on the optical design, there will be small amounts of residual spherical power with the cylinder profile. This is correctible with the proper optical designs as we will further discuss in this dissertation.

## 2.0 HUMAN VISUAL SYSTEM

The properties of the human visual system (HVS) are essential in the understanding and correction of observed ocular aberrations with fluidic lenses. Fluidic lenses will be shown to correct for defocus and astigmatism measured in various optical auto-phoropter designs. We will also discuss approaches in the correction of trefoil and spherical aberration through the use of fluidic technology. Thus, this section is dedicated to analyzing the eyes properties in the support of these fluidic based elastomer designs.

### 2.1 Eye's Anatomy

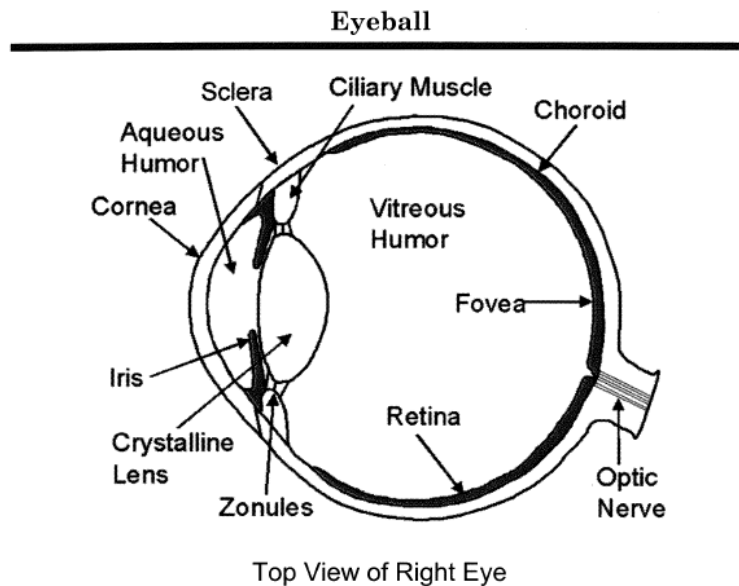


Figure 2-1 **Eye Profile:** Eye's side profile [19].

Light propagates into the eye through the cornea, a durable transparent membrane that produces two thirds of the optical power at a fixed focus location by refraction. The crystalline lens offers the additional third of optical power by focusing light onto the retina. In-between the cornea and the crystalline lens is the iris, where a clear aperture at the center of the iris is known

as the pupil. Traditionally, the combination of the crystalline lens and the cornea focus light onto the retina, but if an individual is suffering from Myopia (nearsightedness) or Hyperopia (farsightedness), then corrective eye wear is necessary to focus the propagating light onto the retina. Retinas are composed of photoreceptors and ganglia that convert the retinal image into neural signals that are then transmitted by means of the optic nerve to the brain. The brain inverts the image and combines the optical information of both eyes to produce stereoscopic imagery.

## **2.2 Eye's Optical Properties**

A fundamental property for an optical detector is the wavelength detection range. The HVS includes wavelength detection from approximately 400 to 780 nm. The crystalline lens absorbs light for wavelengths below 400 nm. On the opposite side of the visual spectrum, longer wavelength reflection is primarily seen at the cornea with additional reflections at the crystalline lens. Thus, in addition to controlling the optical power, the cornea and crystalline lens limit the HVS's detection range.

The iris, which is situated between the cornea and crystalline lens, is the aperture stop of the eye. Depending on the surrounding lighting conditions, the iris relaxes or contracts in order to control the pupil size, adjusting the stop size. Pupil sizes vary between 2 – 8 mm, where 8 mm is necessary for extremely dim lighting conditions. The image of the iris in object space is known as the eye's entrance pupil. Entrance pupil positions vary relative to the iris, depending on the eye model utilized to determine the separation between optical elements. A model known as the Arizona Eye model, as is shown in Figure 2.2 below, is a sophisticated design established to calculate on and off axis aberrations, which is extensively applied in the clinical field [19].

This Arizona Eye Model is utilized to determine that the entrance pupil location relative to the eyes center of rotation is approximately 10 mm.

Name	Radius	Conic	Index	Abbe	Thickness
	7.8 mm	-0.25			
Cornea			1.377	57.1	0.55 mm
	6.5 mm	-0.25			
Aqueous			1.337	61.3	$t_{aq}$
	$R_{ant}$	$K_{ant}$			
Lens			$n_{lens}$	51.9	$t_{lens}$
	$R_{post}$	$K_{post}$			
Vitreous			1.336	61.1	16.713 mm
	-13.4 mm	0.00			
Retina					

where

$$R_{ant} = 12.0 - 0.4A \quad K_{ant} = -7.518749 + 1.285720A$$

$$R_{post} = -5.224557 + 0.2A \quad K_{post} = -1.353971 - 0.431762A$$

$$t_{aq} = 2.97 - 0.04A \quad t_{lens} = 3.767 + 0.04A$$

$$n_{lens} = 1.42 + 0.00256A - 0.00022A^2$$

Figure 2-2 **The Arizona Eye Model:** The fundamental guidelines on applying the Arizona Eye Model [19].

For a rotationally symmetric optical system the entrance pupil diameter is traditionally symmetric about the optical axis. The lens' center of curvature defines the optical axis for these rotationally symmetric optical elements. However, it is fundamentally difficult to classify the eye's optical axis due to the lack of rotational symmetry. Field dependent on-axis aberrations, such as astigmatism, illustrate the eye's asymmetry, whereas symmetric systems have zero field dependence on-axis. Consequently, a technique was necessary to identify the optical axis for this asymmetric system. The optical axis is thus defined as the least gradient slope of the cornea's surface [19].

The visual axis, which defines the gazing direction, is not the optical axis. These two axes overlap only when an individual stares through the cornea's center to an infinite distance.

To account for gaze direction, the visual axis is defined as the axis where the ray propagates from the fixation point to the front nodal point and then from the rear nodal point to the fovea.

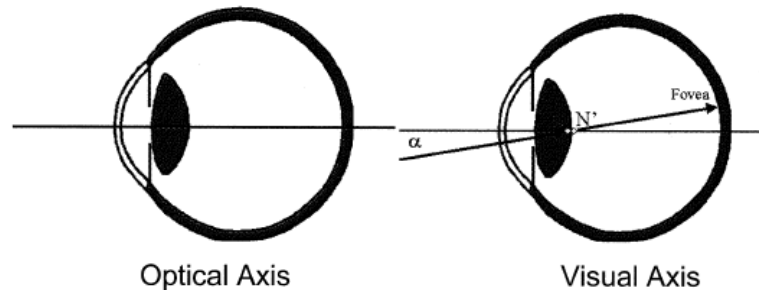


Figure 2-3 **Optical and Visual Axis:** An image defining the optical and visual axis [19].

Nodal points define points in an optical system with unit angular magnification [20]. If the nodal points were overlapping, then the visual axis is continuous from the fixation point to the fovea. However, the nodal points do not overlap, where the visual axis is translated along the optical axis, allowing for the same angular subtend with 1:1 magnification. Hence, the visual axis has the properties of a light ray passing from the location of fixation to the fovea through the nodal points.

Also due to a lack of symmetry, a variation in the eye's rotational field of view exists, where the center of the field of view is relative to the eye's line of sight. Line of sight is defined as the ray path onto the fovea from a fixed location through the pupil's center, known as the chief ray. Four fields of view were determined relative to the eye's line of sight: 1)  $60^\circ$  nasally, as in the direction of the nose, 2)  $100^\circ$  temporally, directed toward the outside of the head, 3)  $60^\circ$  superiorly, directed above the head, and 4)  $70^\circ$  inferiorly directed below the head. For a stationary eye, the horizontal field of view is  $160^\circ$  and the vertical field of view is  $130^\circ$ , which is deduced by summing the respective fields of view. An overlap between the left and right eyes permits  $120^\circ$  of stereoscopic vision, the region of the HVS where depth perception produces

stereoscopic imaging. As the eyes move and rotate, the field of view shifts with a maximum eye rotation between  $25^\circ$  to  $30^\circ$  [21].

### **2.3 Spatial Acuity**

Eye movements evolved as a means to produce a detailed scene; therefore, scanning occurs to shift the scene onto the macula, where a high percentage of the photoreceptors are located. The highest observed resolution is seen from the macula due to the concentration of red, blue and green cones. Each specific cone, also identified as long, middle, and short, detects the light of their specified wavelength region. Color vision is produced when the brain combines data from these three cones.

Cone receptors are intended for day vision due to their low light sensitivity. Cones provide high spatial resolution, with the packing of the red and green cones possessing the highest density. Progressing away from the eyes' line of sight, there is a reduction in cones as well as an increase in ganglia and rods, rods being the eye's second type of photoreceptors. In addition to the reduction in the amount of cones, these photoreceptors become larger and less receptive to temporal resolution. The main focal area, the fovea, requires smaller movements to produce finer detailed images, while larger movements are necessary for the peripheral in order to gather information due to the rods low temporal and spatial resolution. Additionally, the decrease of cones in the peripheral produces a sharp drop in resolution.

Rods are football shaped receptors situated primarily in the macula's periphery. These receptors have high sensitivity to light, gathering single photons in pitch dark conditions, even at night. Rods work well with dim lighting and offer the HVS a dynamic range that no man-made detector has replicated. A lower acuity in the periphery exists since the rods have a low resolution and the presence of ganglia. Ganglia are the cells that transmit the signal to the optical

nerves, and have a ratio of thousands of cells to a few photoreceptors in the periphery compared to half a dozen cones per ganglia in the fovea. Decreased resolution arises in the periphery due to an increased ratio of ganglia to photoreceptors, which poses a greater effect than the decrease in the amount of cones. Hence, there is lower peripheral data resolution, much larger angular subtended angles than the one arc minute resolution found at the fovea's center. The fovea's high concentration of cones closer to the center of gaze produces a region of high resolution known as the area of interest (AOI). A natural exponential drop-off in spatial foveal acuity arises when progressing away from the AOI.

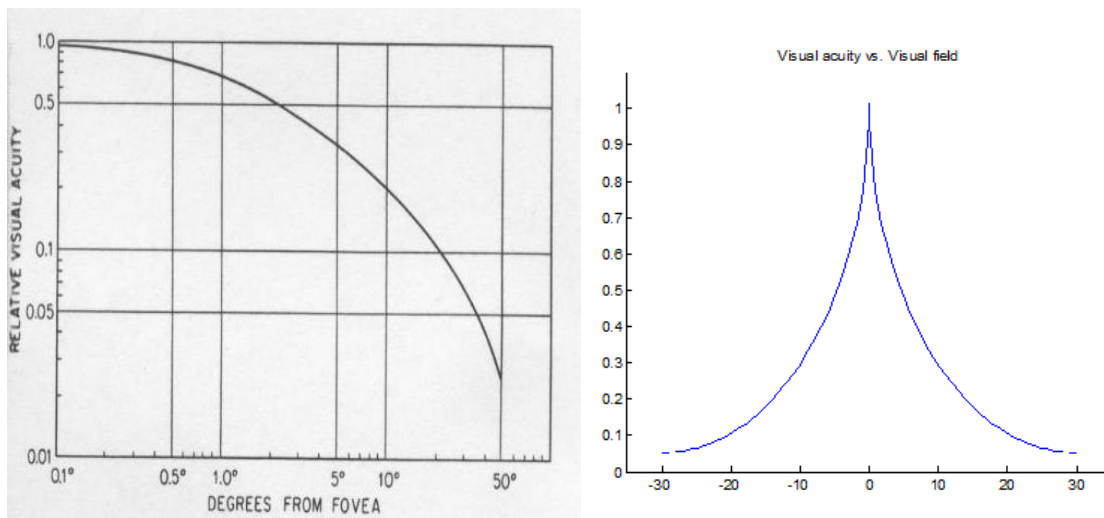


Figure 2-4 **Visual Acuity**: The eye's acuity over a visual field in logarithmic and real scales [22].

### **3.0 ABBERATIONS and ABERRATION CORRECTION**

A capability of optofluidic lens technology, as well as many adaptive optic technologies, is to correct for specific aberrations observed in propagating light and thus it is significant to analyze the optical properties of a wavefront. In addition to the correction of the wavefront, one must measure the aberrations of the wavefront in real time. We offer an objective evaluation of aberrations, as well as an evaluation of aberrations within the human visual system, that enables us to analyze our experimental setups. In the determination of the accuracy and reliability of aberration control within fluidic lenses, we must first establish an understanding for both circularly symmetric and circularly asymmetric optical systems, such as that observed within the uncorrected eye. Lastly, we will discuss generic measuring approaches and the application of Shack-Hartmann sensing in wavefront correction.

#### **3.1 Circularly Symmetric Optical Systems and the Wavefront**

Our assessment of aberrations will begin with a description of aberrations in a circularly symmetric optical system. The wavefront completely describes the image forming properties of any optical system. This ideal wavefront can be referenced as spherical waves focusing to a point with no optical path difference from any sampled location. Aberrations are developed when there is a shift from this perfect sphere due to various shaped optical elements in the propagating wave's path. The aberrated wavefront becomes a sum of the spherical wavefront and the localized wavefront error. Under ideal conditions light in an optical system converges to a focal point where the size is defined by a diffraction-limited spot or Airy disk. Aberrations are observed in the image plane when the energy distribution of the focused spot becomes larger than the diffraction-limited Airy disk in a real optical system. Mathematical expansions

physically describe how the wavefront would be observed relative to a paraxial image plane with differing aberrations. For a rotationally symmetric optical system, the coordinate system becomes a function of the normalized pupil coordinates  $x_p, y_p$  and the normalized image height  $H$  [20]. A wavefront expansion is developed to describe the aberrations through these two coordinate planes in the determination of ray positioning relative to the referenced image plane.

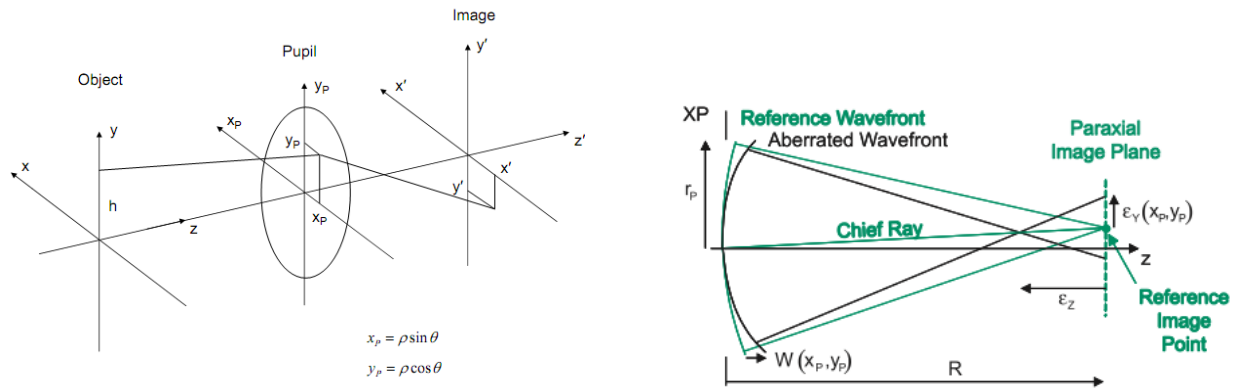


Figure 3-1 **Optical Coordinate System:** Normalized pupil coordinates and a diagram of wavefront aberrations [20].

The wavefront expansion below is a power series expansion for the wavefront aberrations of a rotationally symmetric optical system, where the expansion terms are  $H^2, \rho^2$  and  $H\rho \cos \theta$ . The coefficient subscripts represent the powers of each respective polynomial term:  $W_{IJK} \Rightarrow H^I \rho^J \cos^K \theta$ .

$$W = W_{020}\rho + W_{111}H \cos \theta + W_{040}\rho^4 + W_{131}H\rho^3 \cos \theta +$$

$$W_{222}H^2\rho^2 \cos^2 \theta + W_{220}H^2\rho^2 + W_{311}H^3 \rho \cos \theta$$

3-1

The coordinate terms are called primary or first-order aberrations and third-order, or Seidel aberrations for a circularly symmetric optical system. The wavefront terms represent the

different aberrations: defocus, tilt, spherical, coma, astigmatism, field curvature, and distortion aberrations, respectively [22]. Additionally, higher order aberrations exist beyond the third-order which are higher terms of the series expansion. Due to the lack of rotational symmetry found in the eye, the field aberrations found in eq. 3-1 can also appear on axis. Furthermore, additional aberrations such as trefoil and tetrafoil are found in the eye as well. Many books have been written on optical imaging and aberrations for both ray geometrical and wave diffraction optics. The following subsections offer an overview description of the aberrations that fluidic lens technology can compensate and correct for.

### **3.1.1 Defocus Aberration**

Defocus,  $W_{020}$ , is a monochromatic pseudo-aberration as it is caused when we adjust the focus position. The real wavefront has a parabolic shape with a differing radius of curvature relative to the exit pupil. As one translates across the optical axis the adjustment of focal position enables us to compensate for higher order even aberrations relative to our reference point. There is no field dependence for this aberration. In the human eye specifically, the light properly focuses at the retina (Emmetropia), in front of the retina (Myopia) or behind the retina (Hyperopia). The latter two scenarios result in a reduction of sharpness and contrast of the image at the retinal plane where the cones and rods are located. Corrective eye wear compensates for these conditions to bring the focusing light to the retinal plane.

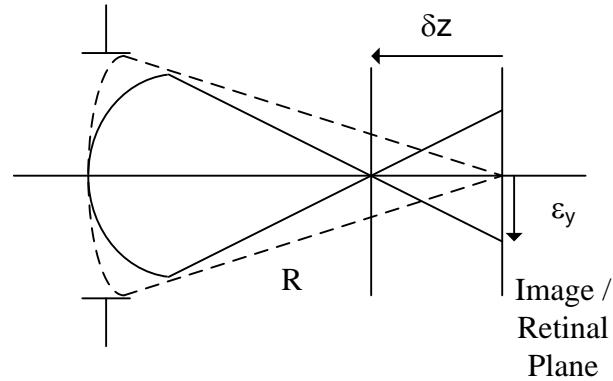


Figure 3-2 **Defocus Aberration:** The real and aberrated wavefronts for defocus are both spherically parabolic approximations with differing radii of curvature.

### 3.1.2 Chromatic Aberration

Refractive index of a given material, whether solid, liquid or gas, depends on the wavelength of light propagating through it. The amount of dispersion that is observed from a given material varies by wavelength and can be quantified into a value known as an Abbe number. The dispersive variation across the wavelength range causes the focal location to vary along the optical axis by wavelength. It is found that the shorter wavelengths with higher energy focus closer to a positive lens and the longer wavelengths focus further along the optical axis. Traditionally, chromatic aberration is defined from blue to red, which is relative to the human visual spectrum. This chromatic focal length variation along the optical axis is known as axial or longitudinal chromatic aberration ( $\delta\lambda W_{020}$ ).

As is observed in Figure 3-3, axial aberration creates an image blur relative to focal position of the axial aberration. If one chooses to place a plane at a given image location, various amounts of blur is observable in size between the blue and red wavelengths. This blur size due to the axial variation in focus perpendicular to the optical axis is known as transverse axial chromatic aberration  $TA_{CH}$  [20]. Both axial or longitudinal chromatic aberration and transverse

axial chromatic aberration are a description of the dispersion caused by wavelength dependence in the spreading of the marginal ray

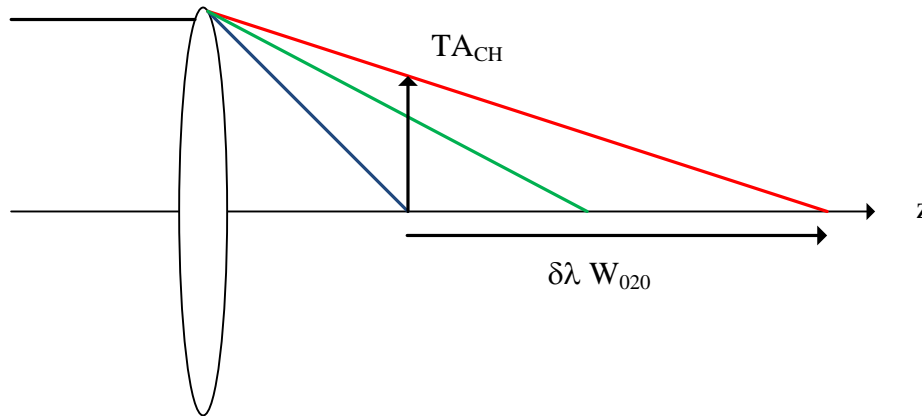


Figure 3-3 **Chromatic Aberration of the Marginal Ray:** Chromatic aberration is observed in a lens as the marginal ray spreads relative to focal length. A blue ray focuses before a red ray, producing longitudinal or axial chromatic aberration  $\delta\lambda W_{020}$  and transverse axial chromatic aberration  $TA_{CH}$ .

A third chromatic aberration exists that describes the dispersion of the chief ray known as lateral or transverse chromatic aberration ( $\delta\lambda W_{111}$ ). It is noted that transverse chromatic aberration is not transverse axial chromatic aberration as we are describing dispersion created by two different rays of light. To alleviate confusion, we will refer to the spreading of the chief ray as lateral chromatic aberration rather than transverse chromatic aberration. Lateral chromatic aberration occurs when there is a radial or angular displacement along the image plane. The displacement of the chief ray is a function of wavelength variation passing through a lens system, where the edge behaves as a prism rather than a lens, causing the chief ray to spread.

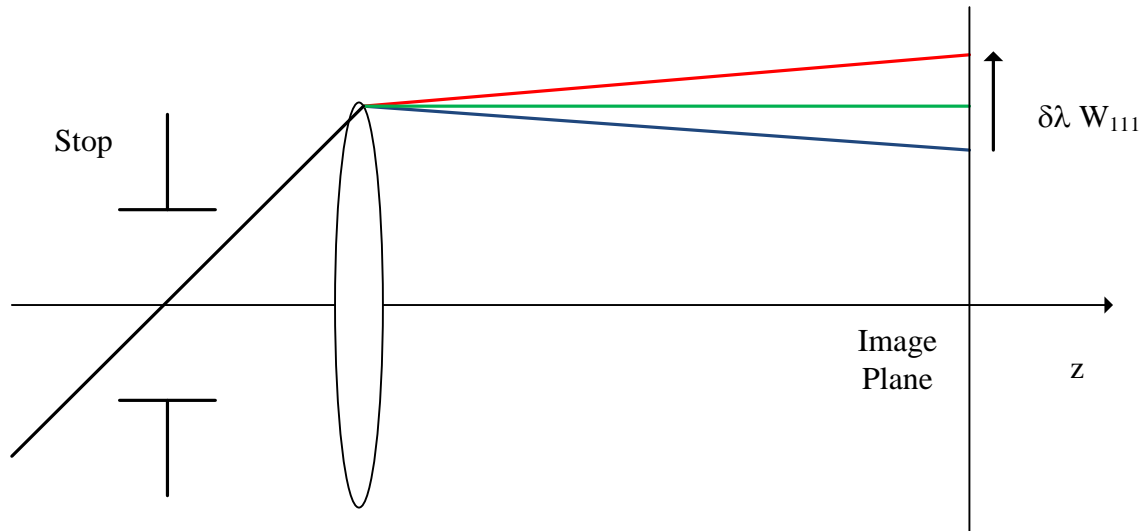


Figure 3-4 **Chromatic Aberration of the Chief Ray:** Chromatic aberration is observed in a lens as the chief ray spreads relative to the image plane. A blue ray focuses below and a red ray above the central green ray, producing lateral or transverse chromatic aberration  $\delta\lambda W_{111}$ .

### 3.1.3 Astigmatism Aberration

Astigmatism,  $W_{222}$ , is a monochromatic aberration in which the unequal curvature along differing meridians of the lens prevents light rays from focusing clearly at one point on the image plane. Astigmatism may be illustrated by extending the focused image along the curved image plane or Petzval surface relative to the flat image plane. The tangential rays lose their axial symmetry as the object point traverses off axis. However, the sagittal rays emanating from the same object point remain axially symmetric and come to a focus at the flat image plane. The difference in focal positions of the tangential and sagittal rays is the cause of astigmatism. The image point is observed as straight lines at the tangential and sagittal focal locations where the line points are orthogonal to one another. In locations between these focal planes the image point appears to be elliptical or oblate, as there is a combination of focusing power. The amount of astigmatism in a lens is a function of the power and shape of the lens and its distance from the aperture or diaphragm [23]. In the eye, the lack of rotational symmetry can introduce astigmatism

on axis. In this case, one or more of the ocular surfaces is toroidal in shape introducing the difference in curvature along orthogonal meridians.

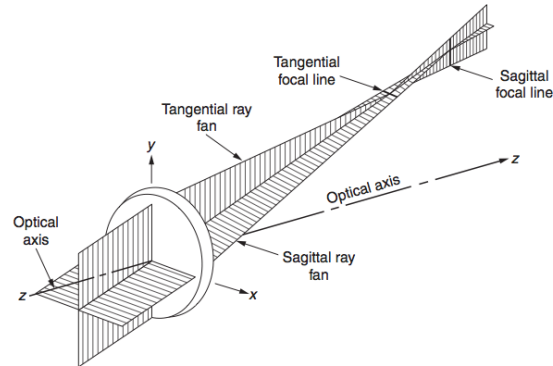


Figure 3-5 **Astigmatism Aberration:** Astigmatism aberration illustrates the variation of focal position between the Tangential and Sagittal planes [22].

### 3.1.4 Spherical Aberration

Spherical aberration,  $W_{040}$ , is a monochromatic aberration caused by the refraction through a spherical surface. Spherical aberration is the variation of focus with aperture size. Rays that are close to the optical axis focus close to the paraxial image plane or paraxial focus. As the ray height increases, the marginal focus moves farther away from the paraxial image plane. The distance from the marginal focus to the paraxial focus is called longitudinal spherical aberration. The distance at paraxial focus from the center to the edge of half the blur size is identified as the transverse spherical aberration. The location with the smallest blur is observed at the circle of least confusion. Spherical aberration can be measured by tracing a paraxial ray and a trigonometric ray from the same axial object point to determine their final intercept distances. The same amount of spherical aberration is present on and off axis [23].

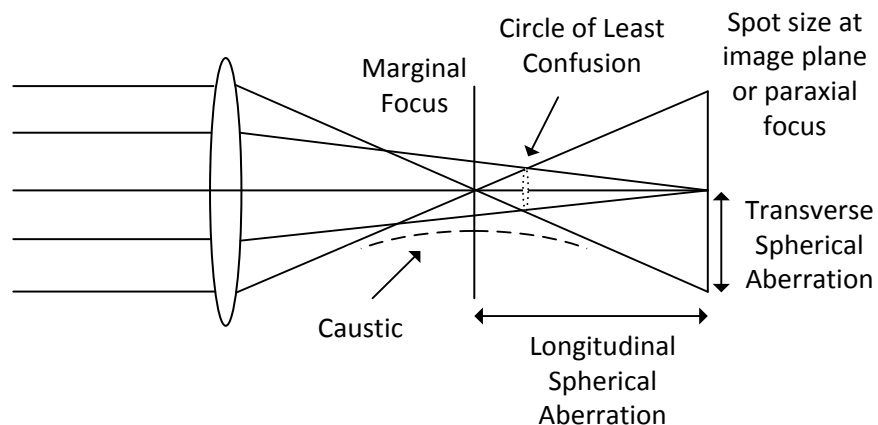


Figure 3-6 **Spherical Aberration:** An illustration of the primary features of a spherically aberrated system.

### 3.2 Asymmetric Optical Systems, Zernike Fitting, and Ocular Aberrations

In optics, there are numerous examples of non-rotationally symmetric or asymmetric optical systems. Optical lenses such as progressive lenses or cylindrical lenses which produce toroid or biconics surfaces are examples of asymmetric lenses. When an optical engineer works with square apertures, birefringence, gratings, or wedges they are producing asymmetric optical systems. Atmospheric turbulence or optical misalignment of mounts or manufacturing errors can also produce asymmetric optical systems. Imaging systems such as the Scheimpflug camera or the eye are also examples of imaging systems that are rotationally asymmetric.

#### 3.2.1 Zernike Polynomials

It is necessary to generalize aberrations to non-rotational symmetric systems, achievable through the use of Zernike polynomials. We can further our series expansion that was stated above to a power series which enables us to assess asymmetric optical systems in addition to rotationally symmetric optical systems. There are several advantages in fitting an optical system to Zernike polynomials. Zernike polynomials are orthogonal over a unit circle. As a majority of

optical systems have circular pupils it is advantageous to apply a weighted sum of power series terms that match the pupil coordinates of our optical function. We can therefore establish a data fitting set that represents a series of wave aberrations. Each term of the polynomial expansion is independent of the other expansion terms as they are mutually orthogonal. This enables for the representation of each aberration independently. Additionally, each of the Zernike terms is continuous, so one can produce a continuous derivative of the function. This allows for the representation of smoothly varying surfaces and also for the identification of discontinuities in the function [24]. The Zernike polynomials form a complete set, meaning they can represent arbitrarily complex continuous surfaces given enough terms. It must be noted that Zernike fitting is a significant issue in the replication of real trends. With too few terms, discontinuities are observed which may cause loss of significant information. When too many additional terms are inserted then the function may also fit noise into the data. The most optimal fit would be to represent numerous data points with as few terms as possible [24].

### **3.2.2 Zernike Fitting and Ocular Aberrations**

There are over half a dozen various Zernike polynomial schemes that exist. A standardized approach in the treatment of Zernike polynomials for ocular aberrations is defined in polar coordinates [25]. There are two standard schemes that are applied for ocular aberrations: 1) a double indexing and 2) a single indexing scheme. These standard Zernike sets are often used to fit the wavefront error of ocular aberrations. We will represent the Zernike polynomials using the double indexing scheme.

There are different ways to group the total ocular aberrations based on the Zernike terms. A common separation for the vision community is in the separation of the ocular aberration

terms into lower order and higher order ocular aberrations. The lower order or second order ocular aberrations, defocus and astigmatism, are the refractive errors in the eye that can be corrected by spectacles, contact lenses or with laser refractive surgery. The term second order comes from the fact that defocus and astigmatism are the coefficients of the second order radial Zernike terms. The lower order ocular aberrations are the most significant aberrations that require correction. The majority of higher order ocular aberrations were thought to be negligible relative to lower order ocular aberrations. It has been found that there are a few higher order ocular aberrations of significance. There is a second grouping for higher order ocular aberrations that emphasizes these relative aberrations individually. These higher order aberrations are spherical aberration, coma, trefoil, fourth order astigmatism and tetrafoil or the third and fourth radial Zernike orders. An additional separation is to divide the aberrations in groups of the same radial Zernike orders. The higher order aberrations are then separated into third, fourth, fifth, and sixth order aberrations.

		<b>Aberrations</b>	<b>Zernike Coefficients</b>
<b>Lower Order</b>		Defocus and Astigmatism	$Z_2^{-2}$ $Z_2^0$ $Z_2^2$
<b>Higher Order</b>		Higher Order Aberrations	$Z_3^{-3}$ to $Z_6^6$
	<b>Individual Aberrations</b>	Spherical	$Z_4^0$ $Z_6^0$
		Coma	$Z_3^{-1}$ $Z_3^1$
		Trefoil	$Z_3^{-3}$ $Z_3^3$
		Fourth Order Astigmatism	$Z_4^{-2}$ $Z_4^2$
		Quadrafoil	$Z_4^{-4}$ $Z_4^4$
	<b>Grouped by Radial Zernike Order</b>	Third Order	$Z_3^{\pm m, odd}$
		Fourth Order Astigmatism	$Z_4^{\pm m, even}$
		Fifth Order	$Z_5^{\pm m, odd}$
		Sixth Order	$Z_6^{\pm m, odd}$

Table 3-1 **Ocular Aberrations:** Describes the various Zernike terms and groups them relative to defined vision terms.

There are several ways of extracting and calculating aberrations from Zernike coefficients. The two most common approaches are to either compare the root-sum-squared (RSS) or the root-mean-squared (RMS) of the coefficients  $a_{m,n}$  [26]:

Root-Sum-Squared: 
$$RSS = \sqrt{\sum a_{m,n}^2}$$

3-1

Root-Mean-Squared: 
$$RMS = \sqrt{\frac{1}{n} \sum a_{m,n}^2}$$

3-2

The RSS corresponds to the wavefront error caused by these terms, where the first piston term  $Z_{0,0}$  is excluded from the calculation. This term is constant over the entire circle where no variance exists. The RMS equals the RSS divided by the square root of the number of coefficients  $n$ . These terms are image quality metrics for aberration extraction. It is significant to recognize which approach is applied for aberration identification.

### **3.2.3 Factors Causing Ocular Aberrations**

It is necessary to understand causes of the ocular aberrations within the eye in order to apply corrective fluidic lens technology to compensate for the ocular error. Image quality at the retinal plane has a high dependence on these ocular aberrations. Therefore, it is significant to identify the location and causes of ocular aberrations.

It is shown that aberrations vary on an individual basis [27] and that room lighting, which affects pupil size, varies the aberrations [28]. Saccadic movements and tear film slightly adjust the aberration readings with the rapid movement of the eye [29]. Additionally, the shape of the retinal plane, which is our image plane, may induce aberrations due to variations in eccentricity [30]. There are, however, two additional factors that cause ocular aberrations to vary dramatically. The ocular elements that produce the highest amount of variation in ocular aberration are the crystalline lens and the cornea. These are the two ocular elements that produce the focusing power onto the retinal plane. As one accommodates to focus at various object planes, the curvature of their cornea and crystalline lens adjusts. This causes a variation in focus power and hence a variation in ocular aberrations [31]. As one ages the dynamic range of the crystalline lens reduces and intraocular lenses (IOL's) may be required for optical corrections. Aging is found to be a significant fact in the reduction of image quality and increase in

aberrations [32, 33, 34, 35, 36]. Lastly, aberrations vary as the eye adjusts relative to room illumination or other external lighting conditions. The iris or system stop varies relative to scotopic or well lit conditions, thus adjusting the pupil sizes. The pupil size is a significant factor in variation of ocular aberrations [37, 38, 39, 40].

### **3.2.4 Measuring Ocular Aberrations and Optical Devices**

Our auto-phoropter designs take advantage of wavefront sensing technology coupled with fluidic lens technology. This offers the capability of ocular aberration measurement and correction in real time. As this dissertation's focuses on the application of optofluidic lens technology and the testing of these systems, we require measurement approaches that measure the wavefront. To correct optical errors with fluidic lenses, a wavefront sensing mechanism is required. The identification of the ocular aberrations is necessary to compensate the wavefront in real time with optofluidic technologies.

There are many wavefront sensing techniques that can measure aberrations. There are direct and indirect wavefront sensing approaches. Direct wavefront sensing approaches measure the wavefront directly, while indirect wavefront sensing approaches indirectly measure signals of the information related to the wavefront. Indirect wavefront sensing includes but is not limited to image sharpness, phase diversity, and phase retrieval. Direct wavefront measuring can be achieved through wave optics such as lateral shearing interferometry or geometrical optical measurements such as that of Shack-Hartmann wavefront sensing. Shack-Hartmann wavefront sensing is the wavefront sensing technique that is applied to aberration identification and correction for our systems.

A Shack-Hartmann wavefront sensor is a modification of the Hartmann screen test [41, 42, 43, 44]. The sensor applies a lenslet array rather than a screen with apertures [42]. A propagating wavefront is divided into discrete points by the lenslet arrays sub-aperture lenses. Each lens of the lenslet array focuses part of the wavefront onto the image plane as a spot, where the centroid of the spot is set as a marker. If a plane wave impinges on the surface of the lenslets, the light focuses directly behind each individual lens on axis. The light forms focused spots which are observed as dots and are of a grid pattern in two dimensions. If there is uncollimated light, or aberrated light, the light from each lenslet no longer focuses directly behind each point. The spot is displaced, where the displacement of each focal position offers data that can be extracted for wavefront measurements. The discrete data points are properly summed and fitted to produce continuous information on the observed aberrations.

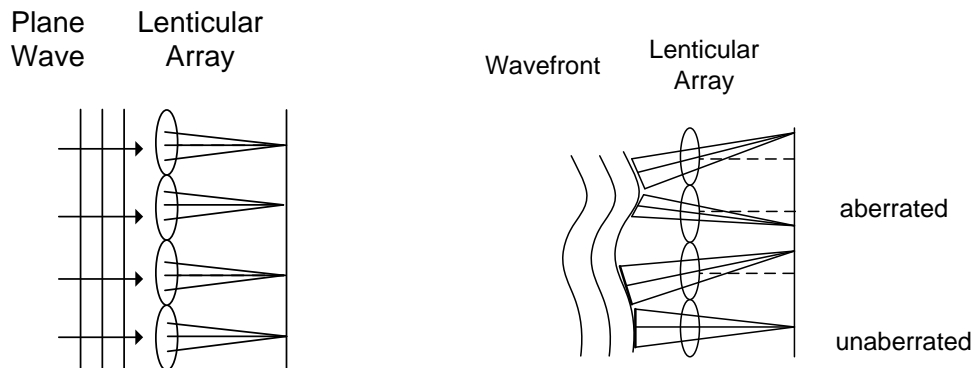


Figure 3-7 **Shack-Hartmann Wavefront Sensing:** Focus spot patterns created in the focal plane of the lenslet array illustrate how the plane wave focuses light on axis while the aberrated shows displacement.

There is a systematic approach in achieving measurable results with a Shack-Hartmann wavefront sensor. The first step is to apply a perfect plane wave to calibrate the sensor. The uniform grid pattern will have the same pitch separation between focused points as that of the pitch of the lenslet array. The next step is to test a system and see where the spots have moved

according to the aberrations. The spot displacement for each spot is then measured in the x and y dimension ( $\Delta x_{ij}, \Delta y_{ij}$ ).

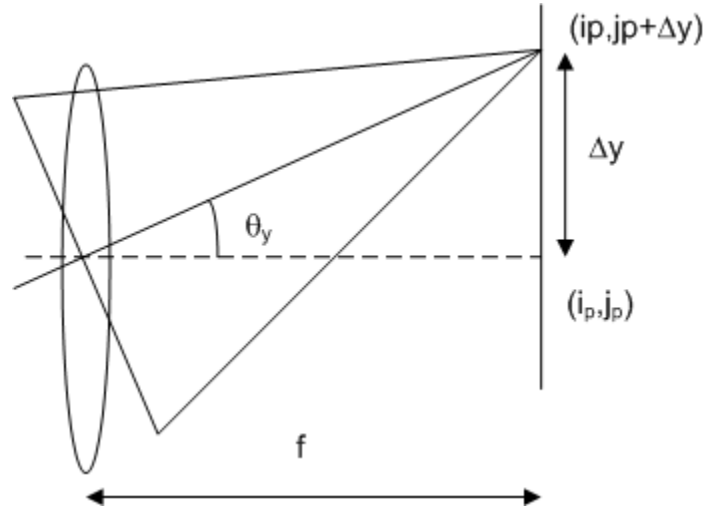


Figure 3-8 **Shack-Hartmann Spot Displacement**: Identification of the displacement of the centroid relative to the on-axis collimated wavefront in the y dimension for lens  $i_p, j_p$  of the lenslet array. This analysis is also performed in the x-dimension.

Here, we examine the position of the spot of the aberrated beam entering a single lens relative to the position of the spot for the collimated unaberrated beam that is on-axis. The lens is localized at pixel coordinates  $(i_p, j_p)$  when on axis, where we locate the center position of a single lens in the lenslet array. Here, we show a displacement in the y dimensions so that the centroid location is displaced to  $(i_p, j_p + \Delta y)$ . We can identify the slope of the wavefront for each lenslet by analyzing the displacement relative to the focal length in the y dimension, where a similar expression holds for the x derivative.

$$\Delta y = -f \frac{\partial W_{ij}}{\partial y}$$

As we know the geometric displacement, we convert the spot displacements into sets of slopes  $(\frac{\partial W_{ij}}{\partial x}, \frac{\partial W_{ij}}{\partial y})$  in both dimensions. At this point one can integrate the slope data to extract the wavefront shape,  $W$ . There are several ways to integrate the term back, where one of the more common approaches is to use least squares method for the discrete function to find the coefficients  $a_{nm}$ . Often times, there is a loss of information from terms with constant shifts such as tilt and piston terms. This approach allows for the Shack Hartmann technology to quickly extract wavefront information of a conjugate plane relative to the lenslet array. It is desired to conjugate the exit pupil of the tested system with the lenslet array through relay optics in order to achieve accurate wavefront measurements of a pupil plane.

### **3.2.5 Light Source of the Shack-Hartmann Wavefront Sensor**

The Shack-Hartmann does not require a temporally coherent light source to achieve results. The operation wavelength is therefore significant depending on the application. In vision research, a wavelength that is not in the visible range but can still pass through the ocular elements is preferred for the application of a Shack-Hartmann wavefront sensor. In early vision application, it was found that a light source in the visible caused a discomfort for patients. At a design wavelength of 780 to 800 nm the light source is at the edge of the visible spectrum, allowing for light to transmit to the retina while no longer providing a target or discomfort to the user. When calibrated at this wavelength the Shack-Hartmann wavefront sensor is also applicable as a measurement device with fluidic lenses.

### **3.2.6 Tradeoffs of the Shack-Hartmann Wavefront Sensor**

There are advantages and disadvantages of any detection system. Shack-Hartmann wavefront sensors are relatively simple setups to produce. There is however a major assumption

that allows for the sensor to function. One must assume that the wavefront that is imaged must be slowly varying over the lenslet aperture such that the wavefront appears as a tilted plane wave at the image plane from a given lens. The pitch between the lenslets defines not only the width of the lenses but also defines the relative shape that is measurable for a given spatial frequency. We are capable of producing a piecewise continuous set of faceted plane waves that impinge on the lenslet surface when assuming each section of the wave is represented by small plane waves. The limitation that develops with such a system is the measurement of a wavefront with a large curve. The spot of the plane wave entering a single lens may overlap with a spot entering from a neighboring lens. The dynamic range of the Shack-Hartmann wavefront sensor is defined as the maximum slope change that the sensor can observe.

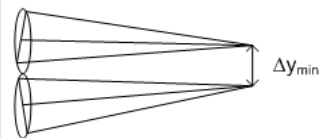
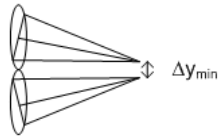
	Long Focal Length	Short Focal Length
Dynamic Range	<p>Lower Dynamic Range</p>  <p><math>\Delta y_{min}</math></p>	<p>Higher Dynamic Range</p>  <p><math>\Delta y_{min}</math></p>
Sensitivity	 <p><math>\Delta y_{sen}</math></p> <p>Higher Sensitivity</p>	 <p><math>\Delta y_{sen}</math></p> <p>Lower Sensitivity</p>

Figure 3-9 **Shack-Hartmann Dynamic Range vs. Sensitivity:** Here we illustrate the fact that longer focal lengths have a higher sensitive but worse dynamic range relative to short focal length lenslets in the array.

This illustration shows that as we decrease the focal length of the lenslet array we can increase the dynamic range. This seems as an advantageous result, but there is a tradeoff in the sensitivity of the sensor. The sensitivity describes the smallest change in slope variation that is

detected by the sensor. Therefore, the tradeoff is between having the capability of measuring higher slope angles and the sampling of smaller features within the wavefront. Determining the proper focal length and pitch relative to the pixel size of the detector varies with application and must be determined by the user.

## 4.0 SPHERICAL FLUIDIC LENSES and NON-MECHANICAL ZOOM

We can begin to explore fluidic optic designs and applications, now that we have established the concepts of fluidic lenses and a wavefront measurement approach for these fluidic lenses. As was described in section 1.3.2, there are two approaches in producing spherical profile shapes, which are both utilized in this work. Our spherical or defocus fluidic lens one produces spherical profiles by taking advantage of a large membrane locked to a frame, giving a freely supported edge design. The active clear aperture area is much smaller than the membrane shape, producing a defocus fluidic lens with no moving parts. Spherical lens two produces the spherical shape by suspension control of the frame or clamped edge design. The clear aperture active area applies a larger proportion of the membrane surface with this lens structure.

Fluidic lenses are adaptive refractive lenses where their optical power is adjustable. From a geometric standpoint, fluidic lenses offer more degrees of freedom relative to static lenses by varying the system focal length through focal position control of the individual fluidic lenses rather than varying the separation between static lenses. There are also fewer physical limitations with fluidic lenses in addition to the lower probability of optical misalignment. Zoom lens designs for optical power variation with no moving parts are achievable through active optics such as fluidic lenses. Active optics allow for optical elements to achieve optical power variation in either refractive or reflective configurations.

Fluidic lenses provide tunable optical power through form control of a surface membrane. Fluidic lenses have been achieved through different driving approaches: electro-wetting [45, 46], mechanical-wetting [47], chemical driving [48, 49], thermal driving [50, 51], radiation pressure [52] and pressure controlled elastic expansion [53, 54, 55]. Our research

focuses on the application of controlled elastic expansion of fluidic lenses. Various fluidic lens designs within our group have produced rotationally symmetric lenses, as well as cylinder lenses in sequence, which will be discussed in chapter 6 [15]. Further advanced technologies within our work have coupled fluidic lenses with variable diffractive lenses to produce a hybrid achromat design, which will be discussed in chapter 5 [56]. As fluidic lens technology has matured, multi-lens zoom systems and aberration correction systems have been analyzed [57, 58, 59]. Furthermore, zoom lens systems with two small aperture fluidic lenses applying piezo-electric actuation have been developed [60]. Our work expands on the concept of applying pressure-controlled fluidic lenses in the development of zoom lenses.

We have developed a variable power zoom system with no moving parts, which incorporates both spherical lens one and spherical lens two. The designed system applies two single chamber plano-convex fluid singlets, each with their own distinct design, as well as a conventional refractive lens. We combine the two fluid elements to form a variable power telescope, while the fixed lens enables image formation. In this configuration, the image plane location is fixed. By synchronizing the powers of the two fluidic lenses, we produce a varying magnification zoom system. The design of each lens and the coupled system is analyzed. The coupled device experimentally produced a magnification range of 0.1 x to 10 x zoom or a 20 x zoom magnification range with no moving parts. Furthermore, we expand on optical performance and capabilities of our system with fluidic lenses relative to traditional zoom lenses.

#### **4.1 Theory of Spherical Fluidic Lenses**

Our spherical lenses take advantage of pretension membranes locked into metal frames. Both designs attempt to produce evenly distributed pressure around the periphery of the membrane. This even force load allows for us to estimate the opto-mechanical designs as a

uniformly loaded circular plate with freely supported edges [17]. At small deflections the following equation is applied to map the deflection properties of our circularly symmetric lenses [61, 62]:

$$z = \frac{pR^4}{64D} \left[ -\frac{r^4}{R^4} + 2 \frac{r^2}{R^2} \left[ \frac{3 + \nu}{1 + \nu} \right] \right]$$

4-1

Where  $r$  is the radial distance from the center,  $z$  is the membrane deflection defined at zero in the center,  $p$  is the pressure,  $R$  is the radial location at the edge of the lens,  $D$  is flexural stiffness, which is a constant for a uniform thickness and material membrane, and  $\nu$  is the Poisson Ratio of the elastomer material. This equation functions as the solution for the freely supported structure and is a fair representation of spherical fluidic lens one for small deflection mappings.

Fluidic lens two has a clamped edge design rather than a freely supported design. Under these conditions the derivative of the deflection term relative to its derivative of radial distance is zero. This makes the deflection properties for a small deflection equal

$$z = \frac{pR^4}{64D} \left[ -\frac{r^4}{R^4} + 2 \frac{r^2}{R^2} \right]$$

4-2

Ultimately we apply equations 4-1 and 4-2 to determine the membrane shape by identifying the deflection  $z$  through its relative radial distance dependence for this circularly symmetric structure. The radial profile of the membrane shape is determined by the amount of deflection as we progress from the center. As one can see, if we were located at the center of the

membrane  $r = 0$  and thus the deflection equals zero. We progress from this center point to identify correlation of the radial positions  $r$  to each  $z$  deflection point. The deflection maps to a continuous radius of curvature shape for the membrane profile.

There is a variation on a constant term between the results of fluidic lens one and fluidic lens two for the defocus term with  $r^2$  dependence. The elastomer that is chosen for these projects is polydimethylsiloxane (PDMS), which has a Poisson ratio  $\nu$  of approximately 0.5. Hence, there is a scaling difference of 2.333 for our  $r^2$  defocus term of the freely supported fluidic lens 1 compared to the clamped fluidic lens 2 with small deflections.

There is a similar relationship for that of large deflections to that of small deflections [61, 63]. Large deflections are classified as deflections three times larger than the thickness of the membrane. Through the combination of large deflections and built-in stress a group was able to identify a scaling factor for large deflections through a continuation of thin plate theory [63]. Therefore, the small deflection equations are applied when the membrane flexes with deflections below three times the thickness of the membrane. The large deflection equations are applicable beyond this limit. The membrane dynamics are active once a high enough tension is introduced through deflection and preload [64].

## **4.2 Fabrication of Elastomer Membrane**

The variable surface membrane material deflected is composed of PDMS, as was previously mentioned. Our designed deformable membrane layers are moldable clear optical elastomers with uniform thickness. PDMS was chosen as the membrane material offers high optical transparency for the visible wavelengths and highly controllable elastic properties [65]. Fabrication of the PDMS membrane within a clean room begins with a PDMS mixture of

Sylgard 184 [66]. The mixture is composed of a 10:1 ratio of PDMS to curing agent, which is deposited into circular molds within a glass optical flat with better than  $5\lambda$  of surface variation. The membrane is then stirred in a vacuum chamber to remove air bubbles within the PDMS solution. The PDMS is then baked at  $140^{\circ}\text{C}$  for 45 minutes to complete the curing process. The membrane layers are removed with nylon tweezers, trimmed and clamped tightly into custom made chambers. We have designed these elastic membranes to range between  $100 - 300\ \mu\text{m}$  in thickness. Note that thicker membranes offer higher control at lower powers [67]. Both fluidic lenses use the PDMS membranes as their flexible surface, but the fluid capacity varies between designs. The variation in the design defines the dynamic range that each of these lenses can achieve.

### 4.3 Spherical Fluidic Lens One

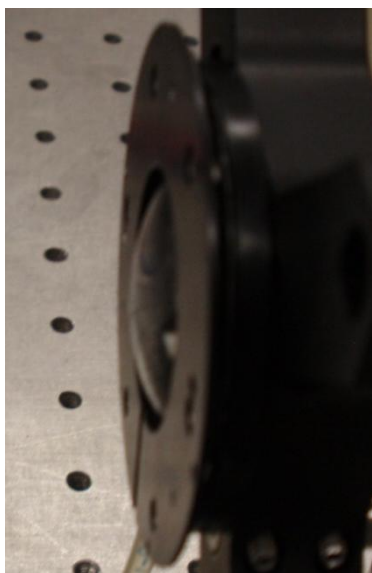


Figure 4-1 **Fluidic Lens 1:** Here is an image of the fabricated, machined and assembled fluidic lens 1.

As was previously described, each refractive fluidic lens is a plano-convex singlet. The plano side of each lens has an optical flat while the optically clear fluid is sealed within a flexible

membrane on the opposing side. There is a predetermined amount of fluid inserted into each lens. The curvature of the membrane surface is altered through the hydrostatic pressure in the fluidic-filled lens cavity. By properly designing the optical lens there is an even distribution and a continuous radius of curvature in the active optical area, which reduces undesired third order aberrations. The fluid control within the active area is achieved with syringes controlling the amount of fluid within the active chamber area. During preparation, fluid is inserted in excess within the chamber as to induce a vacuum pressure to evacuate air. The air would be treated as a second index within the clear aperture if not evacuated, resulting in a drastic alteration of desired lens properties. The change of only the membrane curvature with pumped fluid allows for control of the exiting focal length within our fluidic lenses.

Fluidic lens 1 was designed with a flat glass surface face of 12.5 mm on the plano side and a clear aperture diameter of 10 mm. A circularly shaped opto-mechanical wedge protrudes beyond the rim of the housing to produce a rotationally symmetric base for the fluidic chamber. The membrane is secured onto the top housing with a retainer ring. Physically, the fluidic lens is capable of achieving both positive and negative focal lengths. The amount of fluid infused or withdrawn from the lens cavity was designed for the maximization of positive power as we were developing a Keplerian-type telescope which requires two positive focal lengths lenses. Similarly, we could have chosen to produce a Galilean telescope if we adjusted the amount of fluid within a single fluidic lens chamber to produce negative focal lengths. The selected fluid is infused through a tube from pump controlled syringes to a fluidic fitting connected to the chamber. The syringe infusion or withdrawal of fluid alters the radius of curvature of the membrane and hence the optical power of each fluidic lens.

We have created a test bed to measure the optical power of the fluidic lenses. A collimated laser beam is shone through the fluidic lens. The back focal distance of the lens is measured as a function of fluid volume. By systematically varying the amount of fluid in the chamber, we can relate the lens focal length to fluid volume.

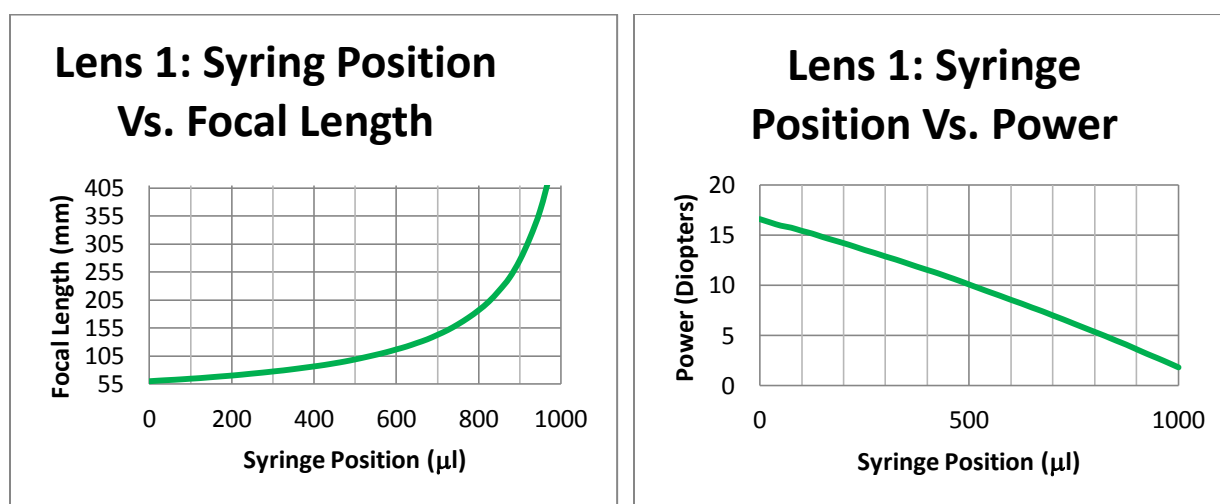


Figure 4-2 **Zoom Control of Fluidic Lens 1:** We observe the variation of focal length on the left and the change in power on the right as fluid is evacuated from the syringe connected to fluidic lens 1.

The plots in Figure 4-2 illustrate the characterization of fluidic lens 1 and the dynamic focal range of our lens. De-ionized (DI) water was placed in the chamber and syringe to characterize the fluidic lenses focal range for both fluidic lenses. DI water has an Abbe number of 55.74 and an index of refraction of 1.34 [68]. Figure 4-2a specifically characterizes the focal length range of fluidic lens 1. The syringe position describes the amount of fluid contained within the syringe. At 0  $\mu\text{l}$  all of the fluid in the syringe is in the lens chamber and the highest radius of curvature observed for the membrane of fluidic lens 1. In this position, fluidic lens 1 has a focal length of 55 mm. When the plunger is fully withdrawn, 1 ml of fluid is removed from the lens chamber, corresponding to a focal length of over 400 mm.

Figure 4-2b identifies the power range that this fluidic plano-convex lens is capable of reaching. We find that fluidic lens 1 has a dynamic range of 15 Diopters with a 1 ml syringe. If we opted to apply a 2 ml syringe instead of a 1 ml syringe the dynamic range of fluid lens 1 would be -17 Diopters to 17 Diopters, assuming the same amount of initial fluid was deposited within the active chamber. Our desire for this Keplerian telescope was to maintain positive lenses and thus a 1 ml syringe was most desirable.

#### 4.4 Spherical Fluidic Lens Two



Figure 4-3 **Fluidic Lens 2:** Here is an image of the fabricated, machined and assembled fluidic lens 2.

Fluidic lens 2 varies in membrane suspension and tension design as this is a clamped edge design. The membrane is compressed between two pre-tensioners, which maintain small amounts of stress on the membrane. These pre-tensioners support the tensioners by applying pressure on the membrane side of the chamber. The pre-tensioners are aligned and connected onto the base of the fluidic lens. A force is applied from the tensioner that locks the base and pre-tensioners together to the tensioner. The base of the fluidic lens possesses an optical flat

which again defines the plano side of fluidic lens 2. Again we have designed a holder for a 12.5 mm flat optical window and the clear aperture of the second fluidic lens is 10 mm. This assembly produces tighter tension for fluidic lens 2 relative to fluidic lens 1, which results in a greater dynamic range for fluidic lens 2. There again is a port that connects the fluid chamber to a syringe pump. Similarly to fluidic lens 1, fluidic lens 2 can produce lens powers that are either positive or negative. We identified the focal length and power range of fluidic lens 2 with our testing apparatus and DI water.

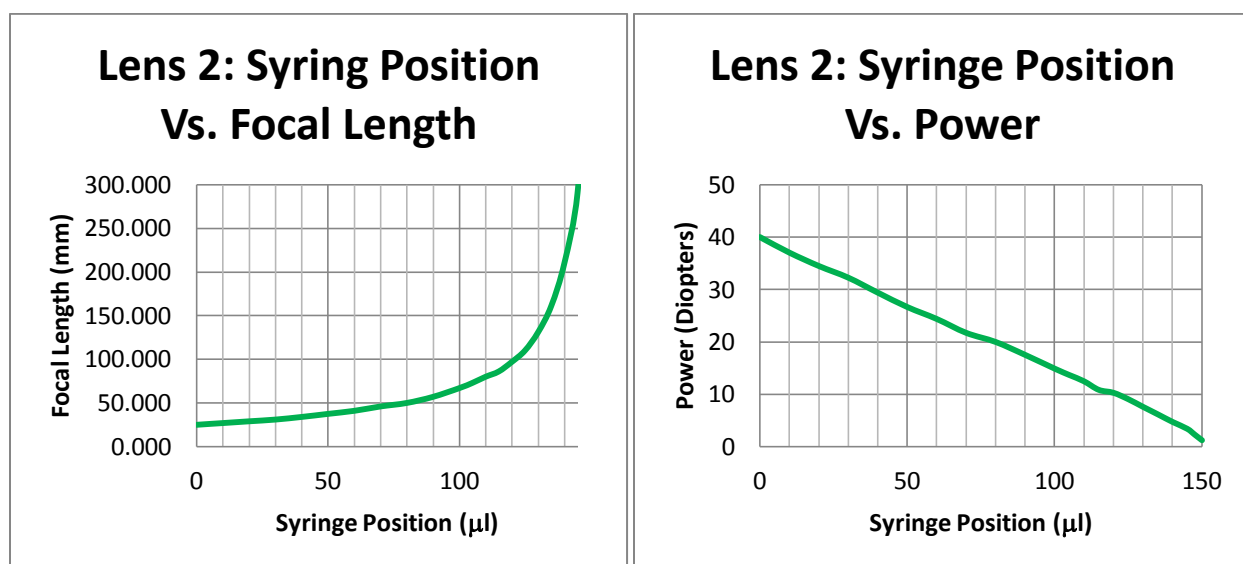


Figure 4-4. **Zoom Control of Fluidic Lens 2:** We observe the variation of focal length on the left and the change in power on the right as fluid is evacuated from the syringe connected to fluidic lens 2.

The plots in Figure 4-4 show the characterization of fluidic lens 2 and the dynamic focal range of our lens with a syringe that applies 150  $\mu\text{L}$  of fluid. De-ionized (DI) water is again used in the chamber. The shortest radius of curvature observed for the membrane of fluidic lens 2 at 0  $\mu\text{L}$  provided a focal length of 25 mm.

#### 4.5 Zoom Lenses

We have designed two fluidic lenses whose elastomer membrane produce spherical profiles. Zoom lenses are often found in imaging systems and are applied within numerous fields of optics. Zoom lenses are devices that maintain focus at a defined image plane while altering the systems optical power. Traditional zoom systems apply physical motion between optical elements to alter the systems optical power through mechanical motion. Mechanical motion of optical elements is often cumbersome, expensive, and optical misalignment can occur due to complex cam mechanics required to drive the individual lenses [22]. Optical lenses with fixed focal lengths limit the dynamic design of zoom optical systems.

We have designed, modeled, and fabricated two separate fluidic lenses with widely tunable zoom capabilities and larger apertures than previous designs. Here, we demonstrate a zoom system with two refractive fluidic lenses that require no translation of the optical elements. Specifically, the fluidic lenses form a Keplerian Telescope with variable angular magnification, combined with a static lens to enable imaging.

#### **4.6 Theory: Variable Power Zoom System**

Traditional zoom systems control optical power by adjusting lens positions. Complex zoom systems apply multiple lens groups that move independently to sustain a fixed image plane. The two lens zoom system is the most basic zoom system with a defined focal length and back focal distance. The separations of the two optical elements, as well as the distance between the rear element and the image plane are adjusted to maintain a fixed image location, while the total system focal length is varied. A second option in controlling the systems optical zoom power develops by adjusting the optical power of each refractive lens rather than adjusting the position of the optics. Variable power lenses differ from traditional zoom lenses, which depend on mechanically moving optics to adjust focus. Fluidic lenses offer the capability of controlling

individual element focal lengths, while eliminating the need to adjust lens positions. Variable power zoom systems are achievable when synchronizing two or more fluidic lenses. Our primary focus is in the production of a zoom system consisting of a Keplerian telescope and a fixed power lens for zoom imaging.

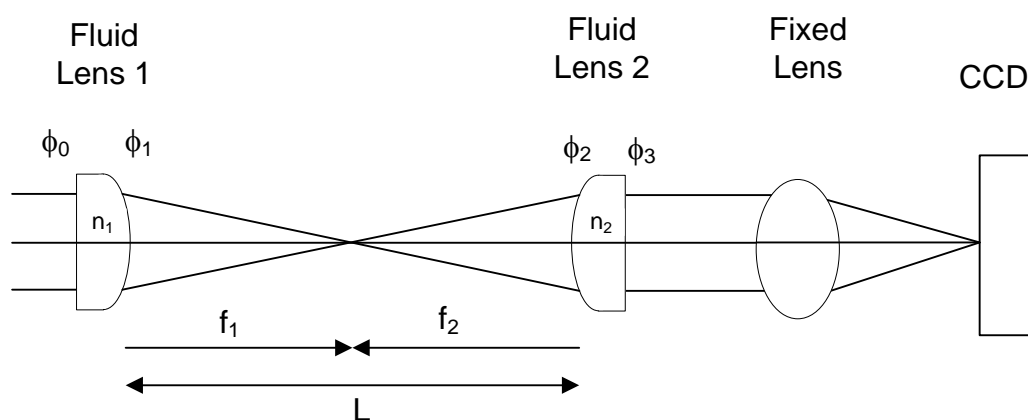


Figure 4-5 **Zoom System:** Schematic of an afocal system with two plano-convex fluidic optical elements coupled with a fixed lens as a relay to produce a zoom lens system.

Figure 4-5 illustrates the configuration of our design. Each of the fluidic lenses offers a single active surface which varies in power. Surface one ( $\phi_1$ ) is the variable power surface for the first fluidic lens and surface two ( $\phi_2$ ) is the variable power surface for the second fluidic lens. Surfaces zero and three are fixed plates that offer no optical power as our fluidic lenses are both plano-convex. The thicknesses of the fluidic lenses does not affect the lens power when we vary the amount of fluid within the chambers as each fluidic lens has a surface of zero optical power. We therefore treat surface 1 and surface 2 as thin lens representations of each liquid lens. If we opted to take advantage of both optical surfaces per fluidic lens, rather than applying a plano-convex lens within a single optic, we would have to characterize the optical effects on the separation of the two surface vertices relative to each other to measure the power exiting each fluidic lens. The final element in Figure 4-5 is a static lens that takes the collimated

light emerging from the second fluidic lens element and focuses it onto a fixed image plane. In this manner, if the first two elements maintain an afocal configuration, then the final element will ensure the location of the image plane remains fixed.

Consider the net power of the first two elements of Figure 4-5. In general, the net power of two thin lenses in free space is given by

$$\varphi_{sys} = \frac{1}{f_{sys}} = \varphi_1 + \varphi_2 - \varphi_1\varphi_2L = \frac{1}{f_1} + \frac{1}{f_2} - \frac{L}{f_1f_2}$$

4-3

where  $\varphi_{sys}$  is the power of the optical system,  $f_{sys}$  is the focal length of the optical system,  $\varphi_1$  and  $f_1$  are the power and focal length of surface one from the first fluidic lens respectively,  $\varphi_2$  and  $f_2$  are the power and focal length of surface two from the second fluidic refractive lens respectively, and  $L$  is the length between the first fluidic lens and the second fluidic lens. Our zoom system seeks to keep  $\varphi_{sys} = 0$  so that the final static element focuses the emerging collimated light onto the image sensor. To maintain the afocal relationship of the first two elements, the separation between the fluidic elements must satisfy  $L=f_1+f_2$ . Each of our fluidic lenses can vary independently in focal length by controlling the fluid pressure within each lens chamber. We are thus able to produce a Keplerian telescope with the first two elements by synchronizing the focal length of the fluid lenses so that the sum of the focal lengths always equals the separation of the two optical elements. The third element then will convert the collimated light emerging from the telescope and form an image at its rear focal point. As the relative focal lengths of the first two elements are varied in sync, the magnification of the entire system changes, but the image location remains fixed.

#### 4.7 Experiment: Zoom System Verification

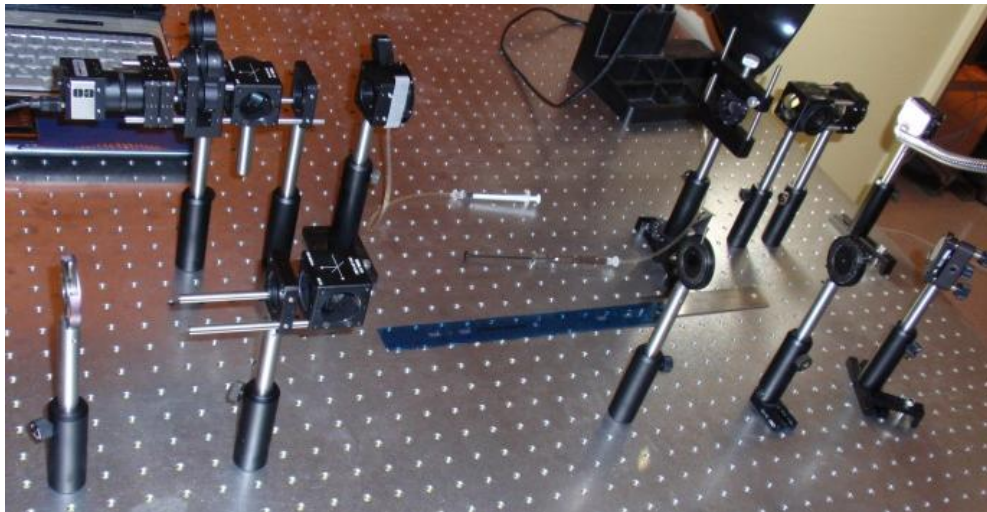
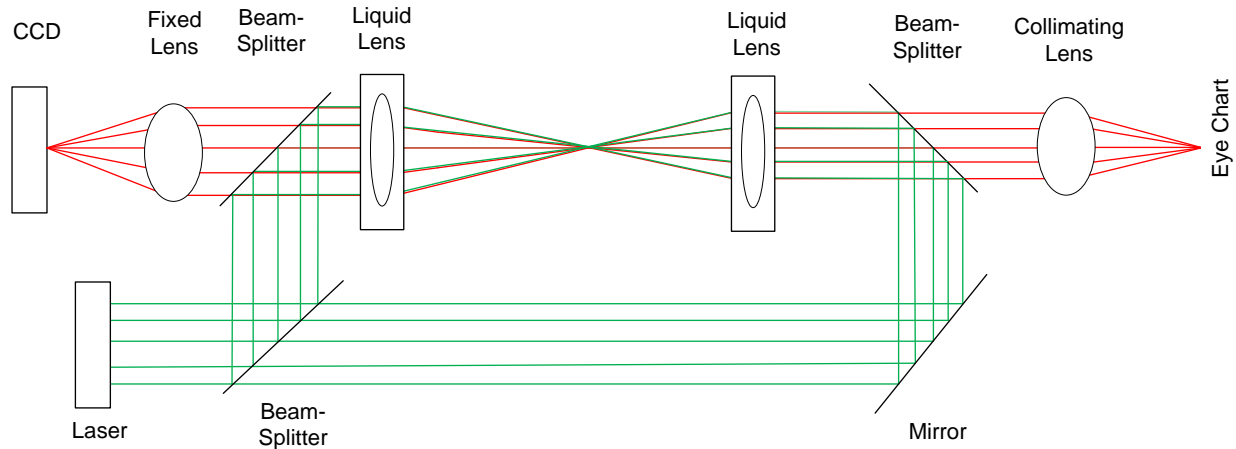


Figure 4-6 **Zoom System Setup:** Above we display the physical setup of the experiment. A laser system was designed to verify the focal location of each of the fluidic lenses separately. A letter chart is placed at a distance while being imaged to our ccd camera through our zoom system.

The setup shown in Figure 4-6 was used to verify the properties of our proposed system. The fluidic lens telescope is placed between two fixed lenses. An inverted letter chart is placed at the front focal point of the first fixed lens. This illuminated letter chart is then projected through the telescopic system and through a second fixed lens which focuses light onto a CCD array. The variation in power of the coupled fluidic lenses produces variable magnification as is observed on the CCD. An additional off axis green laser source was added into the active optical

design to analyze the focal positions of the fluidic lenses. The exact focal position was measured and compared to the expected focal locations of each of the fluidic lenses. We synchronized the two fluidic lenses to gain the desired change in magnification. To increase the dynamic range of the experiment we applied fluidic lens 1 as our objective lens and fluidic lens 2 as our eyepiece for half of the experiment. We then switched the positions allowing for fluidic lens 2 to become the objective lens and fluidic lens 1 to become the eyepiece. This produced a wider magnification range as is observed in Figure 4-7. Table 4-1 summarizes the configuration for the various magnification levels.

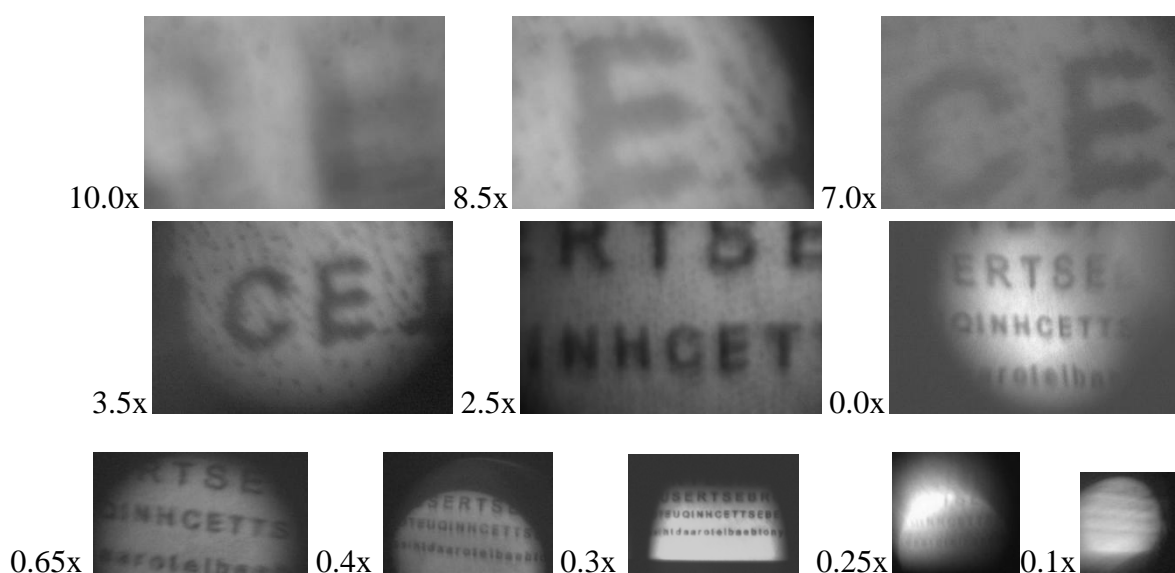


Figure 4-7 **Zoom Magnification of a Letter Chart:** Experimental results achieved by varying the two fluidic lenses as a zoom system. The magnification values shown are approximate magnifications that were achieved. The exact theoretical and experimental values are observed in the chart below. Chart illumination was adjusted as vignetting varied between the two fluidic lenses.

Sample	L <sub>1</sub> (mm)	L <sub>2</sub> (mm)	m <sub>Theory</sub>	m <sub>Experimental</sub>	% Error
1	340	35	0.10294	0.10959	6.46
2	300	75	0.25	0.26027	4.11
3	285	90	0.31579	0.31507	-0.23
4	265	110	0.41509	0.41096	-0.99
5	225	150	0.66667	0.65753	-1.37
6	180	180	1.00	1.00	0
7	107.5	267.5	2.48837	2.46575	-0.91
8	82.5	292.5	3.54545	3.53425	-0.32
9	47.5	327.5	6.89474	6.80822	-1.25
10	40	335	8.375	8.43836	.76
11	32.5	342.5	10.5385	10.65909	1.14

Table 4-1 **Zoom Magnification:** This table shows the experimental magnification of the 11 images shown in figure 4-7. We compare the experimental results to the theoretical results by analyzing the observed percent error.

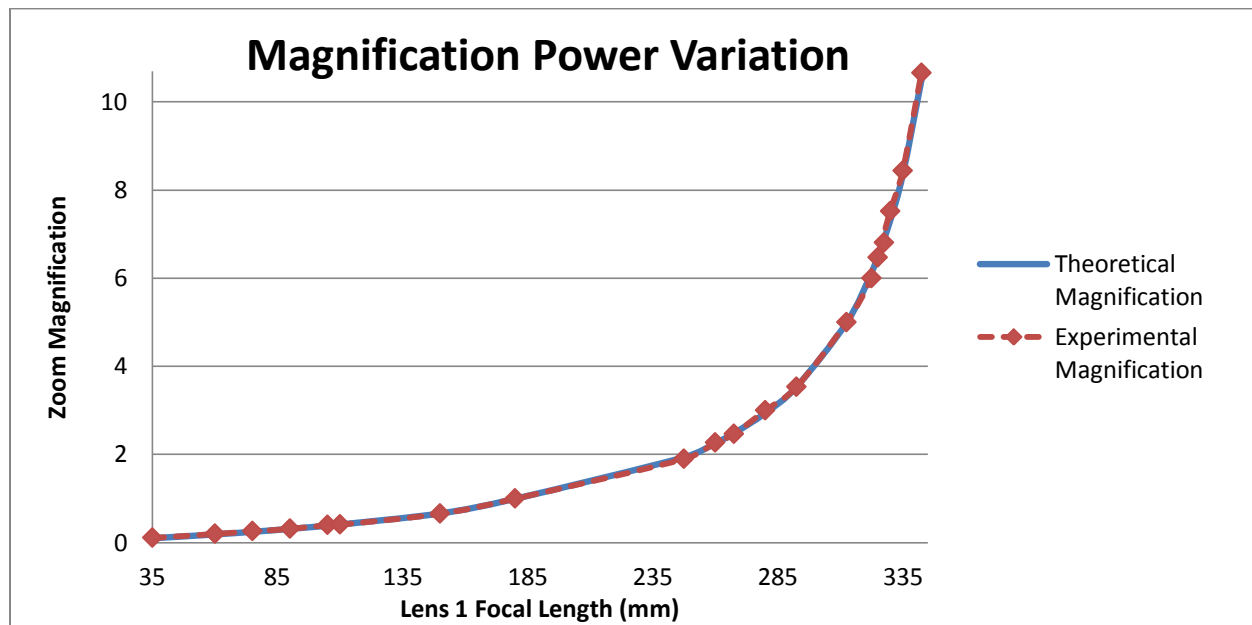


Figure 4-8 **Experimental vs Theoretical Zoom Magnifying Power:** Twenty sample points were measured to produce the continuous experimental magnification compared to the theoretical magnification for the zoom system.

Figure 4-8 shows a plot of the theoretical and achieved magnification. The measurement of the theoretical magnification was determined from the focal lengths of each of the fluidic

lenses. We specifically picked the letter E from the second to bottom line on the letter chart. The experimental magnification was assessed through an analysis of the image height at each magnified configuration relative to the image height of the telescope set at 1:1 imaging. We then analyzed the variation of error between the theoretical magnification and the expected magnification. Theoretically we expected a dynamic range from 0.07 x to 14 x, but were not able to achieve this range experimentally. The achievable dynamic range of our system was from 0.12 x to 10.5 x, offering a change of magnification of approximately 20 x.

#### **4.8 Limitations of Fluidic Zoom System**

The two limiting factors for our zoom optical system are vigneting and aberrations. The limitations on magnifying came from the size of our fluidic lenses. The two lenses offer a clear aperture of 10 mm. These clear apertures block off axis ray bundles from reaching our CCD array. The angular subtend of our off axis ray bundles increases as we increase the radius of curvature, power, of the fluidic lenses. This vignetting effect decreases the systems optical throughput, requiring an increased amount of illumination at the object plane. After a magnification of 3 x we inserted a second light source to increase the etendue off the reflected surface of the object plane. We found that the size of the letter E at approximately 8.5 x magnification no longer fit in the active area of the CCD. In order to attain accurate results for 10 x magnification, analysis of the center line to base line of the magnified image E was compared to the center line to base line of the letter E when the telescope is set to 1:1 imaging. In addition, the light loss beyond 10 x was significant, even with both light sources illuminating the object plane at maximum power, causing poor imaging conditions that limited magnification.

Aberrations were also observed to limit the image quality of the letters. We found that as we altered the amount of fluid in the synchronized fluidic lenses the letter chart drifted up and

down. We found that a slight amount of tilt caused our image plane to slightly move, but was negligible as the results remained on the ccd plane. There was also observed distortion as we observed a slight waviness in the outputted letter lines. Also, a negligible amount of astigmatism can be observed from a slight rotation of the letter lines when comparing the 0.1 x thru to the 10 x magnification. Results were achievable as the aberrations were not dominant enough to destroy resolvability of the letter lines.

We have demonstrated a zoom imaging system that consists of two variable pressure controlled liquid lenses. We used two refractive fluidic lenses to produce zoom power in a Keplerian telescope setup. A static lens in combination with the fluidic Keplerian telescope stabilized the image plane at the CCD array. The fluidic lenses provided continuous variation in focal power, which enabled us to produce zoom magnifications between 0.1 x to 10 x with results that nearly matched the theoretical values. The full range in magnification we experimentally produced a 20 x variation in magnification. This zoom imaging system has no moving parts and offers potential in the stabilization of static refractive zoom systems.

## 5.0 FLUIDIC ACHROMATS

A traditional achromatic lens or achromat corrects for primary chromatic aberration by matching the focal points of a red and a blue wavelength. The dispersion is reduced over the visible spectrum, however residual secondary chromatic aberration remains at the green wavelength. Achromatic doublets consist of a crown glass and a flint. The crown glass has a positive focal length with low dispersion while the flint has a negative power with high dispersion. The combination of these two glass disparities is designed to match the red and blue wavelengths to a common focus along the optical axis (z-axis) to eliminate primary chromatic aberration.

As we have shown in the previous chapter, fluidic lenses are a very powerful tool for systems design. In this chapter, we will describe two designs with fluidic technology that enables for us to correct for chromatic aberration. The first design describes the combination of a variable lens with our fluidic lens 1. Fluidic lens 1 applies the freely supported edge design in the creation of our achromatic design. We have previously discussed fluidic lens 1 and so this section will discuss the facilitation of the lens and its combination to a syringe actuation system. We will also illustrate the diffractive / refractive achromat with discrete focal lengths of correction [56]. The second design is the creation of a dual chamber clamped edge design fluidic achromat. There are two chamber controlled by syringe actuation. When the two surfaces are synched, one can produce the proper achromatization at continuous wavelengths. By reverse engineering data from ZEMAX we determined how to produce an achromat with two known liquid materials. We have designed this achromat in SolidWorks and will explain a structural approach in achieving achromatization with this design.

## 5.1 Achromat One: Diffractive / Refractive Hybrid

We demonstrate a variable focal length achromatic lens that consists of a flat liquid crystal diffractive lens and a pressure-controlled fluidic refractive lens. The diffractive lens is composed of a flat binary Fresnel zone structure and a thin liquid crystal layer, producing high efficiency and millisecond switching times while applying a low ac voltage input. The focusing power of the diffractive lens is adjusted by electrically modifying the sub-zones and re-establishing phase wrapping points. The refractive lens includes a fluid chamber with a flat glass surface and an opposing elastic polydimethylsiloxane (PDMS) membrane surface. Inserting fluid volume through a pump system into the clear aperture region alters the membrane curvature and adjusts the refractive lens' focal position. Primary chromatic aberration is remarkably reduced through the coupling of the fluidic and diffractive lenses at selected focal lengths.

It is known that diffractive lenses have strong chromatic aberration [69]. We have previously reported on designing and demonstrating adjustable focus diffractive lenses using liquid crystal as the variable index medium [70, 71]. In this paper, we present an adjustable liquid crystal diffractive lens and an adjustable pressure-controlled fluidic lens that in combination (Figure 5-1) minimizes primary chromatic aberration. Previously, discrete tunable liquid crystal diffractive lenses [70, 71, 72, 73, 74], continuous tunable liquid crystal refractive lenses [75, 76, 77], and continuous tunable fluidic lenses [78, 79, 67] with variable focal lengths were demonstrated individually. At each focal location chromatic aberration is observable when uncorrected. Chromatic aberration is greater in elements with larger dispersion, such as diffractive lenses, and becomes more significant for materials with lower Abbe numbers. Diffractive and holographic lenses have been proposed to replace the traditional achromatic doublets for fixed focal length designs [69, 80]. More recently, a useful hybrid variable focal

length fluidic/diffractive lens was demonstrated; however, the diffractive component applies a fixed focal length [81]. We have extended this work to include a variable focal length diffractive component. In effect, we have created a variable achromatic doublet with no moving parts.

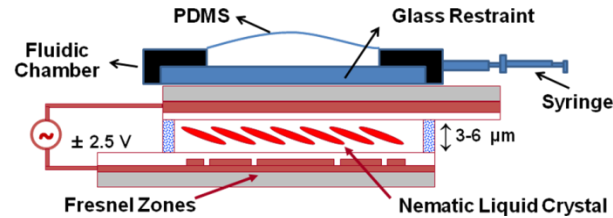


Figure 5-1 **Diffractive / Refractive Hybrid Design:** Schematic of the hybrid liquid crystal diffractive lens and fluidic lens.

Diffractive lenses have an Abbe number much smaller than their refractive counterparts [69]. The Abbe number of a diffractive lens is unique in that it is equal to  $-3.45$ , solely dependent upon the specified Fraunhofer  $d$ ,  $F$ ,  $C$  wavelengths, as given by  $V_{\text{diffractive}} = \lambda_d / (\lambda_F - \lambda_C)$  [69, 80]. The focal length of a Fresnel zone-based diffractive lens is given by  $f = r_1^2 / (2 \lambda)$  where  $r_1$  is the radius of the first Fresnel zone and  $\lambda$  is the wavelength of the incident light [69]. Therefore, the focal length at any other wavelength  $\lambda$ , in nm, can be scaled by the design wavelength according to  $f(\lambda) = (555/\lambda) f_d$  where  $f_d$  is the design focal length at  $555 \text{ nm}$ .

An approach must be established to correlate the diffractive lens with the refractive lens. For certain focal lengths of the diffractive lens,  $f_d$ , we may choose the focal lengths and Abbe number of the fluidic lens such that they satisfy the achromat equation:  $f_f V_f - 3.45 f_d = 0$ , where  $f_f$  and  $V_f$  are the focal length and Abbe number of the fluidic lens, respectively. Refractive lenses have an Abbe number that is related to the indices of refraction as specified by the Fraunhofer  $d$ ,  $C$ ,  $F$  lines where  $V_{\text{fluidic}} = (n_d - 1) / (n_F - n_C)$ . By knowing the focal length of the diffractive lens and the Abbe numbers of the refractive and diffractive lenses, one is able to determine the focal length range of the fluidic lens required to achieve an achromat. Table 5-1 identifies which focal

length ranges are necessary for a variable fluidic lens to produce an achromat with diffractive lenses ranging between 67 mm and 1000 mm focal lengths at specified Abbe numbers of the refractive lens. Optical glasses have an Abbe range between 25 and 65 [20], however using optical fluids increases this range of achievable Abbe numbers. Once the focal lengths are determined to identify what is necessary to match the diffractive lenses, the proper Abbe number and hence fluid may be chosen to achieve this goal.

### 5.1.2. Liquid Crystal Diffractive Lens

We began by designing diffractive elements with known focal lengths and Abbe numbers. We developed two variable focal length diffractive lenses. Diffractive lens A possesses a design focal length of 1000 mm at  $\lambda=555 \text{ nm}$  with a clear aperture of 10 mm and eight binary phase quantization that results in a maximum diffraction efficiency of 94.9% in theory. Diffractive lens B possesses a design focal length of 400 mm at  $\lambda=555 \text{ nm}$  with a clear aperture of 6 mm and twelve levels of binary phase quantization that results in a maximum diffraction efficiency of 97.7% in theory. By properly shunting the electrodes, the diffractive lens A can provide focal lengths of 1000 mm, 500 mm, and 250 mm, and the diffractive lens B can provide 400 mm, 200 mm, 133 mm, 100 mm, and 67 mm focal lengths [80, 81].

Desired phase profiles are achieved by shifting the effective refractive index of a nematic liquid crystal. The nematic liquid crystal is sandwiched between a flat Fresnel zone electrode substrate and a ground reference substrate, where both substrates contain a transparent and conductive Indium-Tin-Oxide (ITO) layer. To maintain the electrical isolation between the electrodes in the diffractive lens A, the odd-numbered and even-numbered electrodes are formed in two separate layers with an insulating layer of  $\text{SiO}_2$  in between [81]. For the diffractive lens B, one-micron gaps are implemented as isolators between the electrodes that reduce the fabrication

steps [80]. The electrodes (or subzones) of the same counting index within each of the Fresnel zones are connected to bus bars through bias made in the insulating layer of  $\text{SiO}_2$ .

Fabrication of our diffractive lenses involves a few steps of deposition, lithography and etching. Ion beam sputtering was the deposition method used to produce uniform films of around 150 nm thick. Then photo-lithography was carried out using a diluted S-1805 photoresist (from Rohm and Hoss) and Karl-Suss MA6 mask aligner. The patterns were then etched using the appropriate acids/etchants for each layer. After the micro-fabrication process, both the patterned electrodes and the reference substrates are spin-coated with a nylon alignment layer. The substrates are then baked at 115 °C, buffed unidirectionally, and put together in the anti-parallel geometry to provide a homogeneous molecular orientation for the liquid crystal. Glass fiber spacers are used in the cell assembly. The lens cell is filled with the liquid crystal (E7 from Merck) via the capillary action at a temperature above the clearing point (60°C) and cooled slowly to the room temperature. Finally, the cell is sealed and connected to drive electronics through a set of thin stranded wires.

Two resistive circuits with eight and twelve potentiometers drive the diffractive lenses. The resistances and the input voltage, hence the driving electric field across different Fresnel subzones, are adjusted to introduce the appropriate phase shift for the maximum diffraction efficiency. The voltages are applied simultaneously and are monotonically increasing from the first to the last subzone. The focal lengths are electronically switchable to fractions of the maximum design focal length in milliseconds. It is also possible to achieve negative focal lengths by reversing the order in which the voltages are applied to the diffractive lenses, thus reversing the slope of the phase profile. [80, 81]

### **5.1.3 Fluidic Refractive Lens**

The refractive lens is the freely supported edge fluidic lens 1. The refractive lens is a plano-convex singlet with a predetermined amount of fluid inserted into the lens chamber. During preparation, fluid is inserted in excess within the chamber as to induce a vacuum pressure to evacuate air. If the air is not evacuated then it is treated as a second index within the clear aperture, resulting in a drastic alteration of desired lens properties. Only the membrane curvature changes when fluid is pumped into the chamber since the frame is metal and the opposing side is transparent glass.

The chamber is a metal frame which the membrane locks into, possessing a clear aperture within the center and flanges on its periphery. Control of the lens' output shape is achieved by controlling the clear aperture's optomechanical shape, where this clear aperture has a circular shape as to produce a rotationally symmetric fluidic lens. There is a retainer ring that has equal and opposite flanges relative to the metal frame. Through pressure, the membrane is applied onto the flat metal frame and the retainer ring locks the membrane onto the frame. This flat frame is then aligned and squeezed into a two part assembly, creating the singlet chamber. The chamber is then mounted onto a frame that has openings to place onto a rail. The chamber posses a single fluidic fitting that connects the fluid chamber to a syringe.

A syringe is placed into a pump system that alters the fluid output, permitting for control of the fluidic lens' radius of curvature and focal length. The applied pump controllers operate at a maximum of 0.0125 ml / sec, an operation rate of 50  $\mu$ l in 4 seconds. This corresponds to a focal shift of approximately 10 mm per 50  $\mu$ l evacuation when there is high lens curvature, and a shift of approximately 50 to 100 mm per 50  $\mu$ l evacuation. The boundary between high curvature and low curvature varies with the designed focal length. With our fluidic chamber, which was designed for an 80 mm base focal length with methanol, an evacuation of 150  $\mu$ l

defines our barrier between low curvature and high curvature. It is observed in Figure 5-4 as the approximate location in which the slope varies in the relative amount of fluid evacuated. Due to drastic fluid removal effects at flatter curvatures, it was opted to decrease the amount of fluid inserted or removed at higher radii of curvature. A plano-convex lens is developed over this region and only positive focal lengths are selectively outputted.

#### **5.1.4. Test Methods and Results of the Hybrid Diffractive / Refractive Achromat**

It is non-trivial to place the proper fluid into the chamber when compensating for the diffractive lens. Identifying the proper fluid came from a four step process. Firstly, one must identify the membrane's radius of curvature range. This allows for one to physically characterize the limitations of the fluidic lens. Also, by identifying the radius of curvature with a known fluid, it is possible to quantify the focal length range of any fluid by knowing the new fluid's index of refraction. Once one knows the achievable radii of curvature and focal lengths of the fluidic lens, it is necessary to specify the focal lengths needed to compensate for the diffractive lens. For our experimental setup, we have already specified the Abbe number of the diffractive lenses and also the focal lengths achievable by our diffractive lenses. Table 5-1 took these values into consideration and found the focal length solutions of fluids at a wide scope of Abbe values. Therefore, we match the physical focal length range of the fluidic lens to a reasonable Abbe number so that a high percentage of achromatic doublets are achievable. The final step is to identify a fluid with the proper index of refraction and Abbe number as was previously assessed. It is also important that the fluid found is non-reactive or absorptive with the membrane that one is applying. Through this approach we satisfy the achromat equation:  $f_1 V_1 + f_2 V_2 = 0$ , where  $V$  is the Abbe number.

Diffractive lens powers and focal lengths	Needed $f_g$ if $V_f=5$	Needed $f_g$ if $V_f=10$	Needed $f_g$ if $V_f=13.66$	Needed $f_g$ if $V_f=15$	Needed $f_g$ if $V_f=20$
1 D (1000 mm)	690.00	345.00	252.56	230.00	172.50
2.0 D (500 mm)	345.00	172.50	126.28	115.00	86.25
2.5 D (400 mm)	276.00	138.00	101.02	92.00	69.00
4.0 D (250 mm)	172.50	86.25	63.14	57.50	43.13
5.0 D (200 mm)	138.00	69.00	50.51	46.00	34.50
7.5 D (133.33 mm)	92.00	46.00	33.67	30.67	23.00
10 D (100 mm)	69.00	34.50	25.26	23.00	17.25
15 D (66.66 mm)	46.00	23.00	16.84	15.33	11.50
20 D (50 mm)	34.50	17.25	12.63	11.50	8.63
25 D (40 mm)	27.60	13.80	10.10	9.20	6.90
30 D (33.333 mm)	23.00	11.50	8.42	7.67	5.75
35 D (28.57 mm)	19.71	9.86	7.22	6.57	4.93
40 D (25 mm)	17.25	8.63	6.31	5.75	4.31
50 D (20 mm)	13.80	6.90	5.05	4.60	3.45
60 D (16.66 mm)	11.50	5.75	4.21	3.83	2.87
	Needed $f_g$ if $V_f=25$	Needed $f_g$ if $V_f=30$	Needed $f_g$ if $V_f=35$	Needed $f_g$ if $V_f=40$	Needed $f_g$ if $V_f=45$
1 D (1000 mm)	138.00	115.00	98.57	86.25	76.67
2.0 D (500 mm)	69.00	57.50	49.29	43.13	38.33
2.5 D (400 mm)	55.20	46.00	39.43	34.50	30.67
4.0 D (250 mm)	34.50	28.75	24.64	21.56	19.17
5.0 D (200 mm)	27.60	23.00	19.71	17.25	15.33

7.5 D (133.33 mm)	18.40	15.33	13.14	11.50	10.22
10 D (100 mm)	13.80	11.50	9.86	8.63	7.67
15 D (66.66 mm)	9.20	7.67	6.57	5.75	5.11
20 D (50 mm)	6.90	5.75	4.93	4.31	3.83
25 D (40 mm)	5.52	4.60	3.94	3.45	3.07
30 D (33.333 mm)	4.60	3.83	3.29	2.87	2.56
35 D (28.57 mm)	3.94	3.29	2.82	2.46	2.19
40 D (25 mm)	3.45	2.88	2.46	2.16	1.92
50 D (20 mm)	2.76	2.30	1.97	1.73	1.53
60 D (16.66 mm)	2.30	1.92	1.64	1.44	1.28
	Needed $f_g$ if $V_f=50$	Needed $f_g$ if $V_f=55$	Needed $f_g$ if $V_f=60$	Needed $f_g$ if $V_f=65$	Needed $f_g$ if $V_f=70$
1 D (1000 mm)	69.00	62.73	57.50	53.08	49.29
2.0 D (500 mm)	34.50	31.36	28.75	26.54	28.75
2.5 D (400 mm)	27.60	25.09	23.00	21.23	19.71
4.0 D (250 mm)	17.25	15.68	14.38	13.27	12.32
5.0 D (200 mm)	13.80	12.55	11.50	10.62	9.86
7.5 D (133.33 mm)	9.20	8.36	7.67	7.08	6.57
10 D (100 mm)	6.90	6.27	5.75	5.31	4.93
15 D (66.66 mm)	4.60	4.18	3.83	3.54	3.29
20 D (50 mm)	3.45	3.14	2.88	2.65	2.46
25 D (40 mm)	2.76	2.51	2.30	2.12	1.97
30 D (33.333 mm)	2.30	2.09	1.92	1.77	1.64
35 D (28.57 mm)	1.97	1.79	1.64	1.52	1.41

40 D (25 mm)	1.73	1.57	1.44	1.33	1.23
50 D (20 mm)	1.38	1.25	1.15	1.06	0.99
60 D (16.66 mm)	1.15	1.05	0.96	0.88	0.82

Table 5-1 **Achromat Lookup Table:** Values needed for fluidic lens focal lengths  $f_g$  (in mm) at different fluid Abbe number values and given diffractive lens focal lengths at the design wavelength of 555 nm.

De-ionized (DI) water was first used to characterize the fluidic lens' radius of curvature range. DI water has an Abbe number of 55.74 and the indices of refraction are known for a wide scope of wavelength ranges [68]. The focal lengths of the DI water fluidic lens were first measured using red (HeNe 633 nm), green (HeNe 543 nm), and blue (Argon 488 nm) lasers with the previously described pump controls. All three laser beams were aligned to the optical axis. The combination of the lasers allows to either individually test the lenses with specific wavelengths or to concurrently test multiple wavelengths as shown in Figure 5-2. The dichroic mirrors have specified bands in which they reflect and transmit. We found the proper dichroic mirrors to pass the previous wavelengths while reflecting the incoming perpendicular laser wavelengths. By mixing the lasers or adding an aperture stop, we varied the desired input wavelengths. We then used a single beam expander using an achromatic objective lens and another achromatic collimating lens to collimate the three beams in this single optical axis. A color CCD camera on a rail was employed to find the best focus spot. The spots were not of a perfect sphere since there was a slight amount of astigmatism observed at the focal spot. This is caused by a slight distribution in tension around the flanges and it is observed more drastically at longer focal lengths.

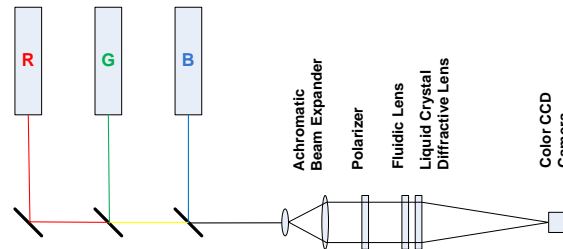


Figure 5-2 **Achromat Test Setup:** Three laser beams aligned and collimated to measure the focal lengths of the diffractive and fluidic lens by a color CCD camera on a rail.

As was previously stated we applied DI water, with known indices of refraction per wavelength, in identifying the fluidic lenses radius of curvature range. For a given amount of fluid in the lens, we measured the focal length at each of the three test wavelengths. The radius of curvature,  $r$ , of the lens surface was calculated using  $\Phi = 1/f = (n_{\text{air}} - n_{\text{DI}})/r$ , where  $\Phi$  is the surface power and  $n_{\text{air}}$  and  $n_{\text{DI}}$  are the indices of refraction for air and DI water per index, respectively. It is noted that with the defined coordinate system the radius of curvatures are negative values as the vertex to the center propagates to the left; however, we are stating the values as definitions of magnitude as to alleviate the constraint of a coordinate system. The index of refraction for air is approximately one at all wavelengths and the index of refraction of DI water is known at each wavelength [68]. The focal length,  $f$ , of each measurement was equal to the back focal distance of the fluidic lens using the thin lens approximation. Each radius of curvature was calculated at red, green, and blue wavelengths and averaged to determine a single radius of curvature per fluid volume. The experiment was repeated as we increased the fluid volume in the lens by increments of  $50\mu\text{L}$ .

To define the workable range for the fluidic lens we quantified the repeatability of outputting the radius of curvature. It was found that the average radius of curvature per fluid volume between the three wavelengths varied in accuracy of 0.02% to 0.88% for a radius of

curvature from 20 to 100 mm. For DI water this corresponded to a focal length range of 60 mm to 300 mm. To clarify, a radius of curvature with an accuracy of 0.02% means that our lens accuracy for a radius of curvature at 20 mm was at 20 mm +/- .004 mm or with an accuracy of 0.88% the radius of curvature outputted at 20 mm +/- .176 mm. Similarly the radius of curvature range for our larger 100 mm varied from 100 mm +/- .02 mm to 100 mm +/- .88 mm respectively. It was found that the smaller radii of curvature actually observed a lower amount of inaccuracy. As we increase the amount of fluid we are reducing the lenses radius of curvature. This suggests that our caustic is not as long and more of the rays are focused in one location. What is occurring is that with a smaller radius of curvature we have almost no effect by the frame which allows for the shape of the membrane to be controlled by the fluid with almost no dependence on the optomechanical structure. With this higher control the smaller the radius of curvature the higher control of aberrations is observed.

We broke up the accuracy of the radius of curvature into two additional sections. The radius of curvature between 100 to 200 mm had outputted an accuracy between 1 and 2 %, which for DI water is a focal length range of 300 to 600 mm. Focal lengths from 600 to 900 mm produced an accuracy on the radius of curvature between 2 and 5% of the expected focal length. Our goal was to apply a highly accurate fluidic lens to couple with the diffractive lens as to diminish in accuracies related to the control of the fluidic lens. These two additional sections had high accuracy and repeatability but were not the best results since they had larger radius of curvatures. Therefore, we defined the highly accurate radius of curvature range between 20 to 100 mm as the fluidic lenses functional range while attempting to determine the best fluid to work with in producing the final achromatic design.

The two most significant fluid characteristics for this experiment, as was observed from the achromat equation, were the fluids focal length and Abbe number. The focal length is dictated by the radius of curvature of the fluidic lens and the index of refraction of the fluid. In the previous paragraph we experimentally assessed the fluidic lenses controlled radius of curvature range to be between 20 to 100 mm with high accuracy. The fluids index of refraction can vary the focal length, but the range would increase or decrease the focal range slightly. This is observable by evaluating  $\Phi = 1/f = (n_{air} - n_{FL})/r$  once more, where now  $n_{FL}$  is the new fluids index of refraction rather than DI water. We observe that our only alteration to the equation is the applied fluids index of refraction. If we find a fluid with a larger index of refraction than the tested DI water, then focal lengths shorter than 60 mm are achievable. As most indices of refraction for glass range between 1.3 and 2.5, a reasonable approximation is that a majority of optical fluids operate within this index range. It is safe to approximate that the calculated focal length range of DI water of 60 mm to 300 mm can be decreased by at least 10 mm to 50 mm or higher. We are not stating that the focal length cannot be further decreased, but rather we are defining a reasonable index of refraction range as to not constrain the fluids when attempting to find the proper Abbe number to produce a functional diffractive / refractive achromatic lens.

With the focal length range approximated it was necessary to determine the proper fluid Abbe number to achromatize the focal lengths of the diffractive lens. On the left hand side of Table 5-1 are the diffractive lens values that would be required to be achromatized. Table 5-1 identifies which focal lengths are needed from the fluidic lens for each Abbe number to achieve achromitization with these designed diffractive lens powers. Our approximation showed that our fluidic lens will achieve focal lengths in the relative area of 50 mm or higher. Our experimental DI water has an Abbe number of 55. It is seen within the table that DI water would only

achromatize the 1 D Diffractive lens with our fluidic lens, due to the constraints on the lenses radius of curvature. A fluid with an Abbe number of 15 would achromatize four of the diffractive lens' focal lengths and an Abbe number of 10 would achromatize five focal lengths above 50 mm. Theoretically, a fluid with an Abbe number of 5, as observed from Table 5-1, would produce approximately all possible achromatic combinations from either diffractive lens developed here, since the greatest Diopter range achieved by the diffractive lenses is 15 D. Finding a fluid with a known index of refraction to achieve a focal length as low as 50 mm and a characterized Abbe numbers from 5 to 15 will offer the capability of illustrating a variable focal length achromat with discrete focal lengths of achromatization.

Methanol (Methyl alcohol) was chosen as the fluid for the fluidic lens due to its high dispersion value and non-reactivity with the PDMS membrane. Methanol has an Abbe number of 13.66 which achromatizes 5 of the diffractive lens focal lengths as is observed in Table 5-1 and is widely available as it is a cleaning agent. The desired focal length range to achromatize all of the diffractive lenses focal locations with the fluidic lens would be from 16.8 to 101.0 mm when coupled with diffractive lens B and from 63.14 to 252.6 mm when coupled with diffractive lens A. As was previously stated, the diffractive lens A provides focal lengths of 1000, 500, and 250 mm, and the diffractive lens B provides 400, 200, 133, 100, and 67 mm focal lengths. As seen from Table 5-1, all three possible focal lengths of the diffractive lens A, and two out of five focal lengths of the diffractive lens B (400 and 200) can be achromatized. Using Table 5-1, we identify the focal lengths of the fluidic lens for every focal length of the diffractive lens. Results of the two combined focal lengths develops a predicted achromatic focal length at green wavelength through  $\Phi_{expected} = \Phi_{diffractive} + \Phi_{fluidic}$  and  $f_{expected} = 1 / \Phi_{expected}$ . The five expected achromatic

focal lengths,  $f_{\text{expected}}$ , for green must be achieved through the experimental setup for the achromat to work properly.

Focal lengths of the diffractive and fluidic lenses were first measured separately using the red (HeNe 633 nm), green (HeNe 543 nm), and blue (Argon 488 nm) lasers. We used a linear polarizer with the diffractive lens to account for the polarization effects of the nematic liquid crystal. We can remove the polarizer so the lens works with any randomly polarized light if we add another liquid crystal diffractive lens with an orthogonal buffing direction to the first diffractive lens. As expected, the red light comes into focus first for the diffractive lens since it has negative dispersion. The test results for the two diffractive lenses are shown in Table 5-2 and 5-3. The experimental and theoretical values of focal lengths at the aforementioned three test wavelengths are presented in Table 5-2 (diffractive lens A) and Table 5-3 (diffractive lens B). The design wavelength for both lenses is  $\lambda = 555 \text{ nm}$ , and the design focal lengths (1000 mm for lens A and 250 mm for lens B) as well as additional observed focal lengths developed when these lenses were shunted as is presented at the design wavelength. The focal lengths at the three test wavelengths are calculated using the diffractive lens formula discussed in the introduction,  $f(\lambda) = (555/\lambda) f_d$  where  $f_d$  is the design focal length at 555 nm.

Wavelength (nm)	f (555nm) = 1000 mm		f (555nm) = 500 mm		f (555nm) = 250 mm	
	Data	Theory	Data	Theory	Data	Theory
633	870	876.8	435	438.4	217	219.2
543	1015	1022.1	505	511.1	252	255.5
488	1125	1137.3	560	568.6	281	284.3

Table 5-2 **Diffractive Lens A:** Measured and calculated focal lengths at the three test wavelengths.

Wavelength (nm)	f (555nm) = 400		f (555nm) = 200		f (555nm) = 133		f (555nm) = 100		f (555nm) = 67	
	Data	Theory	Data	Theory	Data	Theory	Data	Theory	Data	Theory
633	348	350.7	174	175.3	116	116.9	88	87.7	59	58.4
543	405	408.5	202	204.2	135	136.1	102	102.1	69	68.1
488	447	454.9	225	227.5	152	151.6	114	113.7	76	75.8

Table 5-3 **Diffraction Lens B:** Measured and calculated focal lengths at the three test wavelengths.

As an example, the images of three of the focal spots of the diffractive lens B are shown in Figure 5-3. This was for the case when the diffractive lens B was shunted from a 12-level lens to a 4-level lens in order to produce the focal length of 133 mm (at the design wavelength of 555 nm) which is one-third of the design focal length of 400 mm [70]. The focus spots were all nearly round and sharp, with some background scattered light due to lowering of the diffraction efficiency especially at shorter focal lengths.

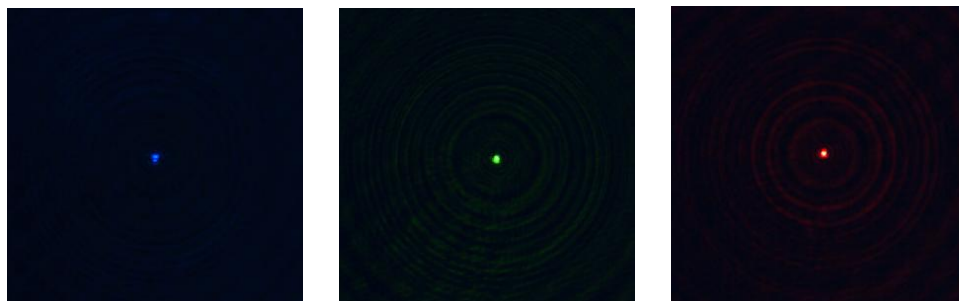


Figure 5-3 **Diffraction Spot's Per Wavelength:** Sample images of the best focus spots for the diffractive lens B when it is set to the focal length of 133 mm at the green wavelength.

The fluidic lens illustrates a nonlinear response as fluid is withdrawn. As the membrane reaches higher radii, the membrane becomes flatter. The sensitivity to the amount of fluid increases within this range since a smaller amount of fluid varies the curvature. The measured

values of the fluidic lenses focal length for the three wavelengths are depicted in Figure 5-4 in terms of the amount of fluid injected in the lens.

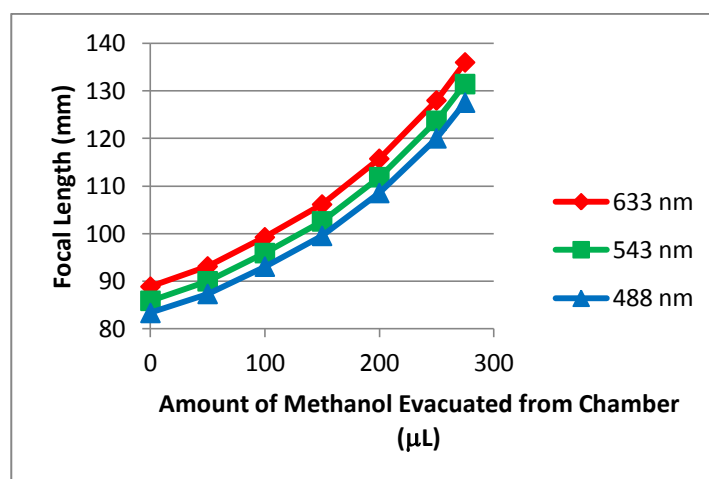


Figure 5-4 **Fluidic Achromat Focal Length:** Chromatic dispersion of the variable focal plano-convex lens alone applying methanol at the three test wavelengths when set for 80 mm focal length and higher.

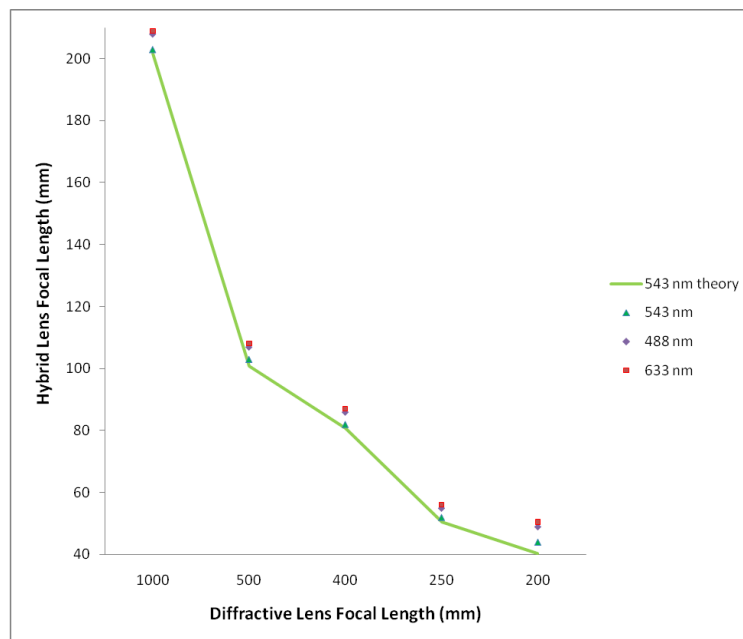
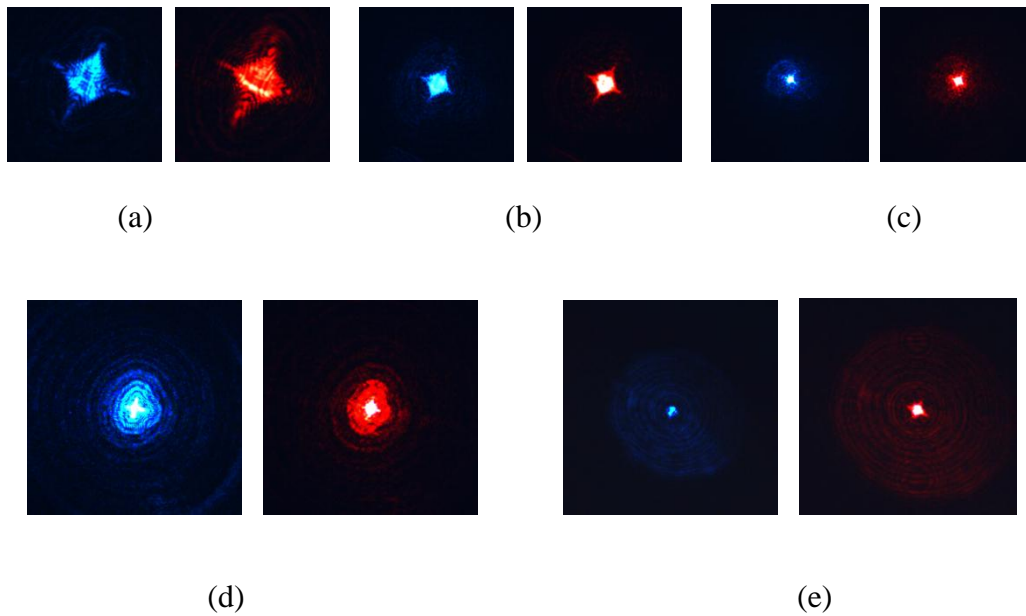
The final step in producing the variable focal length achromat is the combination of the liquid crystal diffractive lens with the pressure controlled methanol fluidic lens. After adjusting the focal lengths of each lens to the appropriate values dictated by the achromat equation we measured the overall focal length of the hybrid lens at the red, green, and blue wavelengths. The experiment verified that the focus spots of the red and blue wavelengths coincided very closely. Figure 5-5 (a-e) depict the focal spots for the red and the blue wavelengths as the focal lengths of the diffractive and the fluidic lenses are varied according to the achromat equation. In Figure 5-5 (a-c) diffractive lens A, and in Figure 5-5 (d, e) diffractive lens B was combined with the fluidic lens. The other three focal lengths from the diffractive lens B could not be used for this experiment because of the limited minimum achievable focal length of the fluidic lens in its current form. As the focal length is decreased, the spot size and aberrations are reduced as

expected; however, the background scattered light is slightly increased. This is caused by the reduction in diffraction efficiency at the shorter focal lengths as the number of binary phase levels decreases due to the electrode shunting [70, 71]. The issue of low diffraction efficiency can be overcome by designing diffractive lenses with higher number of binary phase levels which results in smaller electrode sizes if the design optical power and aperture size are kept constant. This will require a more advanced micro-fabrication technique. On the other hand, the fluidic lens showed nearly round and sharp focus spots at short focal lengths when the curvature of the membrane was high, but at long focal lengths as the membrane became flatter considerable aberrations started to show up, of which astigmatism and coma were more pronounced as evident from Figure 5-5 (a), (b).

Figure 5-5 (f) shows the values of the overall focal length of the hybrid diffractive/fluidic lens for the green, blue and red test wavelengths. As expected, the green light comes to focus first and then the red and blue lights will come into focus near the same plane. The measured focal lengths of the hybrid lens closely matched with the expected focal length values seen from Figure 5-5 (f). Although our hybrid diffractive/refractive lens has the advantage of being multi-focal and non-mechanical compared to the traditional lenses, its current optical qualities are slightly inferior to the conventional lenses because of the few available focal lengths of our liquid crystal diffractive lenses in their current form and low diffraction efficiencies at shorter focal lengths, as well as physical limitations of our fluidic lens in its current form including small fluid pump, limited aperture size, and significant aberrations at longer focal lengths when the membrane's curvature is decreased. The chromatic aberration was significantly reduced but not completely at this time corrected due to the current limitations which can be overcome by improving the fabrication.

The clear aperture of our liquid crystal diffractive lenses is limited by the photolithography capabilities, number of binary phase levels, and diffraction efficiency, whereas the fluidic lens is aperture limited by the pressure control of the mechanical flanges on the periphery. If the aperture becomes too large then we cannot produce an even distribution of pressure holding down the membrane, inducing uncontrollable aberrations. The function radius of curvature of the fluidic lens is limited by the tensile strength of the designed membrane. Using a broad-band positive photoresist (S1805) and Karl-Suss MA6 contact printer operating around i-line (365 nm), we were able to achieve one micron feature sizes. Employing more advanced fabrication tools smaller features can be made and the design aperture can be increased. This is due to the facts that the Fresnel zones get narrower as moving away from center and as the number of binary phase levels or the design optical power is increased. Diffraction efficiency can also become a limiting factor if the zone widths become comparable to the liquid crystal thickness or the inter-electrode gaps (in case of one-layer electrode design) [70, 82].

Diffractive lens A has a maximum design aperture of 10 mm, 8 phase levels, 1 D minimum optical power, no inter-electrode gaps (odd and even electrodes interleaved into two layers), about 8-micron narrowest electrode, and about 7-micron thick liquid crystal. Diffractive lens B has a maximum design aperture of 6 mm, 12 phase levels, and 2.5 Diopter minimum optical power with one micron inter-electrode gaps (one-layer electrode design), about 5-micron narrowest electrode, and about 4-micron thick liquid crystal. To increase the diffraction efficiency liquid crystal thickness can further be decreased by using smaller glass fiber spacer beads during assembly. However, the minimum thickness in order to achieve at least  $2\pi$  phase retardation is  $(\lambda \Delta\Phi_{\max}) / (2\pi \Delta n_{\max}) = \lambda / \Delta n_{\max} = 0.633 / 0.225 = 2.8$  micron.



(f)

Figure 5-5 (a-e) **Discrete Diffractive / Refractive Focal Length Achromat Results:** Focal spots when the diffractive and fluidic lenses are combined to produce the best focus for the red and the blue lights. The focal length values at the green wavelength are: (a)  $f_{\text{diffractive}} = 1000$  mm,  $f_{\text{fluidic}} = 252$  mm; (b)  $f_{\text{diffractive}} = 500$  mm,  $f_{\text{fluidic}} = 126$  mm; (c)  $f_{\text{diffractive}} = 250$  mm,  $f_{\text{fluidic}} = 63$  mm; (d)  $f_{\text{diffractive}} = 400$  mm,  $f_{\text{fluidic}} = 101$  mm; (e)  $f_{\text{diffractive}} = 200$  mm,  $f_{\text{fluidic}} = 51$  mm; (f) overall focal length of the hybrid system for the green, red and blue wavelengths.

In conclusion, we have demonstrated a variable focal length achromatic lens that consists of a variable liquid crystal diffractive lens and a variable pressure-controlled fluidic lens. We used two diffractive lenses that produce multiple discrete focal lengths with an Abbe number of -3.45. The fluidic lens can provide a more continuous variation, and its focal lengths are chosen such that they minimize the dispersion of the diffractive lens. We chose Methanol for the fluidic lens due to its high dispersion properties. Then we combined the fluidic lens and one diffractive lens at a time to minimize the dispersion between the red and blue wavelengths. The lenses showed acceptable optical properties and the test results were close to the theoretical predictions. This adjustable hybrid lens has no moving parts and would be useful for compact color imaging applications, and medical and ophthalmic imaging devices.

## **5.2 Continuous Variable Focal Length Achromatic Fluidic Lenses**

The previous design produced achromatization for specific foci. A more advanced achromatic lens would be to produce any focal length that one is interested in with a continuous variable focal length achromat. We propose the development of a variable focal length achromat. The achromat design is composed of two individual variable lenses, one with a crown-like oil fluid and the other with a flint-like oil fluid, which are combined to correct for chromatic aberration. The fluidic lenses have two elastic membranes, one for each chamber. Fluid pressure causes the membranes to change shape and alter the optical power of light passing through it. By adjusting the fluidic pressure of the two chambers in sync with each other we can produce exact achromatized focal lengths.

As was stated earlier, an achromat corrects for longitudinal chromatic aberration through the combination of a positive dispersive crown glass and a negative dispersive flint glass, where

the high dispersion and low power of the flint lens counter balances the dispersion of a higher power crown lens. Crown and flint glasses typically have an Abbe number above and below 55 respectively for standard glasses. As we shown in the previous section, fluids offer Abbe numbers that can vary from high dispersive  $v=5$  to low dispersive Abbe numbers of  $v=100$ . The flint and crown lenses balance the dispersion and focal lengths in order to match the focal position between designed blue and red wavelengths, where the primary dispersion is therefore corrected for.

### **5.2.1 Variable Focal Length Achromatic Design**

Our fluidic achromat is developed in much the same way. Each chamber has a crown-like or flint-like fluid instead of a solid glass material. Similarly, the crown-like and flint-like fluids are separated, with the crown-like fluid having a lower dispersion. To be used in refractive applications, the control of dispersion, index, transparency within the visible, toxicity, volatility, and transition factors are all significant in the production of the proper fluids. Any fluid including, but not limited to, optical immersion fluids, laser fluids, inter connect fluids, or any other optical fluid's can be applied into these chambers. As long as the optical fluid does not react with the metal frame, any optical fluid is applicable.

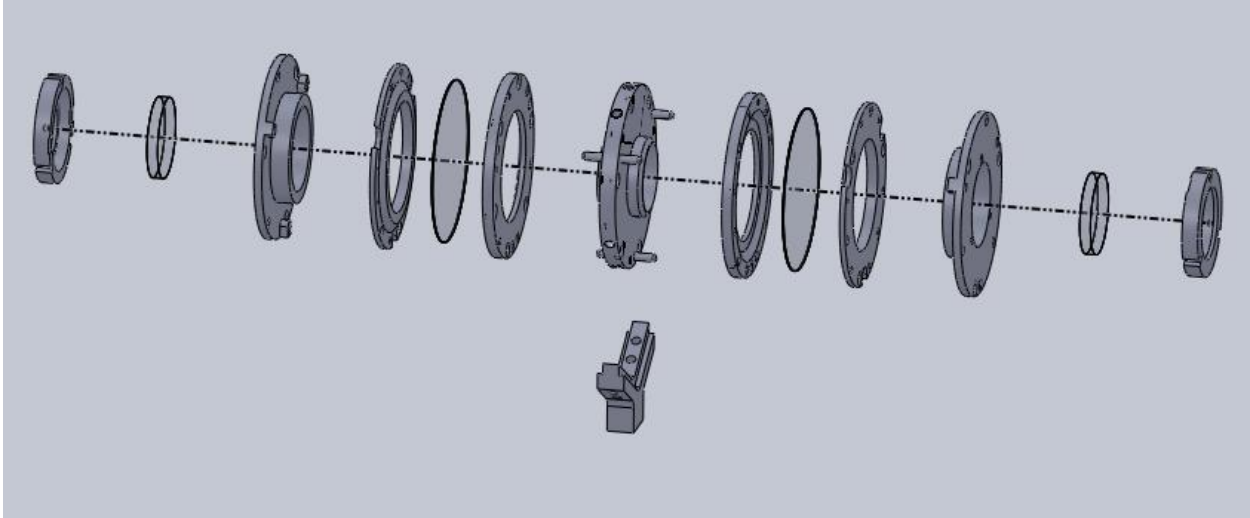


Figure 5-6 **Dual Fluidic Achromatic Lens Design:** The SolidWorks design of our two fluidic chamber system.

Figure 5-6 shows an embodiment of our design with a double fluidic chamber, which functionally acts like a doublet design. Our design is symmetric about the center so the chambers on either side are symmetric. Each chamber has a protective glass window so that our membranes would not collect dust. If we were to pass light through the window, the light passes through the window. The next structure is a pressure based tensioner. There are two pre-tensioners in which the membranes are compressed in between and locked into. The pre-tensioners are locked down onto the central frame. The tensioner which has the window locked onto it is then secured onto the pre-tensioners and locked in. The tensioner applies pressure onto the membrane so that it locks the membrane down in a clamped edge design. The achromatic base connects the same symmetric design on either side of the frame. This allows for us to produce a doublet designed achromatic chamber.

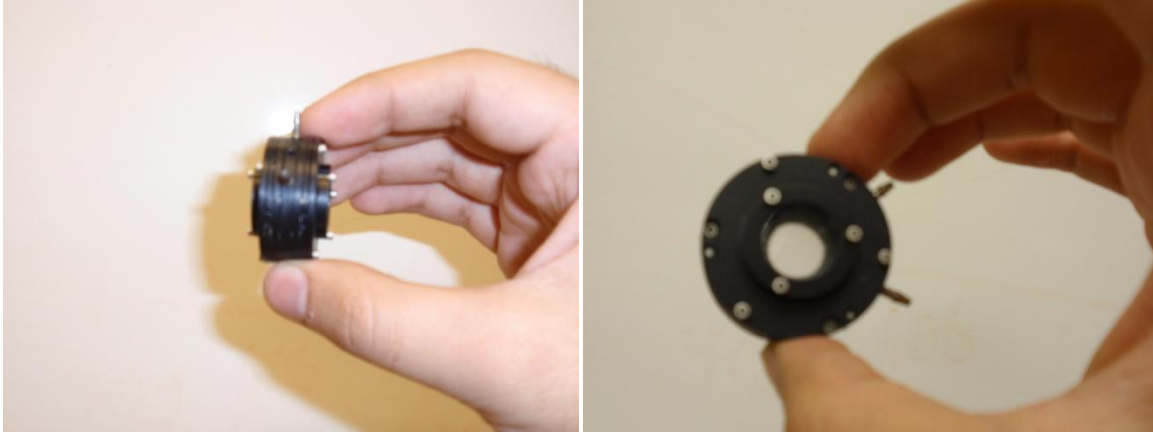


Figure 5-7 **Dual Chamber Fluidic Achromat:** Here is a current image of our double chamber fluidic lens.

A second approach that we have proposed in developing an achromatic lens is in the coupling of two singularly controlled plano-convex singlet fluidic lenses. By altering the curvature of each fluidic device in sync with each other we are able to control the power exiting each single surface.

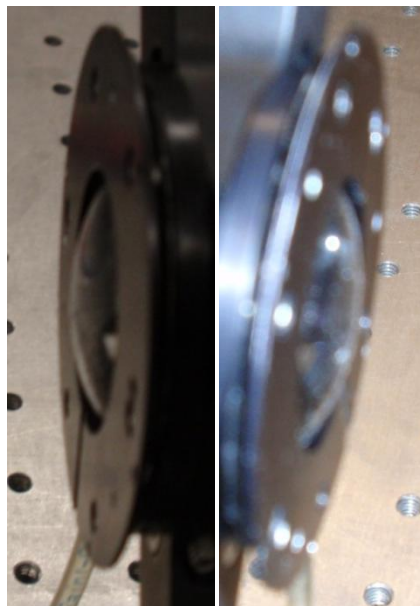


Figure 5-8 **Coupled Single Chamber Achromatic Design:** This shows a combination in concept of two fluidic lenses coupled together.

### 5.2.2 Test Methods for Continuous Variable Focal Length Achromatic

One of the most significant factors in producing an achromatized lens is in the fluid selection. A couple of optical features that are important are the index of refraction and dispersion value. Again, we take advantage of  $f_1 v_1 + f_2 v_2 = 0$  to produce an achromatic lens. The fluids selected determine the amount of dispersion or Abbe numbers  $v_1$  and  $v_2$  that satisfy the equation. Knowing the focal length range of each of the lenses allows for us to know  $f_1$  and  $f_2$ . As was previously described, we can determine the radius of curvature of each radius of curvature surface through our testing apparatus.

Our testing apparatus is similar to the hybrid system except now we only test fluidic lenses. The combination of the various lasers allows for us to either individually test wavelengths for the fluidic lens or to concurrently test wavelengths. The dichroic mirrors have specified bands in which they reflect and so we found the proper dichroic mirrors to pass the previous wavelengths while reflecting the following lasers wavelength. By mixing the lasers or adding a stop we can vary the output of the lasers.

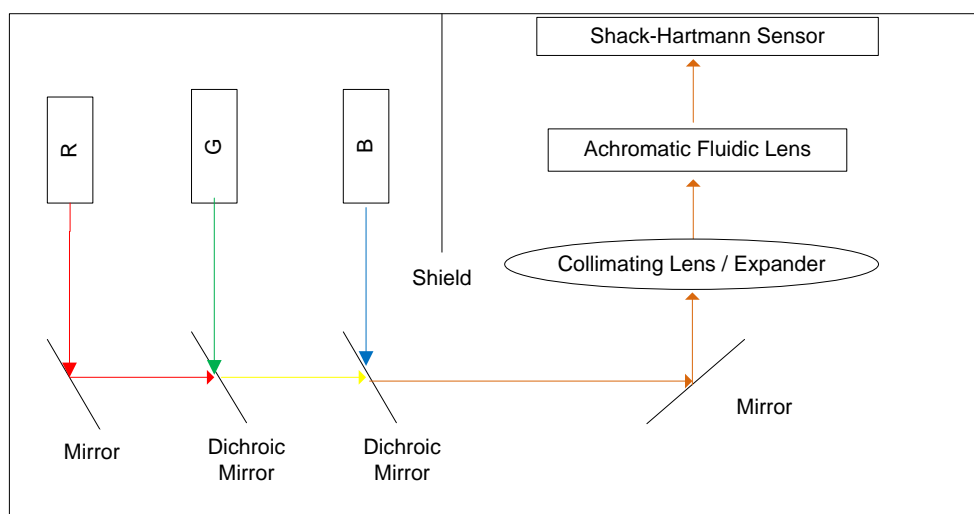


Figure 5-9 **Dual Achromat Testing Design:** Here is the generic setup which we are attempting to test the achromatic fluidic lens.

We mentioned two possible designs of dual fluidic lenses where one has two singlet fluidic lenses coupled together and the second had a single double chamber fluidics as our achromat designs. The two singlet design offers an easier testing approach. We can apply laser light through various pressure volumes on each individual lens and identify where that individual lens focuses. We can then identify the radius of curvature from the determined focal lengths. The radius of curvature will be significant information in the synchronization of the two lenses. As an example we show the radius of curvature of fluidic lens one as was determined through this testing approach with DI water.

Fluid Showing in Pump System ( $\mu$ l)	Focal Length Red (mm)	Focal Length Green (mm)	Focal Length Blue (mm)	Green Light Diopters	Separation between Red and Blue (mm)	Seperation between Red and Green (mm)	Seperation between Green and Blue (mm)	V	Radius of Curvature (rc) mm	Sag (mm)
0	82.250	78.500	71.750	12.7388535	10.500	3.750	6.750	7.476190476	26.0149	1.998759136
50	89.500	83.000	77.000	12.04819277	12.500	6.500	6.000	6.64	27.5062	1.882167561
100	99.750	94.000	87.750	10.63829787	12.000	5.750	6.250	7.833333333	31.1516	1.648681796
150	111.250	107.250	99.000	9.324009324	12.250	4.000	8.250	8.755102041	35.54265	1.435759655
200	131.500	126.000	116.750	7.936507937	14.750	5.500	9.250	8.542372881	41.7564	1.215100798
250	159.750	151.500	140.500	6.600660066	19.250	8.250	11.000	7.87012987	50.2071	1.005952753
300	212.500	202.000	178.000	4.95049505	34.500	10.500	24.000	5.855072464	66.9428	0.751120222
350	323.500	299.500	266.250	3.338898164	57.250	24.000	33.250	5.231441048	99.2543	0.505041428
400	761.250	595.250	473.250	1.679966401	288.000	166.000	122.000	2.066840278	197.26585	0.253628104

Table 5-4 **Analysis of Fluidic Lens Radius of Curvature:** From our testing apparatus we have determined the radius of curvature of fluid lens 1.

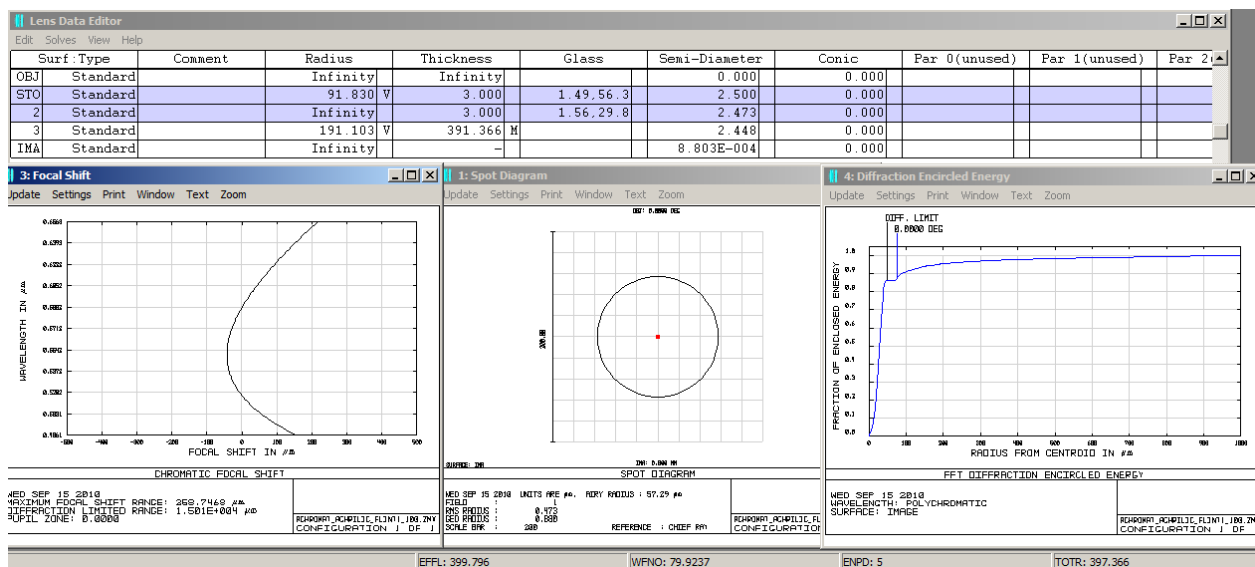
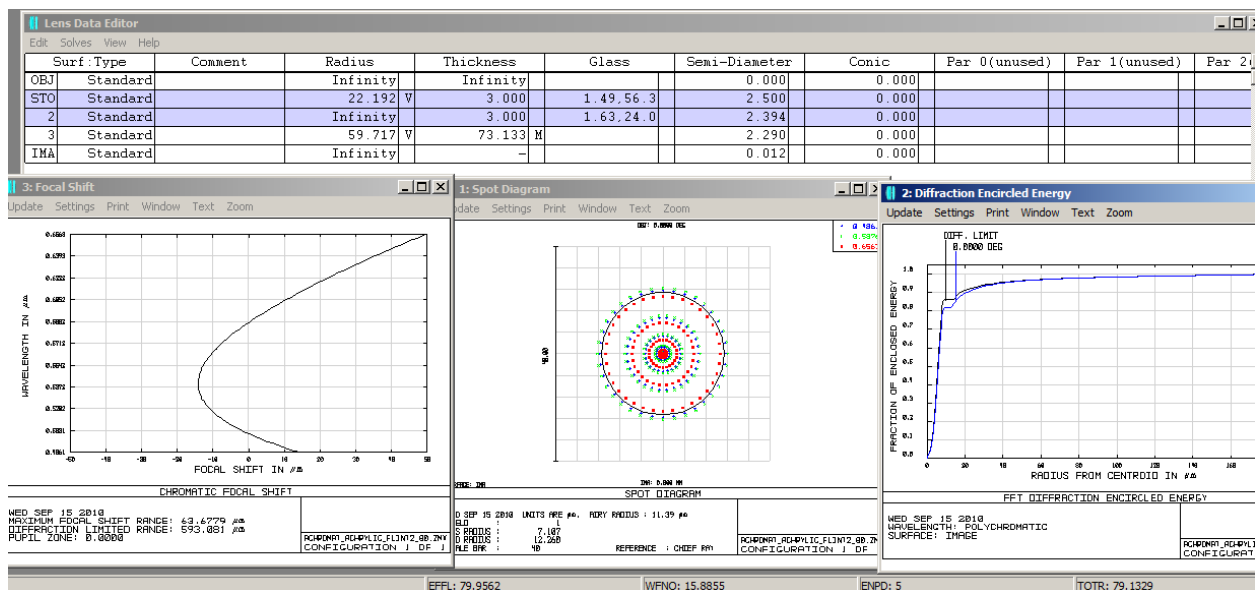
The above table shows an example of us determining the radius of curvature from the three wavelengths that we were testing with. For each fluid extraction we applied multiple tests per laser wavelength. A significant factor is in determining a fluid that is stable and transparent in the visible wavelengths. A stable fluid with no evaporation rate allows for us to verify that the

repeatability of our fluidic lens technology is accurate. This test was for a proof of concept and so we applied DI water for testing purposes. Hence, with a stable fluid volume and knowledge of the index of refraction of fluid and air we were able to determine the radius of curvature of the lens per fluid volume:

$$r_c = \frac{n_{fluid} - n_{air}}{\varphi}$$

The above equation determines the radius of curvature per wavelength as the index of refraction varies for all materials per wavelength. We then averaged out the three radii of curvature to determine the average radius of curvature per fluid volume. The three radius of curvature values were approximately the same value. This measuring approach can be applied to the achromat design by first measuring a single surface with fluid inserted. After the measurements are complete, one must zero out the power of the first lens before inserting fluid for the second chamber. The second chamber can then be measured with the first lens chamber nulled out. From this approach one can determine the radii of curvature of a dual chamber system.

An approach in producing a continuous achromat can be achieved by determining what the radii of curvature must be for achromatization per system focal length. We mentioned several times syncing the two surfaces allows for achromatization and we have been focusing on the radius of curvature identification of our achromat. By knowing the radii of curvature of each surface we can determine where the focal length of each fluids lens would be with a determined fluid that has a known index of refraction and Abbe number. We have begun experimenting with four fluids where two have crown like properties and two have flint like properties.



We can determine the radii of curvature needed from our fluidic lens chamber through modeling in optical design software such as ZEMAX. We place a desired focal length that we would like to optimize in ZEMAX with our two fluids. Again it is significant to know the index

of refraction of the fluid at a designed wavelength and also the Abbe number for that fluid. We set the two fluidic lens surfaces as variable and then optimize for aberration correction. We now know what radius of curvature is desired from our fluidic lenses for an achromatic lens with a given focal length. Above we show an example of a given crown with two different flint fluids. The focal shift is shown to be more of the traditional curved shape in the longer focal lengths in comparison of Figures 5-10 and 5-11. We also see that as the focal length for the achromat is longer, it is easier to produce a diffraction limited achromatic lens as is seen in Figure 5-11. In Figure 5-10, we have an achromatic focal length of 80 mm that reaches the edge of the diffraction limit, where the black circle identifies the diffraction limit. The focal length shift per wavelength has more of a skewed focal length variation on the shorter achromatic focal lengths as seen in Figure 5-10. We can use ZEMAX to fully map the necessary radii of curvature for the two surfaces so that our achromat is continuous.

Focal Length (mm)	Radius 1 (mm)	Radius 2 (mm)	Focal Length (mm)	Radius 1 (mm)	Radius 2 (mm)
80	18.15	34.11	170	38.43	76.55
90	20.10	37.72	180	40.751	81.53
100	22.27	42.13	190	43.08	86.51
110	24.53	46.86	200	45.40	91.49
120	26.82	51.73	210	47.72	96.48
130	29.14	56.66	220	50.04	101.46
140	31.46	61.62	230	52.37	106.44
150	33.78	66.59	240	54.69	111.42
160	36.10	71.57	250	57.01	116.40

**Table 5-5 Table of Fluidic Lens Radius of Curvature for Achromatization of Two Fluids:** We have determined two fluids to map the radii of curvature for each fluidic lens chamber. This enables us to produce an achromatic lens at a given focal length.

These charts coupled with the known radii of curvature per fluid volume enables us to produce a computer controlled achromatic lens that is continuous with variable focal lengths. We can further illustrate that this fluidic lens technology is applicable in the production of negative focal length chromates in addition to positive focal length chromates. We have chosen two more fluids that allow for us to produce negative focal lengths. Here we show two positions of -60 mm focal length and -100 mm focal lengths chromates. We choose -60 mm to show that it is possible to design the achromat so that it is not necessarily diffraction limited but that the aberration is slightly larger than this scenario, making these shorter focal lengths also realizable.

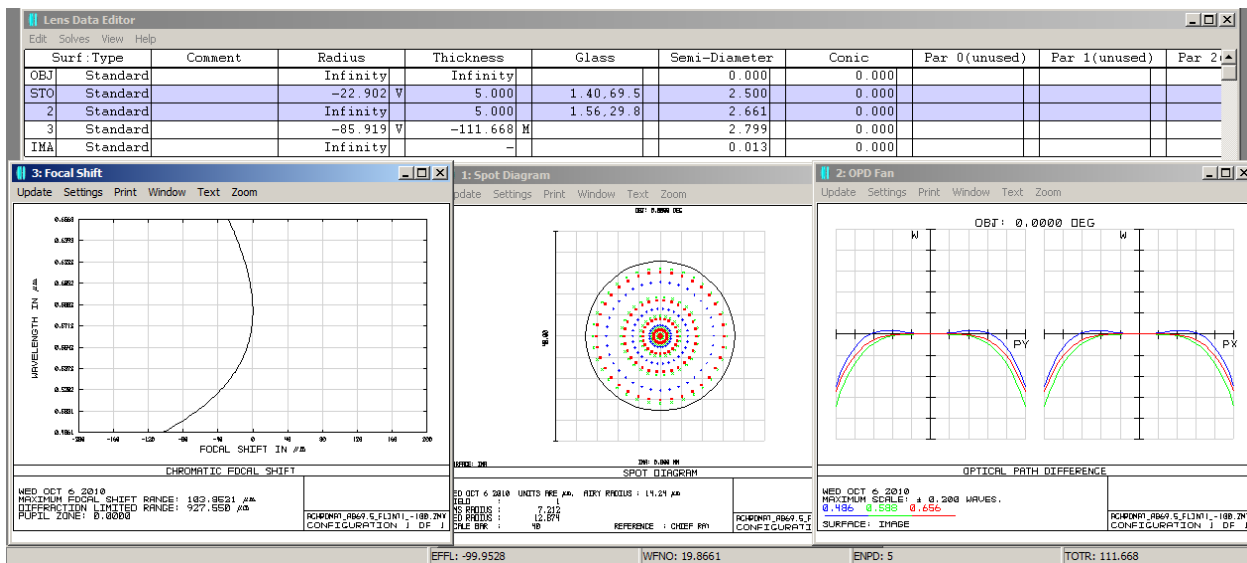


Figure 5-12 ZEMAX Model of an Achromat Design with -100 mm Focal Length: Here we show the radii of curvature necessary from each of the fluidic lens surfaces to achieve an achromatic lens that is diffraction limited at -100 mm focal length.

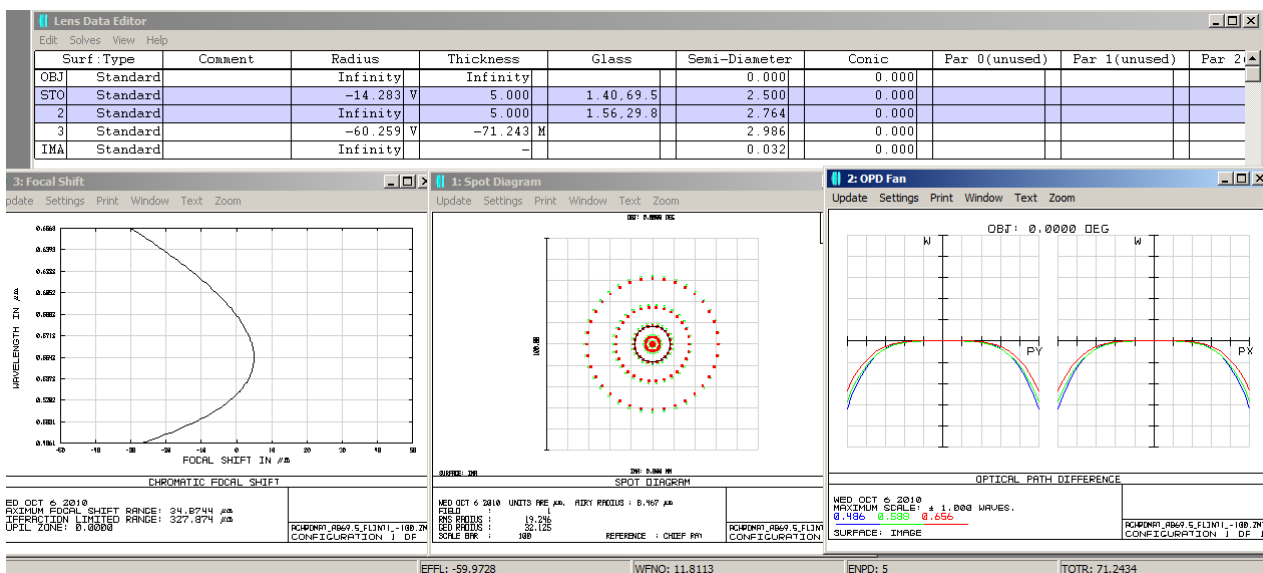


Figure 5-13 ZEMAX Model of an Achromat Design with -60 mm Focal Length: Here we show the radii of curvature necessary from each of the fluidic lens surfaces to achieve an achromatic lens that is diffraction limited at -60 mm focal length.

We can produce tables to identify the radius of curvature for more than these specific fluids and are not limited by these specific fluids. Hence, we choose the two optical fluids to produce the achromat, we identify the radius we need to produce a focal length, and then we

output that achromatic focal length. Once these fluids are inserted into the chambers, the fluidic chromates becomes functional. By syncing the proper curvature between the front membrane and the rear membrane an achromat is produced.

The radii of curvature are mapped to the amount of fluid volume withdrawn or inserted into the fluidic lens. We can replicate the results of these various achromatic designs by setting a look up table to a given focal length for a couple of our fluids. We can then adjust the achromatic focal length according to the desires of the user. Thus, we have created a digital achromatic lens through optofluidic technology.

## **6.0 WAVEFRONT CORRECTION OF THE FLUIDIC PHOROPTER AND FLUDIIC AUTO-PHOROPTER**

We have discussed applications of optofluidic designs of zoom optical systems and achromatic correction mechanisms. Microscopes and other imaging systems are achievable with no moving parts through optofluidic adaptive optic technology. Adaptive optics finds its application in many accommodating designs, but also in wavefront correcting systems. Wavefront correction can be found in a broad array of fields from astronomy to vision science. Wavefront technology has made vision correction and retinal imaging realizable in real time correction of ocular aberrations.

Wavefront sensing technology identifies the aberrations that exist in an optical system such as the eye and adaptive optic technology corrects for the measured wavefront. The Shack-Hartmann wavefront sensor has made measuring of ocular aberrations realizable. The concept of applying the Shack-Hartmann wavefront sensor for ocular measurements of the wavefront was first achieved at the University of Heidelberg in the early 1990's [83]. Adaptive correction of the eye progressed further through automation and the advancement of adaptive optic technology [84].

The first closed-looped adaptive optic technology that coupled the Shack-Hartmann wavefront sensing technology with adaptive optic technology was that of the reflective deformable mirror. This technology has found application in multiple areas of vision science such as ocular correction, retinal imaging, refraction correction, eye tracking and disease identification [84, 85, 86]. Our interest is in the application of the measurement and correction of ocular aberrations in real time. Through real time measurements, one is able to identify and measure a patient's accommodation, and the eye's dynamic range. Also in real time, one can

extract a user's prescription for various focal locations and output the results in an objective manner. This streamlines the subjective eye exam to an automated objective testing device.

Phoropters are used to estimate and correct for the second order defocus and astigmatism aberrations of the eye. Subjects are systematically asked to compare varying amounts of correction to iteratively determine their ideal correction. An optofluidic phoropter, which is an adaptive optic phoropter, takes the entire phoropter system and compresses it into a group of fluidic lenses. This grouping of fluidic lenses enables for the correction of ocular second order aberrations. Furthermore, advances in fluidic lens technology may lead to systems that can correct higher order aberrations as well.

It is necessary for wavefront technology to couple the adaptive optic technology to produce a correction in real time. A fluidic auto-phoropter discussed here takes advantage of the closed-loop technology to measure and correct the low order aberrations in the human eye. Auto-phoropters have been produced when coupling Shack-Hartmann wavefront sensors with the adaptive optic technology of either a deformable mirror [84] or liquid crystal technology [87]. Deformable mirror technology is often times expensive and bulky and requires large relay systems to work. Also, scaling is required to match the pupil size of the deformable mirror with the pupil size of the human eye. The adaptive optic liquid crystal auto-phoropter has limitations in that it is strongly wavelength dependent, has high noise limitations, and also the system is bulky [88]. There has been an expansion on adaptive optics and optofluidic technology in the field of ophthalmology [17, 89, 90, 91, 92]. We have designed optofluidic auto-phoropter systems with the focus on producing a cheap, compact, mobile, and quick device that at the same time achieves the goal of identifying a prescription in real time.



Figure 6-1 **Fluidic Phoropter Compared to Standard Phoropter:** The motivation is the have our fluidic phoropter on the left completely replaces the standard phoropter system on the right.

Our fluidic auto-phoropter combines a Shack-Hartmann wavefront sensor with a compact and inexpensive refractive fluidic phoropter. Our system has an open-view design, where the user observes real objects at various image depths. Furthermore, the elements are transmissive, allowing for a more compact design when compared to reflective systems. The goal is to develop an adaptive binocular see-through auto-phoropter that automatically measures a patient's spherical and cylindrical error, nulling this error with a stack of sphero-cylindrical fluidic lenses. We expand on see-through auto-phoropter systems, rather than reflective systems, to offer a natural scene for the user. This will offer more accurate readings on the user's prescription at various object distances. The measurements from the Shack Hartmann wavefront sensor directly identify an individual's wavefront slope. The wavefront slope directly offers information for astigmatism and defocus aberrations, in addition to higher order ocular aberrations. This slope information in turn drives pump mechanisms for the fluidic lenses.

This chapter focuses on the wavefront theory of how the adaptive optical fluidic phoropter functions and how the auto-phoropter functions. We begin with an organization of the optofluidic phoropter, or fluidic phoropter, as was discussed in the dissertation by Randal Marks of "Fluidic Astigmatic and Spherical Lenses for Ophthalmic Applications" [17]. The

predecessor of this dissertation was focused on design and testing of the optofluidic phoropter. We will describe the theory that enables this fluidic phoropter to compensate for the vision error of a user. The end of the chapter is focused on the wavefront correction of auto-phoropter designs.

## **6.1 Fluidic Phoropter**

Traditional phoropter systems primarily focus on correction of the lower order aberrations of astigmatism and defocus. Therefore, it is necessary to produce spherocylinder correction for a standard fluidic auto-phoropter design. In chapter 1 section 3, we focused on the fundamental theory of membrane shape control through deflection of our fluidic lenses. This theory identified the type of deflection that was necessary to reproduce specific lens types. We had found that we were able to replicate a spherical lens, which we will call a defocus lens. We also produced a spherocylinder lens by fabricating a pair of lenses with a rectangular framed membrane. We had found that if the rectangle was infinite in one direction then we would have pure cylinder, but since we needed a clear aperture active area we would require a lens that produces spherocylinder results. The additional spherical power induced by these lenses will need to be compensated by the defocus lens.

### **6.1.1 Wavefront Analysis of Defocus and Astigmatism Lenses**

We can identify the aberrations that are exhibited by each of these lenses through the measurement of a Shack-Hartmann wavefront sensor.

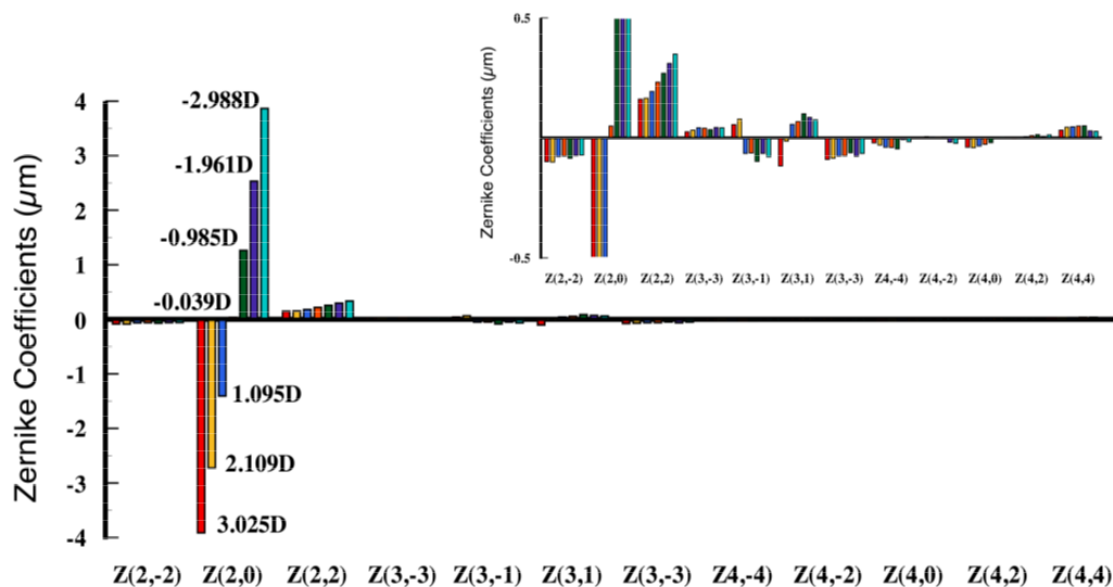


Figure 6-2 **Wavefront Measurement of Defocus Lens:** The defocus lens shows residual astigmatism in the  $Z_2^2$  term [17].

As was mentioned, we find that our defocus lens has residual astigmatism error. This residual error is caused by the clamping approach of our membrane to the frame at the screw locations. It is observed that this defocus lens exhibits a high control of defocus and low amounts of residual astigmatism aberration. Each one of the colors on the wavefront scale measures the wavefront at different settings in fluid volume ranging from -3 to +3 Diopters. The higher order aberrations are measured to be negligible beyond the astigmatism measurement of either  $Z_2^{-2}$  or  $Z_2^2$ . Even when we focus within  $0.5 \mu\text{m}$  of RMS of the wavefront measurement, the primary observed aberrations are the second order radial Zernike's. The third order radial Zernike's are the next highest terms with less than  $0.1 \mu\text{m}$  RMS for up to 3 Diopters of power. Therefore, the third order radial Zernike's are observed to be negligible relative to the functionality of the fluidic lens.

A similar observation is made when analyzing the astigmatism lenses. As was anticipated, there was an observation of spherocylinder aberrations. The higher order aberrations measured through the cylinder lens is even smaller than the higher order residual aberrations observed in the defocus lens. There is less than 0.1  $\mu\text{m}$  RMS Error observed from these higher terms. The cylinder lens is primarily dominated by astigmatism and has less defocus aberration. Once the astigmatism lens reaches + 3 D of astigmatism we find that there is an increase in residual astigmatism in the opposite orientation. This residual astigmatism is below a quarter of a Diopter; however, it is not negligible like the additional higher order terms. The additional residual astigmatism in the opposite orientation is due to the relative orientation of the two fluidic lenses to the wavefront sensor. The two astigmatism lenses are orientated at  $45^\circ$  relative to each other, but are also orientated relative to the lenslet array of the Shack-Hartmann wavefront sensor. Residual astigmatism error in the opposite astigmatic Zernike term is produced with a slight misalignment of the astigmatism lenses relative to the Shack-Hartmann wavefront sensor. This assembly error must be taken into account while producing measurements.

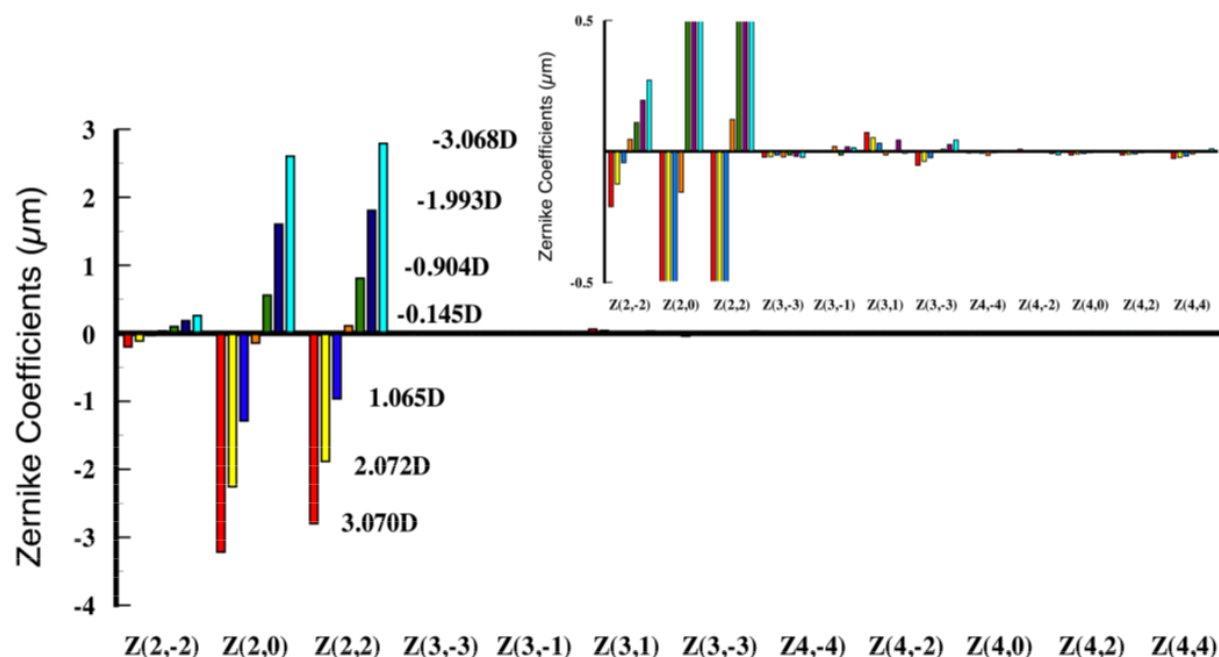


Figure 6-3 **Wavefront Measurement of Astigmatism Lens:** The astigmatism lens has the anticipated defocus aberration in addition to a residual aberration of the additional second order Zernike astigmatism term of the opposite orientation [17].

### 6.1.2 Wavefront Analysis of Fluidic Phoropter

We are able to correct for given amounts of astigmatism and defocus by compensating for aberrations with a stack of two cylinder lenses and a defocus lens, our fluidic phoropter. It is advantageous that the cylinder and defocus lenses produce negligible aberrations for all terms except our second order Zernike polynomial terms of astigmatism and defocus.

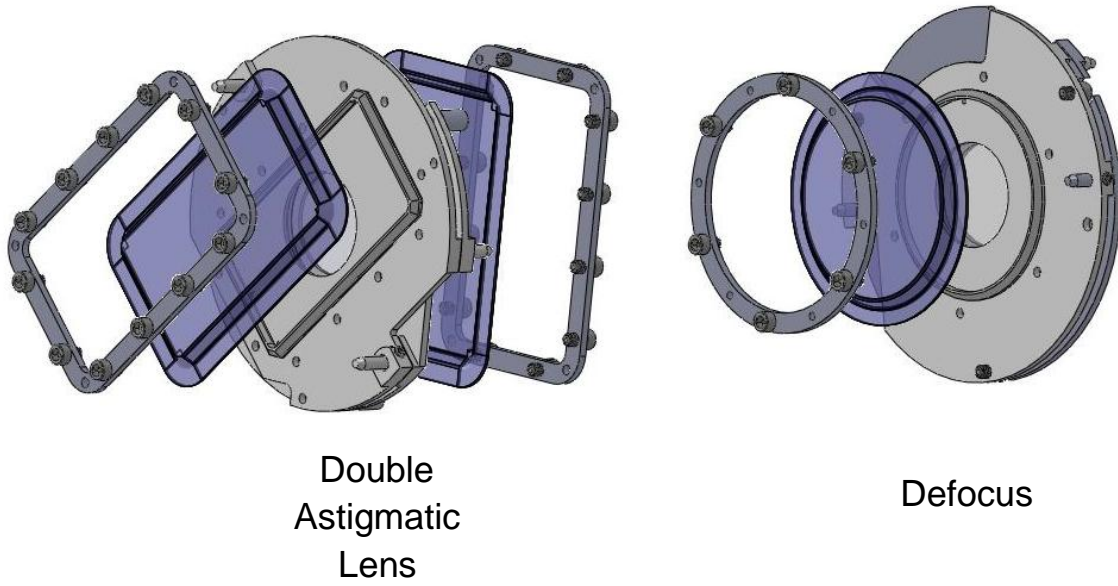


Figure 6-4 **Fluidic Phoropter Orientation:** Here we show a mechanical model view of phoropter with a defocus lens and two astigmatic lenses that are oriented  $45^\circ$  to each other [17].

The fluidic phoropter produces power and cylinder correction at any angle. The designed system is a compilation of two astigmatism lenses oriented  $45^\circ$  relative to each other and a defocus lens. Ideally, the defocus lens would only produce power variation and each astigmatism lens would produce a defocus and astigmatism term. By orientating the two astigmatism lenses  $45^\circ$  relative to each other, we can correct for any orientation of astigmatism error in addition to power error.

$$W(v_d) = b(v_d) Z_2^0$$

6-1

$$W(v_{a_{45^\circ}}) = b(v_{a_{45^\circ}}) Z_2^0 + c(v_{a_{45^\circ}}) Z_2^2$$

6-2

$$W(v_{a_0^\circ}) = a(v_{a_0^\circ}) Z_2^{-2} + b(v_{a_0^\circ}) Z_2^0$$

From our stack of fluidic lenses, each one of these wavefronts is a description of a single fluidic lens. Equation 6-1 is the results of purely defocus power where no residual wavefront measurements are observed. The summed astigmatism lenses orientated at  $0^\circ$  and  $45^\circ$  relative to each other produce correction for the two astigmatism orientations while also summing the defocus term with no residual terms. The combination of the three fluidic lenses therefore produces the theoretical fluidic phoropter wavefront:

$$w_{phor} = a(v_{a_0^\circ}) Z_{-2}^{-2} + (b(v_d) + b(v_{a_{45^\circ}}) + b(v_{a_0^\circ})) Z_2^0 + c(v_{a_{45^\circ}}) Z_2^2$$

We find that all three fluidic lenses alter the properties of the defocus lens while each of the astigmatism lenses produces a Zernike astigmatism term. With an ideal system, we can balance astigmatism through proper pressure control of the astigmatism lenses. After identifying the amount of ocular astigmatism error in a given orientation, we control the two astigmatism lenses to correct for the astigmatism errors. When setting the two astigmatism lenses, we additionally set the constants that effect the defocus terms for the astigmatism lenses,  $a(v_{a_0^\circ}) + a(v_{a_{45^\circ}})$ . The defocus lens can then be applied to compensate and null the defocus caused by the astigmatism lenses coupled with the eyes defocus error. This setup allows for the fluidic phoropter with no residual aberrations to correct for defocus and astigmatism error at any given orientation for an eye.

Experimentally, the defocus and astigmatism lenses do not only produce these specific aberrations but additional residual aberrations, as we have observed from the Zernike wavefronts

of the Shack-Hartmann wavefront sensor. We had found that the defocus lens produces additional  $Z_2^2$  astigmatism. In addition, the astigmatism lenses produce residual Zernike astigmatism to the orthogonal astigmatism Zernike term due to the misalignment of the fluidic lenses relative to the lenslet array. We can therefore expand the terms of 6-1 through 6-3 to include the residual wavefront terms that affect the wavefront of the fluidic lenses. The residual terms will be represented with an R subscript.

$$W(v_d) = b(v_d) Z_2^0 + c(v_d)_R Z_2^2$$

6-5

$$W(v_{a_{45}^o}) = a(v_{a_{45}^o})_R Z_2^{-2} + b(v_{a_{45}^o}) Z_2^0 + c(v_{a_{45}^o}) Z_2^2$$

6-6

$$W(v_{a_0^o}) = a(v_{a_0^o}) Z_2^{-2} + b(v_{a_0^o}) Z_2^0 + c(v_{a_0^o})_R Z_2^2$$

6-7

This observed residual aberration has been found to be in the second order Zernike terms that we are correcting for. This is advantageous in that we are able to compensate for the residual aberration without adding any additional Zernike terms. A second advantage of these residual terms is that their magnitude is much lower than the actual correction Zernike terms in each of the fluidic lenses for their respective wavefront correction. As these residual aberrations are slight, we are able to compensate for these terms in an optimization approach similar to that of an optical design software such as ZEMAX or CodeV. We run several iterations of compensation between fluidic lenses in adjusting the fluid volume per lens to increase the accuracy of our phoropter system relative to the wavefront measurement until we reached the desired correction

result. We analyze the summed Zernike terms for the wavefront of the fluidic phoropter that takes into account all of the residual terms:

$$w_{phor} = \left( a(v_{a_{45}^o})_R + a(v_{a_0^o}) \right) Z_2^{-2} + \left( b(v_d) + b(v_{a_{45}^o}) + b(v_{a_0^o}) \right) Z_2^0 \\ + \left( c(v_d)_R + c(v_{a_{45}^o}) + c(v_{a_0^o})_R \right) Z_2^2$$

6-8

## 6.2 Wavefront Analysis of the Fluidic Auto-Phoropter

An objective eye exam is created to identify a patient's prescription. The adaptive optic technology must compensate for the users wavefront error to null the wavefront error out for the auto-phoropter to identify that a patient observes a fully corrected view. The sum of the wavefront error of the eye and the phoropter must therefore equal zero to null the wavefront error out and produce a clear image.

$$w_{null} = 0 = W_{phor} + W_{eye}$$

6-9

The closed loop system allows for real time correction of the wavefront. As we established earlier, the wavefront correction comes from the optofluidic technology while the eye's wavefront measurement is calculated from the Shack-Hartmann wavefront sensor. The Shack-Hartmann wavefront sensor can measure higher order Zernike's. We can represent the wavefront error of the eye as the terms that exit the wavefront sensor.

$$W_{eye} = W_{SH} = Z_2^{-2} + Z_2^0 + Z_2^2 + Z_3^{-3} + Z_3^{-1} + Z_3^1 + Z_3^3 + Z_4^{-4} + Z_4^{-2} + Z_4^0 + Z_4^2 + Z_4^4$$

6-10

Equation 6-9 includes defocus, astigmatism, trefoil in x and y, coma in x and y, tetrafoil in x and y, secondary astigmatism in x and y, and primary spherical aberrations or  $Z_2^{-2}$  through  $Z_4^{-4}$ . In the future, optofluidic technology can be applied to correct for higher order aberrations, but here we are focused on the second order radial Zernike terms. Our fluidic phoropter corrects for on  $Z_2^{-2}$  through  $Z_2^2$  as on average the second order terms of defocus and astigmatism account for approximately 90% of error in the human eye population.

$$w_{eye} = a(v_{eye}) Z_2^{-2} + b(v_{eye}) Z_2^0 + c(v_{eye}) Z_2^2$$

6-11

We can identify the amount of compensation required for the fluidic lenses that are required to correct for each of the Zernike terms. At the same time, we can extract the wavefront measurements of astigmatism and defocus for readable prescriptions by combining equations 6-8, 6-9, and 6-11. The auto-phoropter designs adjust the fluidic lens pressure to adjust the weighting of 6-12 through 6-14 of each fluidic lens until the most optimized nulled out solution is achieved.

$$a(v_{eye}) = - \left( a(v_{a_0^o}) + a(v_{a_{45^o}})_R \right)$$

6-12

$$b(v_{eye}) = - \left( b(v_d) + b(v_{a_{45^o}}) + b(v_{a_0^o}) \right)$$

6-13

$$c(v_{eye}) = - \left( c(v_{a_{45^o}}) + c(v_{a_0^o})_R + c(v_d)_R \right)$$

6-14

## 7.0 FLUIDIC AUTO-PHOROPTER PROTOTYPE ONE: SYSTEM DESIGN

Our first fluidic auto-phoropter is designed in order to produce automated eye examinations through the combination of a fluidic phoropter and the objective analysis of a Shack Hartmann wavefront sensor. A see-through adaptive phoropter provides the ability to measure a patient's refractive prescription at any plane. This allows for prescription measurement at any distance from the eye such as a distance of 20 feet for a Snellen eye chart, a distance used for reading glasses or even a far enough distance where it is relatively infinity. The power of a see-through system allows for natural distances to be observed by the patient.



Figure 7-1 **Targets at Multiple Planes for Focusing Through Fluidic Auto-Phoropter:** View of targets at various depths where the eye natural focuses on a target and the defocus lens compensates to clear the image.

An accommodating prescription is achieved experimentally by varying the target locations. As the system is see-through, the patient can focus at various depth locations. By focusing at

different depths, it allows for the eyes to accommodate and converge while we are measuring the refractive error. The major assumption is that the field of view of the fluidic phoropter is not occluding the convergence angle of the object location. The mapping of these measurements develops multiple prescriptions and is corrected almost instantaneously for a patient. The auto-phoropter design also enables for a smaller compact size than is possible with other adaptive optic systems. Our first auto-phoropter system uses a fluidic lens module that is combined with a Shack-Hartmann wavefront sensor to automatically determine a sphero-cylindrical refraction applicable for any prescription measurement. This design is also capable of measuring higher order ocular aberrations from a patient's eyes and in the future will be able to correct for higher order ocular aberrations. Our first auto-phoropter design is compact and covers a working area of 1 ft by 1ft. Current models in the market apply reflective rather than refractive elements as the adaptive optics, which eliminates see-through capabilities. We are designing a compact, quick, and in expensive approach in measuring an individual's accommodating visual error.

### **7.1 Design of Fluidic Auto-Phoropter Prototype One**

The design consists of two optical paths that are combined into a single system. There is an illumination/sensor path and also a line of sight path of the eye. Our designed system is comprised of three main modules: a fluidic lens, a relay telescope and a Shack-Hartmann wavefront sensor. We will explain a progression of the light traveling through the optical system from the source to the detector. After the system design is explained we will summarize the functionality of the whole system to produce a clearer image of our control mechanisms.

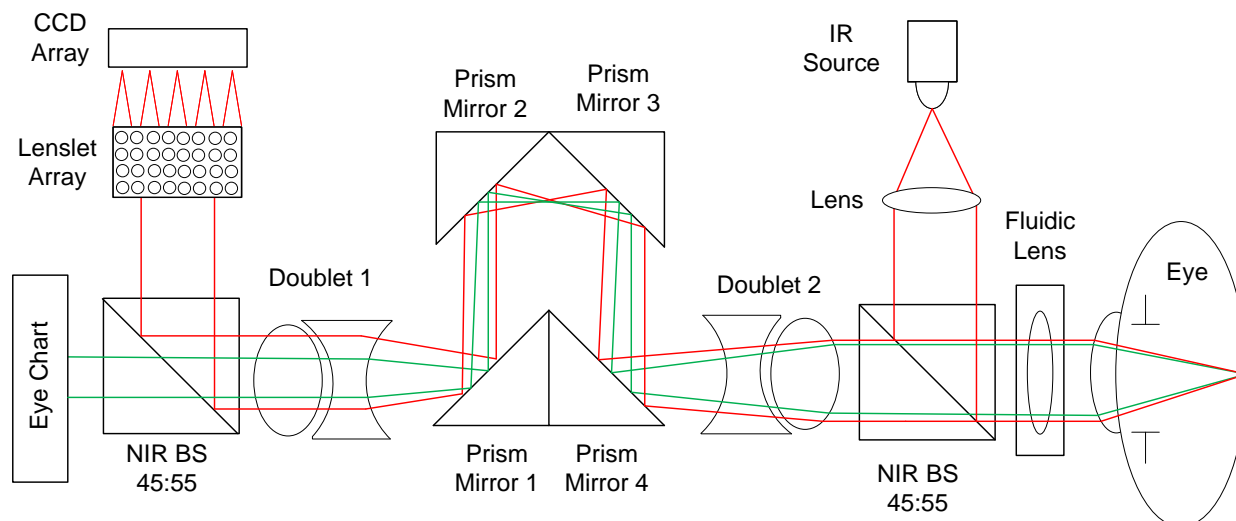


Figure 7-2 **Layout of Optofluidic Auto-Phoropter Prototype One:** The Theoretical Setup where we propagate through fifteen surfaces and reflection points. The green light represents the line of sight of the prescribed user while the red light represents the light from the IR Light Source to the Shack Hartmann wavefront sensor.

### 7.1.1 Fluidic Auto-Phoropter Prototype One: Light Path from Source to Fluidic Phoropter

We first begin with our light source, which has changed through experimentation to a fiber coupled super luminescent diode (SLD) that operates at 780 nm. We discovered that coherent light induces high amounts of scatter from the relative close proximity of our optical parts. In addition, interference is observed between multiple surfaces, destroying point information of the Shack-Hartmann measurements. A super luminescent diode (SLD) with low coherence was the solution to overcome this problem, which works well in the Shack-Hartmann design; however, the beam shape was harder to control. We were attempting to produce collimated light reaching the eye location as to have a plane wave propagate through the system. Our first SLD source was at the focal location of a lens in order to collimate the SLD light source. The output that was produced was an elliptical beam shape.

To correct the beam shape we made our SLD into a point source design by fiber coupling the SLD source. We achieved a collimated circular plane wavefront by using a fiber coupled SLD operating at 785 nm. The SLD diode that we choose outputs up to 6.3 mW and is the LPS-

785-FC SLD from Thorlabs. The output of NIR light exiting the fiber was placed at the focal point of a collimating optical lens. The light exiting the fiber was a point source placed at the focal point of the collimating lens, thus producing a 785 nm collimated circular beam.

Specification	Value	Specification	Min	Typ	Max
LD Reverse Voltage	2 V	Wavelength	776 nm	785 nm	800 nm
PD Reverse Voltage	30 V	Output Power	5.0 mW	6.25 mW	7.5 mW
Operating Case Temperature	-10 to 60 °C	Threshold Current	-	30 mA	50 mA
Storage Temperature	-20 to 85 °C	Operating Current	-	65 mA	90 mA
Pin Code	5A	Operating Voltage	-	-	-
Laser Diode	DL4140-001S	Slope Efficiency	0.3 mW/mA	0.6 mW/mA	0.8 mW/mA
Fiber	SM800-5.6-125	Monitor Current	0.3 mA	0.8 mA	1.5 mA
Connector	FC/PC				

Figure 7-3 **Specifications of Fiber Coupled SLD:** We define the circuit specifications required for our SLD's to run properly.

The collimated light source was driven by a circuit coupled with a variable power supply. This circuit was designed in PCB software to run our SLD's. The circuit board contains two individual circuits to control each SLD of a binocular system. Each individual closed circuit system consists of a potentiometer, a resistor, and the SLD. Each separate closed loop circuit requires a separate variable power supply to run each SLD.

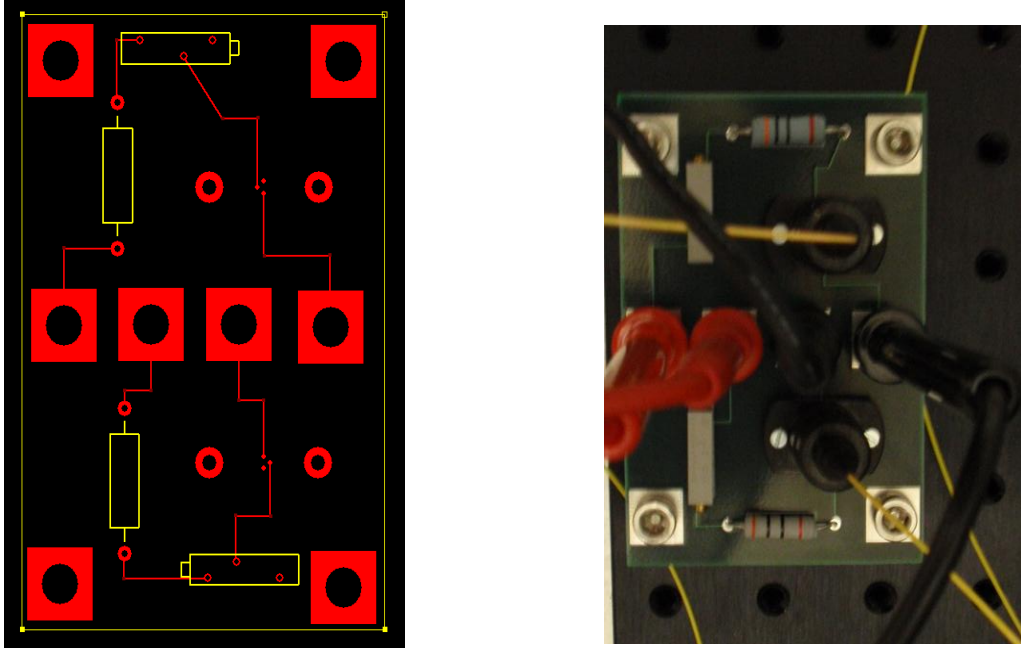


Figure 7-4 **Circuit used to drive the SLD's:** This is the circuit designed in PCB software coupled with a variable power supply to run the SLD's.

Each closed circuit allows for us to drive a single SLD. The variable power supply has controls to vary the voltage and the current. The potentiometer offers control of the resistance. We know the basic correlations of current, voltage, resistance and power through Ohm's and Joule's Laws:

$$P = IV \tag{7-1}$$

$$V = IR \tag{7-2}$$

Through these equations we determined the proper amount of current and voltage to run the circuit. We then applied a power meter at the location of where the eye would be placed to measure the output power of each of the collimated light sources. We added variable power ND filters and identified the amount of filtering that was required to reduce the light source power.

The maximum amount of permitted exposure (MPE) for the near infrared wavelength of 785 nm with an 8 hr exposure applied onto the eye is approximately 125  $\mu\text{W}$  [93]. The near infrared light at the eye plane from the SLD is controlled to around 10 to 15  $\mu\text{W}$ , which is about 10 times less than what is acceptable by the American National Standards Institute's maximum permissible exposure. Each of the SLD sources had a different amount of ND filtering as the current through each circuit was slightly different. Both paths were controlled down to this low power range.

The SLD is placed off-axis relative to the line of sight of the patient. In order to achieve a see-through phoropter it is necessary to shift the light source and detector out of the line of sight of the user. We achieved this through the application of 55:45 pellicle beamsplitters that operate between 700-900 nm in the near infrared. Collimated NIR light propagates to a coated pellicle beamsplitter that reflects light towards the eye or the eye model. There is a screwed on pinhole on the beamsplitter relative to the entrance of the NIR light in order to stop down the source if necessary. The beamsplitter is fully transparent in the visible. An additional advantage of applying pellicle beamsplitters is that they slightly vibrate, where the vibration averages out noise in the system. The NIR light from the beamsplitter reflects 45% of the light to the fluidic phoropter and to the eye or eye model.

### **7.1.2 Fluidic Auto-Phoropter Prototype One: Light Path from Optofluidic Phoropter through the Eye Model**

Throughout this work we have developed a foundation in the description of our fluidic technology. Thus, we have described the theory and mechanical structure in producing lenses for ophthalmic correction. We have explained how our astigmatism and defocus lenses combined to produce ophthalmic correction for defocus, cylinder, and axis. In this section we

will discuss additional topics that affect our fluidic phoropter. We will then continue following the photons within our optical design through the fluidic phoropter back to the telescope system within our auto-phoropter design. There are a couple of topics that have not yet been explored in the discussion of our optofluidic phoropter. The two factors are a discussion of fluid selection and the second is showing the range of the astigmatism and defocus lenses.

### **7.1.2.1 Fluid Selection for Fluidic Phoropter**

Fluid selection began in section 5.2.1 and also in the selection of Methanol in section 5.1.4 where we focused on the optical properties of the fluid for our achromat designs. In those sections the optical properties that were mentioned were the fluids optical properties of dispersion control (Abbe number), index of refraction, transparent in the visible spectrum, toxicity, volatility, and viscosity. In those sections we focused on the Abbe number, and visibility. The topics of transparency in the visible and toxicity are necessary for a safe lens design. These topics were inherently taken into account in the fluid selection, but we have not expanded on the concepts of volatility and viscosity. In addition, we have not focused on the concept of fluid density, fluid reactivity, and corrosive effects to other materials in the fluidic phoropter design.

The resistance that a fluid produces when in the actuation chambers is significant in determining the rate of change of the lens curvature. Highly viscous fluids increase motion resistance and hence slow the force of fluid evacuation. The density of the fluid material works in tandem with the viscosity of the material. One would prefer a fluid with a lower density per area if that fluid is observed to have a high viscosity. The combination of fluid density and viscosity are significant in determining the rate of flow of the liquid.

From a mechanical standpoint, the fluid volatility and reactivity to system materials are as important as the optical properties of the fluidic phorofter. The volatility is a direct correlation to the vapor pressure which identifies the point the fluid turns from a liquid to a vapor. If the fluid is unstable, then the fluid will vaporize and produce a double index effect within the liquid lens. This in turn alters the index of refraction and fluid thickness of our liquid lens. Optical oils, laser fluids, and emersion fluids offer high stability for many years, making them great options as desired fluids.

It is necessary to select fluids that have a high stability and do not react to any materials in the full assembly of the pump control system. There are eleven materials that the fluid interacts with that can be traced from the lens chamber to the pumps. The fluidic lens frame is composed of anodized aluminum and a transparent glass window. Epoxy is used to glue the window onto the metal frame. The connectors between the frame and the tubing are composed of stainless steel. We apply a valve control as to identify the exact amount of oil for our base zero point. The tubing in combination with our valves is composed of Polypropylene, Polyurethane, Polytetrafluorethylene, and Chlorotrifluorethylene. Finally, the fluid reaches the glass syringe that is controlled by the actuator. These eleven materials must not react with any of the fluids as to not cause corrosion of the parts. The combinations of the 11 materials in addition to the 7 requirements of optical and material fluid properties were assessed in the fluid selection process. There were a total of 5 optical fluids found that satisfied a majority of the 18 requirements. The following two charts identify the fluids with numbers 1 to 5. Three of the fluids are laser fluids and two are index matching fluids. It was found that immersion fluids did not have stability for long term application of liquid lenses.

Fluid	1	2	3	4	5
Glass	x	x	x	x	x
Polypropylene	x	x	x	x	x
Polyurethane	x	x	x	x	x
Polytetrafluorethylene	Polyethylene Compatible				
Chlorotrifluorethylene	x	x	x	x	No
Aluminum	x	x	x	x	No
Acrylic	x	x	x	x	x
Stainless Steel	x	x	x	x	x
Sylguard 184	x	x	x	x	x
Epoxy	x	x	x	x	x
Latex	x	x	x	x	x

Table 7-1 **Fluid Compatibility with Auto-Phorofter Material:** Here we identify the compatibility of a fluid with an x for the 11 materials the fluids come into contact with. If the materials were not compatible then we placed a no in the box.

Fluid	1	2	3	4	5
Refractive Index	1.3	1.4	1.51-1.512	1.49-1.50	1.57-1.61
Abbe Number	101	69	52.8	56.3	29
Viscosity cst	5	17	1,450	10,000	177
Density g / cc	1.9	1.9	1.32	0.888	1.092
Stability	High	High	High	Slight Precipitation in 18 Years	High
Toxicity	None	None	Low	Low	None
Transparent in Visible	100%	99-100%	97-100%	99-100%	96-99%

Table 7-2 **Fluid Optical and Chemical Properties:** Here we identify 7 optical, material, and chemical properties that affected the fluid selection process.

Not all of these fluids match the full requirements of our fluidic phorofter. Fluid 5 functions well with fluid 2 in producing an achromatic lens due to the two fluids dispersion values. Both fluids have relatively low viscosities and thus fluid flow should not be a problem. A limitation of fluid 5 is that it reacts with the plastic inside the valve and also with aluminum.

We have run experiments with fluid 5 and did not experience corrosion. It is highly likely that as our aluminum is anodized and is protected from direct contact of fluid 5 with the aluminum. The valves have not been used with fluid 5, but an option would be to select a different valve for this fluid in order to achieve the achromat design.

It would be best to test the fluidic phoropter system with a lens material that is commonly known. Fluid 3 and fluid 4 are Bk-7 and Acrylic matching fluids respectively. The index of refraction of these two fluids is within an index variation of  $1 \times 10^{-3}$  for every wavelength in the visible spectrum relative to the actual glass material. The more common glass material in glass production is that of Bk-7 or fluid 3. When we reach further into this dissertation we will describe test results of experiments with fluid 3 and the testing of the liquid lens with this liquid material. The downfall of fluids 3 and 4 are that they are highly viscous materials. The density of fluids 3 and 4 is lower than fluids 1, 2, and 5 which increase fluid flow rates. However, the viscosity of fluids 3 and 4 are orders of magnitude higher than the other 3 liquids. The Acrylic has a viscosity of 10,000 cst and BK-7 of 1,450 cst. To put this into perspective water has a viscosity of 1 cst, honey a viscosity of 3,000 cst, and molasses a viscosity of 5,000 to 10,000 cst. We find that our acrylic fluid material has a resistance that is higher than molasses. Bk-7 is slow moving and requires a longer time for fluid evacuation to occur. This fluid is advantageous as it matches glass properties but is not for long term use for the fluidic auto-phoropter

The final two fluids, fluids 1 and 2, are both laser liquids that match the 18 requirements that we have previously desired. Both of these fluids show no reactivity to the parts used to assemble fluid control in the system. These fluids show a slighter higher density in composition relative to the other fluids but have a much lower viscosity, in orders of magnitude. This allows for a more optimal fluid flow within our chamber system. In addition the materials have a 99% -

100% transmission throughout the entire visible range, where these transmission ranges describe the transmission of the fluids in a 1 cm thick chamber at room temperature.

In comparison of the two fluids, it is found that fluid 1 has a couple of advantages over fluid 2. The first advantage is in the dispersion of the relative fluid. Chromatic dispersion is a major concern, as each of the fluid chambers in the stack of fluidic lenses are singlets. With an Abbe number of 69, liquid lens 2 has a lower amount of dispersion than typical glass, which ranges between 25 and 65. There are few crown glasses such as FK51 that have a lower dispersion than this fluid material. This dispersion however may not be low enough to fully compensate for chromatic effects. There are currently liquid lenses in the market with a single surface interface. These liquid lenses have an Abbe number of 100 which matches that of fluid 1. Fluid 1's second advantage is that it is a highly viscous material. Its viscosity is 5 cst, which is almost equivalent to that of water. Therefore, it would be advantageous to test with liquid 1 in our optofluidic auto-phoropter as a next step in advancing our research.

#### **7.1.2.2 Test Results with Fluidic Phoropter**

We have established control of radius of curvature of the lens, fluid selection, and the theory behind our liquid lenses. In our auto-phoropter system we have traveled from the light source to the fluidic phoropter system and the model eye. Here we will show how the fluidic phoropter functions through fluid control of each lens. The fluidic lens, which is our fluidic phoropter, are a stack of three adjustable lenses composed of a spherical lens and two astigmatic lenses oriented  $45^\circ$  to one another that are placed at approximately the spectacle plane of the user. Any sphere, cylinder and axis combination can be achieved by adjusting the fluid volume within the fluidic lenses. The defocus lens and the coupled astigmatism lenses have been tested

separately. The following results are achieved through the measurement of the defocus lens by itself in Figure 7-5 and also the measurement of the astigmatism lenses coupled with each other Figure 7-6. These figures are actual experimental values that were taken with the fluidic lenses. The lenses performed similarly to what was expected, where the discrete steps within the fluidic lens control mechanism eliminated the continuity of the circular patterns [17]. There is slightly an elliptical shape as the cylinder power from each of the astigmatism lenses are not exactly the same at the zero points.

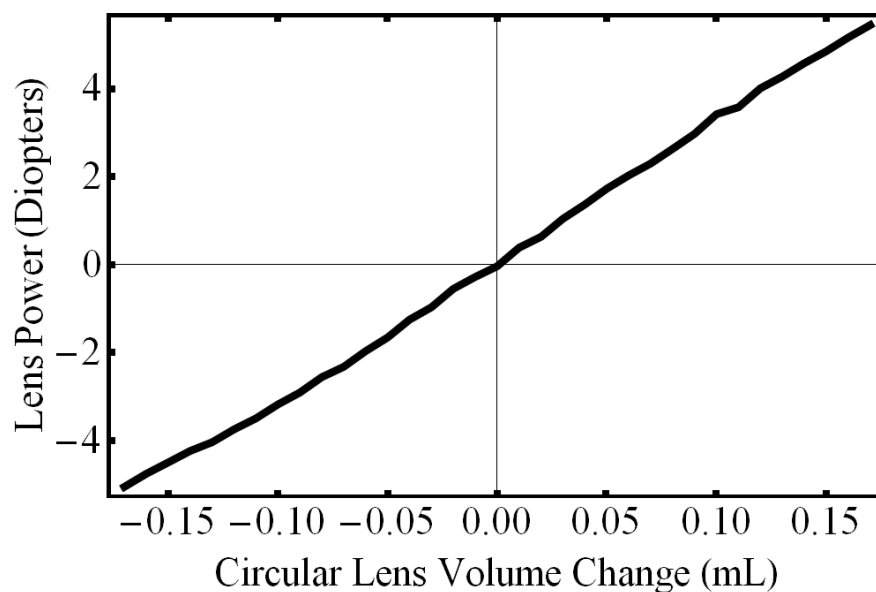


Figure 7-5 **Defocus Lens Power Profile:** This shows the variation in defocus power relative to fluid power within +5 to -5 D [17].

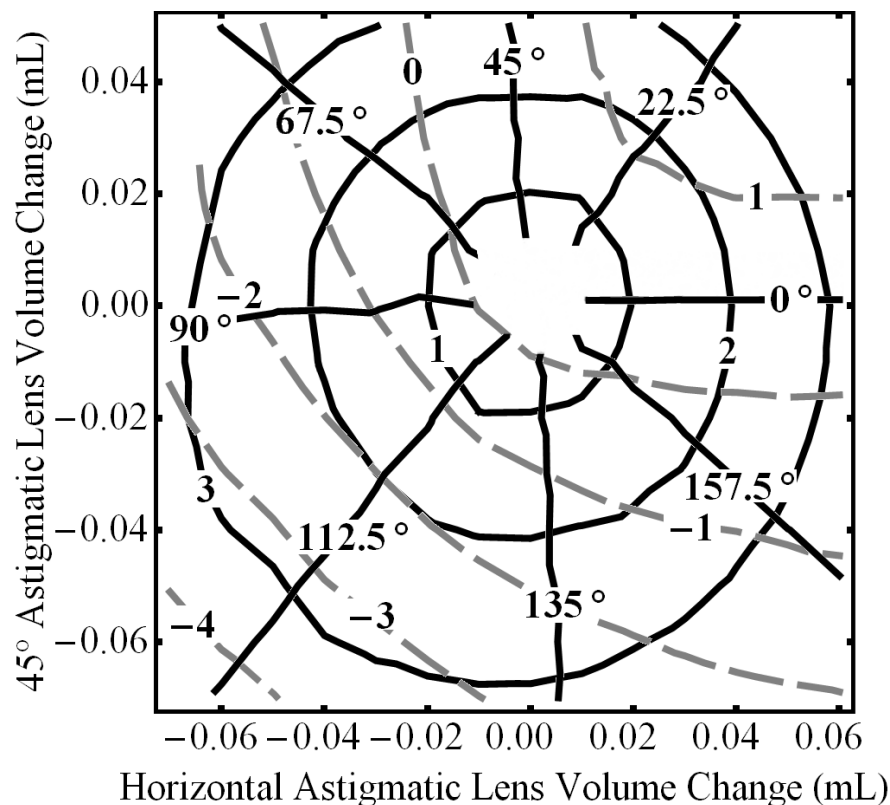


Figure 7-6 **Double Astigmatic Fluidic Lens Power Profile:** The circular plots are cylindrical power, the radial lines are cylinder angle, and the dashed lines are residual power. This shows that the lens is capable of 3D of cylinder at any angle [17].

The combination of these fluidic lenses produces the fluidic phoropter and can correct for error on any axis. The combination of an eye model with the fluidic phoropter produces a clearer picture of the systems capabilities. The eye model with the fluidic phoropter was focused onto an image of a cat. The image of the cat was then blurred by placing astigmatism and defocus lenses in front of the image of the cat. Our fluidic phoropter was applied in the correction of these lenses through the combination of our fluidic lenses [17].

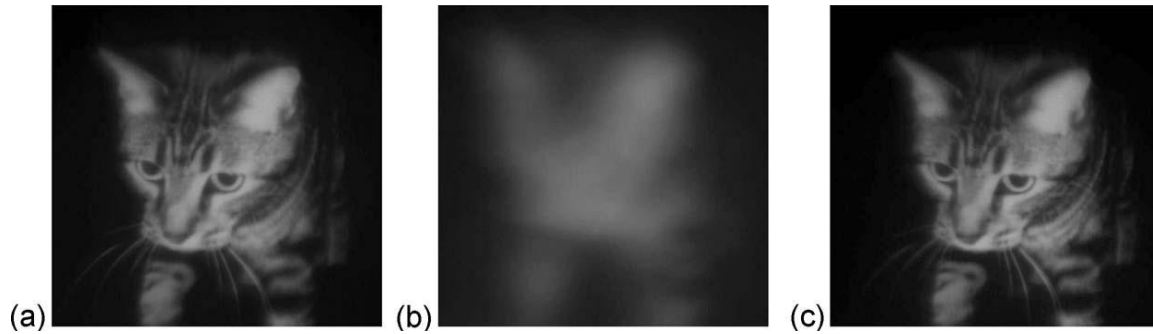


Figure 7-7 **Imaging Results of Model Eye Viewed Through the Fluidic Phoropter:** The cat is pictured (a) with no power to the fluidic phoropter, (b) no power to the fluidic phoropter and an induced refraction error of 1D cylinder and 2D sphere at  $120^\circ$ , and (c) the refractive error is corrected by the fluidic phoropter [17].

This same correction concept is applied in our fluidic auto-phoropter design. The collimated NIR light passes through our phoropter and eye model or eye which is then reimaged into the Shack-Hartmann wavefront sensor. The system automatically determines the wavefront that requires correction through a closed loop interaction between the fluidic lenses and the Shack-Hartmann technology. The users' error will be automatically corrected once the wavefront is properly assessed.

If the eye does not require correction then a plane wave emerges from our pupil plane. If the eye requires correction, then the wavefront exiting the eye is spherical. Hyperopic or far sighted individuals produce a diverging wavefront exiting the pupil. Myopic or near sighted individuals produce a converging wavefront exiting the pupil plane. The power conditions can be replicated through a lens and a mirror. The mirror can be thought of as our retinal plane. The relative position of the mirror to the doublet lens adjusts the shape of the outputting wavefront. If the mirror is placed at the back focal length of the individual then we are replicating an Emmetropic eye. By moving the mirror within the back focal length of the doublet we are replicating the Myopic condition where the light focuses at a location in front of

the retinal plane. Similar to the real situation the far point is no longer at infinity but at a location in front of the eye. If instead we opted to move the mirror further outside the back focal distance of the doublet, then we are replicating Hyperopic conditions. The far point shifts to a location behind the eye in addition to the focal location.

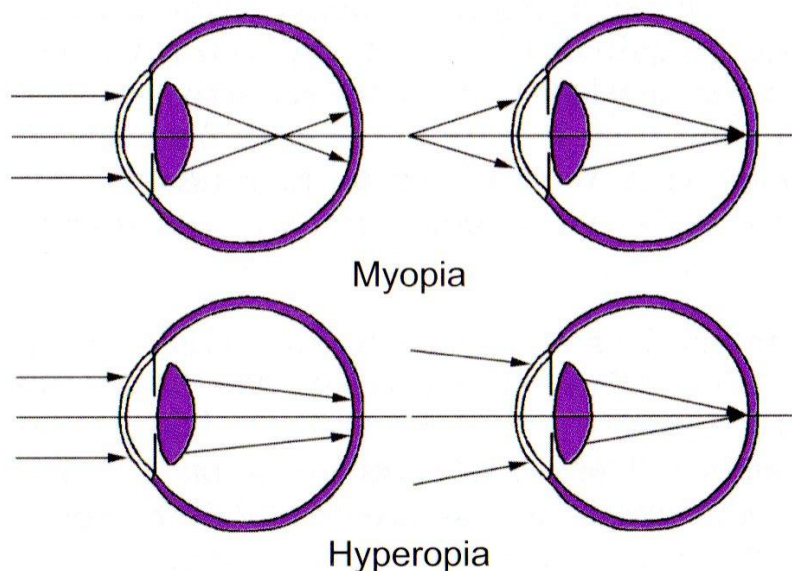


Figure 7-8 Modeling **Myopia and Hyperopia**: The position of the mirror relative to the back focal length of a doublet replicates these conditions within a model eye.

At this point we have established that the NIR light passes through a beamsplitter into our fluidic phoropter. On the opposite side of the phoropter is the described model eye that replicates power conditions of an eye. Additionally, we can add cylinder lenses to adjust the astigmatism to any orientation. Once the light reflects out of the eye it holds the shape of the wavefront exiting the eye at the pupil plane. The next step in the propagation of the light through the system is for the light wave exiting the eye to be reimaged into the Shack-

Hartmann sensor. A Keplerian telescope is applied to reimage the wavefront from the pupil location of the eye model to the lenslet array of the Shack-Hartmann wavefront sensor.

### 7.1.3 Fluidic Auto-Phoropter Prototype One: Light Path Through Keplerian Telescope

The relay telescope is used to image the eye's pupil to the lenslet array and to preserve the shape of the wavefront. The lenslet array samples the incident wavefront and provides the wavefront shape information as feedback to the fluidic lens stack. The fluidic lenses are adjusted to null the sphero-cylinder error of the eye and flatten the wavefront incident on the lenslet array. The relative position of the lenses and telescope system are significant in reproduction of prescriptions.

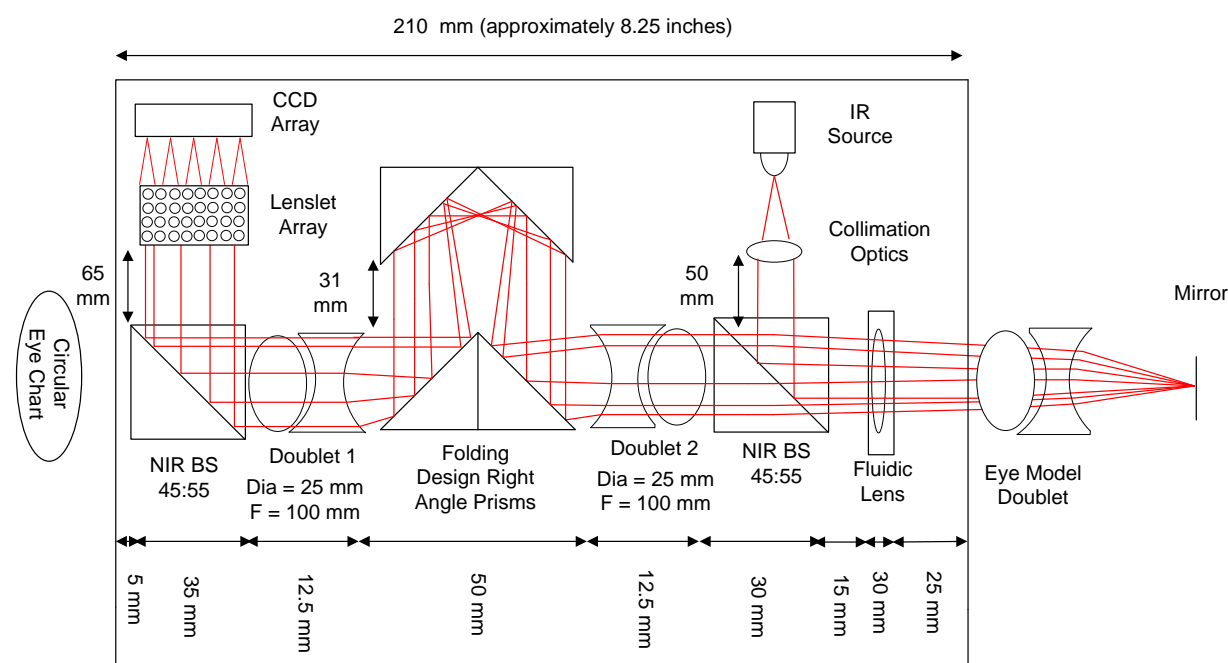


Figure 7-9 **Design of Fluidic Auto-Phoropter Prototype One:** Here we identify the physical positions of all the optical elements to replicate our 4F imaging system. The line of sight of the user for a monocular setup is transparent.

The second purpose of the relay telescope is to preserve the shape of the wavefront. If the wavefront exiting the eye is a plane wave, then the wavefront hitting the lenslet array is a

plane wave. If the wavefront exiting the eye is a converging spherical wave, then the wavefront hitting the lenslet array is a converging spherical wave with the same curvature and magnification. Preservation is achieved by creating 1:1 angular magnification of the eye's pupil plane relative to the lenslet array in addition to achieving lateral magnification. We are therefore preserving the full wavefront by preserving both the angular and lateral size of the wavefront that is exiting the pupil of the eye. We achieve preservation of lateral magnification by having the focal length of doublet 1 equal to doublet 2. Also, the separation between the two lenses is two times the back focal distance of these equivalent powered lenses as is understood for a traditional Keplerian telescope. The 1:1 angular magnification is achieved by producing a  $4F$  imaging system. The pupil location is placed  $1f$  from doublet 2 while the lenslet array is placed  $1f$  from doublet 1. The combination of these positions allow for the reimaging of the pupil plane to the lenslet array.

A motivation for this design was to compress the optical system into a small region. We require a physical focal length of each doublet to be at least 75 mm with no tolerance for mechanical parts as we require the location of the pupil plane to telescope and the lenslet array of the Shack-Hartmann to the telescope to each have a  $1f$  separation. This minimal distance develops from the fact that relative to the pupil plane we require a beamsplitter and stack of fluidic lenses in front of the eye which accounts for 75 mm of space. However, the eye also requires eye relief of at least 20 mm. This causes the smallest separation between doublet 2 of the telescope system and the pupil plane to be 95 mm. We therefore chose to apply 100 mm focal length doublets for our telescopic system. To maintain the integrity of the telescope setup the doublet separation is 200 mm.

In order to keep this system in a compressed region we added folding optics. The folding optics was a series of four triangle mirror prisms that added a y-dimension component to our optical system. There are two significant angles that would allow for us to compress the system. We needed to produce a 200 mm separation between the two doublets while at the same time not adding stray light into the optical system. The  $\theta_u$  angle identified the angular separation between the top of prism 1 to the edge of prism 3. This produced the limit of not reimaging from prism 3 directly into the doublet, hence causing stray light to enter the system. The second significant angle is that of  $\theta_l$  which identifies the largest angle that is acceptable to maintain the light into the prism from prism 1 to prism 2. We wanted to ensure that our system would not maintain stray light so we calculated for a doublet separation of 150 mm rather than 200 mm. This tight tolerance allowed for us to find the right prism length  $L_p$  which will give results for 75 mm focal length lenses. If the folding mirror prism functions at 150 mm, then it will function with any telescope system that uses doublets that have longer than 75 mm focal length. The identification of the prisms and separation calculations were necessary to eliminate stray light data from skewing our prescription analysis. In addition, when we are testing Myopics or Hyperopics, the light will vary in reflection location due to change in the power of the optical system. Therefore, the higher tolerances were necessary to reduce stray light effects with varying degrees of power induced in the optical system by the eye.

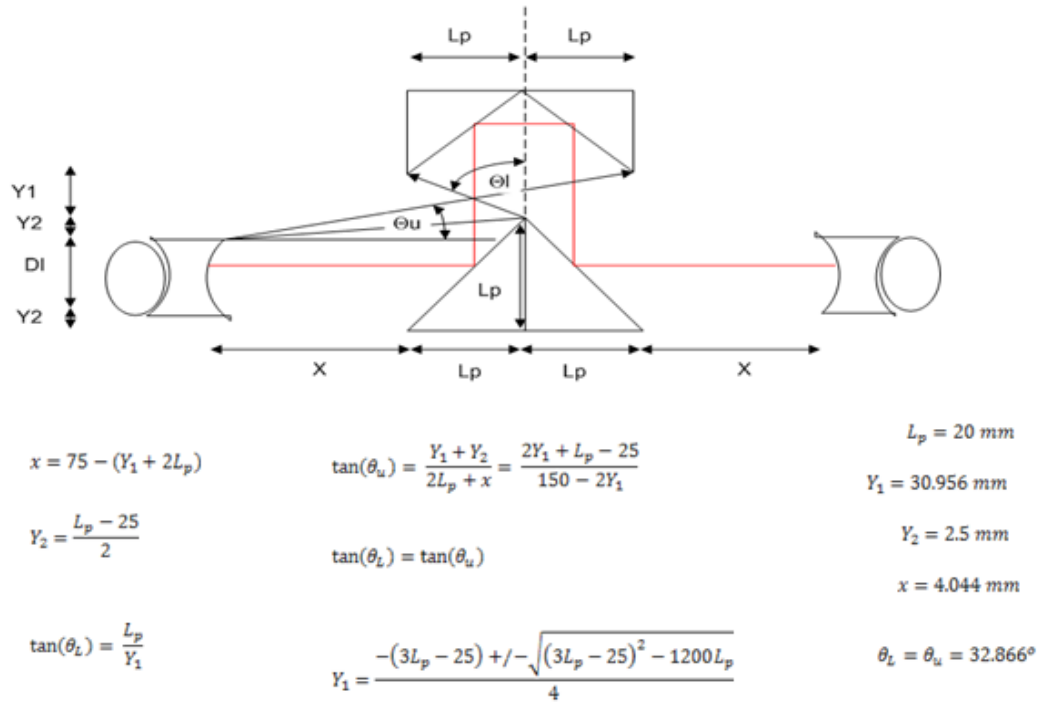


Figure 7-10 **Folding Mirror Analysis:** This is the setup of the monocular system with the dimensions of the prism region size as to compress the system.

#### 7.1.4 Fluidic Auto-Phoropter Prototype One: Light Path From Keplerian Telescope to Shack-Hartmann Wavefront Sensor

Now that we have established the folded mirror telescope system, we must have the light reach the Shack-Hartmann wavefront sensor. The lenslet array of the Shack-Hartmann wavefront sensor is 1F beyond the telescope system, but also it must not be in the line of sight of the user. An NIR beamsplitter is inserted to direct infrared light towards the final off-axis Shack-Hartmann module to achieve these results. This second NIR beamsplitter separates the optical paths of the IR light source and the line of sight of the user. The beamsplitter passes visible light, allowing for the subject to view external targets such as an eye chart. Concurrently, it reflects the NIR signal to the Shack-Hartmann wavefront sensor. The system has a self-aligning feature where a slight red dot is observed in the center of the field. If the dot is not in

the center of the users' field, then we can adjust the position of one of the monocular arms of the fluidic auto-phoropter. This NIR light is magnified in Figure 7-11 to show the self aligning feature within each fluidic auto-phoropter monocular arm.

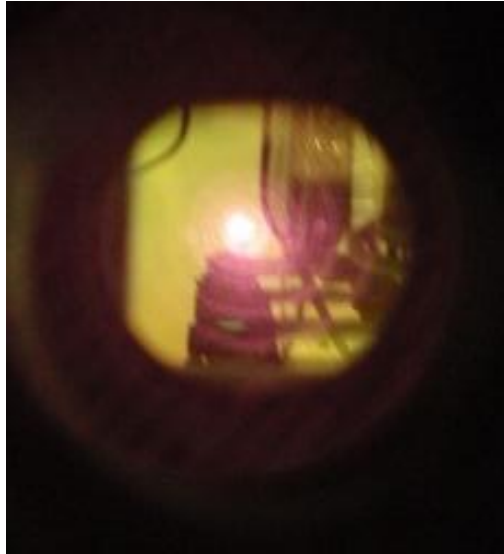


Figure 7-11 **Line of Sight of User:** This is the view through a monocular system with the self aligning NIR source where on the opposite side is a scene of the lab.

The Shack-Hartmann wavefront sensor is placed in a conjugate distance to the location of the pupil plane. As was explained in the telescope section, we achieve 1:1 angular and lateral magnification with this design. We experimented with two Shack-Hartmann wavefront sensors. The first sensor was built in house built. The lenslet array was fabricated on a 25 mm radius lens with 18 mm focal length lenslets at a pitch of 250 microns. The second Shack-Hartman wavefront sensor was bought from Thorlabs. We have fully described the system design by tracing the photon propagation from the source to the detector.

To simplify the functionality of the design we can break down the system as follows: (1) Infrared light is shone into the eye and scatters from the retina. (2) The scattered light exits the eye as an emerging wavefront that is relayed through the fluidic lens to the Shack-Hartmann sensor. The sensor reconstructs the wavefront and extracts the sphero-cylindrical refractive error.

This prescription is then applied to adjust the volume of the fluidic lenses in an attempt to null out the refractive error. Feedback of the wavefront from the eye/fluidic lens combination is then used to monitor the fluid volume and keep the net refractive error at a minimum. In theory, prescriptions and automatic correction is achievable within seconds of a patient looking into the system. The key to achieving these goals is to identify the amount of illumination necessary to hit the eye that is detectable and ensure this value is below the eyes threshold.

## 7.2 Fluidic Auto-Phoropter Prototype One: Alignment for Monocular Setup

The alignment of the optical system can be simplified by taking advantage of the opto-mechanical structure of our optical parts. By purposefully applying cage rods to connect optical parts we were able to quickly align our optical system.

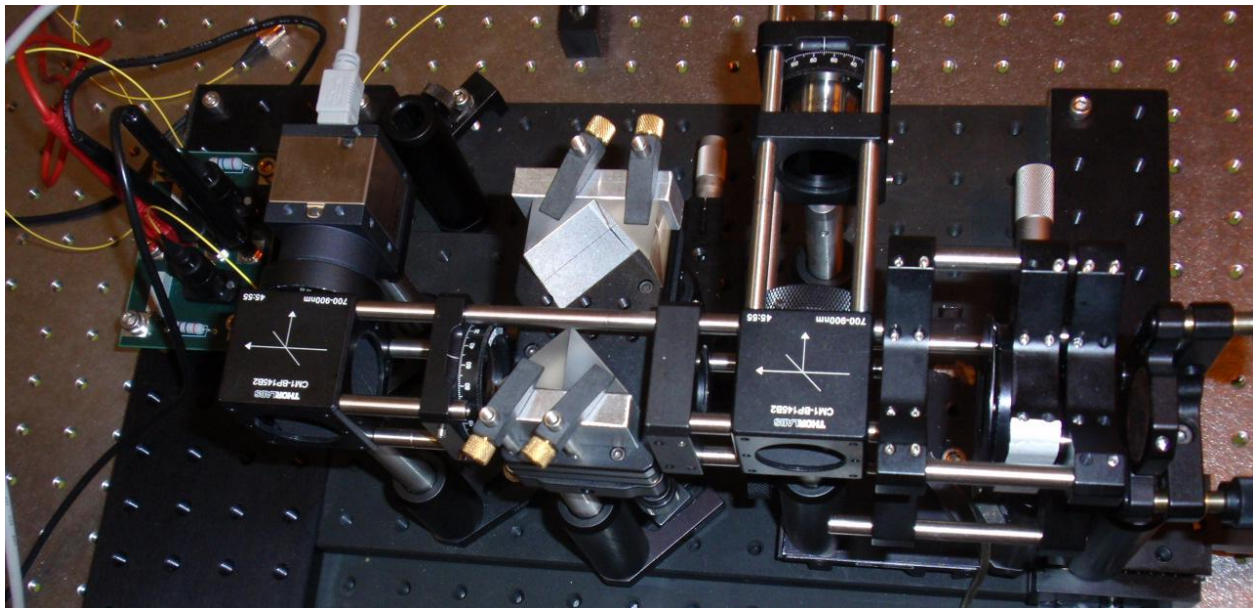


Figure 7-12 **Alignment of Monocular Fluidic Auto-Phoropter Prototype One:** This is the prototype of phoropter one showing the cage assembly setup of an aligned system.

The two NIR beamsplitters are the central pieces of our alignment process. Cage rods attach the majority of the optics in a t-shape relative to these cube mounted beamsplitters. We will again follow the photons from start to finish in explaining the alignment of the optics. The first row of rods connects the light source directly to the first NIR beamsplitter. Both

beamsplitters are posted down as they are our support locations. The ND filter in the optical path between the light source and the NIR beamsplitter is also posted down so that tilt will not be induced from the source.

The optical path continues upon reflection from the NIR beamsplitter toward the model eye. Our fluidic phoropter is mounted onto a 30 mm to 60 mm cage plate adapter. The fluidic phoropter is larger than 30 mm and is blocking the 30 mm cage holes as connectors. We therefore mount a second 30 mm to 60 mm cage adapter onto the first beamsplitter. We then apply cage rods from the cage plate adapter attached to the beamsplitter to the cage plate adaptor connected to the fluidic lens. This allows us to align the center of the fluidic lens to the center of our light source. Behind the fluidic lens there is an additional 30 mm to 60 mm cage adapter. Inside this additional adapter is our 18 mm focal length doublet that replicates the focal length of the eye focusing onto the retina, which as we described is our flat mirror.

As we reflect through the mirror we now propagate the light back through the optical system to the telescope system. The telescope system is comprised of the two doublets and the folding prism setup, where the folding prisms configuration is the second optical sub-system. These two optical sub-systems had to be aligned separately. It is important that the doublets were in alignment with the fluidic lens and the beamsplitters. The doublets for the telescope system were aligned into cage rods that connected each beamsplitter to the nearest doublet. A single rod connects in between the two beamsplitters to ensure that both beamsplitters and doublets were aligned. This single cage rod allowed for the folding prisms to be placed in the optical path between the two beamsplitters. At the same time we were able to align both sides of the telescope system.

The alignment of the four prisms in the folding setup was a separate sub-system. There are two platforms holding two prisms on each platform. A rectangular plate that was machined in the machine shop was placed behind each pair of prisms to make sure that they were aligned flat relative to each other. The two platforms with the four prisms were then aligned by using pinholes set at the same height. Each prism platform offered two degrees of freedom in tip and tilt. The pinholes were placed at a meter separation and the prisms were tipped and tilted until a collimated light exited out of the system. The prisms were then slide into the optical setup. The final step in aligning the telescope system was to achieve the proper separation between the two doublets. The wavefront sensor was applied in producing the proper separation between the doublets of the telescopic system. To align the sensor we applied the laser beam directly onto the sensor. We then adjusted the tip and tilt of the reflecting mirror to zero out the residual aberrations from the mirror. The fluidic lens and eye doublet were removed from the optical setup and the mirror was placed back into the system. One of the sets of prisms was posted onto a actuator controlled micrometer translation stage. The wavefront sensor was placed on the opposite side of the telescope system. We then adjusted the micrometer that shifted the prism location until the defocus was zeroed out. This approach created a corrected telescope system with the wavefront sensor placed in its proper distance relative to the pupil plane of the eye model.

### **7.3 Fluidic Auto-Phoropter Prototype One: Binocular Alignment and Inter-pupillary Distance**

We can duplicate this monocular auto-phoropter setup, thus producing a binocular testing system. The alignment of the second auto-phoropter is achievable by again aligning the beamsplitters, but this time the four beamsplitters that are aligned are between the two monocular arms. We must first begin the alignment process externally from outside the auto-

phoropter system. This is achievable by using a beamsplitter, four mirrors, multiple pinholes, and an external laser. We first align these external parts so that we have created an optical path in the shape of a rectangle in free-space outside of the auto-phoropter design. The height of the rectangular cavity is equivalent throughout this area. The rectangular cavity has two light paths where half the light propagates in a rectangle from one direction and the other half of the light propagates from the second direction. Both paths follow the same rectangular trajectory which allows for us to test both auto-phoropters simultaneously. If there is a misalignment or we need to block any light from one path we can simply place a stop between the two arms. We will at a later point slide the phoropter setup into the beam path of one of the legs of this rectangular beam for alignment. This external laser will help us align two beamsplitters, one from each of the monocular setups.

Before sliding the binocular setup into the path of one of the channels in the rectangular laser beam path we have to ensure certain conditions. The first condition is that the first monocular setup is aligned and locked down. The second condition is that the second monocular setup's base must be in the same exact position on axis as the first monocular setups base. There are three additional base's that were required to achieve alignment of the two monocular bases. There was a much larger base underneath the monocular bases. The two monocular bases were wedged between two machined base wedges.

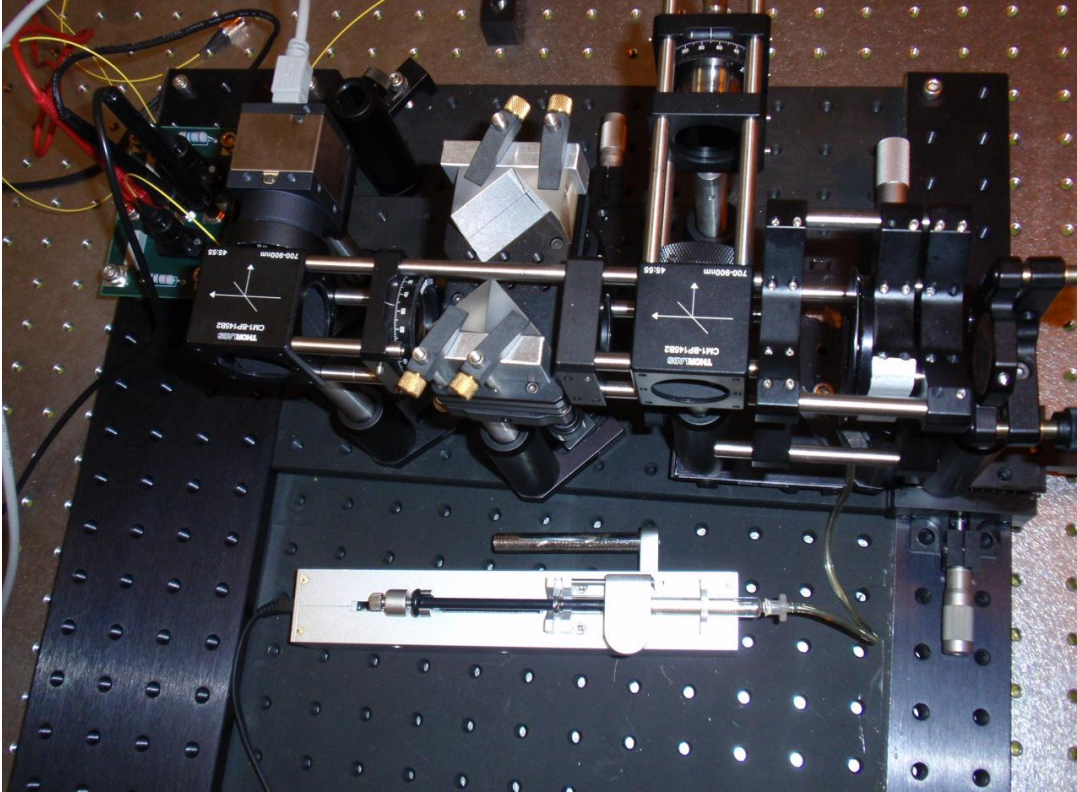


Figure 7-13 **Base Setup of the Binocular Fluidic Auto-Phoropter:** We have removed one of the arms of the binocular setup to observe the base. There are two metal frames in which the base is screwed onto. The monocular setup is tightly secured between the two frames.

The combination of these three bases with our two monocular setup bases allowed for a few additional features that were not capable before. The system became mobile, where by lifting from underneath one can move the entire system to any clinic required for testing. A second feature is that we were able to adjust one of the arms according to the inter-pupillary distance of the users. The base of one arm is locked down while the second fluidic auto-phoropter setup is mobile. The second arm slides until the user observes the self aligning NIR light source at the center of their line of sight. In order to achieve the proper inter-pupillary distances a modification was necessary in our 30 mm to 60 mm adapters. These adapters have an x shape to them. When the second monocular arm slides toward the first monocular arm the x mounts would hit into each other. We modified the x mounts so that half of the x mount was

rounded off on the inner segment where the two monocular setups interact with each other. By segmenting the x shaped adapter mounts we were able to reduce the separation between the two monocular systems down to 35 mm. For a small child the inter-pupillary distance is about 40 mm and so this system is applicable to people of all ages and eye separations. Figure 7-14 shows the removal of the fluidic lenses so that we can observe the machined 30 mm to 60 mm adapters.

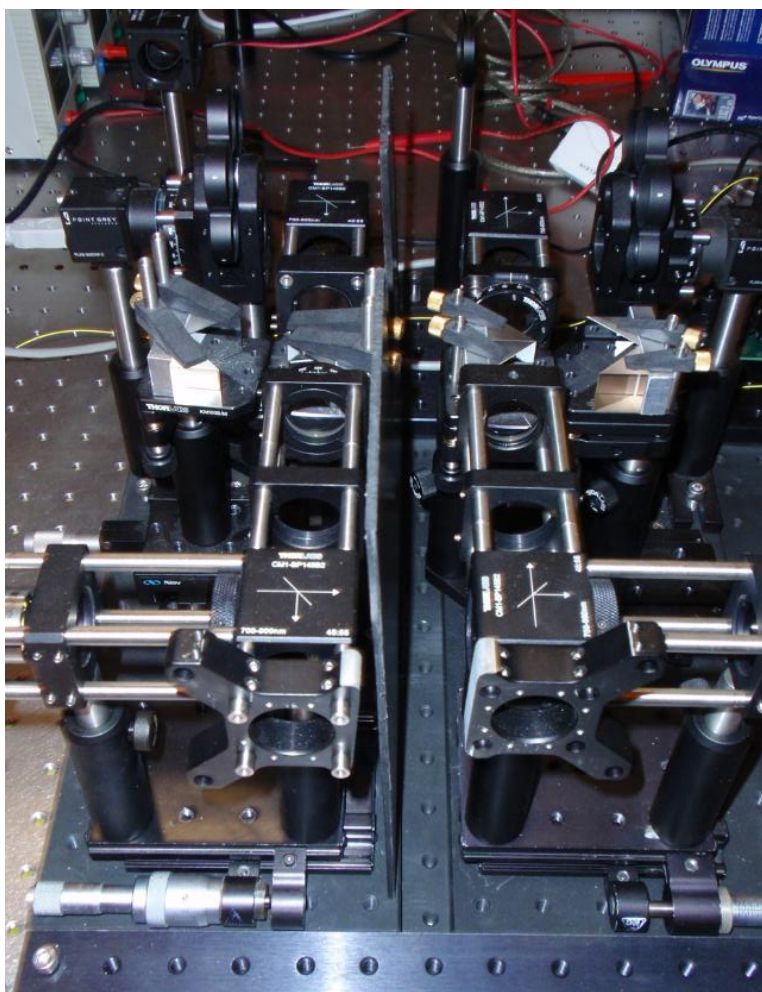


Figure 7-14 **Machined Adapters for Inter-pupillary Distance of Binocular Fluidic Auto-Phoropter:** The fluidic lenses are removed to show the machined optics where the 30 mm to 60 mm x mounts are trimmed, allowing for a 35 mm inter-pupillary separation.

The machining of the base and the 30 mm to 60 mm adapters allowed us to position the two monocular fluidic auto-phoropter systems next to each other. In order to align the two phoropter systems relative to each other we must first remove the light sources from each auto-phoropter system. We then slide the binocular setup into the path of our external light source. The first alignment occurs with the first adaptive phoropter. Each system is aligned to two subsystems where one group is that of the folded prisms and the second group is that of the rest of the system as was described in section 7.2. We have a pinhole facing the input of the external laser source as was described in 7.1.1. We stop down the pinholes on the beamsplitters and slid down the binocular system until the light from the external laser passes through the center of the pinholes which identifies the optical axis of both auto-phoropter arms. In this instance the group attached to the beamsplitters for both auto-phoropters were raised to the same height and aligned.

The next step in the alignment process was to align the four prisms for each arm of the binocular auto-phoropter. We removed the fluidic lens and eye model for this alignment and replaced the optics with a flat mirror. This flat mirror allowed for the light source to propagate through the entire optical system. The prisms were raised to the height of the rest of the binocular auto-phoropter system. The prisms had a coarse alignment as they were aligned before combining the two systems as described in section 7.2. With the raising of the prism bases there was slight misalignment. A block in between the two auto-phoropter arms was added to separate the light in each arm. We then aligned the light traveling through both optical arms at a distance of 15 feet from our optical setup. After the points were completed aligned we identified that the height and separation between the beams at 15 feet away were at the same height and separation of the beamsplitters between the two optical arms.

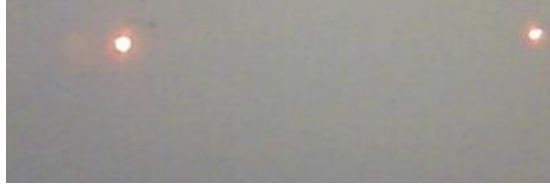


Figure 7-15 **Spots of Alignment Beam at 15 Feet Away of Binocular Fluidic Auto-Phoropter:** The spots from the external light source through our fully aligned first binocular fluidic auto-phoropter prototype.

After alignment was completed, we added both of the NIR SLD light sources back onto the rails. We then tested to ensure that the separation has not changed as observed 15 feet away. The binocular fluidic auto-phoropter system had been aligned after the spot positions have been verified. The fluidic lenses are then added onto the system and testing of the system can begin.

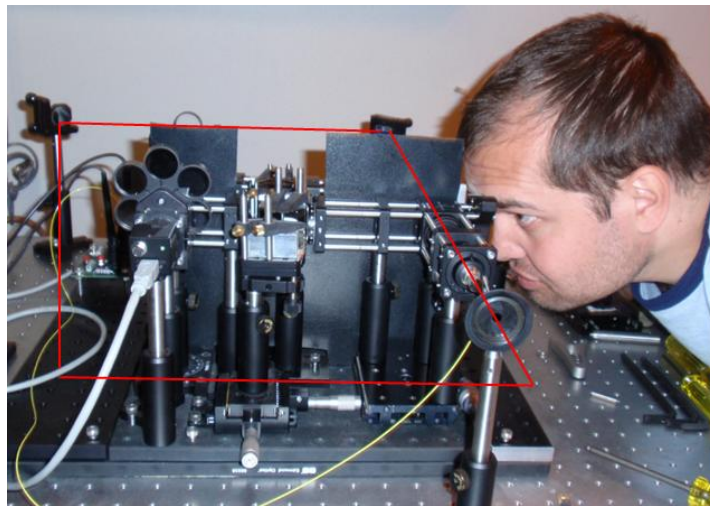


Figure 7-16 **User Position in a Fully Aligned Binocular Fluidic Auto-Phoropter:** The position of the user is observed relative to the designed system. The red lines indicate the optical path of the external source. This external source was turned off and blocked by the SLD as this image represents the fully aligned system.

## **8.0 FLUIDIC AUTO-PHOROPTER PROTOTYPE ONE: MODELING**

A significant step prior to testing a system is to model the functionality of the design. We modeled the system first with ZEMAX lens design software. This modeling scheme did not include power in the fluidic lenses. We were identifying the dynamic range of the sensor with the relative position of the cornea, telescope, and wavefront sensor. The relative positions of the optics define the expected measurable results. The next step was to model the system with illumination software. The fluidic phoropter was varied for defocus and astigmatism in this modeling when coupled to the test system. The illumination software was applied to identify if stray light will reduce the optical quality of our results. In addition, we modeled the expected results of both the astigmatism and defocus lenses. The results of the ZEMAX model are not altered by the fluidic lens, as we did not apply power into the fluidic lenses to adjust the power of our system. The ZEMAX modeling was created to determine the physical range of the auto-phoropter system. The following step was to determine the amount of power variation that is measurable with the fluidic phoropter while keeping the model eye constant. This was achieved in our modeling of the system in FRED. The FRED illumination software additionally will accurately identify stray light and point resolution. The difference between the results of the physical measurements in the next section and the modeling of the system in this chapter is in that our modeling matches ideal control of the fluidic phoropter with no residual error rather than experimental results of the fluidic phoropter.

### **8.1 Lens Design Model of Dynamic Range of Auto-Phoropter**

We first begin with a model of the auto-phoropter system. We are testing a single monocular setup to determine the dynamic range of our optical setup with the designed positions.

It is assumed that both monocular setups in the binocular setup will have approximately the same results as the two arms are mirror images of each other. The optical design for the auto-phoropter can be replicated non-sequentially within ZEMAX and recombined to develop a fully functional monocular design. A code was developed to achieve the design of the optical system. The design of the phoropter was developed to the dimensions of the optical elements chosen. This allowed for us to achieve the proper vignetting of the optical system.

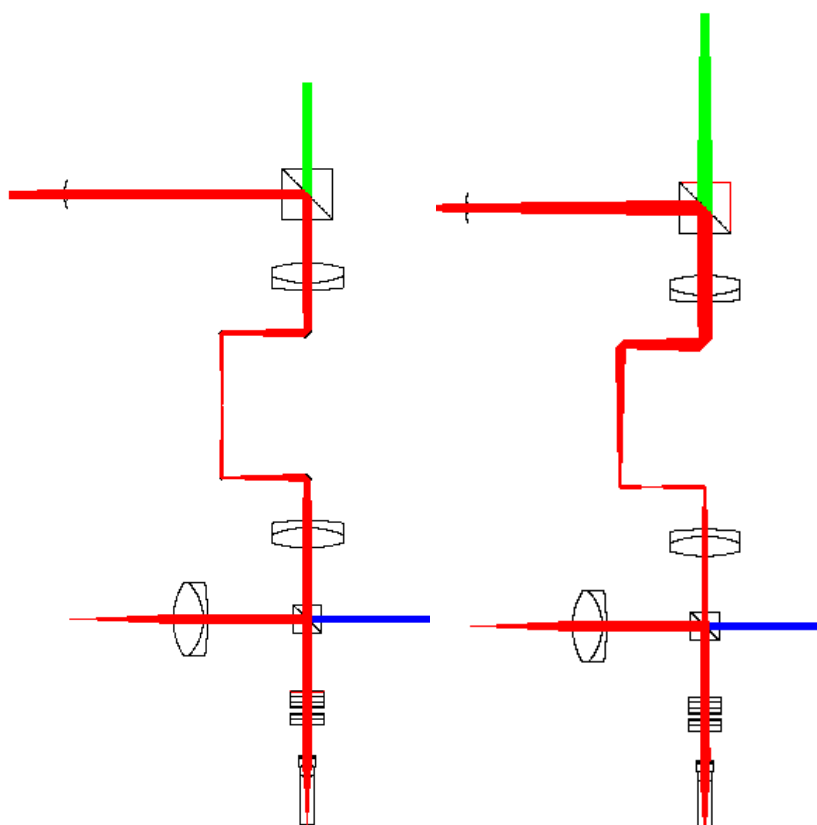
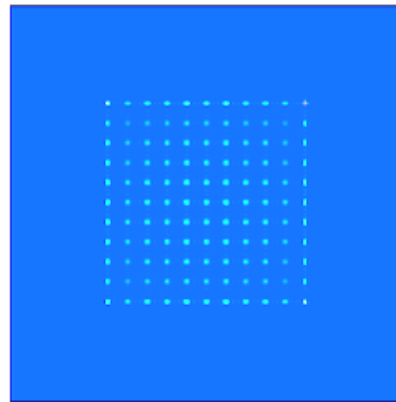


Figure 8-1 **ZEMAX Layout of Monocular Setup of Auto-Phoropter:** The blue light is a collimated light coming out of the SLD where half of the light is stray and passes through. The red is the reflected light that hits the eye and then reflects through the optical system to the sensor. The Green light is the line of sight of the user. The designed system on the left shows a fully collimated system while the system on the right shows the system with a corneal radius of -7.3 mm.

The above design describes a collimated SLD light source propagating through our optical system. The first beamsplitter drops about 45% of the light as stray light passing through the optical system. A stop is placed between the two arms of the optical system to ensure this light is not trapped between one arm to the other. The rest of the light reflects to our fluidic phoropter that offers zero power variation and then the eye model. Our eye model is designed to the radii of curvature as prescribed by the Arizona Eye Model. The light reflects through the model back through the phoropter and beamsplitter to the telescopic system. The telescopic system is compressed to two doublets with equal focal length and 4 mirror prisms. The 4 mirror prisms are represented as flat mirrors in ZEMAX. The telescope reimages in the same fashion as was described in earlier sections. The green light that passes through the beamsplitter is stray light loss of NIR light for the ZEMAX model, but also identifies the line of sight of the user.

It is important to remember the intensity of light that the system operates with. The intensity of the NIR light must be between 10-25  $\mu\text{W}$  as we do not want to induce damage to the eye. Light reflects off of two beamsplitters, where 45% of the energy is reflected per reflection, and also light is transmitted through a beamsplitter, where transmission is 55%. The output of the light source is setup that 10-25  $\mu\text{W}$  reaches the eye model after these two reflections occur. Therefore, the intensity at the light source is higher than the 10-25  $\mu\text{W}$  and is designed for this intensity at the eye model. Approximately 10% of the light reflects out of a human eye and so the amount of energy from our source drops down to 1-2.5  $\mu\text{W}$  reflecting out of the eye. We observe one transmission and one reflection off of the beamsplitters before reaching the detector, dropping the intensity at the detector plane from the source to 0.25 to 0.62  $\mu\text{W}$ . Energy conservation is therefore a significant factor in the positioning of the optical telescope relative to the eye model and lenslet array and this requires continued review when testing with humans.

ZEMAX model does not identify the intensity of light propagating through the system to the sensor as we did not prescribe energy loss coefficients for the surfaces. The collimated design provided the following irradiance pattern, identifying that the lenslet array and the collimation systems were modeled properly.



**Figure 8-2 Model of Image Plane of Shack-Hartmann Wavefront Sensor in ZEMAX:** The designed results of collimated light reaching the detector of our Shack Hartmann wavefront sensor after propagating through our design.

Figure 8-2 shows the point by point identification of collimated light reaching the detector plane with our aligned optical system. In this design, we have produced a collimated system with a corrected eye that has a corneal radius of -7.8 mm, where the points in the horizontal and vertical direction have a  $\Delta x$ ,  $\Delta y$  separation of about 250 microns. The 250 microns show that the model separation matches the separation of the lenslet in the lenticular array. The spot diagram has continual even separation on axis for each of the lenslets, producing a properly aligned optical system.

To identify the dynamic range of the optical system, one must vary the curvature of the test plane, such as the radius of curvature of the cornea, to measure the slope variation at our detector plane. We can therefore apply the slope variation that was described in section 3.2.4 to

allow for us to reconstruct the wavefront. By adjusting the power in the optical system the observed wavefront error is measured through slope measurement equations:

$$w = \frac{r^2}{2R}$$

$$\Delta x = \Delta y = -f \frac{\partial w(x_o, y_o)}{\partial x}$$

$$\partial \varphi = \frac{1}{r} * \frac{\partial w(x_o, y_o)}{\partial r}$$

$$\Delta x = \Delta y = -f * r \partial \varphi$$

$$\partial \varphi = \frac{\Delta y}{-f * r}$$

8-1

A well functioning system would allow for the measurement and correction of defocus aberration in the eye that varies between -20 to 20 Diopters. To see if this optical design is physically capable of replicating the required Diopter range the power variation was modeled by controlling the surfaces at the model eye location. We modeled the amount of power correction at the cornea by creating compensating power at the fluidic lens location. This was achieved by shifting the x and y dimension as the radius of the cornea was adjusted. For each corneal radius the positions were mapped relative to the amount of shift. A second approach was to introduce a paraxial focal length in front of the cornea and identify the point variation at various focal lengths. With both approaches, the shift was identified and then equations from 8-1 were applied to determine the change of power observed for each corneal radius.

Corneal Radius (R) mm	(x,0) in mm	(0,y) in mm	D <sub>x</sub> in mm	D <sub>y</sub> in mm	r (mm)	f (mm)	df (Diopters)
-7.3	214.34	213.92	-38.16	-38.58	54.26	18.53	38.09
-7.4	224.18	224.22	-28.32	-28.28	40.022	19.174	36.8784
-7.5	232.58	231.96	-19.92	-20.54	28.612	19.733	35.9535
-7.6	240.16	240.01	-12.34	-12.49	17.557	20.226	34.9174
-7.7	246.72	246.56	-5.78	-5.94	8.288	20.655	34.6983
-7.8	252.5	252.5	--	--	--	--	--
-7.9	257.5	257.43	5	4.93	7.0217	21.41	-33.26
-8.0	262.5	262.53	10	10.03	14.163	21.731	-32.49
-8.1	266.66	266.61	14.16	14.11	19.99	22.023	-32.08
-8.2	270.83	270.86	18.33	18.36	25.943	22.290	-31.75
-8.3	274.16	274.14	21.66	21.64	30.617	22.536	-31.36
-8.4	277.9	277.8	25.4	25.3	35.850	22.762	-30.943
-8.5	Diffraction Limit						

Table 8-1 **Power Shift of Auto-Phoropter System Due to Variation in Corneal Radii:** Identifying the amount of compensating power produced by varying cornea radii.

The lenslet array produced resolvable points that were outputted in a spot diagram from ZEMAX. To achieve quantifiable results from the spot diagram, the image plane was scaled to the size of the CCD array. From this information we can visually verify the limit of our auto-phoropter range. The higher limit, as is shown in Figure 8-3, was measured to + 500 D. The system could have been measured even further; however, the majority of eyes do not exhibit higher than + 20 D of defocus error. For this reason we find that there are no system limitations on the higher positive powers. The higher Diopter powers will be limited by the power range of the fluidic lens.

The lower limit of our auto-phoropter was identified to be approximately -30 D by both modeling metrics. Figure 8-3 shows the lower range of detection from both systems. The two approaches show that at these higher negative powers our points form coma shapes and reach resolvable limits. This suggests that our auto-phoropter system can measure optical error from the eye between -30 to 30 Diopters, with prototype one at 4f imaging with two 100 mm focal length lenses. The dynamic range of our auto-phoropter measures the entire Tscherning ellipse, which identifies the amount of power correction needed for spectacle lenses. Our system can therefore measure the prescriptions for the majority of users. The additional component of our auto-phoropter includes for the correction achieved by the fluidic lenses. If for example our fluidic lenses compensate for -30 to 30 Diopters of defocus power, our system would automatically correct for the full range of prescriptions. If our fluidic phoropter technology reaches a dynamic range of -35 Diopters to 35 Diopters of correction, we will be limited by the system design. The system would have the capability of correcting the upper limit of 35 Diopters defined by the fluid lenses and a lower limit of -30 Diopters defined by the auto-phoropter design. The model shows that our optimum range would be for the fluidic lens to

operate between -30 Diopters to 30 Diopters. This will allow the sensor to be the limiting factor and thus we have optimized the physical system as is observed with the physical positions prescribed in prototype one.

- Approach 1: Vary the radius of the cornea and identify the point separation in the x and y dimension, determining power variation.
  - Approach 2: Introduce a paraxial focal length in front of the cornea and identify the point variation at various focal lengths.
  - Phoropter Range: -30 D to 45 D
- 
- The figure consists of three vertically stacked diagrams, each showing a grid of points. The top diagram is labeled '32 mm F (-31.25 D)' and shows a central blue 'X' shape formed by the points. The middle diagram is labeled '31 mm F (-32.258 D)' and shows a similar blue 'X' shape, but with a slightly different point distribution. The bottom diagram is labeled '-2 mm F (500 D)' and shows a regular grid of points with no central 'X' shape.

**Figure 8-3 Dynamic Range Limits of Auto-Phoropter:** Here we identify the limits of the auto-phoropter system where the fluidic lenses were zeroed to model the limits of the physical position of the optics by varying the power of the eye.

## 8.2 Illumination Model of Dynamic Range of Fluidic Auto-Phoropter

We have defined the physical measuring range of the auto-phoropter without the fluidic phoropter compensation. We require additional modeling on the effects of the fluidic auto-phoropter and also the stray light entering the system. FRED illumination software was selected to fully model the functional fluidic auto-phoropter design. Here we model the setup exactly as we had modeled the system in ZEMAX. The illumination software identifies the blurring of points, if overlapping occurs, and the amount of correction in both cylinder and defocus lenses.

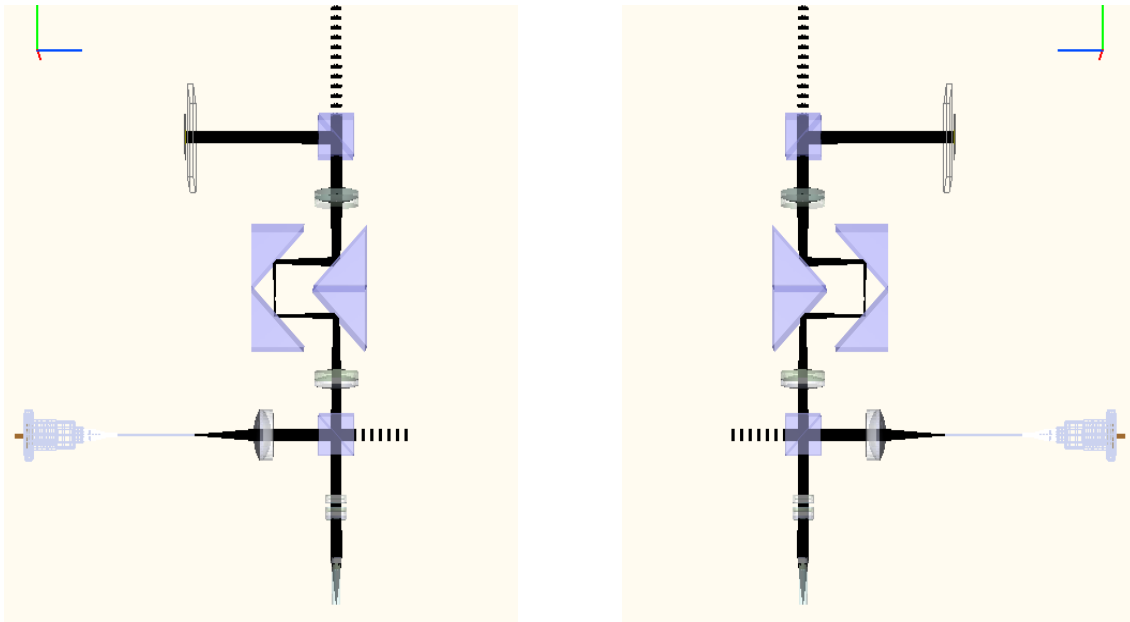


Figure 8-4 **FRED Model of Binocular Fluidic Auto-Phoropter:** The SLD light source was imported directly from Thorlabs while the rest of the optics was modeled to the specifications of our optical system. We show how two monocular systems combine to produce a binocular system.

The FRED model replicates the physical system. The light source was imported through a CAD file in Thorlabs. The optical beamsplitters are of the same size and reflective properties in the NIR range of 700-900 nm. The doublets were imported from the Edmund catalog. Our fluidic lenses were designed relative to DI water in the chamber system. When we measured the results at the detector plane we measured each monocular surface at a time. The system was fully aligned as we observed equally spaced points in the image plane. Figure 8-5 illustrates the light intensity distribution of the focused singular points with equal physical separation. Here we imaged a small area to magnify the effects of power variation from the fluidic lenses.

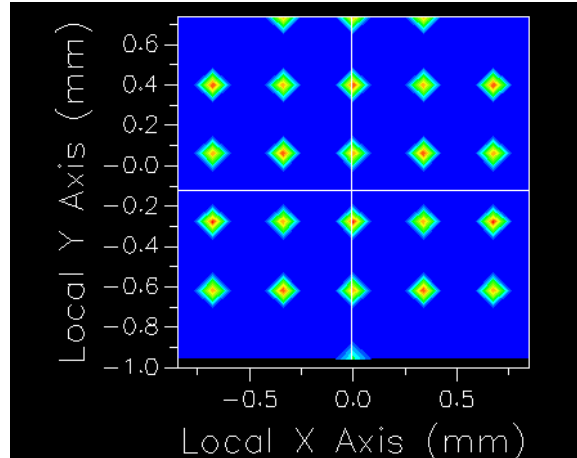


Figure 8-5 **Model of Image Plane of Shack-Hartmann Wavefront Sensor in FRED:** The designed results of collimated light reaching the detector of our Shack Hartmann wavefront sensor after propagating through the full optical system. The fluidic phoropter lenses exhibit zero power variation. Here the intensity distribution is shown to vary from the center of each point.

We first identify the limiting factors of the system to accurately assess the compensation range that our fluidic auto-phoropter can achieve. As we had identified through ZEMAX modeling, the system has a capability of measuring - 30 to + 30 D of error. Our fluidic phoropter does not have this physical range and thus our limiting factor is the fluidic lens. In order to model the fluidic auto-phoropter properly, we first identify the fluidic lenses physical range. The fluidic lenses power range was calculated empirically by determining the physical range of the phoropter's radius of curvature as was described in section 5.1.4. De-ionized (DI) water was first used to characterize the fluidic lens' radius of curvature. DI water has an Abbe number of 55.74 and the indices of refraction are known for a wide scope of wavelength ranges [68]. The focal lengths of the DI water based fluidic lens was first measured using red (HeNe 633 nm), green (HeNe 543 nm), and blue (Argon 488 nm) lasers.

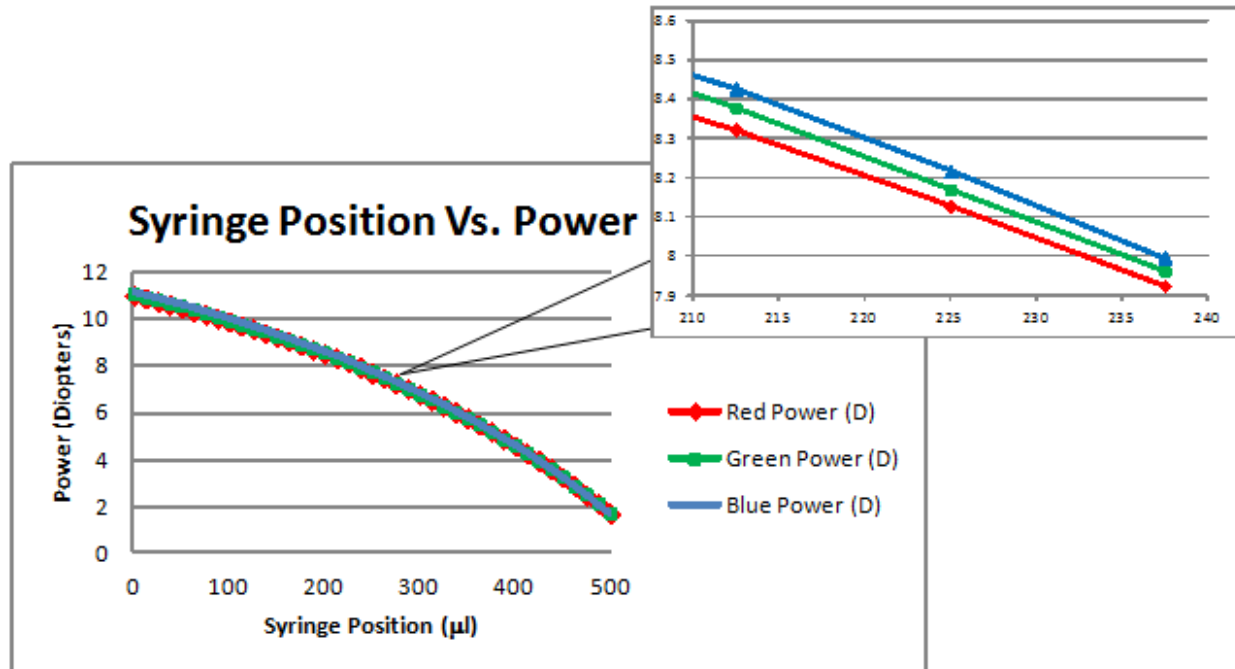


Figure 8-6 **Power Range of Defocus Lens of Fluidic Phoropter:** The physical range of the fluidic lens for 0.5 mm evacuation of fluid is about 10 Diopters, which is much smaller than the dynamic measuring range of the auto-phoropter. Thus the limiting factor of the system is the fluidic lenses.

As was previously stated, we applied DI water with known indices of refraction per wavelength in identifying the fluidic lenses radius of curvature range. For a given amount of fluid in the lens, we measured the focal length at each of the three designed wavelengths. The radius of curvature,  $r$ , of the lens surface was calculated using  $\Phi = 1/f = (n_{\text{air}} - n_{\text{DI}})/r$ , where  $\Phi$  is the surface power and  $n_{\text{air}}$  and  $n_{\text{DI}}$  are the indices of refraction for air and DI water per index, respectively. The focal length,  $f$ , of each measurement was equal to the back focal distance of the fluidic lens using the thin lens approximation. Each radius of curvature was calculated at red, green, and blue wavelengths and averaged to determine a single radius of curvature per fluid volume. The experiment was repeated as we increased the fluid volume in the lens by increments of 50  $\mu\text{L}$ . We averaged several tests to determine the range of the radius of curvature for our

fluidic defocus lens. The following chart illustrates how we placed empirical data into an excel spread sheet to determine the radius of curvature range. The pump control broke our increments to 41 values that ranged from a notch of 20 to a notch of -20, where each notch identified a fluid evacuation of 50  $\mu\text{l}$ . We were measuring radii of curvature limits and so the large notches away from the center location were the most relevant results.

Pump Control Notch	Focal Length Red (mm)	Focal Length Green (mm)	Focal Length Blue (mm)	Green Light (D)	Separation between Red and Blue (mm)	Separation between Red and Green (mm)	Separation between Green and Blue (mm)	Vf of fluidic lens using $\delta f$	Radius of Curvature ( $r_c$ ) mm	Sag (mm)
20	138.80 0	139.65 0	141.60 0	7.1607 5904	-2.800	-0.850	-1.950	-49.87	46.28001	1.0932
19	140.83 3	142.00 0	144.13 3	7.0422 53521	-3.300	-1.167	-2.133	-43.03	47.0588	1.0747
18	143.13 3	144.65 0	146.83 3	6.9132 38852	-3.700	-1.517	-2.183	-39.09	47.93701	1.0546
17	145.96 7	147.30 0	149.53 3	6.7888 66259	-3.567	-1.333	-2.233	-41.29	48.81522	1.0352
16	148.70 0	150.00 0	152.70 0	6.6666 66667	-4.000	-1.300	-2.700	-37.5	49.71	1.0162
15	151.86 7	153.20 0	156.16 7	6.5274 15144	-4.300	-1.333	-2.967	-35.62	50.77048	0.9945
14	154.96 7	156.72 5	159.83 3	6.3806 02967	-4.867	-1.758	-3.108	-32.20	51.938665	0.9717

**Table 8-2 Empirical Measurements of Defocus Lens and Radii of Curvature:** Identifying the amount of compensating power and change in radii of curvature of the fluidic lens by altering the amount of fluid in the lens cavity. We show only 7 of the 41 notches as an example of our measuring approach. Defocus lens one has a 40 mm radius of curvature while defocus lens one has a 25 mm radius of curvature.

These empirical results define the fluids range in which we simulate the fluidic lens within the FRED software. The approach in simulating the change in power of the fluidic lens was to adjust the radius of curvature in FRED, where the radius of curvature and focal length ranges are now predefined by the actual lens range. When we adjust the radius of curvature of the lens, we are physically adjusting the power of the full optical system. The following two figures are a clear illustration of how the propagating rays alter in direction once the power of the fluidic lens is changed. Figure 8-6 on the left shows collimated light entering the detector. With no power from the fluidic lens, the light is also exiting the eye model and the relay telescope collimated. Once we induce power to the fluidic lens we induce power entering the users' eye. In this model, the retina is perfectly collimated but the fluidic defocus lens induces power. The defocus power variation continued through the entire optical system. Where when power is induced by the fluidic lens we observe a focusing location along the optical axis as is observed in figure 8-7. This condition identifies a limit of our fluidic auto-phoropter system. If the focal location is at the lenslet array we find that the wavefront slopes are not measurable with our wavefront technology. The physical limitation in the system can also be observed by the eye model inducing power and no power from the fluidic lens. There will still be a variation in the slope variation of the propagating rays. By producing a power from the fluidic phoropter that is equal and opposite of a user's eye, we are able to correct prescriptions in real time.

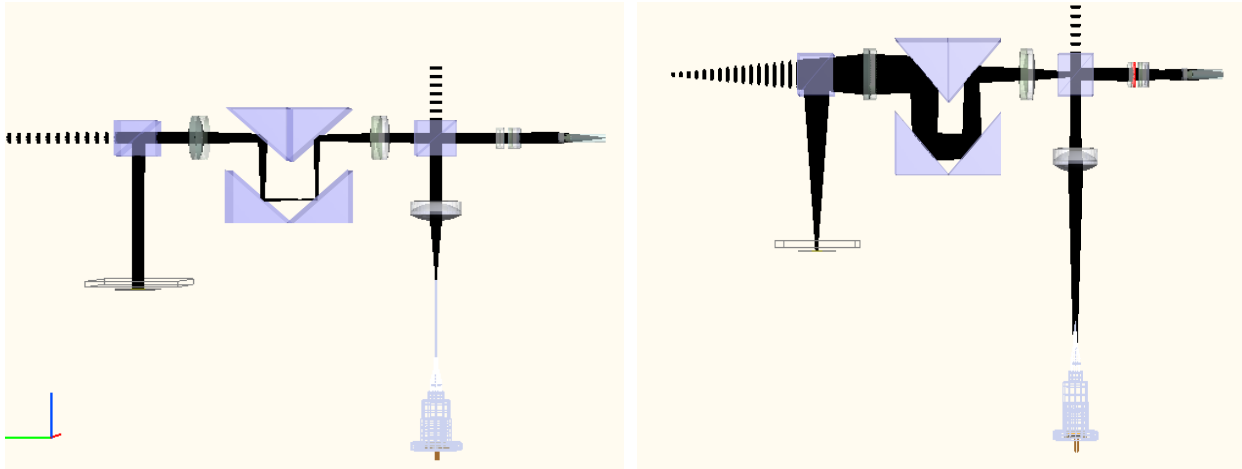
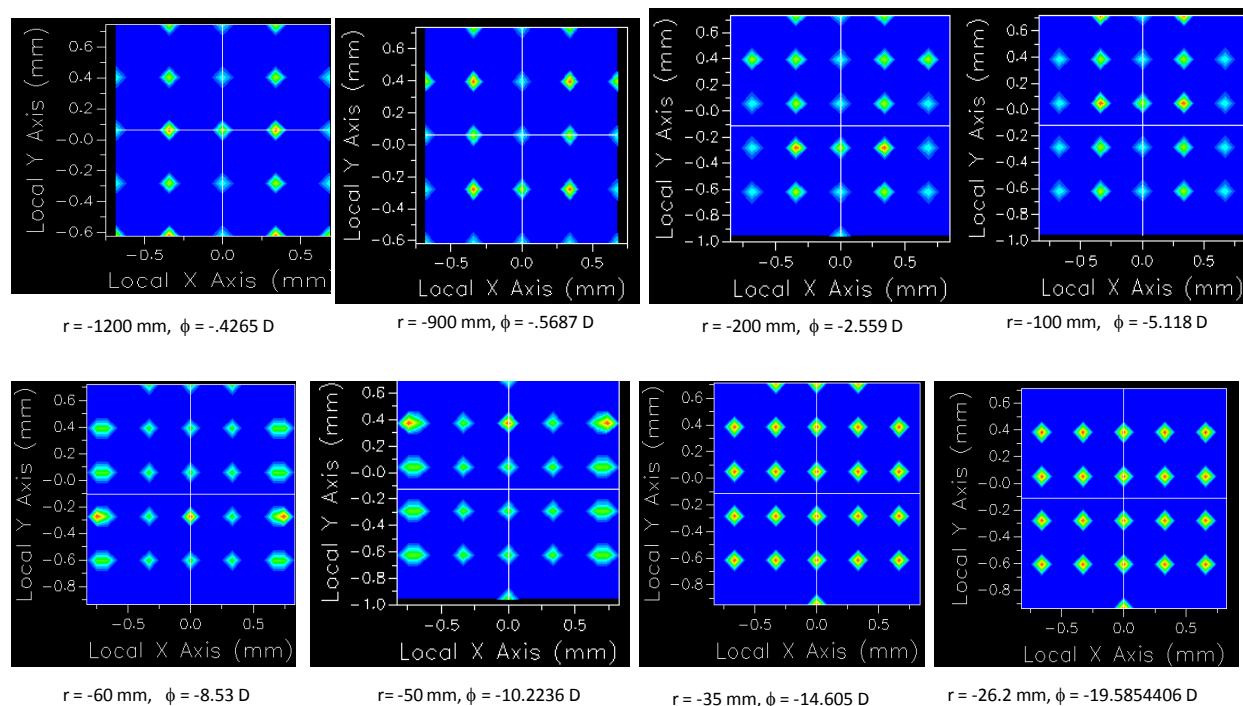


Figure 8-7 **Power Variation of Defocus Fluidic Lens in FRED of Fluidic Phoropter:** The traces of rays have shifted from a neatly collimated beam entering the sensor in the left to an optical system with high amounts of power when defocus is induced by the fluidic lens.

The defocus is detectable when we vary the radius of curvature as was previously stated. Between infinity and the near focal point we can control the radii of curvature. The following images show the induction of negative power into the phoropter's defocus lens. We observe that the points are collapsing inwards, indicating that the negative power is causing the slopes of the wavefront to shift inward. By assessing the slope we are able to determine the actual power that is observed relative to this image location for the whole system.

## Changing Curvature of Defocus Lens



**Figure 8-8 Defocus Lens Power Variation and Effects on Fluidic Auto-Phoropter:** The radius of curvature is altered matching the physical range of the defocus lenses. The point separation observed on the Shack-Hartmann wavefront sensor identifies changed power observed in the system caused by the defocus lens.

Modeling of astigmatism with FRED had been advantageous. FRED allows for the user to enter a surface plane and quickly alter the lens shape in one dimension. This enables us to replicate cylinder lenses with varying powers. As we have two fluidic astigmatism lenses that are orientated  $45^\circ$  relative to each other, we must control each surface individually with deflection direction  $45^\circ$  relative to each other. We modeled several conditions where the fluidic lens had various amounts of cylinder power. To magnify the great variation that our optical system can measure we choose extreme amounts of astigmatism correction. A traditional phoropter system would require less than -5 to +5 Diopters of astigmatism correction to cover a

majority of astigmatism cases. The following three images show various amounts of astigmatism. Figure 8-9 shows 20 Diopters of astigmatism in the x plane. This amount of astigmatism reaches about the limitation of our detector system, as the lenslet focal points approach each other. Figure 8-10 shows 10 Diopters of astigmatism in the y plane. It is seen that the amount of astigmatism in each plane is controllable. As we increase the power on the fluidic phoropter, the points come closer in one dimension. By showing that we are able to measure conditions well beyond the astigmatism observed in the human eye, we can prove our fluidic auto-phoropter is able to measure power variation due to the eye and the astigmatism fluidic lenses can compensate the eye's power. We can therefore identify the wavefront variation caused by the eye in our optical system. We can then compensate the wavefront error with our control in cylinder and power on any axis with our fluidic phoropter. After the error is nulled out, we are able to produce an automated prescription.

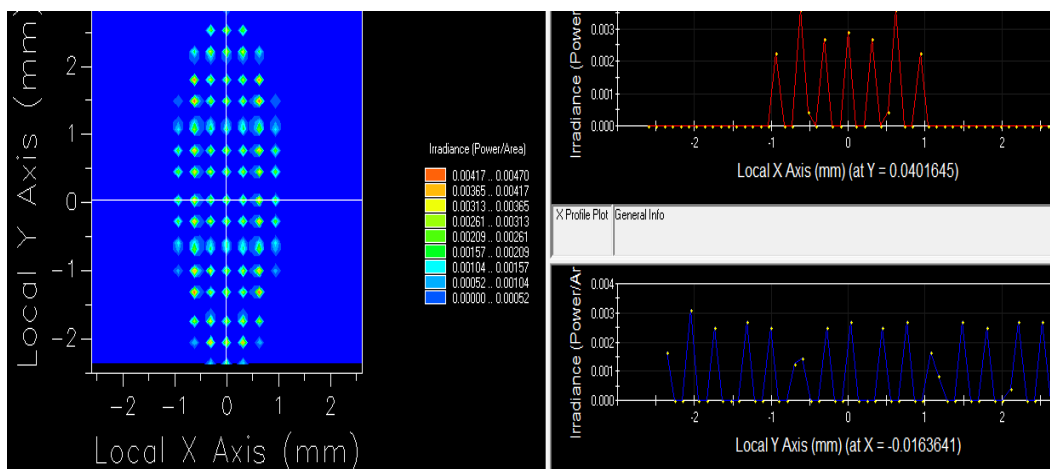


**Figure 8-9 Astigmatism Lens One Power Variation and Effects on Fluidic Auto-Phoropter:** The radius of curvature is altered on one of the astigmatism lens. The point separation observed on the Shack-Hartmann wavefront sensor outputs astigmatic variation of 20 Diopters in the x dimension.

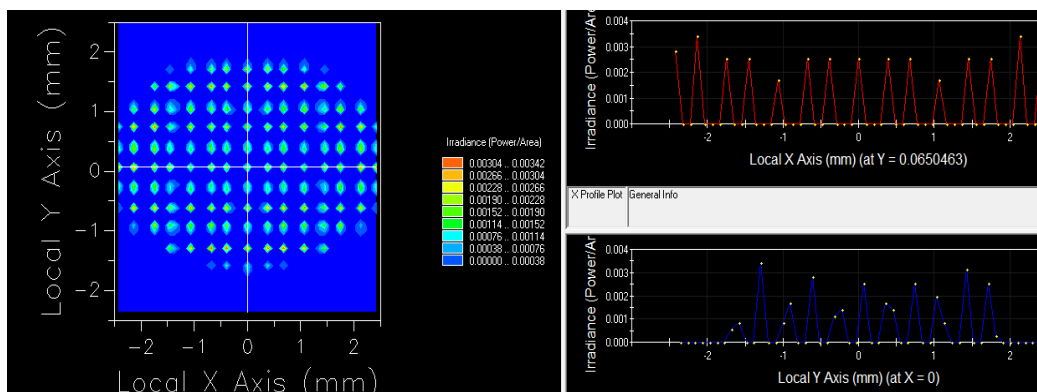


Figure 8-10 **Astigmatism Lens Two Power Variation and Effects on Fluidic Auto-Phoropter:** The radius of curvature is altered on the second of the astigmatism lenses. The point separation observed on the Shack-Hartmann wavefront sensor outputs astigmatic variation of 10 Diopters in the y dimension.

Figures 8-9 and 8-10 are extreme values of astigmatism that are not reasonable for human vision correction. We can replicate conditions that are more reasonable to what would be expected from human vision. As there are three fluidic lenses, we can correct for astigmatism and defocus simultaneously. As an example, we show in Figure 8-11 a combination of 4 D of defocus and 2 D of astigmatism. This figure illustrates that any combination of astigmatism and defocus is correctable by our fluidic phoropter within a reasonable range of human vision wavefront error.

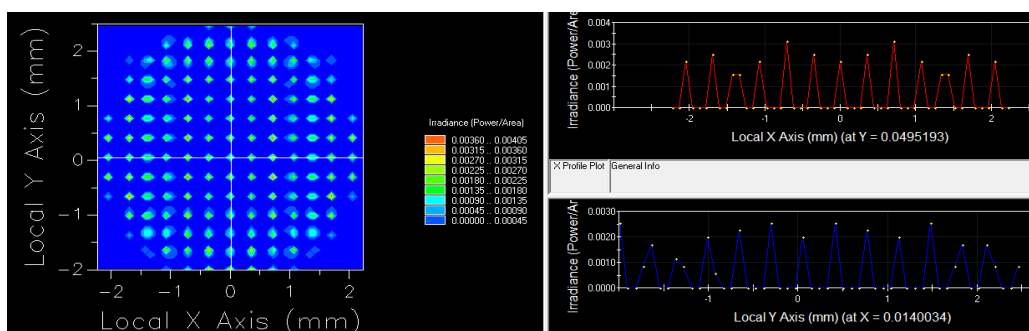


Figure 8-11 **Defocus and Astigmatism Lens Two Power Variation and Effects on Fluidic Auto-Phoropter:** The radius of curvature is altered on the second of the astigmatism lenses and also the defocus lens. The point separation observed on the Shack-Hartmann wavefront sensor outputs astigmatic variation of 2 Diopters in the y dimension and 4 Diopters of Defocus.

## 9.0 OPTOFLUIDIC AUTO-PHOROPTER PROTOTYPE ONE: TESTING

Chapters 7 and 8 have described the modeling and design of the first prototyped auto-phoropter. After a system is modeled and designed the next logical step is testing of the optical system. The system has not yet been tested with humans and so as a proof of concept we must establish an alternate approach in testing the system. In this chapter we will describe an approach for testing on either a human eye or a model eye. From there we expand on our measuring approaches for the model eye when coupled with our auto-phoropter system that excludes the fluidic phoropter. The exclusion of the fluidic phoropter enables us to measure various amounts of power induced by the model eye and the measurements extracted by the system. The model eye is then removed and replaced with the fluidic phoropter system.

In this section we test the defocus phoropter with DI water and also with one of our selected oils. Test results describe the variable wavefronts for astigmatism and defocus and also the sphere, cylinder and axis for all of our fluidic setups. These readings are a description of the entire auto-phoropter system. We can compensate the model eye and the auto-phoropter combined to null out the error as was previously described. The two defocus lenses are compared in optical quality relative to each other. In addition, both lenses are tested with 3 mm and 6 mm stops setup for the auto-phoropter designs. These stop sizes were determined to replicate the variation in Iris size within the eye dependent on lighting conditions. We identify the significance of stop size and how it alters our prescription results from the designed system.

The astigmatism lens has been tested with auto-phoropter prototype one. When testing the astigmatism lens we measured each individual lens separately. We then combined the two astigmatism lenses to measure the variation of astigmatism power. Variable amounts of fluid

were withdrawn from either the horizontal or the  $45^\circ$  set fluidic lenses and then the wavefront was measured. These measured values are lastly compared to the fluidic phoropter system.

Testing of the auto-phoropter is achieved through four basic steps. The first step is to zero out residual aberrations within the system. This was achieved in chapter 7 when we aligned the optical system. Secondly, we add a model eye to calibrate the optical system. The model eye is tested with known amounts of power to identify the auto-phoropter system wavefront measurements with each power measurement. The third step is to remove the model eye and insert our fluidic phoropter system. The fluidic phoropter is calibrated within the auto-phoropter system. Wavefront measurements are performed by varying the fluid volume in the actuated syringes and identifying the wavefront correction that occurs with the optical system. These wavefronts can be transferred to prescriptions based on sphere, cylinder, and axis for the entire auto-phoropter system. Lastly, the measurements from the model eye with the entire auto-phoropter system are nulled by the entire auto-phoropter system and the fluidic lens adjusted to the proper amount of fluid. Once the entire system is nulled out, we are able to identify the correlation of a given amount of defocus power within the eye model or the eye to the reading of our nulled system.

### **9.1 Testing Approach: Measurements of a Model Eye**

Here we begin with the first step in the testing process as the eye or eye model is placed in the conjugate plane of the detector. We place a flat mirror as our retinal plane and remove the fluidic lens to eliminate any undesired distortion of the wavefront. The model eye is first aligned so that collimated light is outputted from the optical system. This is achieved by placing the mirror at the back focal length of the eye model lens. The back focal distance of the eye model

lens was 14.91 mm. We then identify any residual aberrations which occur within the optical system. The mirror is adjusted so that the tip/tilt values are zeroed out and the optical axis of the model eye is aligned with the optical system. There should be no optical power induced at this point as we are applying our collimated eye model in addition to a telescopic system.

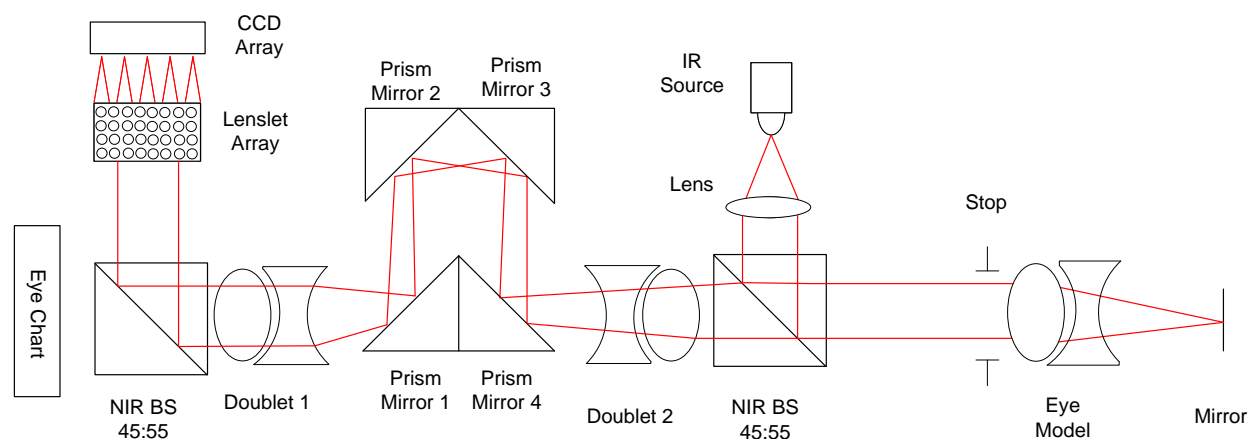


**Figure 9-1 Step 2: Testing Auto-Phoropter with Eye Model:** The fluidic phoropter is removed as to not induce undesired wave distortion. By adjusting the mirror of the model eye we are replicating power aberration of an eye. We then measure the wavefront power variation of the full optical system and determine the wavefront variation at a given amount of power error from the model eye.

After this alignment is achieved, we recalibrate the model eye to identify the amount of aberration induced to the full auto-phoropter system. It is non-trivial to note that this defocus wavefront is a measurement of the power of the eye or model eye, in this instance a model eye, coupled with the full auto-phoropter. The power exiting the model eye can be explained through an unfolding of the optical system. The eye model, as in the actual eye, has a double pass of the light entering the eye and then exiting the eye. We are able to unfold the optical path of this propagating light to treat the model eye as a telescopic system. We are able to model this telescopic condition in ZEMAX.

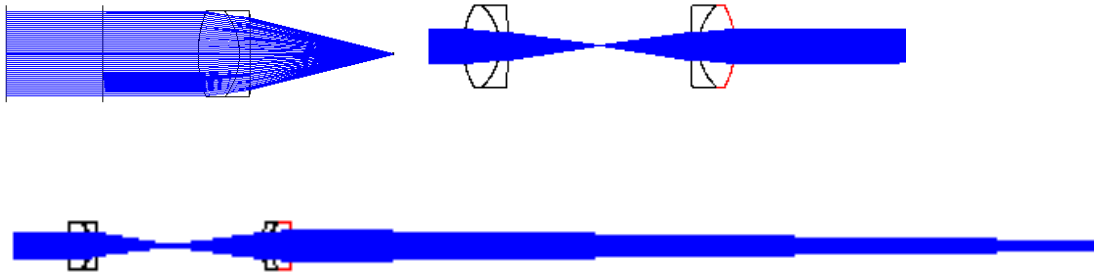


Figure 9-2 **Unfolded Eye Model:** The top left eye model shows the double pass of the propagating light. This eye model is Emotropic and so when the optical path is unfolded the system is replicated as a telescope. As we adjust the separation of the mirror to the doublet, we are adjusting the power of the model eye. The bottom image shows when we alter the separation that power is produced by our lens system.

The separation of this telescopic system is twice the 14.91 mm focal distance, which represents a collimated and corrected Emotropic eye, as this system is a double pass design. The power of the physical system is measured through  $\varphi_{sys} = \varphi_1 + \varphi_2 - \varphi_1\varphi_2\tau = \varphi_{EM}(2 - \varphi_{EM}\tau)$ , where  $\varphi_{EM}$  is the optical power of the doublet eye model lens and  $\tau$  is the separation between the two lenses in the unfolded system or twice the mirror shift distance. The doublet that is used for the eye model is Edmund Optics 49-314 which has a focal length of 18 mm and a back focal length of 14.91 mm. This back focal length is applied for the optical power of the eye model lens and thus is the variable separation between the lens to the mirror. The power that is outputted from the model eye can be measured by controlling the lens separation. By slightly adjusting the physical separation of the lens with the mirror at a rate of 50 microns we are able to replicate power variations of our eye model in approximately .25 Diopter increments. Current eye exams have .25 Diopter shifts in their lenses. By decreasing the shift of the mirror to less than 50 microns, we can measure defocus power of the model eye in less than .25 D increments.

For a proof of concept we have applied 50 micron shifts of the mirror in our eye model. We then measured the aberrated wavefront exiting the optical system. The eye model was properly aligned to the auto-phoropter system and thus additional odd aberrations were negligible. The only term that was observed to drastically vary was that of the defocus term, as this was the expected result. This defocus term of the full optical system was then correlated to the power variation in the model eye. This is significant, as our fluidic phoropter is coupled to the full optical system. We are able to null out a given amount of defocus error of the eye with the fluidic phoropter, but we must also know the amount of error that this equates to in a users eye. The described approach was modeled for both 3 mm and 6 mm stop sizes. The doublet was chosen with a 9 mm active area as to ensure stop control of the system. We additionally stopped down the optical system to a 3 mm to 6 mm range. We chose this range as this is approximately the dynamic range of the iris size within the user's eye. We are replicating the stop size to identify how the defocus values within our full auto-phoropter design shifts.

Auto-Phoropter 3 mm Stop			Auto-Phoropter 6 mm Stop		
Model Eye Power	Actual Separation (mm)	$Z_2^0$ Defocus Wavefront	Model Eye Power	Actual Separation (mm)	$Z_2^0$ Defocus Wavefront
+5 D	15.75	2.47	+5 D	15.75	8.63
	15.7	2.36		15.7	8.29
	15.65	2.24		15.65	7.8
	15.6	2.12		15.6	7.36
+4 D	15.55	2	+4 D	15.55	6.96
	15.5	1.86		15.5	6.53
	15.45	1.7		15.45	5.98
+3 D	15.4	1.55	+3 D	15.4	5.42
	15.35	1.47		15.35	5.13
	15.3	1.38		15.3	4.8
+2 D	15.25	1.24	+2 D	15.25	4.36
	15.2	1.03		15.2	3.63
+1 D	15.15	0.88	+1 D	15.15	3.02
	15.1	0.7		15.1	2.44
	15.05	0.6		15.05	2.01
0 D	15	0.49	0 D	15	1.61
	14.95	0.17		14.95	0.48
	14.9	0		14.9	0
	14.85	-0.1		14.85	-0.29
-1 D	14.8	-0.32	-1 D	14.8	-1
	14.75	-0.43		14.75	-1.47
	14.7	-0.69		14.7	-2.4
-2 D	14.65	-0.88	-2 D	14.65	-3.07
	14.6	-1.09		14.6	-3.81
	14.55	-1.31		14.55	-4.61
-3 D	14.5	-1.58	-3 D	14.5	-5.58
	14.45	-1.81		14.45	-6.41
	14.4	-2.03		14.4	-7.16
	14.35	-2.25		14.35	-7.94
-4 D	14.3	-2.47	-4 D	14.3	-8.67
	14.25	-2.64		14.25	-9.28
	14.2	-2.84		14.2	-9.95
-5 D	14.15	-3.04	-5 D	14.15	-10.82
	14.1	-3.22		14.1	-11.38

Table 9-1 **Results of Auto-Phoropter with Eye Model:** The amount of power measured within the eye is correlated through the separation of the mirror and lens to the defocus power of the full optical system. This defocus power will be negated by the fluid phoropter.

The chart shows the system capabilities of measuring power separation for the model eye. We measured the defocus wavefront of the optical system relative to the power of the model eye. There are two trend lines that are observed when the model eye power is graphed relative to the defocus wavefront. It is seen that the slope of the wavefront is linear as we adjust the power of the model eye. This is necessary to be able to provide a controlled correlation between fluid volume, wavefront readings of the system, and equivalent ocular error measurements. The slope of the 6 mm pupil is approximately 4 times the slope of the 3 mm pupil. The slope radius of the larger pupil is twice that of the smaller pupil and this radius term squared equals 4. Radius squared can be correlated to f-number squared which matches the anticipated change in defocus relative to a shift in the image plane, showing these results match theory. An important factor identified from these results is that the shift in defocus slope shows the significance of stop size at the iris when determining the wavefront correction needed for the error term. The pupil size is an important factor in determining the correction required for our optical system.

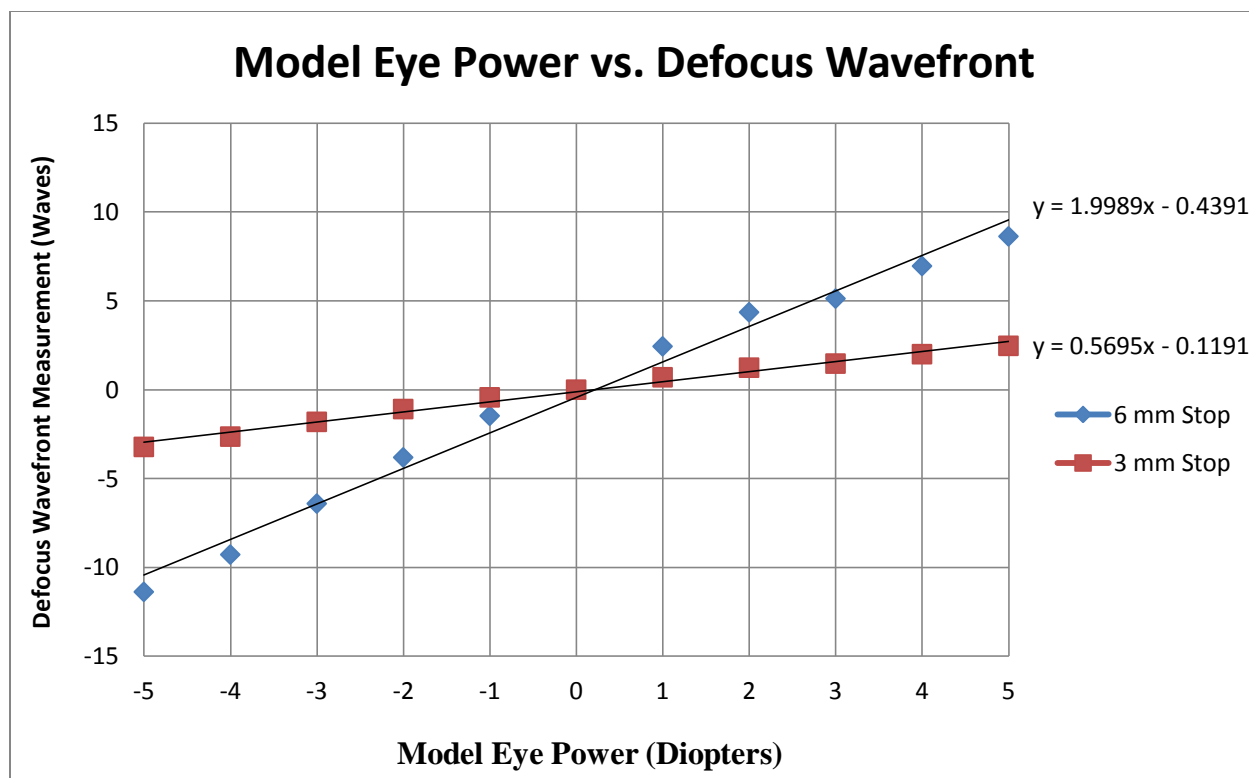


Figure 9-3 **Model Eye Power vs. Defocus Wavefront Relative to Pupil Size:** It is observed that our auto-phoropter produces linear measurements with varying slopes as we adjust the pupil size.

Table 9-1 and Figure 9-3 have mapped the effects of a model eye that varies in defocus between -5 D to 5 D. This power range is efficient for proof of concept measurements but does not encapsulate the entire population that requires vision correction. This is not the physical limitation of our optical system or the measurement capabilities of our model eye. We applied this range to show that the auto-phoropter can detect these defocus powers. Furthermore, we experimented with replacing the model eye lens with various powered lenses. As was described in chapter 8, the system can detect from -30 D to +30 D. Figure 9-4 shows an example of two eye lens systems that we have replicated. This figure shows that we are able to experimentally identify users with over -20 D of error. The points for -20 D have a large separation between them in that we observe a further power range that is achievable. The experimentally observed limit of our phoropter with the model eye is at -28 D, slightly less than the theoretical -32 D

range that was modeled through ZEMAX. This auto-phoropter design is capable of measuring severe Myopia and Hyperopia beyond the common populous.

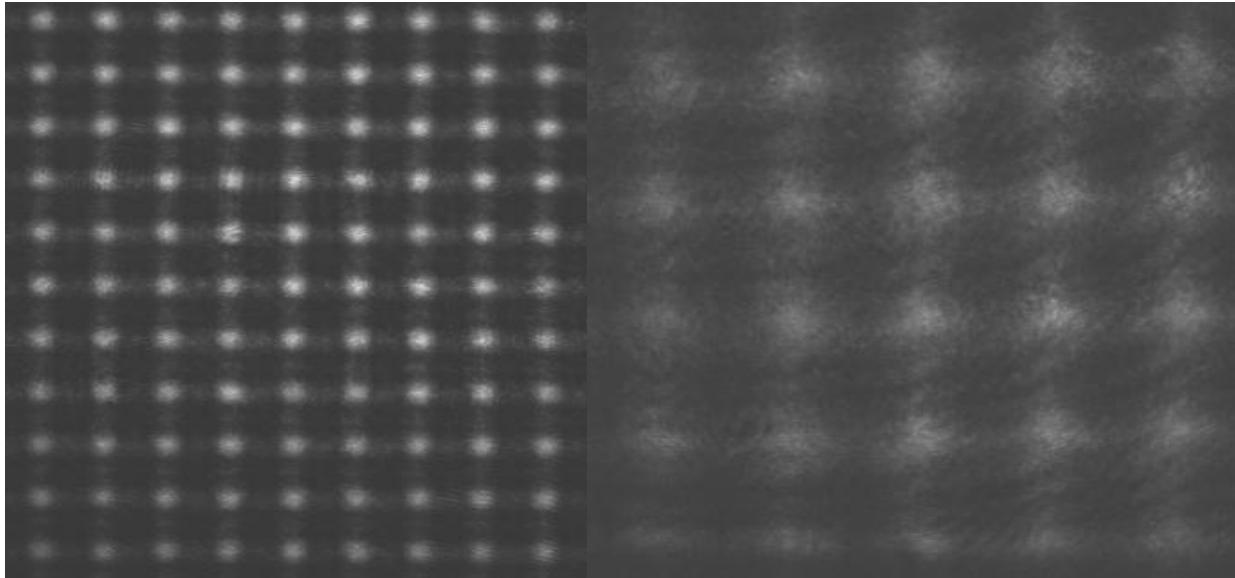
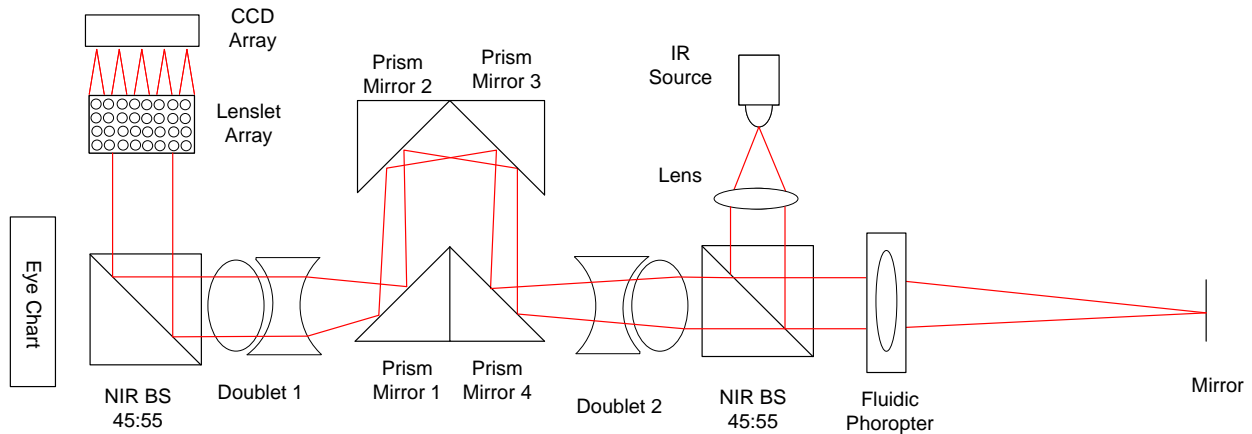


Figure 9-4 **Defocus Measurements through our Auto-Phoropter System:** To the left is 1.5 Diopters of Defocus and to the right is 20 Diopters of Defocus induced by our eye models, the system limit.

## 9.2 Testing Approach: Measuring Fluidic Phoropter

To compensate for the ocular errors, one must identify the correlation between fluid volume and power induced in the full optical system. After alignment and identification the correlation between ocular error and wavefront measurements, the third step in calibrating the optical system is producing measurements of the auto-phoropter coupled with the fluidic phoropter stack. Here we remove the focusing lens of the model eye. The mirror in the model eye represents the retinal plane. Therefore, the mirror is left in the location of where the model eye was calibrated. We place our fluidic phoropter into its designated location after removing the model eye lens. To test the fluidic lens surfaces we measure the results one surface at a time. When testing the defocus lens we test the system with the single fluidic defocus lens and the

astigmatism lenses removed. After measuring the defocus lens we lock the stack of astigmatism lenses to the defocus lens. We zero out the defocus lens so that no astigmatism is induced by the defocus lens. A fixed amount of defocus is added to the auto-phoropter system from the defocus lens. We then measure the outputted wavefront for the fluidic auto-phoropter system.



**Figure 9-5 Step 3: Testing Auto-Phoropter with Fluidic Phoropter:** The fluidic phoropter is placed into the system and the lens for the eye model is removed. We alter the curvature of the fluidic lenses by adjusting the fluid pressure. We then measure the wavefront variation by the full auto-phoropter system and map the fluid volume relative to the wavefront error.

We can quickly convert from the Zernike values that are in microns and the radius in terms of mm to the refraction terms that are set for prescriptions through the following definitions:

$$\theta_1 = \frac{1}{2} \tan^{-1} \left( \frac{Z_{2,-2}}{Z_{2,2}} \right) \quad (9-1)$$

$$\varphi_1 = - \left[ \frac{2\sqrt{6}}{r_{max}^2} (Z_{2,-2} \sin(2\theta_1) + Z_{2,2} \cos 2\theta_1) + \frac{4\sqrt{3}}{r_{max}^2} Z_{2,0} \right] \quad (9-2)$$

$$\varphi_2 = \left[ \frac{2\sqrt{6}}{r_{max}^2} (Z_{2,-2} \sin(2\theta_1) + Z_{2,2} \cos 2\theta_1) - \frac{4\sqrt{3}}{r_{max}^2} Z_{2,0} \right] \quad (9-3)$$

The Zernike coefficients can be converted into the sphere, cylinder, and axis prescriptions through the above definitions to the plus cylinder form or the minus cylinder form [19]. The refraction formulas can be written in two distinct formulations:

$$Sph = \varphi_1$$

$$Cyl = \varphi_2 - \varphi_1$$

$$Axis = \theta_1$$

(9-4)

$$Sph = \varphi_2$$

$$Cyl = \varphi_1 - \varphi_2$$

$$Axis = \theta_1 + 90^\circ$$

(9-5)

The determination of which set is minus cylinder and which set is positive cylinder is formulated on the magnitude of our defined terms  $\varphi_1$  and  $\varphi_2$ . Under the condition that  $\varphi_2 - \varphi_1 > 0$ , then the form of 9-4 is plus cylinder and the form of 9-5 is minus cylinder. If the condition is inverted that  $\varphi_1 - \varphi_2 > 0$ , then the form of 9-5 is plus cylinder and the form 9-4 is minus cylinder. In the world of prescriptions, ophthalmologists traditionally prescribe plus cylinder and optometrists traditionally prescribe minus cylinder. The axis term has one

additional stipulation in that the axis may not be lower than  $0^\circ$  or higher than  $180^\circ$ . If the Axis term is below  $0^\circ$  then  $180^\circ$  is summed to that value to correct for the term. If the axis term is above  $180^\circ$  then the axis term is subtracted by  $180^\circ$  for correction of the value. Through this approach we are able to convert from our optical Zernike polynomial terms to prescription terms applied in ophthalmic optics. These conversions will be applied in the following sections with the forms displayed.

### **9.2.1 Defocus Lens Filled with DI Water Based Fluid Volume Tested with Auto-Phoropter for 3 mm and 6 mm Stop Sizes**

Two defocus lenses were tested with the first being filled with DI water and the second with oil #3. Tests for both oil # 3 and DI water were applied to the limits of our stop size of 3 mm and 6 mm. The measured defocus error of the model eye coupled with the auto-phoropter system was measured for both these stops. To null the defocus error we would require the coupled fluidic lens with the auto-phoropter system to have an equal and opposite defocus measurement to the model eye. This is required to null out the measurements at either the 3 mm or 6 mm stops. Again, this is testing the system with one fluidic defocus lens. With this stipulation, we can equate the fluid volume necessary to correct for a given amount of defocus error to the equivalent error in a users eye. We are able to prove experimentally that our optical system can identify and compensate for the eye model error by showing that we can compensate for the iris stop size of 3 mm to 6 mm.

By identifying the change in astigmatism and defocus we are able to model the prescriptions produced by the fluidic lenses. The sphere, cylinder and axis prescription is correlated to these wavefront results. The results that we have graphed identify the prescription of the full auto-phoropter system that includes the telescope system, the fluidic lens, and the

relative position of the mirror coupled with the eye doublet. The relative positions of the optics define the defocus variation that is observed in the optical system.

We can map the prescription that would be observed through the use of the second order radial Zernike terms of defocus and astigmatism when comparing the limits of our stop size range of 3 mm to 6 mm. Again, we observe that the defocus terms have been scaled by approximately 4 times for the defocus terms when comparing Figures 9-6 and 9-7. There is a difference in scaling however, as the physical position of the fluidic lens and the model eye lens varies, causing different power effects on the system. For this reason it is significant as a next generation system to identify the pupil size when measuring ocular error.

Figures 9-6 and 9-7 map the wavefront error compared to that of the fluid volume. The fluid volume is measured in  $\mu\text{L}$  and the sampling between fluid volume was performed at every 5  $\mu\text{L}$ . The 3 mm stop required fluid volume extraction that ranged from 25 to -55  $\mu\text{L}$  while the 6 mm stop required 30 to -70  $\mu\text{L}$  of fluid extraction to compensate for the eye model results observed to distort the wavefront from -5 to +5 D of optical error for the model eye for prototype one, as seen in section 9.1. Again, the stop size effects the amount of fluid volume required to compensate for the measured wavefront error. Both stop sizes require 100  $\mu\text{L}$  or less of fluid volume to compensate for a 10 D range of ocular error. Fluid volume within the defocus lens can vary up to 2 ml or 20 times the range required for compensation of the fluid lens required for the 10 D change in power.

The chart shows that the values of the measurements for both defocus and astigmatism were linear, which again is the desired results of our fluidic lens. The defocus lens shows a much larger variation in defocus than was observed in astigmatism for both the 3 mm and 6 mm

stopped systems. The slight amount of astigmatism was predicted by our analysis of the fluidic phoropter wavefront in section 5.2.1. We observe that both for the 3 mm and 6 mm stop sizes the astigmatism lens has a negative slope. We can further determine the effects of the astigmatism terms in the cylinder and axis refraction terms.

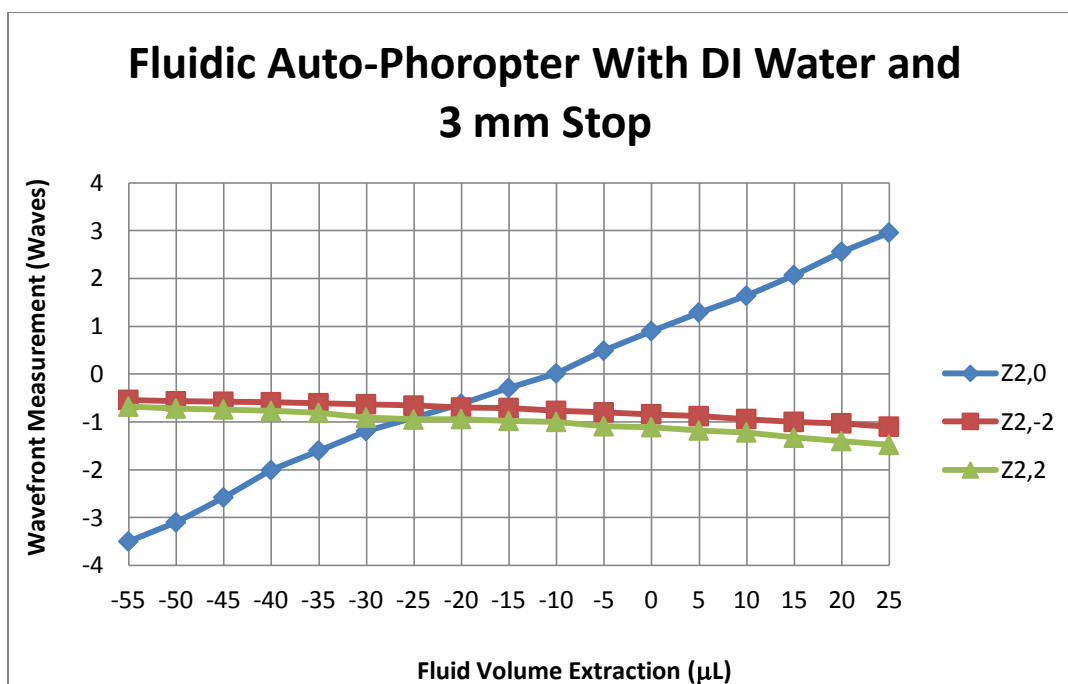


Figure 9-6 **Wavefront Measurements with DI Water and 3 mm Stop for Defocus Lens:** Empirical data of the linear effects on astigmatism and defocus when altering the fluid volume inserted into the defocus lens.

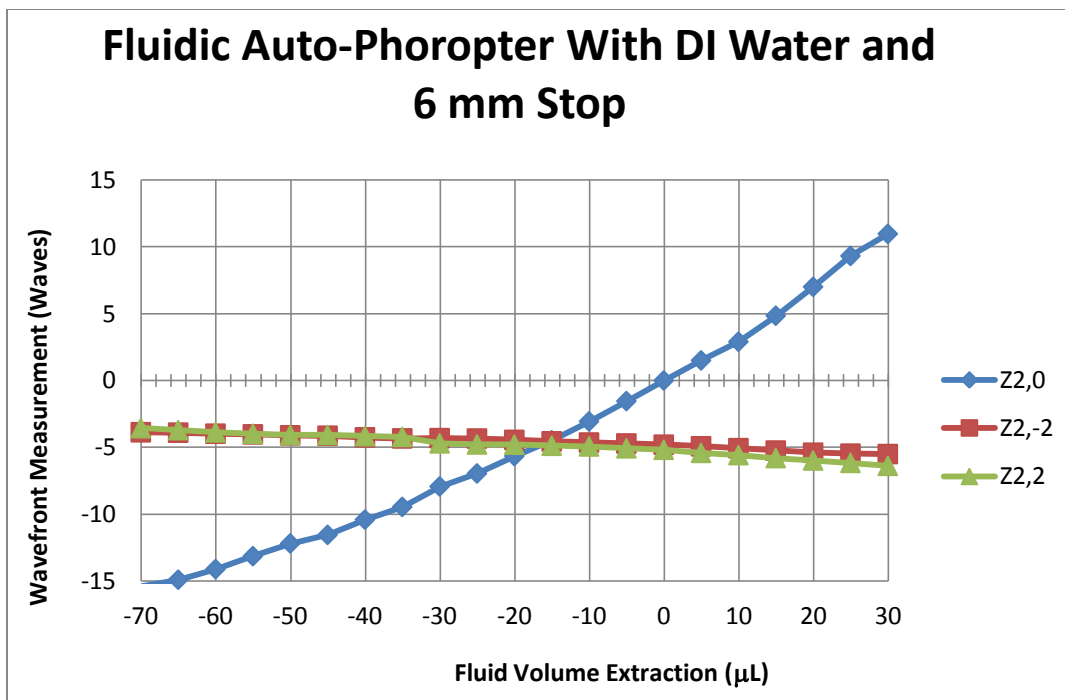


Figure 9-7 **Wavefront Measurements with DI Water and 6 mm Stop for Defocus Lens:** Empirical data of the linear effects on astigmatism and defocus when altering the fluid volume inserted into the defocus lens for a 6 mm stop in the auto-phorofter system.

Figures 9-8 and 9-9 show the variation of the sphere, cylinder, and axis variation between the 3 mm and 6 mm. The slope of the sphere term produces the same values between the 3 mm and 6 mm terms. The variation between the 3 mm and 6 mm stop sizes were found in the cylinder and defocus terms. It appears that the fluid lens has relatively stable axis values of  $18^\circ$  for the 3 mm stop. The 6 mm was also observed to hover around  $18^\circ$  but the values do not follow a constant line. The error varies within a couple of degrees relative to the average. It appears that the DI water, with a viscosity of 1 cSt, enters the chamber quickly and alters the pressure in the fluid chamber. With the tensioner locked symmetrically about the center, it is possible that the surface is not equally locked down in the periphery. The peripheral flanges cause slight variations to the circularly symmetric pressure, which appear to be observed in the cylinder and astigmatism terms of the wavefront. There also is evaporation of the fluid volume

which causes pressure variation in the fluid chamber at different times, where results vary over 4 hour increments which can also skew the results.

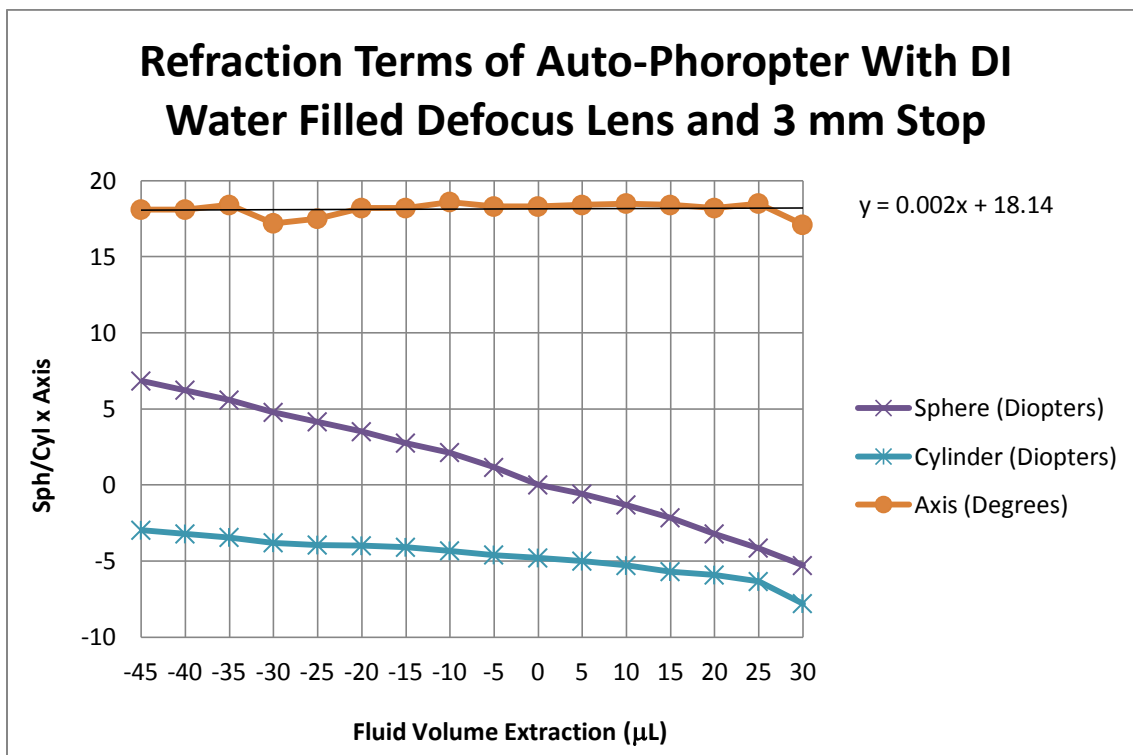


Figure 9-8 **Refraction Terms with DI Water and 3 mm Stop for Defocus Lens:** From the data sets we are able to determine the refraction terms that are produced for a prescription. These terms are inclusive the fluidic lens within the auto-phoropter system where the stop is set at 3 mm.

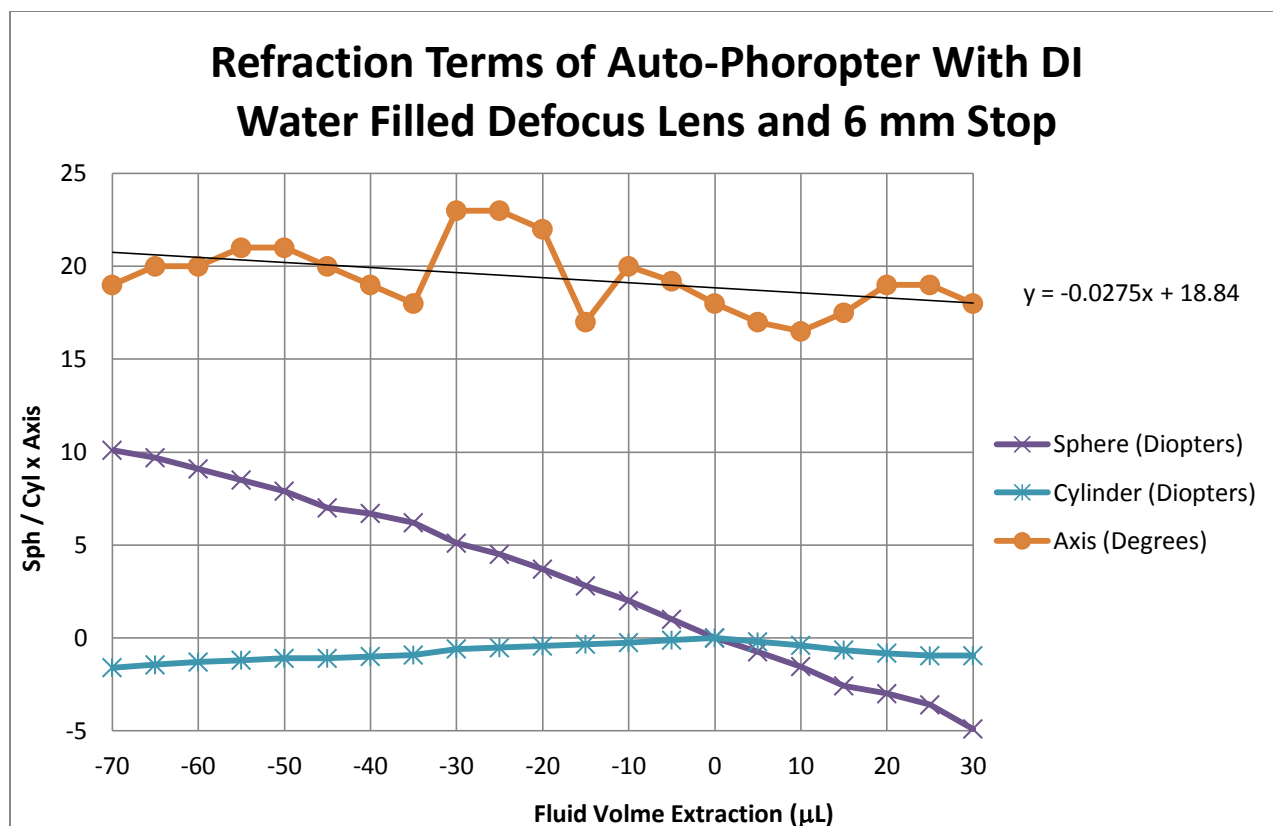


Figure 9-9 **Refraction Terms with DI Water and 6 mm Stop for Defocus Lens:** From the data sets we are able to determine the refraction terms are produced for a prescription. These terms are inclusive the fluidic lens within the auto-phoropter system where the stop is set at 6 mm.

### 9.2.2 Defocus Lens Filled with BK-7 Oil # 3 Tested in Fluidic Auto-Phoropter for 3 mm and 6 mm Stop Sizes

It is necessary to compare the defocus lens filled with DI water to a second defocus lens to determine the consistence of our auto-phoropter system and defocus lens designs. In addition, we can compare the variation of fluid volume and its effect on the stability of our results. The second fluidic phoropter applies oil # 3, which is a BK-7 index matching fluid. The optical properties almost replicate that of BK-7 glass in the visible spectrum. Again, we measure the wavefront properties of the propagating light to identify the BK-7 based oil measurements relative to fluid volume.

We begin by comparing the wavefront measurements between the BK-7 defocus lens set with a 3 mm and 6 mm stop. Similarly to previous experimentation, the defocus lenses fluid range was used to compensate our eye model wavefront error, proving that we are able to correct for power error from -5 to + 5 D.. In this instance we set a standard amount of fluid volume range of -35 to 25  $\mu\text{L}$  as to compare the wavefront directly to each other. The defocus terms appear to have a similar ratio of 4 times the defocus term for fluid volumes from 20 to -15  $\mu\text{L}$ , where -15  $\mu\text{L}$  is the intersection of 0 Defocus error for both stop sizes. The slope changes for the experiments with the BK-7 oil and 6 mm stop when extracting fluid from -15 to -35  $\mu\text{L}$ . The ratio of defocus wavefront error for 6 mm to 3 mm stop size reduces by half of the previous slope. The measurements in this range appear to have altered trajectory with the 6 mm stop size. This trend did not occur with the DI water based defocus lens. We believe this is due to the viscosity of the fluid. The viscosity of Bk-7 oil # 3 was 1,450 cSt, which is thick and shows high resistance. As the fluid was withdrawn by the actuator system, suction was observed that varied the relative evacuation rate of the fluid volume. This higher resistance caused a variation in wavefront slope measurement for our thicker fluids.

There appears to be more consistent readings for the astigmatism terms of the defocus lenses between the data for prototype one stopped at 3 mm and 6 mm. stop. The ratio between the two Zernike terms of the stop sizes is proportional to the expected values. It is observed that this defocus lens has larger amounts of astigmatism compared to the DI water based fluidic lens. In addition, the astigmatism Zernike terms for the fluidic auto-phoropter with a 3 mm stop appear to be symmetrical about 0 waves of error. There is also symmetry between the astigmatism Zernike terms of prototype one stopped at 6 mm, however the mirror symmetry appears to match relative to 2.5 D of wavefront error. These values follow similar slopes relative

to each other but different slopes compared to the first defocus lens with DI water. The DI defocus lenses slopes were both negative slopes as we increased fluid volume. The slopes for the DI water based defocus system had both Zernike terms with approximately the same point values. The difference between these two terms is further expanded when observing the axis values of the refraction terms for the fluidic auto-phoropter.

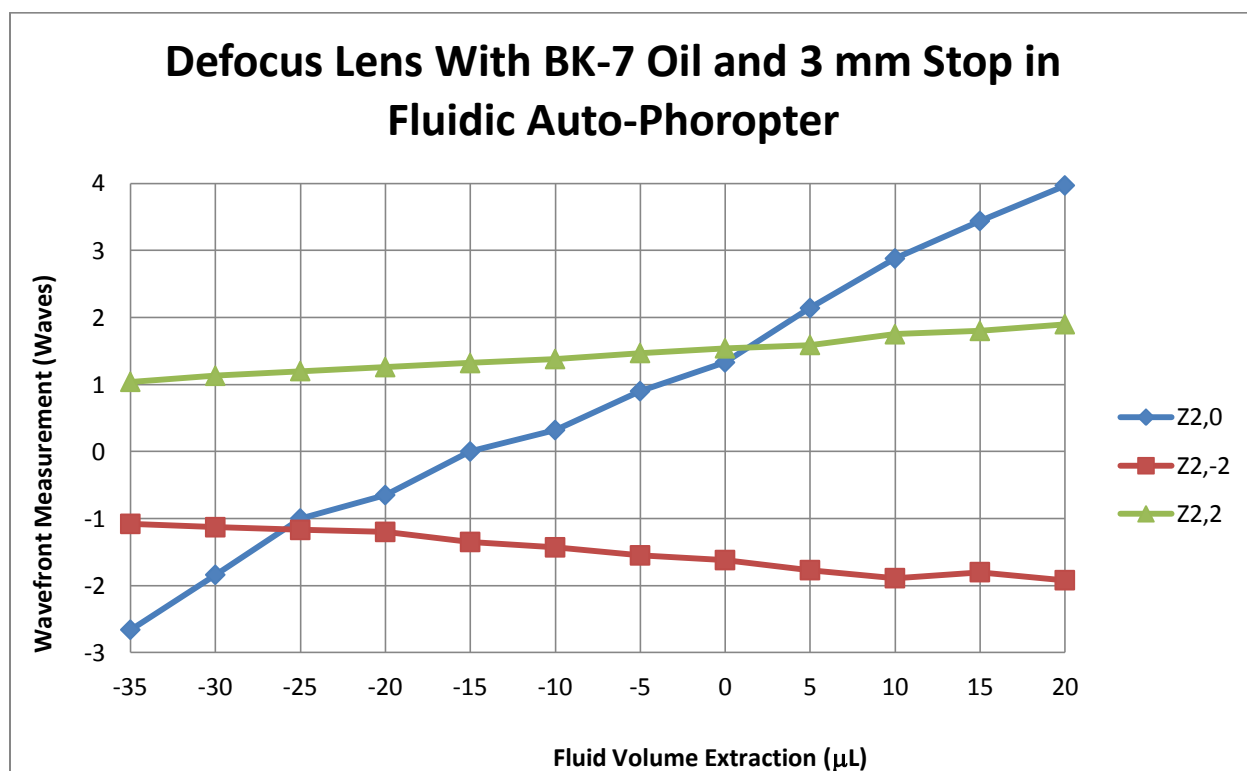


Figure 9-10 **Wavefront Measurements with Bk-7 Oil and 3 mm Stop for Defocus Lens:** Empirical data of the linear effects on astigmatism and defocus when altering the fluid volume inserted into the defocus lens. The slope of the defocus Zernike is much larger than the astigmatism Zernike terms. The astigmatism Zernike terms have equal and opposite slopes that are mirror images about the 0 axis.

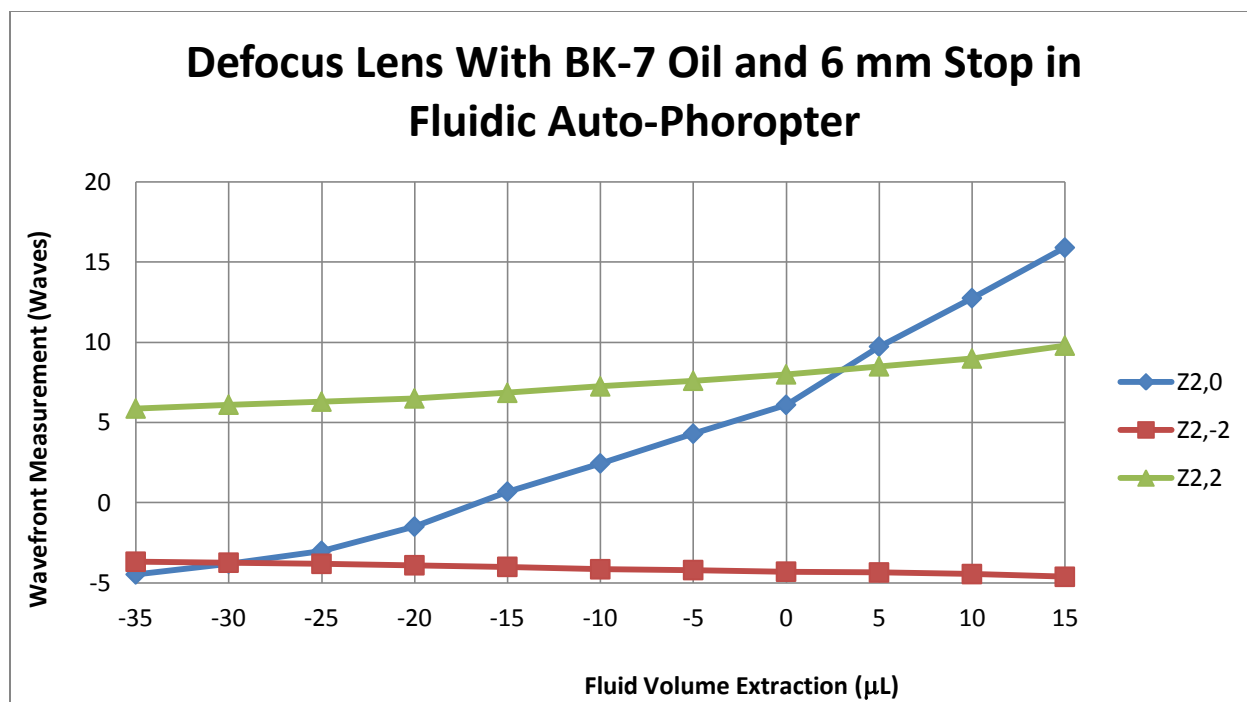


Figure 9-11 **Wavefront Measurements with Bk-7 Oil and 6 mm Stop for Defocus Lens:** Empirical data of the linear effects on astigmatism and defocus when altering the fluid volume inserted into the defocus lens. The slope of the defocus Zernike is much larger than the astigmatism Zernike terms. The astigmatism Zernike terms has equal and opposite slopes that are mirror images about the 2.5 waves error line.

The refractive terms of the fluidic auto-phoropter with the BK-7 oil in the defocus lenses appear to have the same pattern. The sphere and cylinder terms of Figures 9-12 and 9-13 have the same slopes and values as we adjust the fluid volume of the liquid lens. The observed difference between the refraction terms of the auto-phoropter with the 3 mm and 6 mm stops is that of the axis value. The auto-phoropter system with a 3 mm stop has an average axis value of  $67^\circ$  while the system with a 6 mm stop has an average axis value of  $76^\circ$ . The sampled point at each shift of  $5 \mu\text{L}$  appears to have almost no variation in either of the graphs. We believe that the thicker fluid material with the higher viscosity produces a more stable and repeatable results as is seen in Figures 9-12 and 9-13.

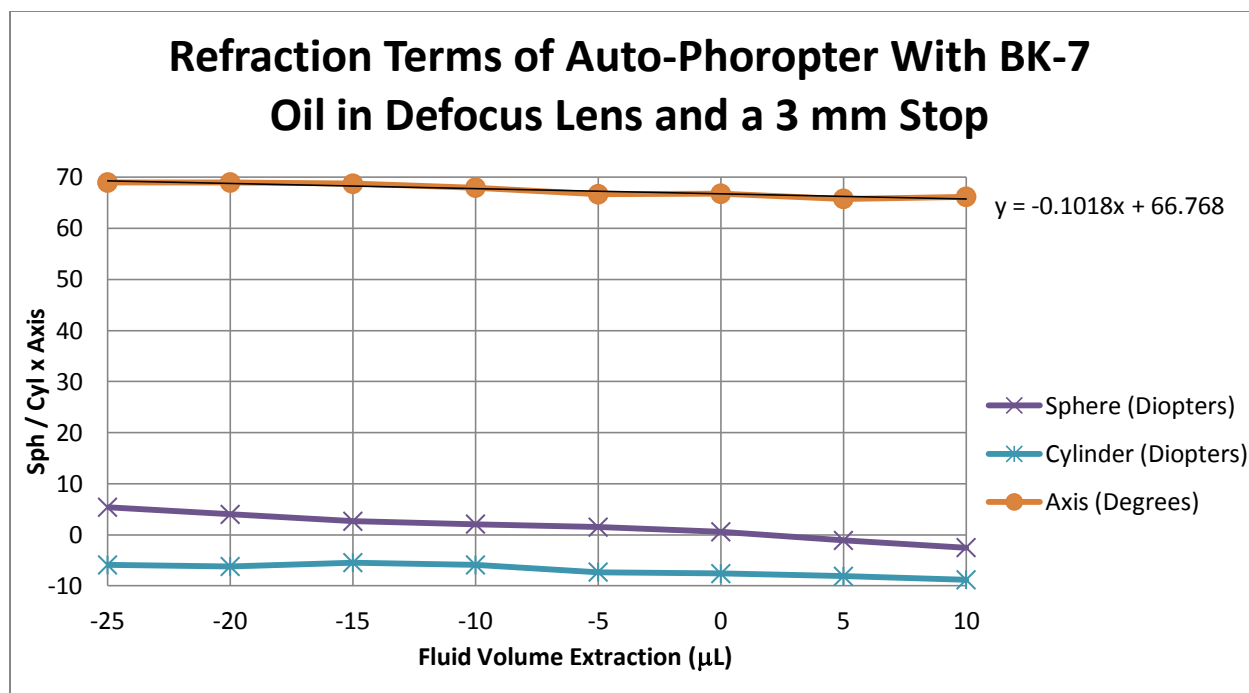


Figure 9-12 **Refraction Terms with BK- 7 Oil and 3 mm Stop for Defocus Lens:** From the data sets we are able to determine the refraction terms are produced for a prescription. These terms are inclusive the fluidic lens within the auto- phoropter system where the stop is set at 3 mm.

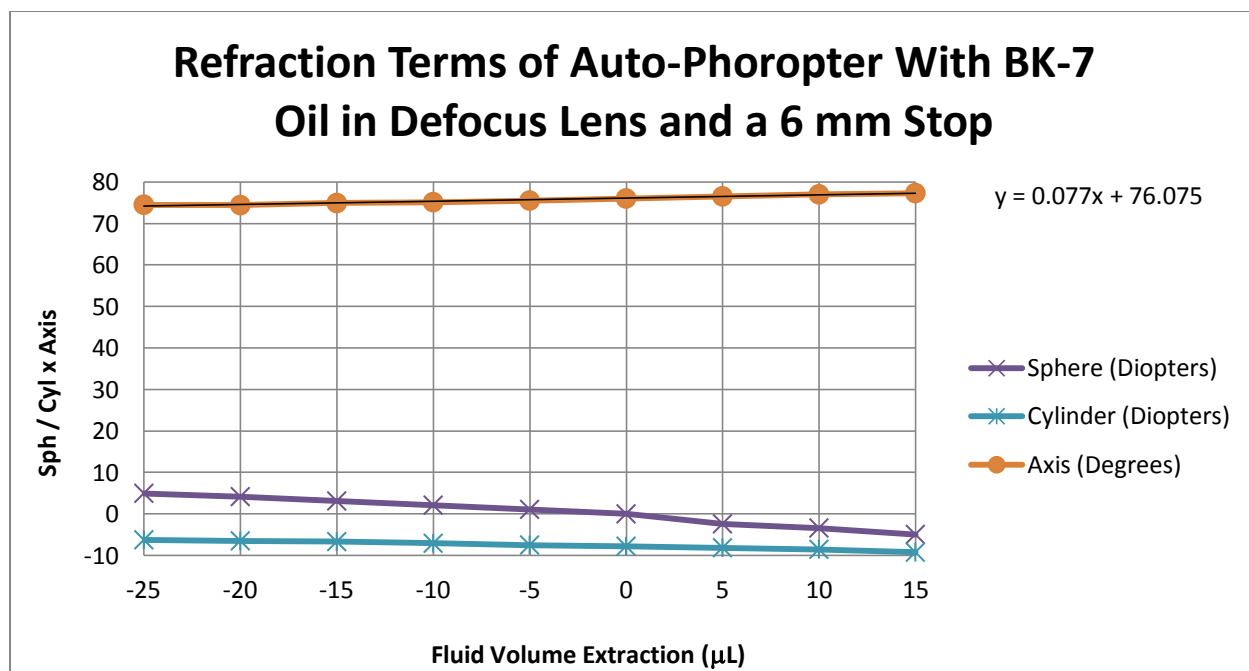


Figure 9-13 **Refraction Terms with Bk-7 Oil and 6 mm Stop for Defocus Lens:** From the data sets we are able to determine the refraction terms are produced for a prescription. These terms are inclusive the fluidic lens within the auto- phoropter system where the stop is set at 6 mm.

There are tradeoffs when using thicker fluids with higher friction forces. We believe the fluid with the higher viscosity is stabilizing the repeatability of the fluidic lens. It is observed when comparing the defocus lens with DI water to the lens with BK-7 oil that the BK-7 oil has higher viscosity which produces higher repeatability. The tradeoff with a higher viscosity is that there is a loss in actuator speed as the fluid takes longer to evacuate out of the fluid chamber. This decreases the system response time which becomes detrimental for patient care. It is desirable to test an oil based fluid such as fluid #1 or fluid #2 from Table 7-2 that has a much lower viscosity and is an oil based fluid. If fluid # 1 or 2 produces stable and repeatable results similar to the BK-7 fluid (fluid # 3 of Table 7-2) then a different factor relative to viscosity was causing the instability of our first defocus lens with DI water. Another possibility of lens instability for the axis values would be the volatility of DI water as it evaporates. This was mentioned in the previous section as a cause of variation in accuracy of the fluidic lens relative to the axis. DI water produces stable and repeatable results in the order of 4 hour increments. As the fluid evaporates, there are variations in power control by approximately half a Diopter.

### **9.2.3 Astigmatism Lens Filled with DI Water and Fluidic Auto-Phoropter Set at a 3 mm Stop Size**

Adjustments were made for testing of the astigmatism lens. The mounts of the fluidic phoropter to the external adapter is attached to the frame of the defocus lens. As was mentioned in section 9.1, the astigmatism lens locks onto the defocus lens and thus forms the stack of fluidic lenses. In order to measure the astigmatism power of only the astigmatism lenses we zero out the astigmatism value of the defocus lens prior to adding the astigmatism lenses onto the frame. This induces a slight amount of defocus by the astigmatism lens which we null out with

the Shack-Hartmann wavefront sensor. We then lock the astigmatism lenses onto the defocus lens and mount it into the auto-phoropter system. We are now able to measure results from the astigmatism lenses with the optical system. In order to achieve zero power from both lenses we added a dual fluidic valve controller for each of the fluidic astigmatism chambers.



Figure 9-14 **Fluidic Valve Control System:** The valve controls the exact amount of fluid with one valve direction. When we switch to the opposite direction, which is set half way in between, we can control the exact amount of fluid we are testing with.

This valve has direct path with only one of the two paths to the fluid chamber. Each of the astigmatism lenses has a 3-2 valve connected to their channel. The fluid chambers are manually adjusted until we observe zero astigmatism power on the Shack-Hartman wavefront sensor. We then switch both valves to the second path that is connected to another syringe. These syringes hold 100  $\mu\text{l}$  with a notch identification of 1  $\mu\text{l}$ . We can create as small as 1  $\mu\text{l}$  iterations manually with this setup. Each of these syringes was set at 50  $\mu\text{l}$  which allowed for a range of  $\pm 50 \mu\text{l}$  relative to our identified zero points. The measurements that were performed were again 5  $\mu\text{l}$  increments from -30 to +30  $\mu\text{l}$  for each of the fluidic lenses.

Each of the fluidic astigmatic lenses of the fluidic auto-phoropter was measured individually while the opposite fluidic lens was set at zero astigmatism. The auto-phoropter was

set at a 3 mm stop to more accurately represent the iris size in lighted conditions. Plots 9-16 and 9-17 identify the wavefront measurements observed from the two fluidic lenses. The slope for astigmatism lens one offers less of a power variation than astigmatism lens two. The two astigmatism lenses are coupled onto each other with a glass plate separating the two fluidic chambers. The physical position of the membrane surface is therefore displaced by about 30 mm. This displacement within the fluidic auto-phoropter design induces a shift along the optical axis, causing a defocus shift along the image plane. The physical position of astigmatism lens 1 is external to the stack of fluidic lenses. The physical position of astigmatism lens 2 is within .5 to 5 mm relative to fluidic defocus lens, but approximately a 20 mm separation with astigmatism lens 1. The separation between the lenses would require further testing when syncing the three lenses together; however, our goal here is to illustrate that the fluidic astigmatism lenses can function together to produce any cylinder power with any axis orientation.

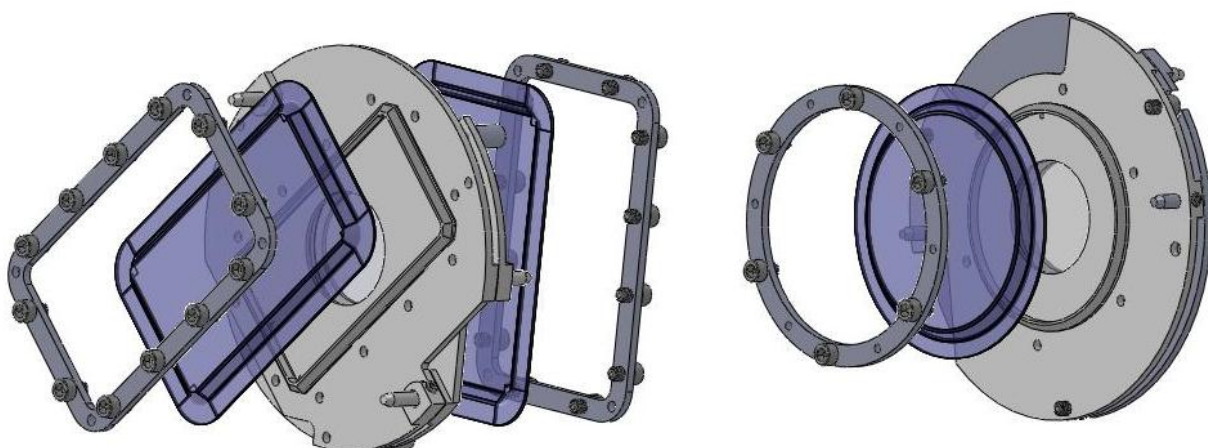


Figure 9-15 **Fluidic Phoropter Combination:** This is also Figure 6-3 and is a refresher of the physical position of the three lens combination. Astigmatism lens 2 is placed on the interior facing the defocus lens. The separation between these two optical elements varies between .5-5 mm depending on the chosen deflection angle, power and separation. Astigmatism lens 1 is on the external surface.

The orientations of the astigmatism chambers cause the astigmatism lenses to have a  $45^\circ$  rotation relative to each other. This  $45^\circ$  relative position is observed in the slopes of our Zernike terms  $Z_2^{-2}$  and  $Z_2^2$  when comparing the terms between the two astigmatism lenses as seen in Figures 9-16 and 9-17. The slopes of astigmatism lens one are in the matching negative direction while the slopes of astigmatism lens 2 are in opposite directions. This is a clear indication that these lenses are producing different axis values. The combination of these axis values will allow for us to replicate axis control.

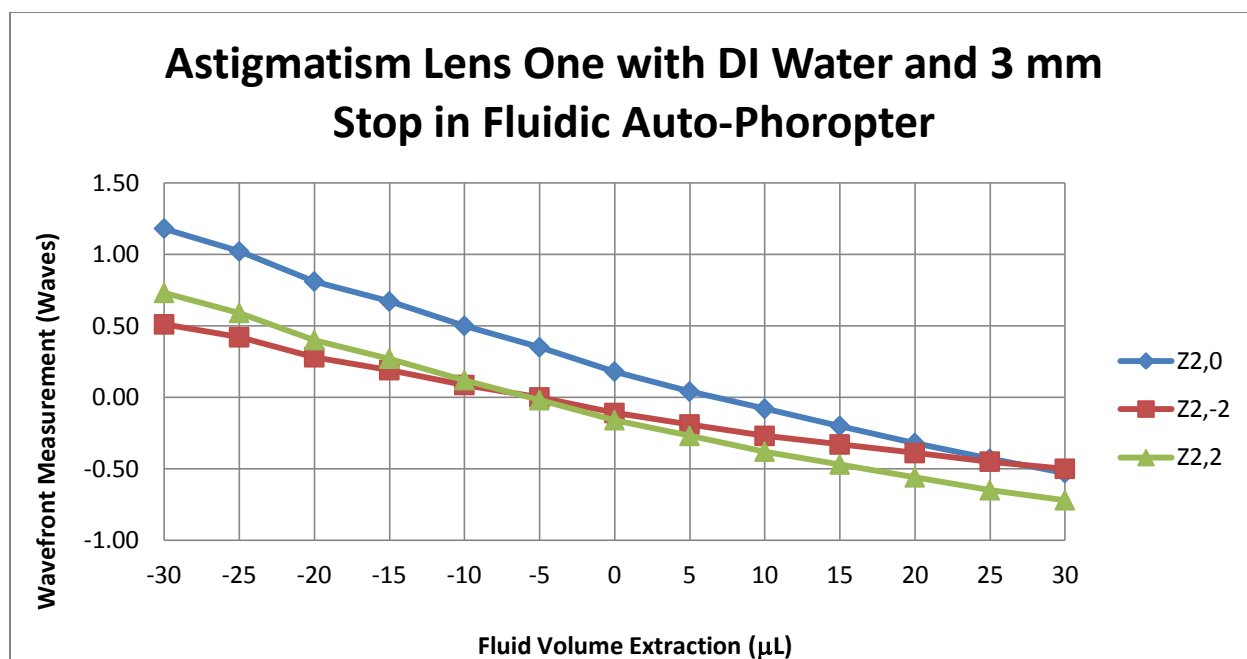


Figure 9-16 **Wavefront Measurements with DI Water and 3 mm Stop for Astigmatism Lens One:** The slope of the defocus term  $Z_2^0$  shows a higher amount of power variation than the astigmatism terms. The astigmatism terms have slopes that are in the same direction with each other.

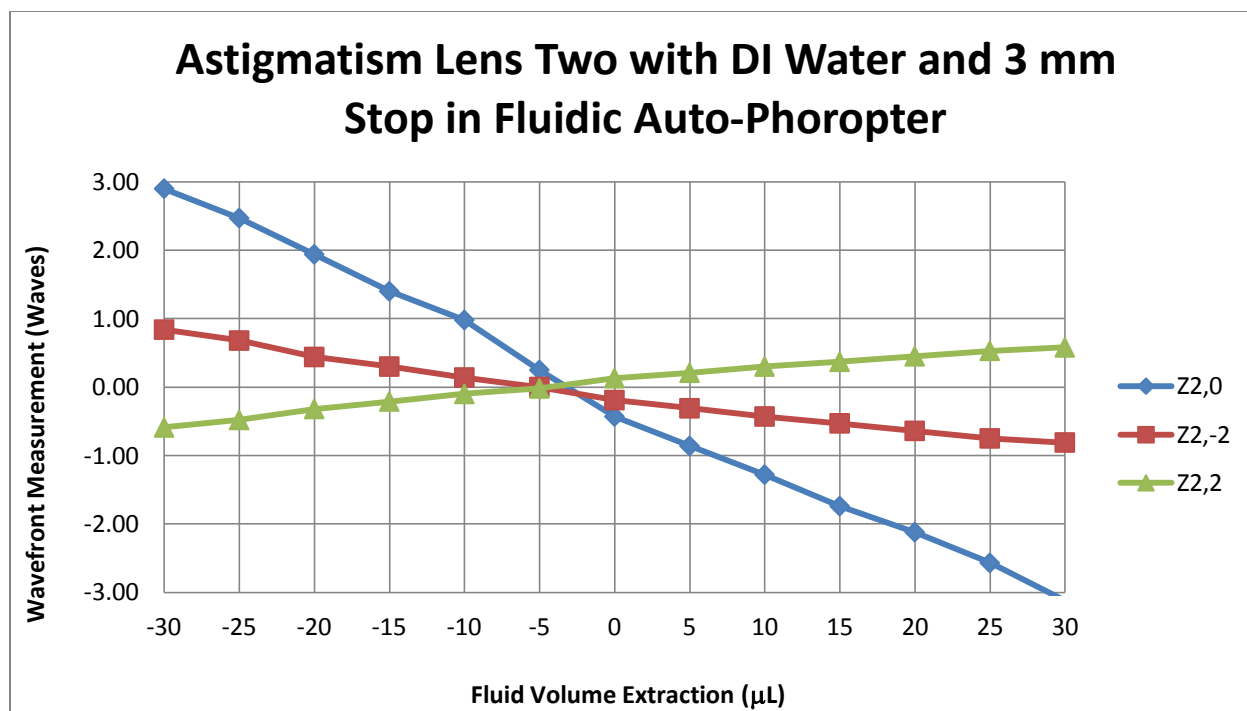


Figure 9-17 **Wavefront Measurements with DI Water and 3 mm Stop for Astigmatism Lens Two:** The slope of the defocus term  $Z_{2,0}$  shows a higher amount of power variation than the astigmatism terms and also the slope of astigmatism lens one. The physical position of the astigmatism lenses in the auto-phoropter system causes this steeper slope in variation of defocus to be observed.

The axis values produced by each of these astigmatism lenses individually, in addition to their combinations, shows the capabilities of replicating astigmatism values with any orientation and cylinder power. When we analyze the axis values of our refractive measurements from Figures 9-18 and 9-19, we observe that each lens produces two axis values. The orientation of the stack of astigmatism lenses is so that astigmatism lens one when fluid is inserted faces the auto-phoropter's Shack-Hartman wavefront sensor. Another way to phrase this is that as we insert fluid into astigmatism lens one, the deflection flexes in a positive power direction away from the users eye. Inversely, the withdrawal of fluid causes the cylinder to have a concave shape relative to the users' eye. This allows for fluidic lens one to have two defined axis orientations. Astigmatism lens one produces axis values of  $107^\circ$  when we withdraw fluid and  $17^\circ$  when we insert fluid relative to our zero axis point. The axis values are exactly  $90^\circ$  apart as

is expected with the inversion of the surface. The zero axis point is observed to be between a fluid volume of 0 and  $-5 \mu\text{l}$ , but close to  $-5 \mu\text{l}$ . We measured in  $5 \mu\text{l}$  increments so our sampling is not high enough to identify the exact zeroing of our fluid system.

Similarly, fluidic astigmatism lens two produces two orientations, but the orientations are inverted relative to fluid insertion and withdrawal. The physical position of fluidic lens two is in that the fluid chamber faces the user. As we insert fluid into the lens, we produce a concave deflective surface relative to the perspective of the users. If we withdraw fluid, the fluid curves closer toward our astigmatism chamber. The astigmatism chamber is further from the user than the membrane surface of astigmatism lens two. This creates a positive cylinder lens relative to the user. Astigmatism lens two produces two axis orientations as was observed with astigmatism lens one. Astigmatism lens two has fluid orientations of  $62^\circ$  and  $152^\circ$  with again a zero point near  $-5 \mu\text{l}$ .

It is observed that with the design of the astigmatism lens the axis are highly stable. Axis stability is necessary to control astigmatic power. There are a total of four orientations that are produced from the combination of the two astigmatic lenses:  $17^\circ$ ,  $62^\circ$ ,  $107^\circ$ , and  $152^\circ$ . Each of these orientations are  $45^\circ$  relative to each other and if we subtract  $17^\circ$  from all 4 axis values we see the follow four orientations:  $0^\circ$ ,  $45^\circ$ ,  $90^\circ$ , and  $135^\circ$ . The constant  $17^\circ$  shift of the four terms is caused by the relative orientation of the coupled astigmatic lenses relative to our Shack-Hartmann wavefront sensor. We therefore have identified a constant rotation within the optical system. More importantly we have identified that our two astigmatism lenses can produce four primary axis orientations within our fluidic auto-phoropter system. We can combine any two of these four orientations to replicate astigmatism power in any direction. This allows for us to produce correction of cylinder errors in real time of any cylindrical power and axis.

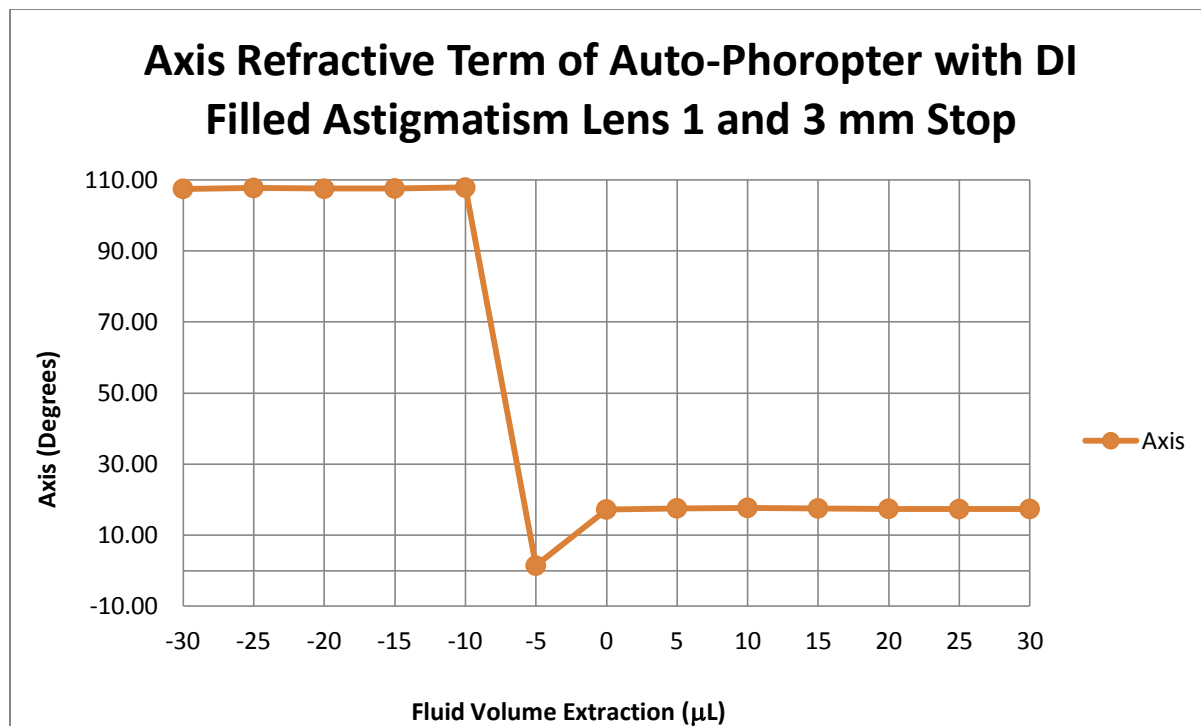


Figure 9-18 **Axis Term for Astigmatism Lens One with DI Water and 3 mm Stop for Fluidic Auto-Phoropter:** We observe the two orientations of fluidic lens 1 of  $107^\circ$  and  $17^\circ$ , which are  $90^\circ$  apart. We also observe the stability of the two axis and the zero point as measured.

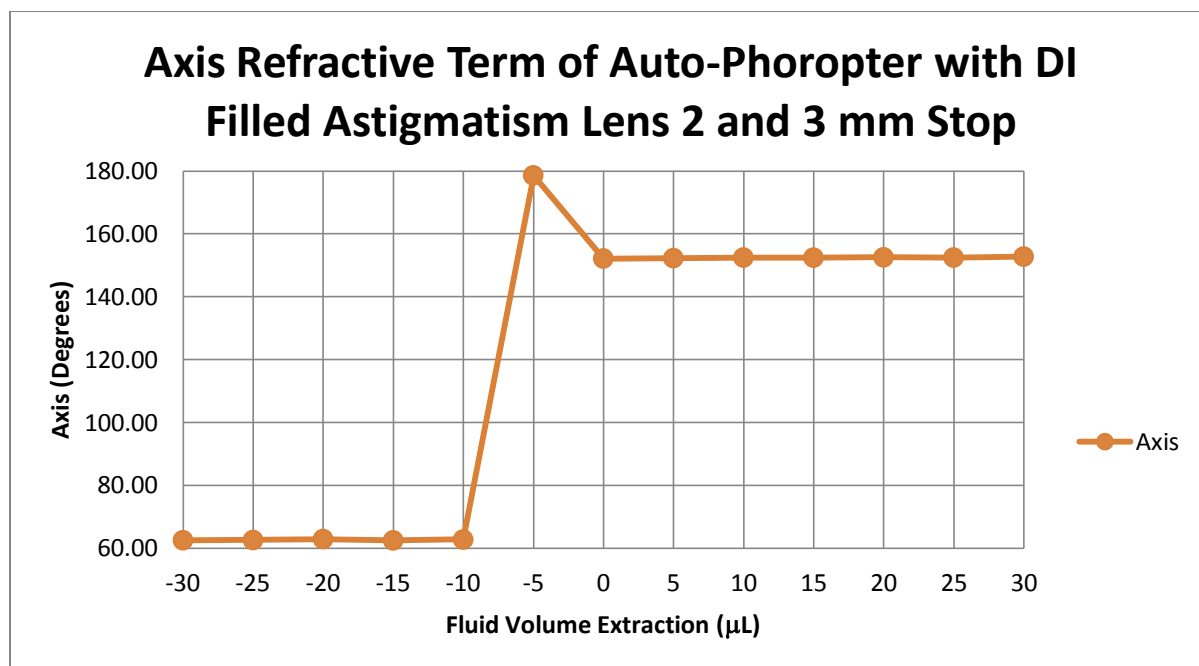
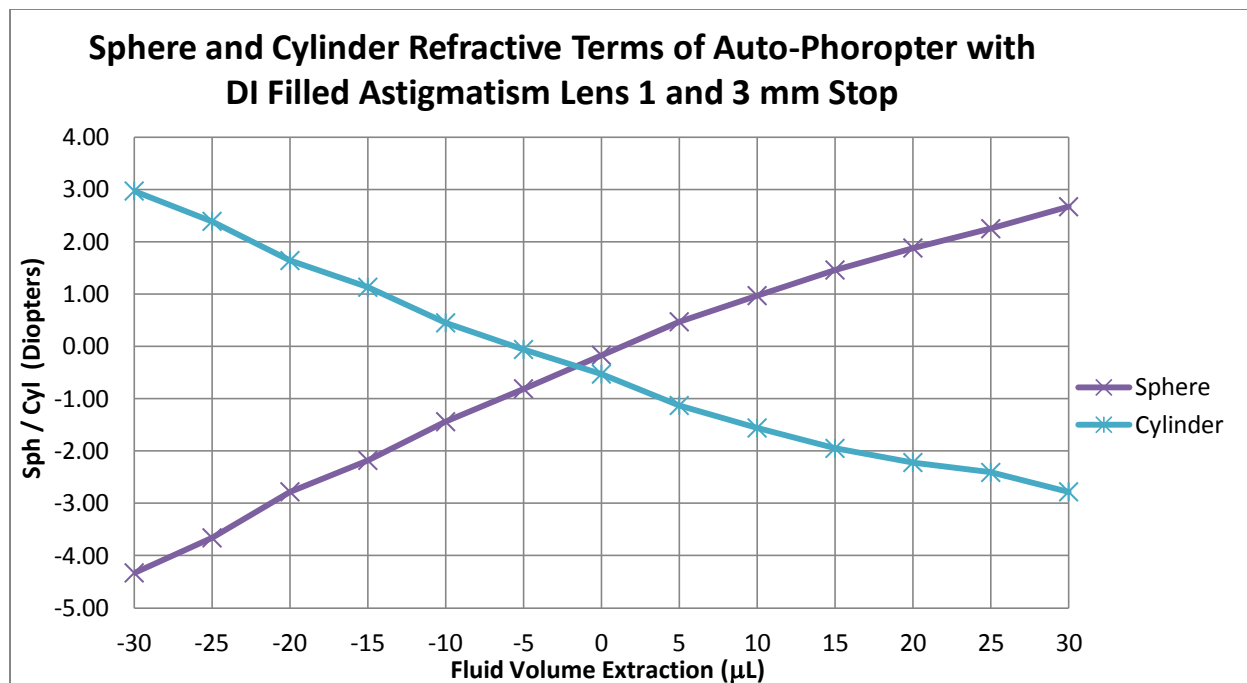


Figure 9-19 **Axis Term for Astigmatism Lens Two with DI Water and 3 mm Stop for Fluidic Auto-Phoropter:** We observe the two orientations of fluidic lens two of  $62^\circ$  and  $152^\circ$ , which are  $90^\circ$  apart. We also observe the stability of the two axis and the zero point as measured.

The combination of two axis values allows for us to produce any orientation of astigmatism but the magnitude of the astigmatism is determined by the magnitude of our cylinder values relative to the fluid volume from both astigmatic lenses. Figures 9-20 and 9-21 show each fluidic lens and the magnitude of their cylinder power. The cylinder values measured between -30 to + 30  $\mu\text{L}$  was found to have a range of -3 to +3 D for both lenses. Again the cylinder slopes are inverted as is expected by the orientation of the astigmatic lenses relative to each other. The magnitude of the spherical terms of the fluidic astigmatism lenses possesses variation in physical position in the fluidic auto-phoropter.



**Figure 9-20 Cylinder and Sphere Term for Astigmatism Lens One with DI Water and 3 mm Stop for Fluidic Auto-Phoropter:** The cylinder value exhibits -3 to 3 D of power between our 60 µL selected range. The orientation of the slope is defined by the physical position of the membrane being further then the separation relative to the users' eye.

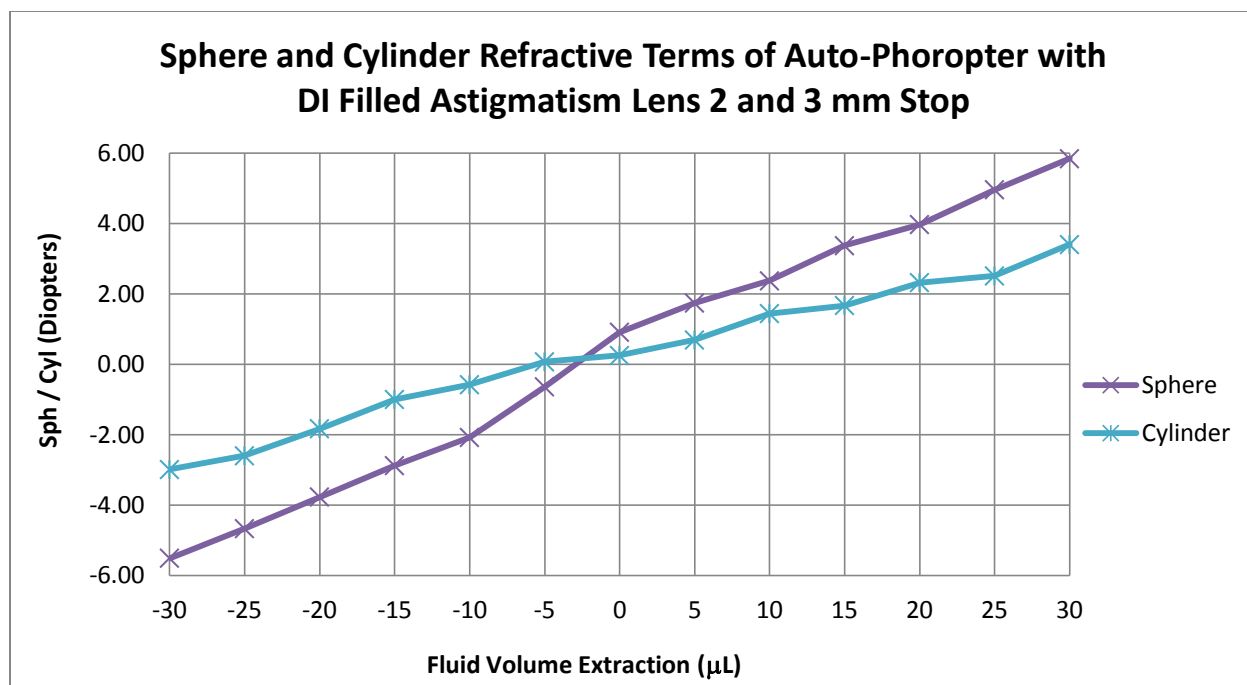


Figure 9-21 **Cylinder and Sphere Term for Astigmatism Lens Two with DI Water and 3 mm Stop for Fluidic Auto-Phoropter:** The cylinder value exhibits -3 to 3 D of power between our 60 µl selected range. The orientation of the slope is inverted relative to astigmatism lens One as the position of the astigmatism glass separator is further than the position of the membrane relative to the eye.

From the experimental results of each astigmatism lens we can produce a mapping of the combined cylinder powers and axis values. The previous charts show that we have the sphere, cylinder, and axis values of each of our sphero-cylinder astigmatic lenses individually. This identifies that for every given amount of inserted or withdrawn fluid volume, in 5 µl increments, we have sphere, cylinder, and axis values of each lens. Through power vector analysis or astigmatic decomposition, we are able to produce a summed sphere, cylinder, and axis value at the summing of measured fluid volumes of the previous section. Astigmatic decomposition combines the sphere, cylinder, and axis orientation through the following equations [19].

$$SEC = sph + cyl / 2$$

$$J_0 = -.5 * \text{Cyl}[\cos(2 * \text{Axis})]$$

9-7

$$J_{45} = -.5 * \text{Cyl}[\sin(2 * \text{Axis})]$$

9-8

$$S_R = \sum SEC - \sqrt{(\sum J_0)^2 + (\sum J_{45})^2}$$

9-9

$$C_R = 2 * \sqrt{(\sum J_0)^2 + (\sum J_{45})^2}$$

9-10

$$\theta_R = \frac{1}{2} \tan^{-1} \left( \frac{\sum J_{45}}{\sum J_0} \right) + 90^\circ \text{ Subtract } 180^\circ \text{ if } \theta_R > 180^\circ$$

9-11

From the sum of these equations we are able to identify the amount of fluid from each astigmatic lens and the amount of cylinder power that is outputted from that lens. Figure 9-22 shows the combination of our two fluidic lenses and their cylinder power for our fluidic auto-phoropter. A similar graph was formed in the description of the fluidic phoropter by itself as was reimaged in Figure 7-6 [17]. Our graph shows a mapping of the cylinder power from 0 to + 3 Diopters. We are able to reproduce the power with any axis direction, where the cylinder power near circles. The wavefront measurements for astigmatism lens one and astigmatism lens two

were measured manually at 5  $\mu\text{l}$  increments. We believe that we under sampled and should have used 1  $\mu\text{l}$  increments to achieve higher quality data points. In addition, we have a pump control system that more accurately shifts the fluid volume. The fluidic auto-phoropter results show in Figure 9-22 did not apply pump controls as we did for the fluidic phoropter results show in Figure 7-6, but rather used manual control of the syringes to achieve measurements. Our manual approach has a fluid variation of 200 nl, which skews the quality of our circular cylinder powers. As a proof of concept however, we show that we are capable of producing cylinder power in the auto-phoropter design at all axis directions.

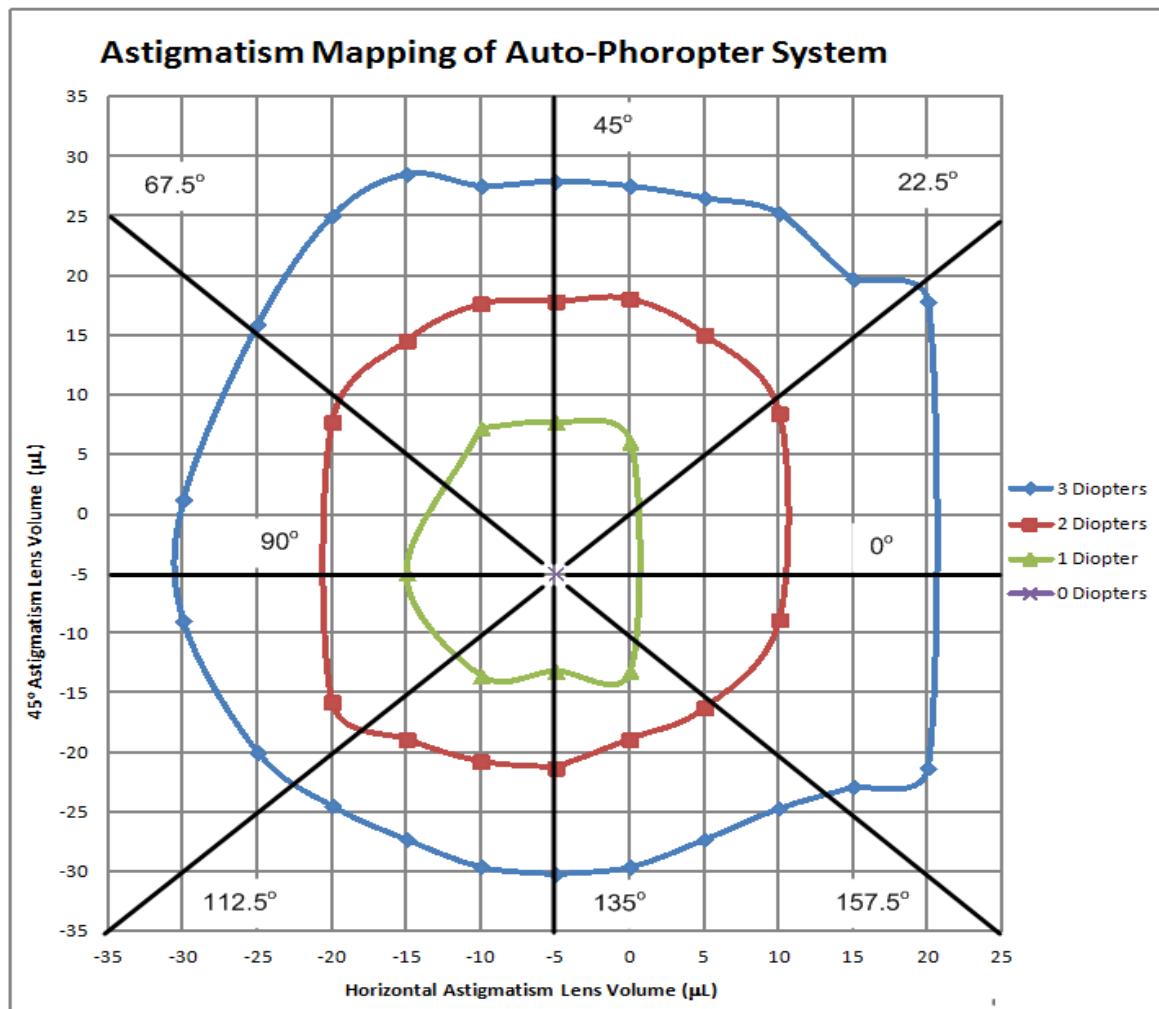


Figure 9-22 **Astigmatic Mapping of Auto-Phoropter System:** The cylinder power and axis are mapped relative to the fluid volume of each of the fluidic lenses.

### 9.3 Nulling Error with the Fluidic Auto-Phoropter: Fluidic Phoropter Cancels Model Eye Error

Sections 9.1 and 9.2 described the empirical data required to perform a correction of a user's measurement. We equated the wavefront error in the optical system to defocus error within a model eye. We also identified the compensation for the model eye at various pupil sizes and different fluids in correcting for that error. Similarly, we showed that our fluidic auto-phoropter can correct for sphere and cylinder error at all orientations. The last step was to show that the defocus lens can compensate for the error in the model eye which is shown in Figure 9-

23. The error is compensated so that once the wavefront measurement observes zero defocus error we have a fully corrected system. The model eye was set to have an error of 1 D and the fluidic lens compensated -1 D to null the error out.

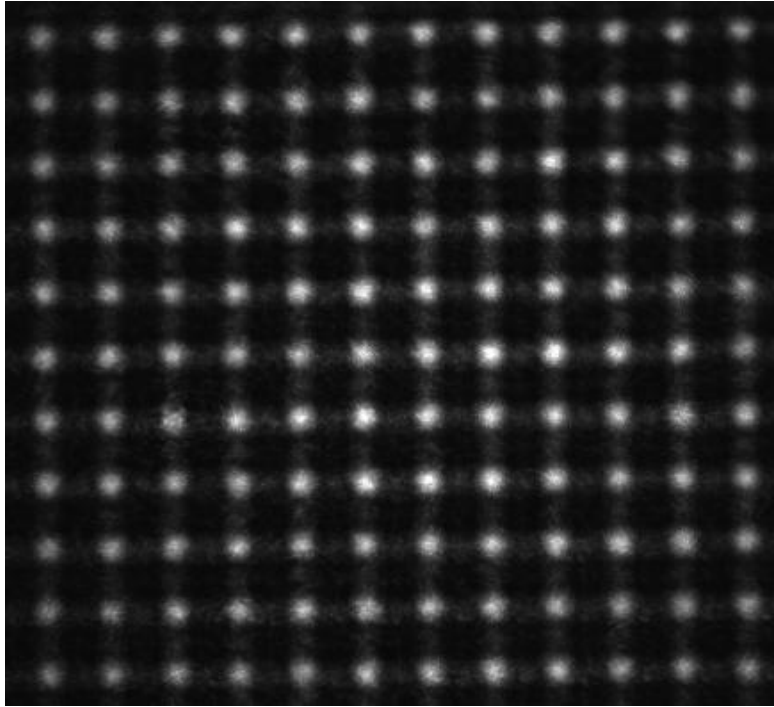


Figure 9-23 **Nullled Defocus Error with Eye Model at 1 D defocus and -1 D defocus of Fluidic Phoropter:** Within the system, this is the corrected output viewed on the Shack-Hartmann Sensor when viewing the correction of the eye model.

#### 9.4 Limits of the Optical Design

There are limitations to our optical design that affect the dynamic range, field of view, optical quality, and induced aberrations that would require for modifications to the design. We first begin with a discussion of the propagating wavefront. When the user has an Emotropic eye, approximately 10% of the collimated light entering the eye reflects back collimated as is observed from the exit pupil of the eye. Under these conditions, the system is fully unvignetted. As we increase the power as in Myopia or decrease the power as in Hyperopia, we find that the power variation propagates in a converging or diverging fashion. The higher the power variation

induced by the eye, the less light passes through the optical system. As was mentioned earlier, only a fraction of the light passing through the system reaches the detector plane. If the light intensity becomes so small that the detector plane cannot detect a signal we must take advantage of our fluidic lens technology. We can adjust the defocus lens until enough positive or negative power is induced to reduce the amount of vignetted light.

As we discuss the signal at the sensor plane it is important to achieve only a single image plane that reflects back through the optical system to the detector, rather than the multiple reflections, and that is the light exiting from the retina. A problem in testing of the astigmatism lens was that more than one plane of information reached back to the Shack-Hartmann wavefront sensor. It was discovered that the fluidic phoropter caused more than one image plane to reflect as the two flats in the fluidic phoropter design were uncoated surfaces. These surfaces were too close to either the beamsplitter or the model eye, causing more than one surface to be observed as power changed on our fluidic lenses. We determined that the flats were causing the multiple signals and turned the fluidic phoropter so that astigmatism lens one faced the auto-phoropter system. We reduced the effect of the multiple signals by adjusting the orientations of the fluidic phoropter so that the membrane surface faced the auto-phoropter plane and the glass flat faced the model eye plane, with a 30 mm separation between the fluidic phoropter and beamsplitter. This worked well for testing with the single defocus lens. We found that with the three lens system the double pass of light caused two signals to return from the optical system when testing the astigmatism lens. We were able to thus individually test each astigmatism lens, but could not couple the two fluidic lenses together. For this reason, we assessed the combination of the two astigmatic lenses through our experimental results of each lens and combined the lenses mathematically in section 9.2.3 rather than direct measurements of varying each fluidic lens. We

believe the multiple reflections are caused by the double pass through the fluidic phoropter with multiple reflections between the two glass surfaces. The reflections are correctable if we replace the two flat optics with flat optics that are coated in the NIR. Theoretically, this will reduce the reflections that are producing multiple signals and only the aberrated light exiting the retina will be signaled back.

We must analyze the telescopic system when discussing induced aberrations and aberrated light reflecting in the optical system. If the telescopic system is slightly misaligned, the aberrated wavefront can be corrected. Prior to testing we null out the aberrated wavefront induced by the telescopic system by placing a flat mirror in the location of the eye. The concern however with this design is that the telescopic system is in the line of sight of the user. If there is a slight variation in power from the telescope the user will also observe this power variation and it will alter the eyes power required to resolve our targeted images. This in turn would produce an inaccurate prescription. Therefore, it is desired to take the telescopic system out of the line of sight of the user. By bringing the telescope off axis with the Shack-Hartmann wavefront sensor we can still correct for any slight misalignments of our telescopic system relative to each other. In addition, the only optical power in the line of sight of the user is now the fluidic phoropter. This allows for a higher control of aberration compensation. A second desired advantage of shifting the optical system off axis is to increase the field of view.

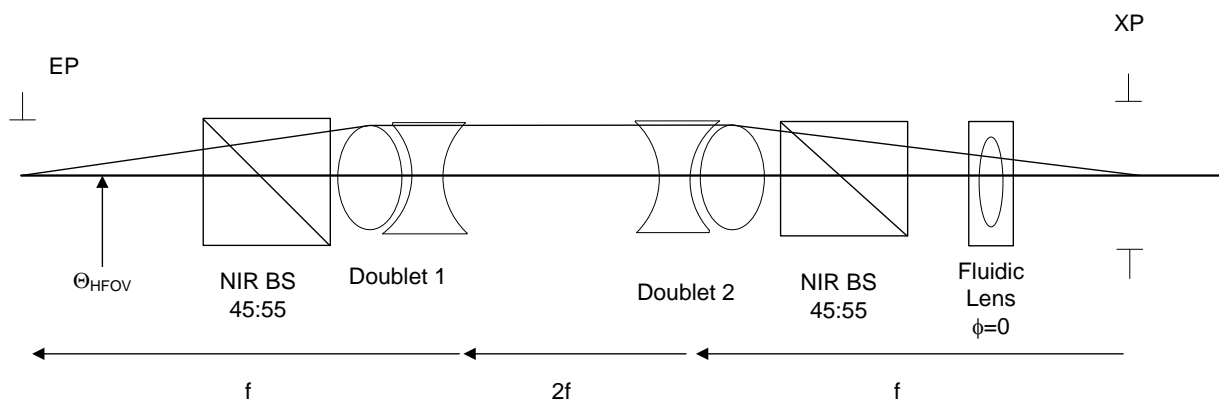


Figure 9-24 **Line of Sight Limit of Fluidic Auto-Phoropter:** The limit for our 4f imaging systems field of view is that of the pellicle beamsplitter.

The field of view is quickly measurable for our 4F imaging system. The entrance pupil of the eye is matched at the exit pupil (XP) of the telescopic system. The fluidic lens is placed at zero power as to not adjust the entrance pupil position. We created a 4F imaging system to eliminate cropping of the wavefront and vignetting at the reimaged plane. Therefore, as is shown in Figure 9-24, the half field of view ( $\theta_{\text{HFOV}}$ ) is equivalent to the subtended angle of the chief ray entering the telescopic system. The limiting factor of this design is the size of the beamsplitter. The beamsplitter has a 25.2 mm sized clear aperture but is set at  $45^\circ$  to the optical axis. This causes the lateral clearance on our line of sight perpendicular to our optical axis to have a width of 17.8 mm. As the edge of our beamsplitter is near the doublet, we estimate with a slight tolerance that the length of the edge is 100 mm along the optical axis from the stop. With a lateral width of 17.8 mm and a distance of 100 mm our full field of view is  $10^\circ$ . Similarly we can identify the field of view of a new design where a cubed pellicle beamsplitter reflects the optical system off axis.

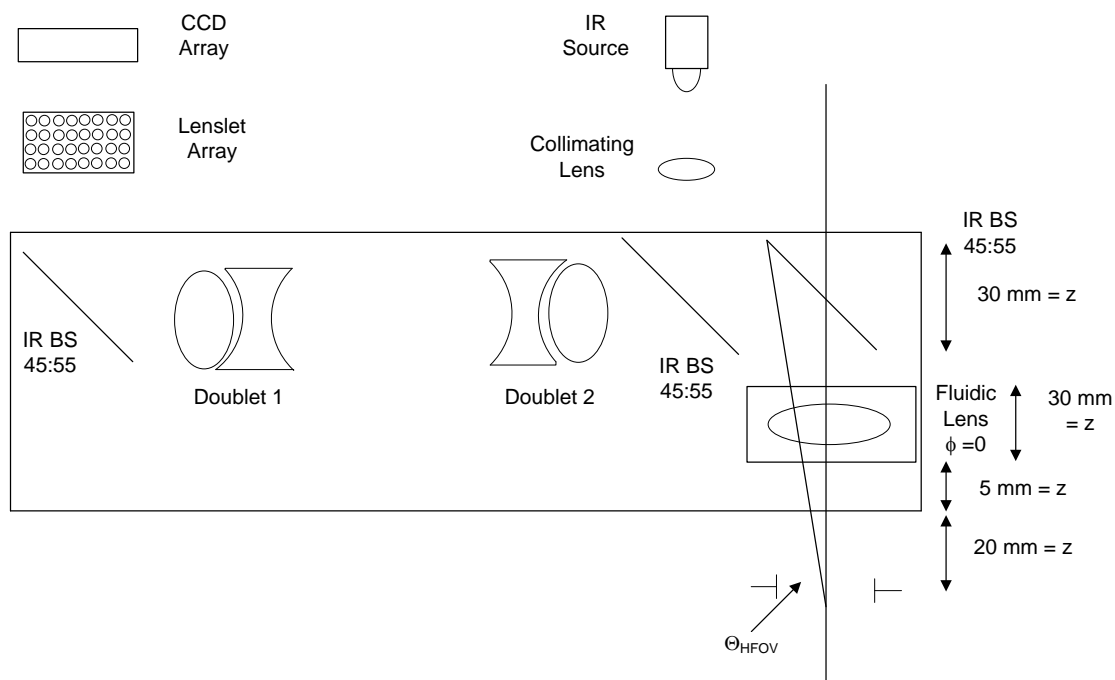


Figure 9-25 **Line of Sight Limit of Off – Axis Fluidic Auto-Phoropter:** The beamsplitter now brings the optics off-axis to slightly increase the field of view while still maintaining the same optical components in the system.

As is seen in Figure 9-25, we have decreased the optical elements in the line of sight of the user. There is a total of two optical elements in the line of sight of the user: a pellicle beamsplitter and our fluidic lens. There still is an eye relief of 25 mm between the pupil and the fluidic lens. By keeping the fluidic lens at zero power, this optical system has no power in the line of sight along the optical axis, which implies that our field of view is at the pupil of the eye. The subtended angle is again limited by the occluded object with the least width which again is the beamsplitter. Through this approach we have eliminated the separation between the fluidic lens and the beamsplitter, making the separation between the 17.8 mm lateral width and the pupil 85 mm along the optical axis, which equates to a full field of view of  $11.8^\circ$ .

The most optimal design for field of view is when the fluidic phoropter becomes the limiting factor in the field rather than the fluidic auto-phoropter. The fluidic phoropter is fixed near the spectacle plane of the user, which is around 25 mm for eye relief. There are two flats in

the fluidic phoropter, that of the astigmatism lens and that of the defocus lens. The astigmatism lens is further from the eye by approximately 15 mm in addition to the eye relief or a total of 40 mm along the optical axis. This suggests that the maximum field of view with the current fluidic phoropter is the 10 mm lateral width at a distance of 40 mm from the pupil location or a  $14^\circ$  field of view. In order to achieve a field of view where the fluidic phoropter is the limiting factor of our system, we must make the beamsplitter wider laterally. It is calculated that the lateral width of the beamsplitter must be at least 25 mm to have the fluidic phoropter as the limiting factor in the field of view with this second design. The beamsplitter must be at an angle to split the light and so the size of our beamsplitter becomes a function of  $25/\sin(x)$ , where  $x$  is the relative angle chosen for the beamsplitter to deflect the light towards the rest of our optical system. If the beamsplitter is set at  $45^\circ$ , for example, then the beamsplitter size must be larger than 36 mm along the hypotenuse of the triangle. This relation will become useful when we use optics such as holographic optical elements as our beamsplitters.

We have described limiting factors of field of view, vigneting, induced aberrations, and reflections. Lastly, we will discuss the limiting factor on the dynamic range of our power measurements. Through experimentation we have found that defocus by the eye alters the location of the focal plane. There are two reference points that are applicable when performing measurements with the Shack-Hartmann wavefront sensor: the plane where light focuses to infinity and the plane where light focuses on the detector. We find that the relative positions of the optics completely define the dynamic range of each designed optical system. When measuring with this optical system it is helpful to identify when the Shack-Hartmann sensor focuses at infinity and when the light is focused at the detector.

## 10.0 FLUIDIC AUTO-PHOROPTERS: OFF-AXIS OPTICAL DESIGNS

Chapters 6 through Chapters 9 described in detail the functionality of our fluidic auto-phoropter design. These chapters described the design fabrication, design, and testing of the first prototype of the automated see-through fluidic auto-phoropter. The additional systems described in this section are comprised of the same three module design: a fluidic lens, a relay telescope and a Shack-Hartmann wavefront sensor. The stacks of fluidic lenses are the same three adjustable lenses composed of a spherical lens and two astigmatic lenses oriented  $45^\circ$  to one another. Any sphere, cylinder and axis combination can be achieved by adjusting the fluid volume within the fluidic lenses as was shown in Chapter 9. We will not focus on this aspect of the fluidic lens coupled with our optical system as we have proven this functionality. As a proof of concept for additional systems we will show a nulled image of the fluidic auto-phoropter and its functioning results with a model eye.

In this chapter our primary focus is on the telescopic system and redesigning the auto-phoropter. The telescope will be designed so that the primary optics with power will not affect the line of sight of the user. This is highly advantageous as the user will observe a natural scene as they view through the system. In other words, the only optics with power in front of the user will be the fluidic phoropter. We will show the testing of an off-axis design and describe the testing of a second design, which we will call our second and third prototypes. Both systems take advantage of a traditional telescopic system with two lenses off axis forming a telescope system. At the end of the off axis telescope is the same Shack-Hartmann wavefront sensor technology that was previously described. To prove that prototype two functionally work, we have tested the system with our eye model approach described in 9.1. For the fluidic auto-phoropter system, we nulled out a given amount of optical error observed for an eye model with

our defocus lens. This shows that the fluidic lens technology is capable of nulling out the error from the eye within our optical system.

Further, we will expand on the shortfalls of the second prototype in field of view and the geometric optical properties. We then will propose a third prototype that is a combination of prototype one and prototype two. We will produce an off-axis telescope so that the only power in front of the users' eye is that of the fluidic phoropter. In addition, prototype three is designed so that we can maintain 4f imaging capabilities.

### **10.1 Fluidic Auto-Phoropter with Traditional Off-Axis Optics**

There are several advantages to producing a fluidic phoropter with an off axis telescopic system. As was described in section 9.4, we are able to increase the field of view, compress the size of the optical system, and also produce a more natural view for the user. The field of view and natural view of the user is significant. This allows for us to measure the true accommodation and convergence of the user as they observe images at various plane. Convergence has a direct correlation to the field of view and hence maximization of the field of view improves the convergence range of the optical system.

The optical functionality of our second prototype was altered to reduce the system size. The first prototype was setup to produce a 4f imaging system. There were many advantages to our 4f design such as wavefront preservation, increased throughput, and hence a higher quality measurement of the aberrated wavefront at the detector plane. The binocular system of the first prototype was approximately a 1 ft by 1 ft area. We reduced the size of the optical system to an approximately area of 3.5" by 1.5' area by eliminating the 4f properties of the optical system.

This was achieved by changing the focal length of our optical system from 100 mm focal lengths to 35 mm focal lengths and shifting the optical elements off axis as was mentioned earlier.

Functionally, the second prototype operates in the same fashion as the first prototype. (1) Infrared light is shone into the eye and scatters from the retina. (2) The scattered light exits the eye as an emerging wavefront that is relayed through the fluidic lens to the Shack-Hartmann sensor. The sensor reconstructs the wavefront and extracts the sphero-cylindrical refractive error. This prescription is then applied to adjust the volume of the fluidic lenses to null out the refractive error. Feedback of the wavefront from the eye/fluidic lens combination is then used to monitor the fluid volume and keep the net refractive error at a minimum

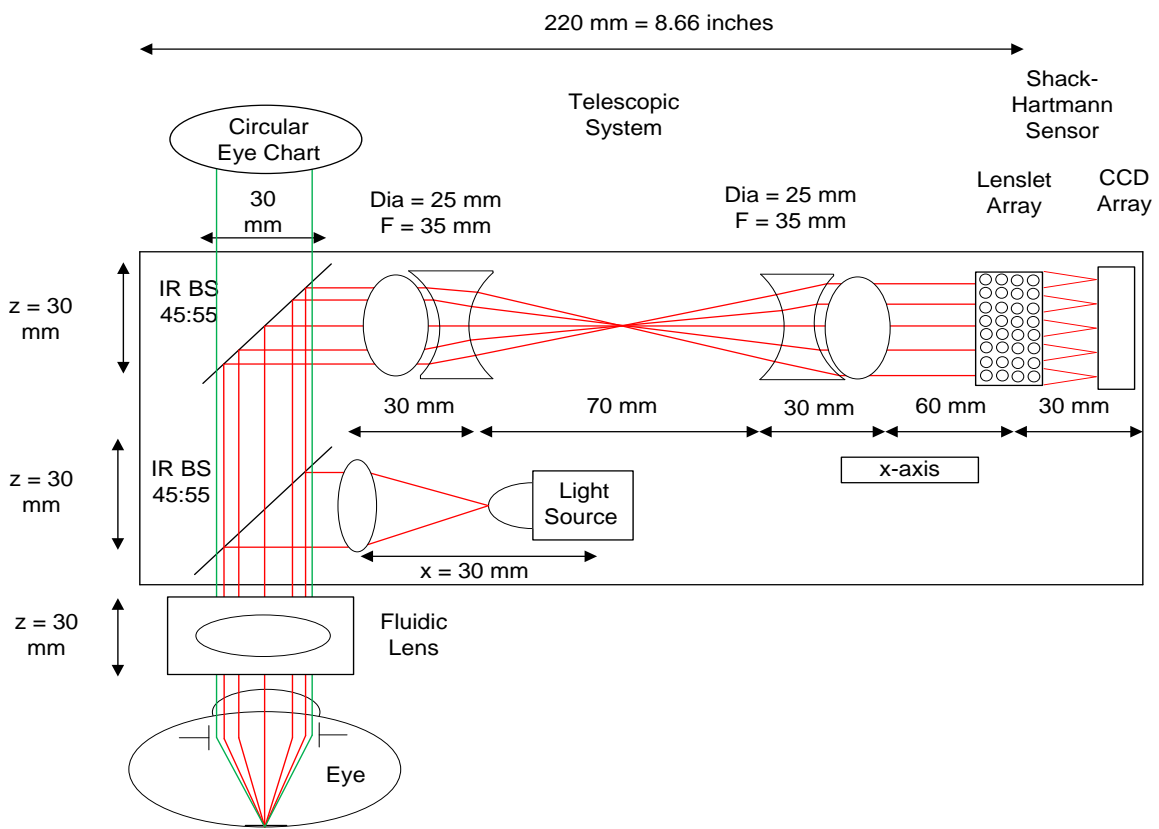
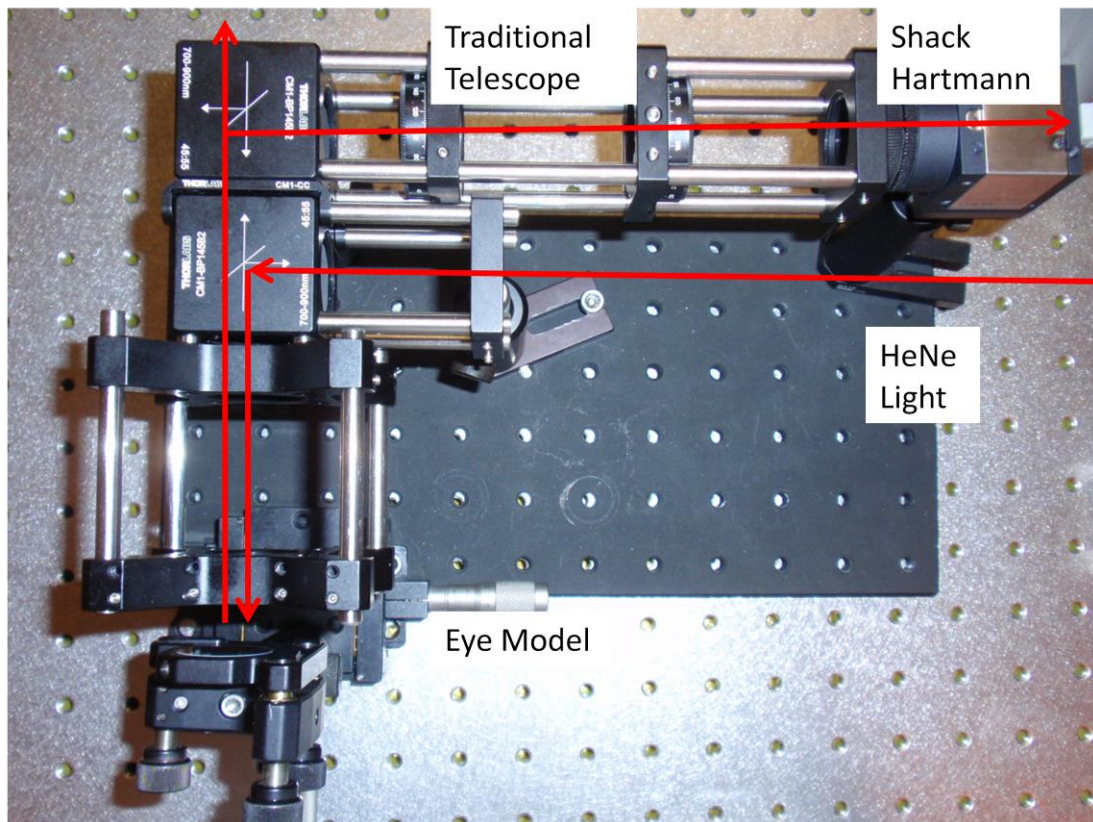


Figure 10-1 **Fluidic Auto-Phoropter Prototype Two:** The system model shows the dimensions of the compressed design with the optics shifted out of the line of sight of the user. A natural view allows for the user to naturally adjust their eyes to targets.

### **10.1.1 Design Setup of Fluidic Auto-Phoropter Prototype Two**

As a proof of concept, we experimented with a 5 mW HeNe laser at a wavelength of 633 nm. The wavelength length is shorter and the intensity is higher than what will be designed for actual use with our fluidic auto-phoropter. The choice of this wavelength was to identify if our optical system functions experimentally and also for comparison to the first prototype and third prototypes. The alignment of the optical system is again constructed around the beamsplitters. We applied connection rods to align the telescopic system off axis to the second pellicle beamsplitter. Light propagates from the source to the first pellicle beamsplitter, which reflects 45% of the propagating light toward the eye model. The fluidic lens would be locked onto the first beamsplitter as was previously shown in the first prototype. During experimentation we removed the fluidic phoropter to test the eye model and the defocus wavefront error, similarly to section 9.1. Showing that we can measure the eye models defocus error identifies that our system is capable of power variation measurement and thus proves system functionality.



**Figure 10-2 Testing Fluidic Auto-Phoropter Prototype Two:** The fluidic phoropter is removed as to not induce undesired wave distortion. By adjusting the mirror of the model eye we are replicating power aberration of an eye. We then measure the wavefront power variation of the full optical system and determine the wavefront variation at a given amount of power error from the model eye.

After light reflects out of the eye model it propagates through the system. There are two beamsplitters and a fluidic phoropter in the line of sight of the user. When the fluidic phoropter is set at zero power, there is no power in the viewer's line of sight. The wavefront sensor can measure the prescription required under these conditions. 55% of the laser light that reflects off of the eye propagates through the first beamsplitter and 45% of the remaining light reflects off axis toward the telescope system. The propagating light reflected into our telescopic system is reimaged onto the lenslet array of the wavefront sensor.

There are two designs with this optical setup that were created. The first design is a table top version of the optical system. The second design has the capability of becoming mobile. The difference between the two designs is very slight. The first design has a Shack-Hartmann wavefront sensor that is disconnected, making the system discontinuous. By combining the sensor to the connection rods off of the second pellicle beamsplitter, we were able to produce one mobile optical setup that did not require to be set on a table top. The sensor was combined to the connection rods through c-mounts and adaptors.

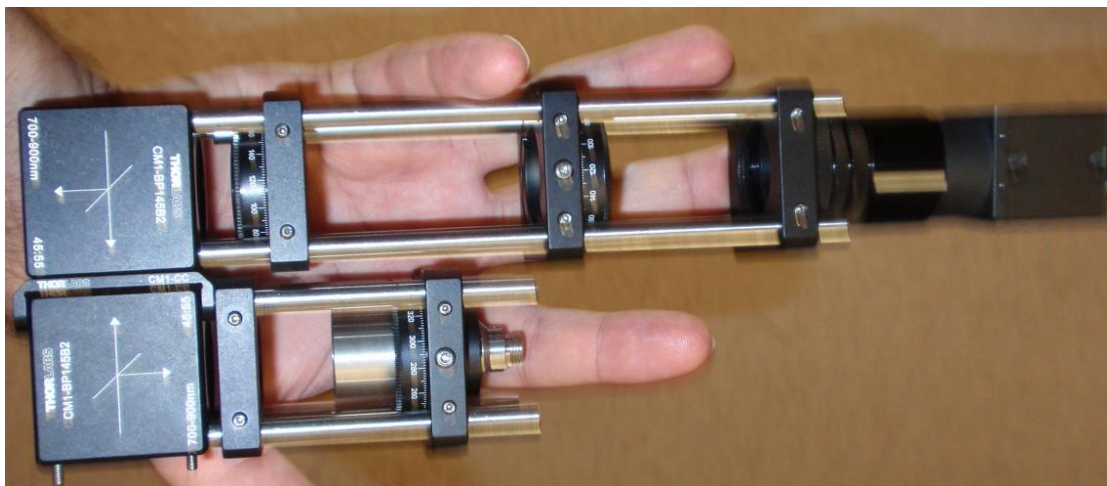


Figure 10-3 **Mobile Fluidic Auto-Phoropter Prototype Two:** Prototype Two is assembled so that it has become small and mobile with the light source and sensor locked onto cage rods.

### 10.1.2 Modeling and Testing of Fluidic Auto-Phoropter Prototype Two

As we no longer observe one to one conjugation between the pupil plane and lenslet array we begin to see cropping of the wavefront and magnification effects of the measured slope. There will also be an increased amount of light loss as we are no longer matching pupil planes to the lenslet array. The goal is to identify if under these new optical design conditions we can extract data and correlate prescriptions. The system was modeled in ZEMAX to identify the amount of error that the fluidic auto-phoropter can measure and the range. The exact positions

of the fluidic auto-phoropter and optics were placed into the design. The eye model was adjusted in the ZEMAX model to replicate 50 micron increments, identifying power variation observed in the system with the new physical positions of the optical lenses. The amount of error that the system was capable of measuring was from the range of -15 to + 15 D for our system stopped down to 3 mm.

The results for the dynamic range showed that there was variation in the slope of the second prototype. In order to verify the model, we experimentally replicated power variations of the model eye by shifting the mirror relative to the eye lens of our eye model. We include values of -5 to + 5 D in our experimentation as to compare the results of the second prototype with the results of the first prototype. As shown in Figure 10-4, the wavefront measurement of the second prototype shows a very gradual slope relative to the first prototype. For plus or minus five Diopters of defocus the slope of the second prototype is within 0.3 Diopters of zero. This suggests that as we can achieve more accurate measurements with the first phoropter design as the slope sensitivity is less. With smaller slope sensitivity a reading of 1 wave of defocus error for example clearly indicates our model eye with defocus power. Whereas, it is harder to identify 0.2 waves of defocus error from prototype two as the slope is gradual. It is noted that the testing of the first phoropter was operating at 785 nm and the testing of the second phoropter was operating at 633 nm. The wavefront sensor was adjusted and calibrated to test for the proper wavelengths.

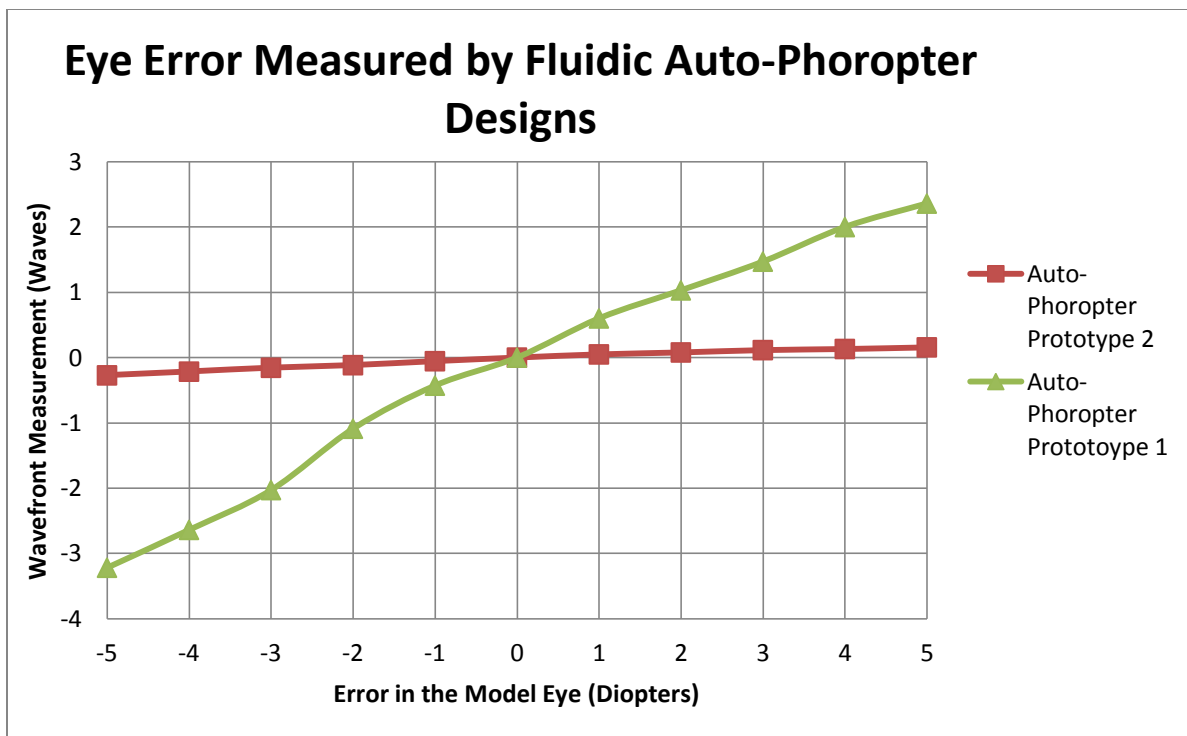


Figure 10-4 **Comparing Wavefront Error of Prototypes One and Two Relative to Defocus Power of the Model Eye:** The larger slope variation of prototype one allows for clearer defocus measurements as there is higher differentiation between power variation in the model eye.

Figure 10-5 shows further examination of the second prototype's wavefront measurement relative to defocus power of the model eye. This wavefront measurement shows that there is in fact a slope that is differentiable with the setup of prototype two. Although not as steep of a slope as prototype one, we are able to extract model eye measurements and differentiate between various amounts of power at the eye location. As was discussed in Chapter 9, what is necessary is the identification of a linear change in wavefront error relative to the amount of error identified by both the model eye and the fluidic phoropter to compensate for that error for a functional system. Showing that there is a linear variation of the model eye readings in the fluidic phoropter proves that error correction is achievable with this second prototype.

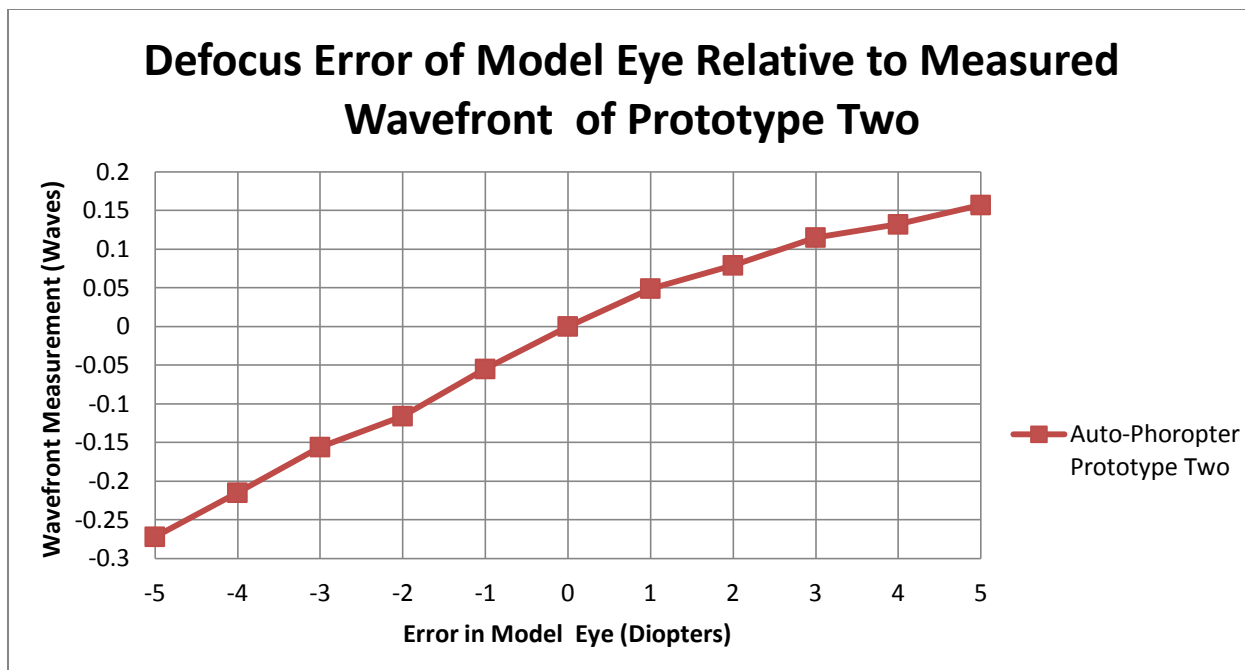


Figure 10-5 **Wavefront Error of Prototype Two Relative to Defocus Power of the Model Eye:** The slope variation of the model eye's defocus measurements proves that fluidic auto-phoropter two can functionally measure power variation induced by either the fluidic phoropter or the eye model.

## 10.2 Nulling Error with Prototype Two Fluidic Auto-Phoropter

In section 10.1 we proved through shifting the mirror position of the model eye that our wavefront sensor is capable of measuring wavefront error variation in the functional second prototype. To further verify that our second prototype can in fact correct for wavefront error we tested the second prototype with our fluidic lens. For both the null test and the model eye test of prototype two we set the auto-phoropter so that it was stopped down to 3 mm. The eye model mirror was shifted relative to the eye model lens so that -5 D of defocus power error was induced and measured in the system with -.275 waves of defocus aberration. We then adjusted the power of the defocus fluidic lens to null this measured error until the wavefront sensor identified zero defocus error. Figure 10-6 shows the setup with both the fluidic defocus lens and the model eye

represented in the setup. Figure 10-7 shows the nulled out wavefront that was outputted by the Shack-Hartmann wavefront sensor.

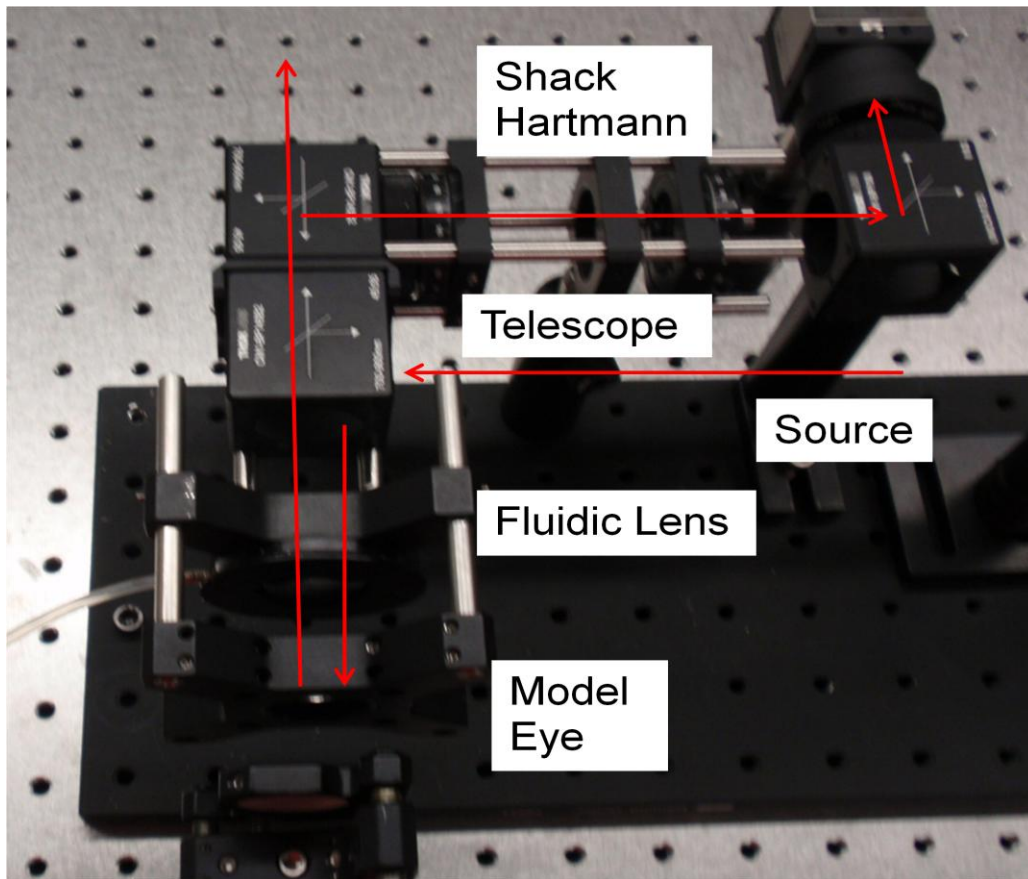


Figure 10-6 **Nulling Power Error with Fluidic Auto-Phoropter Prototype Two** The defocus component of the fluidic phoropter was inserted into the system. The eye model is adjusted to -5D of defocus and nulled out with the fluidic defocus lens in the setup of fluidic auto-phoropter prototype two.

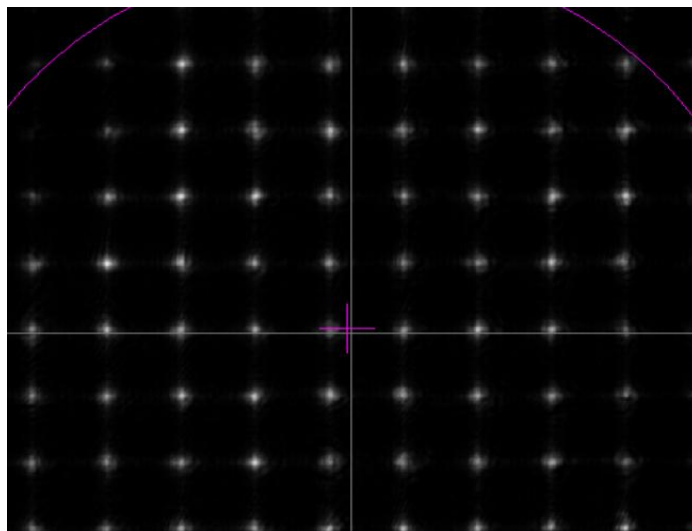


Figure 10-7 **Nulling Power Observed for Fluidic Auto-Phoropter Prototype Two from Shack-Hartmann Wavefront Sensor:** The Shack-Hartmann image of when the -5 D of eye model error is nulled by the fluidic phoropter's defocus lens

### 10.3 Limits of Optical Design

Fluidic auto-phoropter prototype two was designed with the motivation of proof of concept. We proved that we are capable of taking the optics off axis and achieve measurable results. The advantage of a natural scene for the user is very significant and more off-axis designs must be tested. This specific design does have shortfalls that are significant: 1) Lack of 4f imaging and 2) Field of View.

The field of view was meant to be increased by taking the optics off-axis. For this specific design we doubled two beamsplitters in the line of sight of the user while applying the same pellicle beamsplitters with a 17.8 mm lateral width in order to take the optics off axis. By having two sequential beamsplitters have added 30 mm along the optical axis relative to a one beamsplitter setup as discussed in section 9.4. This reduces the field of view from  $11.8^\circ$  with a single beamsplitter to  $8.8^\circ$  with two beamsplitters. Prototype one had a field of view of  $10^\circ$  and so this second prototype exhibits a worse field of view than our first prototype.

Transitioning to 4F imaging, the first shortfall in losing 4f imaging is that our throughput has decreased. Depending on how far adjusted we are from 4f imaging we can determine what percentage of the light is lost. We were able to achieve measurable results with our HeNe laser as the intensity of the light was at 5 mW. If this intensity of light was placed into an eye it would create severe damage. The power range that our light source functions is between 10-15  $\mu$ W or almost 3 orders of magnitude less than the power we tested with.

A second approach in increasing throughput was in how we designed the eye model. Prior to discussing the eye model, we will discuss the other locations where light loss occurs. The light propagates through our 45:55 beamsplitters once and then reflects through the beamsplitters once after exiting the eye, giving approximately 75% light loss after exiting the eye. We pass through the fluidic phoropter twice where we have two uncoated glass plates that give 4% light loss every time we pass. The remaining 24.75 % of light will drop to 21.0 % after the four passes through the optical flats of the fluidic phoropter. When we designed the eye model we placed a flat mirror and a power lens which produce negligible light loss. This allowed for the 21.0 % of light coming from the 5 mW laser at 633 nm to reach the Shack-Hartmann wavefront sensor, or 1.05 mW of energy. In actuality, an eye will only reflect approximately 5-10% of the light back through the system. This amount of light loss would bring the throughput of the 1.05 mW to 105  $\mu$ W reaching the detector plane. This means that about 2.1 % of the light exiting the laser source reaches the detector plane when dealing with a real eye. The 2.1 % of power that would be transmitted through the system is relative to only the transmission of the optics and not the physical placement of the optics. The physical position and lack of 4F imaging further decreases the throughput of the system.

The second shortfall in the factor of losing 4F imaging is the physical magnification induced within the system. As was mentioned earlier, we are no longer producing 1:1 angular magnification as we have shifted our conjugate planes to compress the system. The shift in physical position of the optics causes cropping of the wavefront, induces aberrations and shifts the amount of vigneting. There are shifts in the measured error as is observed from Figure 10-4 between the two systems. Even though we nulled the eye model error with the defocus lens we were not necessarily placing the correct power for the user. We were nulling the error of the whole auto-phoropter system with the relative position of the eye model relative to the Shack-Hartmann wavefront sensor. The nulling power for the eye coupled with the fluidic lenses may not produce the desired results.

The best approach in verifying whether prototype two can measure accurately on a human eye is to adjust the system and to compare the model to a 4F imaging system that is off axis. The adjustment with prototype two is to remove the laser source and insert our NIR source that operates at 15  $\mu\text{W}$  reaching the eye position. It is significant to note that the output of the NIR source is not 15  $\mu\text{W}$  but the amount of light reaching the eye location is 15  $\mu\text{W}$  as to maximize the amount of light that is used at the eye location. The second adjustment to prototype two is in the eye model. Instead of using a plane mirror we can replace the mirror with a Tums. Tums have advantages beyond heart burn in that they also have similar scatter effects as observed by light propagating through an eye. We can replicate the 10% light loss at the eye experimentally with this approach.

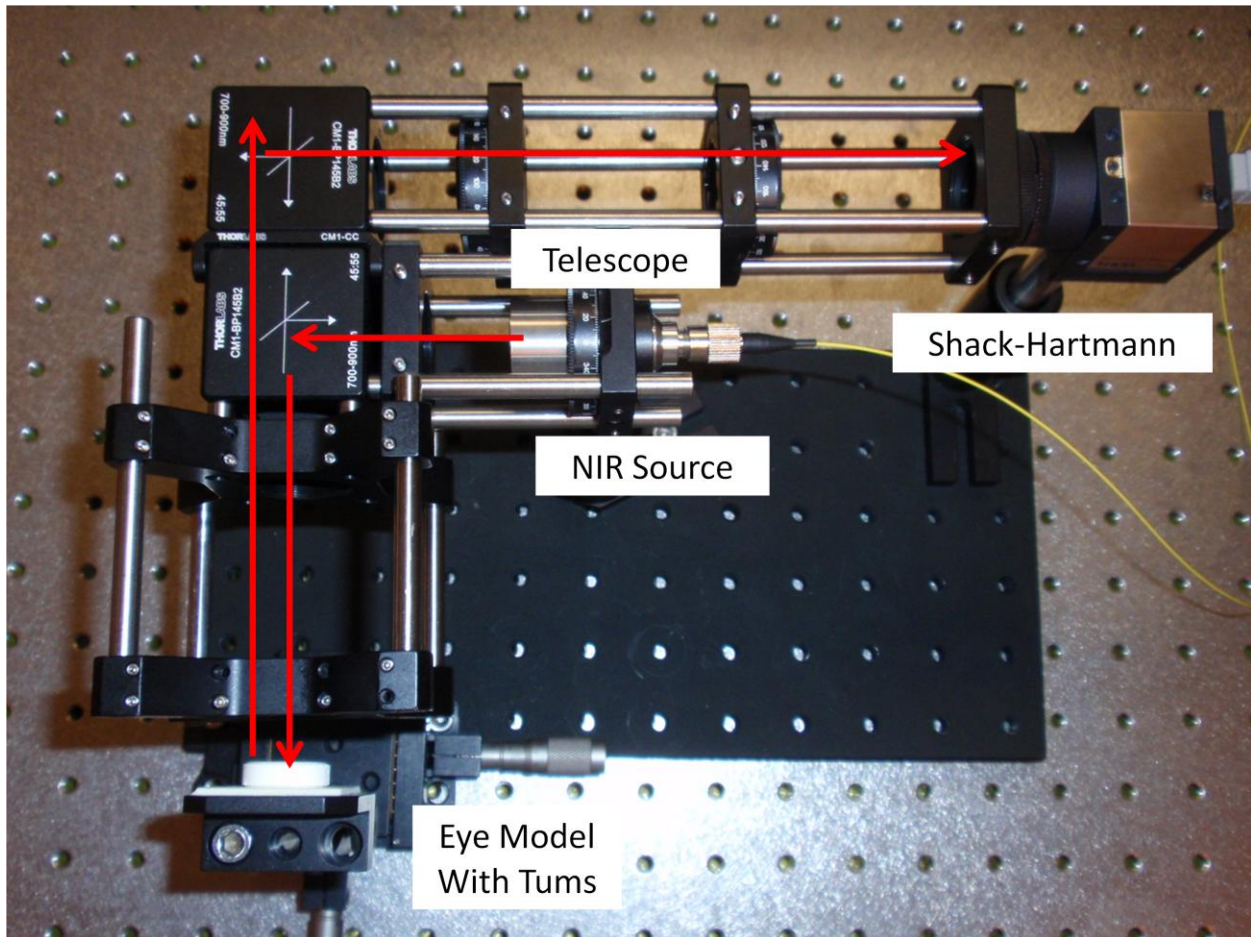


Figure 10-8 **Modified Fluidic Auto-Phoropter Prototype Two:** The light source and eye model are modified to produce a better representation of a real time examination.

An additional system, which we will call prototype three is designed, but not yet tested, to improve on the system limitations of prototype two. In the line of sight of the user, it is preferred to have one beamsplitter rather than two beamsplitters. This will give us a field of view of  $11.8^\circ$  for the user, rather than the  $8.8^\circ$  viewed in prototype two and the  $10^\circ$  field of view from prototype one. Again, we set the NIR light source with its power output is  $10\text{-}15\ \mu\text{W}$  at the location of the model eye. Also the model eye applies a Tums rather than a flat mirror to replicate the energy loss at the eye. This optical systems primary modification relative to both prototype one and prototype two is that of the telescopic system. We would like to compare a 4F imaging system with off-axis optics to both prototype one and prototype two. This will give a

clear indication on whether prototype one is realizable without a 4F imaging system and also if 4f imaging systems different focal lengths produce variable results.

The third prototype requires longer focal lengths. We shifted the optics in front of the 1<sup>st</sup> doublet relative to prototype one so that there are two beamsplitters on the front side of the optical system. If we also include tolerance of the beamsplitters, eye relief, and fluidic lenses then a focal length of 125 to 150 mm would be optimal. With this alteration, the 2f separation between our optical doublets with the same focal length is required to be between 250 to 300 mm. We will require our folded optical system, but we must adjust the dimensions of the separations in a fashion similar to the calculations for the size of the prisms and locations of the separations as we have shown in Figure 7-10 in section 7.1.3. Once we have remodeled the system and chosen a focal length for the doublets we can match the length behind the telescope to the Shack-Hartmann wavefront sensor with a distance of F.

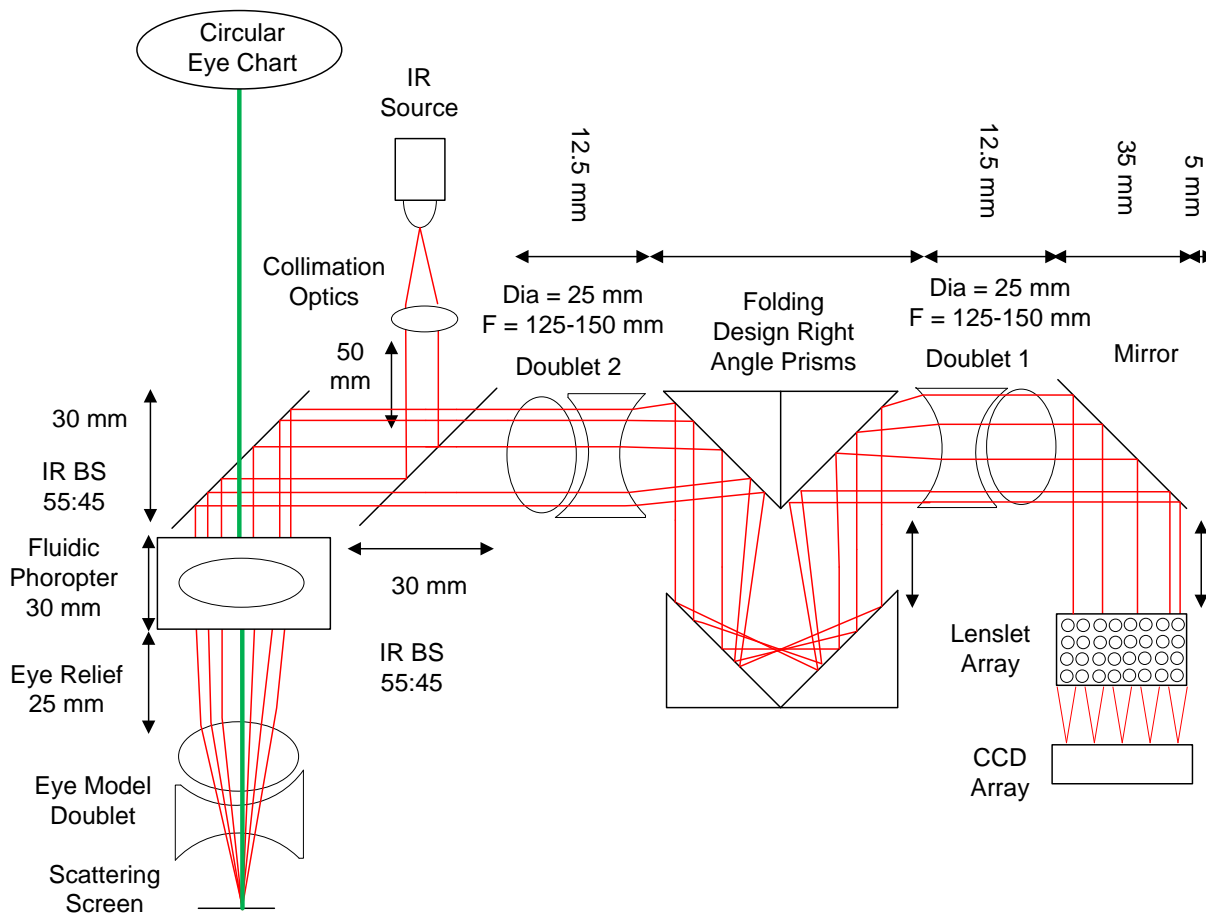


Figure 10-9 **Fluidic Auto-Phoropter Prototype Three:** This design will give us a 4f imaging system with a wider field of view and a natural viewing in front of the user. Prototype three is a modification of the first two prototypes.

This system will produce a 4f imaging system for an off-axis optical system. It will not reduce the size of prototype one, but will geometrically verify the significance of 4F imaging. In addition, we increase the field of view by removing a beamsplitter in the line of sight of the user who is observing a clear view in front of them. We can replicate the amount of light that propagates through the system. An additional advantage of prototype three and prototype two are that we can place additional optics between the beamsplitter next to the doublet and the doublet of the telescopic system. If we are not able to produce enough light to reach the detector plane a signal amplification method can be inserted in front of the telescopic system. Signal

amplification was not possible with the telescope in the line of sight of the user as it would block the viewer from seeing through the optical system. By placing the optics off axis we can insert a signal amplifier to improve the signal at the sensor plane. This of course would require further experimentation.

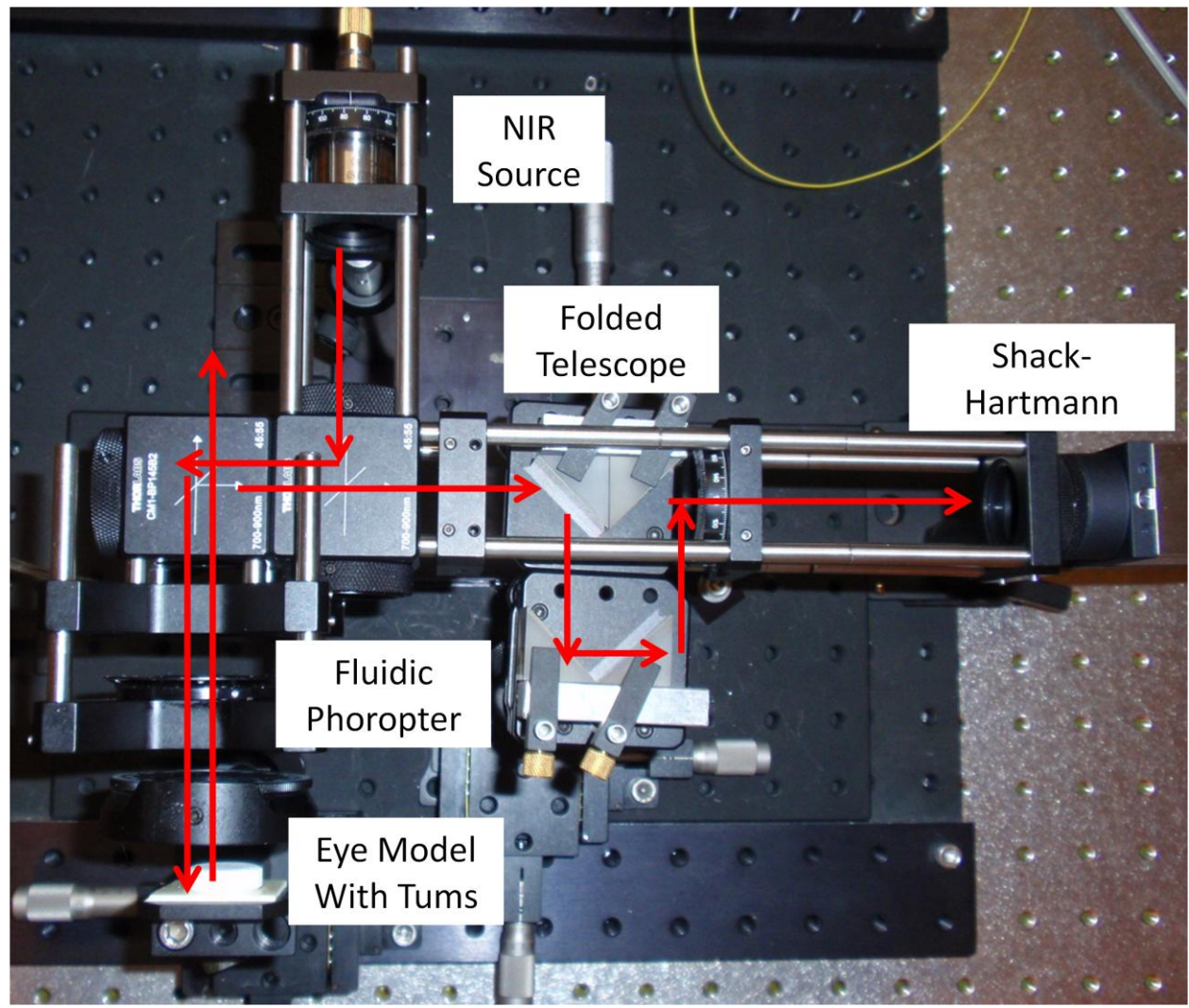


Figure 10-10 **Image of Fluidic Auto-Phoropter Prototype Three:** Prototype three is built here to show the functional form of the optics. This system was a model and was not tested with.

## **11.0 FLUIDIC AUTO-PHOROPTERS: OFF-AXIS OPTICAL DESIGNS WITH HOLOGRAPHIC OPTICAL ELEMENTS**

Our previous systems have taken advantage of traditional optical lenses in reimaging of the wavefront. The telescopic system and the lenslet array of the Shack-Hartmann wavefront sensor are composed of standard optical lenses. There are many advantages to shifting from traditional optics to holographic optical elements (HOE's). HOE's are lighter, quickly repeatable, and cost much less than traditional optics. Adding HOE technology to our existing fluidic auto-phoropter design will also assist in miniaturizing our optical design as single HOE elements can become transparent in certain wavelengths, act as a lens in other wavelengths, and also act as beamsplitters. We will show the advancement and progression of the fluidic auto-phoropter with the use of HOE's for the telescopic system with an off-axis design. As a proof of concept, in the same way we proved prototype two, we will show a nulled image of the fluidic auto-phoropter and its functioning results with a model eye.

Functionally, the produced system is similar to the previous design with the exception of the modification to the telescopic system as coupled HOE's. The compact systems are comprised of three modules: our fluidic phoropter with any sphere, cylinder, and axis combination, a holographic relay telescope and a Shack-Hartmann sensor. This fluidic auto-phoropter system will concurrently measure refractive error by: (1) Shining infrared light that scatters off the retina. (2) The scattered light exits the eyes as an emerging wavefront that is relayed to the Shack-Hartmann wavefront sensor. (3) The sensor reconstructs the wavefront and extracts the sphero-cylindrical refractive error. (4) This prescription is applied to adjust the fluid volume, nulling out each eye's refractive error while the user views an eye chart. The users' field of view is drastically enhanced with the HOE in the line of sight of the user as we can produce

large substrates. This allows for the system field of view to be limited by the fluidic phoropter and no longer by the auto-phoropter design. The HOE's can be designed to be transparent in the visible wavelengths, allowing for the subject to view external targets such as an eye chart with ease. The HOE's additional desired capabilities are to direct infrared light toward the eye and to act as a lens at the 785 nm wavelength. When the HOE acts as a lens, it is at a designed wavelength and that wavelength range is towards an off axis location where a second HOE is placed for the telescopic system. The exiting light of the off-axis holographic telescopic system reaches the final module: a Shack-Hartmann wavefront sensor. The holographic telescope applies volume holograms operating at Bragg's Regime to drastically reduce the system size. The desired wavelength of the holographic optical elements operates in the infrared and produce direct geometry optical lens replication. The adaptive phoropter prototype fits in a 60 mm long by 240 mm wide area.

It was mentioned a few times in this section that our desired wavelength was at 785 nm for reading and writing. There were no HOE's available that operating at this wavelength. For testing purposes, the standard wavelength of 633 nm was applied into our fluidic auto-phoropter. This design with this wavelength will not be tested on humans, but rather it was to develop a proof of concept for the combination of fluidic adaptive optics, wavefront sensing and holographic optical elements into an advanced fluidic auto-phoropter. If the system operates at 633 nm for reading and writing then it should operate at 785 nm once the technology for this wavelength becomes available. In this chapter, we will be assessing the physical capabilities of the holographic phoropter relative to prototype two of our fluidic auto-phoropter with off-axis traditional lenses from Chapter 10.

## 11.1 Holography and Holographic Lenses

Holography has evolved over the years in a progression that has shifted holograms from static 3D imaging to mobile 3D image replication. In 1947, Gabor proposed a holographic theory which recorded the light field's amplitude and phase [94]. Stationary 3D replicas of written objects are observed when the recorded information is properly illuminated in traditional holograms at a designed writing and reading wavelength. In-line transmission holography produced lenses that are on axis such as "Gabor" zone plates (CGH's). This type of HOE operates on-axis for large holograms with wide-band illumination. Unfortunately, Gabor geometry based holograms produced large amounts of background noise as the 0,-1, and higher order diffraction orders were reimaged onto the writing material. There had been a large focus in holography in the late 1960's and 1970's in the expansion of holographic technology. For a further background in holographic theory one should read Chapter 9 of Goodman's "Introduction to Fourier Optics".

The desire of our research was in the progression of HOE's as optical lenses. Beyond Gabor zone plates, Fresnel lenses and volume hologram lenses were two options for the creation of HOE optical lenses. Fresnel lenses work efficiently with profiled grooves when refraction and diffraction angles of these grooves are matched. However groove profiling drops lens resolution and there is a degradation of image quality. The best viable option was the use of volume holograms in the design of our holographic lenses under designed conditions. In the past couple of years there has been a progression of polymer based volume holograms. Our volume holograms apply the Bayer photopolymer, which is a new holographic recording material developed in the past half decade, in the creation of our volume holograms [95].

There are several advantages in applying Bayer photopolymer based volume holograms as our lenses. From a design stand point, the Bayer material does not require chemical or thermal treatment, which makes them cheap and easily replicable. From an optical standpoint, under certain conditions these HOE's exhibit high optical qualities. The main restrictions of the HOE's for our fluidic holographic auto-phoropter is that the HOEs geometry can be designed as a lens for only a particular wavelength because (1) focal length of the holographic lenses is roughly proportional to the operating wavelength and (2) HOEs work efficiently in only off-axis geometries known as Bragg's angle and this diffraction angle is also wavelength dependant.

In our approach we are using volume holograms as our holographic lenses operating in the Bragg regime, which requires off axis geometry when operable. Standard HOE's are designed in the visible wavelength where our HOE's was designed at 633 nm for testing purposes. After proof of concept, which will be shown in this chapter, the next generation HOE's will be designed for a band at 785 nm and will be transparent in the visible. The HOE's appear on 2.3 mm thick glass substrates with a rectangular shape and have a 2 inch diameter size. HOEs recorded in such a regime can achieve more than 90% diffraction efficiency, less than 1% background noise, a transparency in wavelength ranges from 350 nm to 1500 nm, and high angular selectivity.

These qualities of the holographic lens are desirable in our final HOE design. The high angular sensitivity allows for almost no diffraction outside of the controlled angular range. This allows for the rest of the range between 350 nm to 1500 nm to be transparent. Thus when we design at 785 nm, the HOE will act as a clear window in the visible where the viewer looks through while at the same time acts as a lens at our testing wavelength of 785 nm off axis. As these HOE's function as a lens off axis, we have now replaced the need for a beamsplitter as the

HOE lens functions as a lens at our operating wavelength, but simultaneously acts as a beamsplitter with a clear window in the rest of the visible spectrum. At our operating wavelength, we have high diffraction efficiency of over 90% with negligible amounts of background noise. Instead of losing approximately half the operating light every interaction with the beamsplitters, we now lose less than 10 % of the light from each of the holographic lenses.

### **11.2 Design of Fluidic Holographic Auto-Phoropter with Holographic Optical Elements as Lenses**

As was stated, the first motivation was to prove the functionality of the HOE's as a telescopic system in our fluidic auto-phoropter in the creation of a fluidic holographic auto-phoropter. Our comparison of the functionality of the HOE based auto-phoropter was relative to prototype two. Prototype two applied two 35 mm focal length doublets as the telescope design in an off axis setup. We therefore replicated these two 35 mm focal length lenses as HOE lenses. Both HOE's were positive powered lenses that were exactly of those used in the design of prototype two. The combination of the two HOE lenses at a 2F separation produced a Keplerian holographic telescope with an afocal design. As we were replicating prototype two, there was a loss of 4F imaging in which the telescopic system would produce 1:1 angular magnification at the lenslet array relative to the pupil plane. We will describe a correction for this later on. The operating wavelength for the HOE prototype was at a HeNe wavelength of 633 nm, the same wavelength as that of prototype two. The system was drastically compressed and efficiency improved by removing the beamsplitters in the optical setup. The length in front of the user is still 3.5" in the z-axis for the line of sight. The width of the optical system was compressed to 100 mm or roughly 4". The Shack-Hartmann wavefront sensor in this design is described with a position vertically above the second HOE lens in the telescopic system.

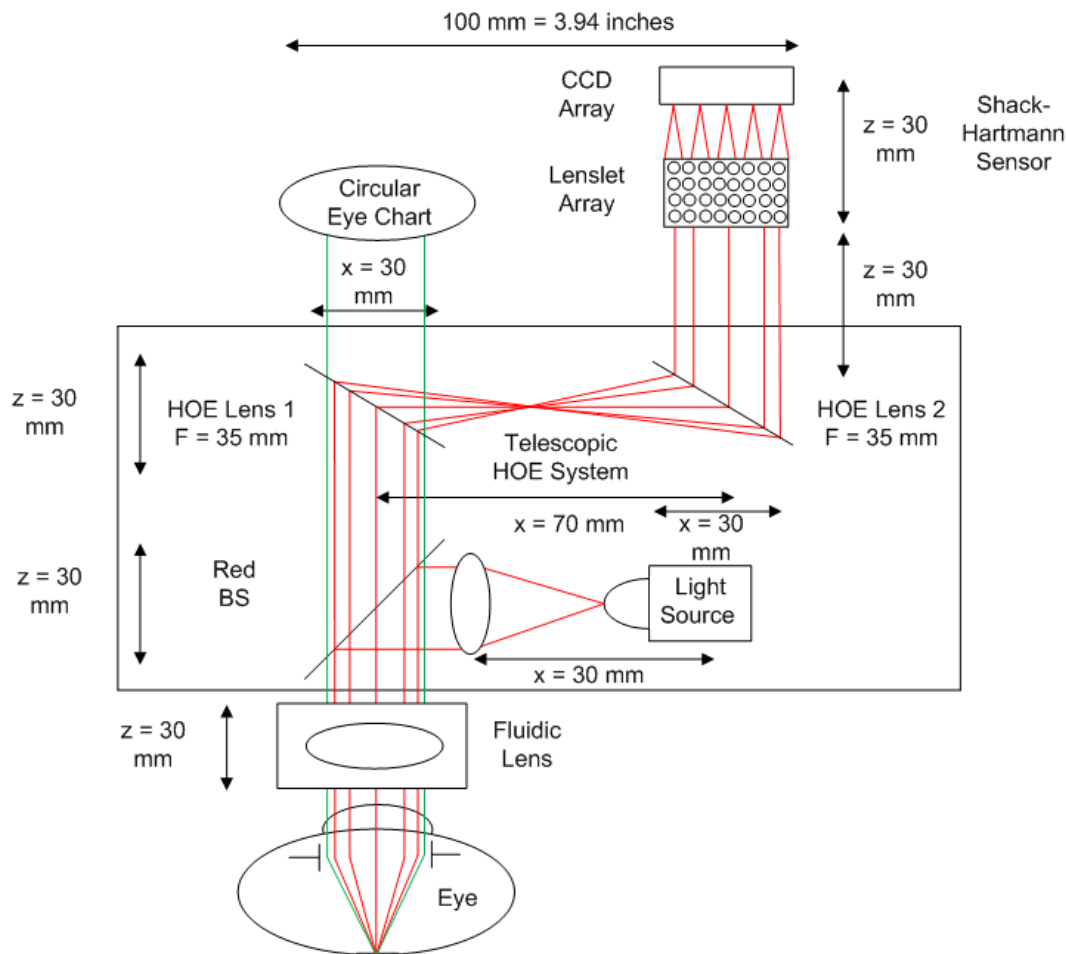


Figure 11-1 **Fluidic Holographic Auto-Phoropter:** The HOE lenses replace the telescope lenses and a beamsplitter in prototype one of our fluidic holographic auto-phoropter.

### 11.3 Modeling Fluidic Holographic Auto-Phoropter Prototype One

We modeled the holographic auto-phoropter in ZEMAX prior to building the system. We used the same approach in proving the functionality of the fluidic holographic auto-phoropter by testing the slope variation of the model eye as we did in the previous systems. The holographic auto-phoropter was modeled so that the two holographic elements were set in a position relative to each other to produce a telescope. After the HOE's were set to produce a holographic telescopic system we began adding components of the holographic auto-phoropter. The light source enters from off axis onto a beamsplitter and half the light reflects toward the eye

model. The fluidic phoropter was set at zero power as again we were testing to verify if there was a power variation due to the shifting of the mirror position in the eye model and what range is achievable. Figure 11-2 shows the holographic telescope in alignment with the model eye. This optical path is a representation that the testing light follows through the system and not the path that the user observes through the system.

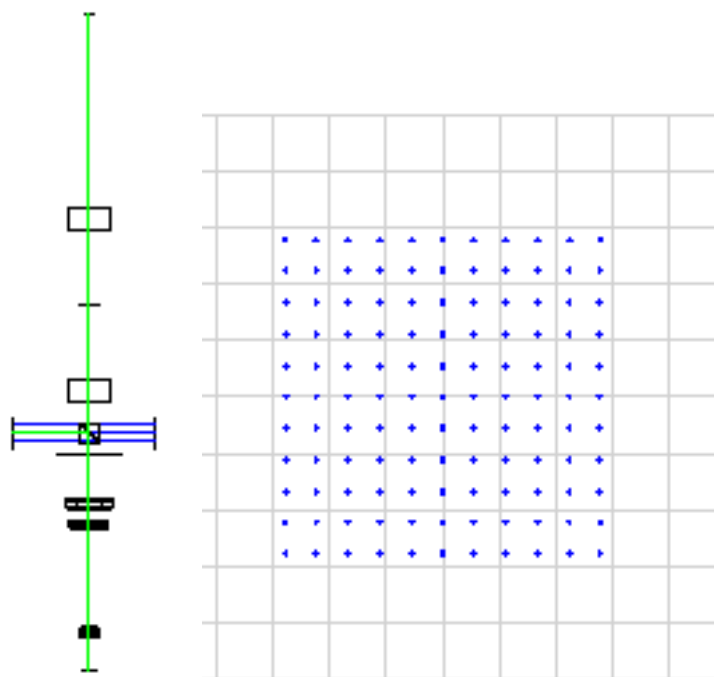


Figure 11-2 **Fluidic Holographic Auto-Phoropter ZEMAX Model:** The fluidic holographic auto-phoropter was designed so the fluidic phoropter applied zero power into the system. The system is aligned for a corrected eye model before power variation in the model testing occurred.

Once our model was fully aligned we tested power variation of the model eye caused by shifting the mirror position. The ZEMAX model identified the physical range in which our holographic auto-phoropter functions. The lower limit, as seen in Figure 11-3, was observed as the lenslet points began focusing on a single point location. The dynamic range that was observed in the physical model was down to about -16 D of power. With the specified optical separations that we modeled in ZEMAX, we were able to model powers that ranged between -15 D to + 15 D.

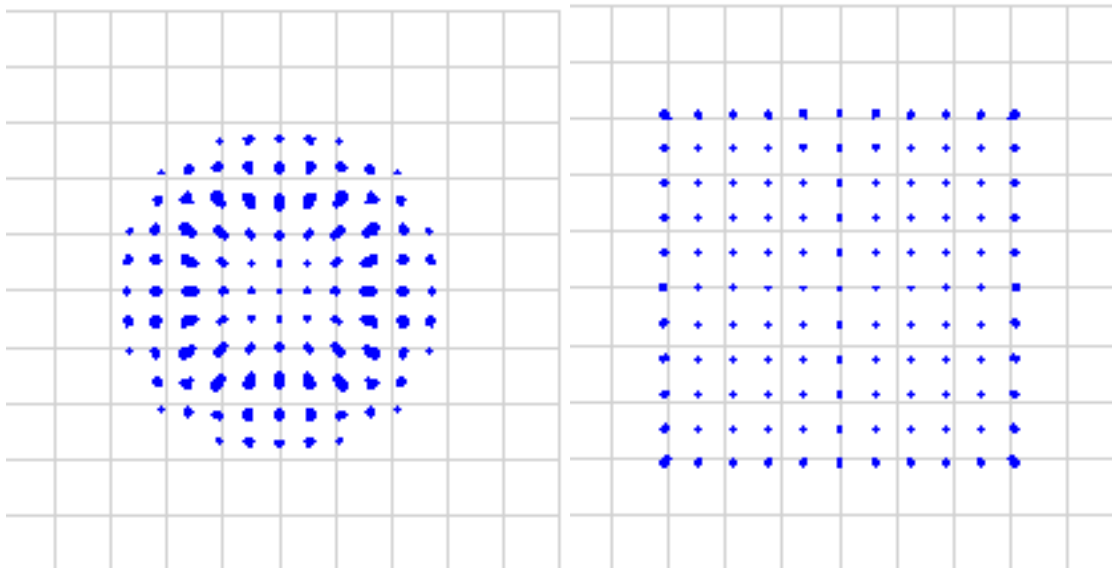


Figure 11-3 **Fluidic Holographic Auto-Phorofter Power Range:** We measured the power range for our designed separations. The images above show the point separation and shifts relative to mirror position in the model eye. As the points focused closer to the detector plane, the resolution between points diminished.

#### 11.4 Design and Setup of the Fluidic Holographic Auto-Phorofter

As a proof of concept, we experimented with a 5 mW HeNe laser at a wavelength of 633 nm as was used in prototype two. The wavelength length is shorter and the intensity is higher than what will be designed for actual use with our fluidic holographic auto-phorofter. The choice of wavelength was defined by the available HOE lenses. The testing with these HOE lenses and wavelength gave us the opportunity to verify if the systems produced meaningful results experimentally. These results would then be compared to prototype two as both systems used the same focal length lenses and telescope setups.

The alignment of the optical system is no longer constructed around the beamsplitters like previous fluidic auto-phorofter designs but rather centered around the two HOE lenses. The alignment of the two HOE lenses relative to each other is achieved by taking advantage of two lasers, both operating at the HeNe 633 nm wavelength. Each HOE is aligned individually so that

the maximum intensity reaches the focal location of that HOE lens. The HOE's are aligned relative to each other so that the focal location of the two HOE lenses is at the exact same location. The direction of the optical axis for both HOE lenses must be exact. Once the HOE's are aligned with the two lasers entering the system from both sides, the telescopic HOE system is ready for use.

The lasers are then removed and the rest of the system is aligned. One of the HeNe lasers is placed off axis and light enters the system through a beamsplitter. Half the light reflects toward the fluidic phoropter and the eye model. We have removed the fluidic phoropter as to test the accuracy of the auto-phoropter system with the eye model. The Shack-Hartmann wavefront sensor was placed at the proper position off axis to HOE lens 2 in order to focus light at the center of the sensor plane.

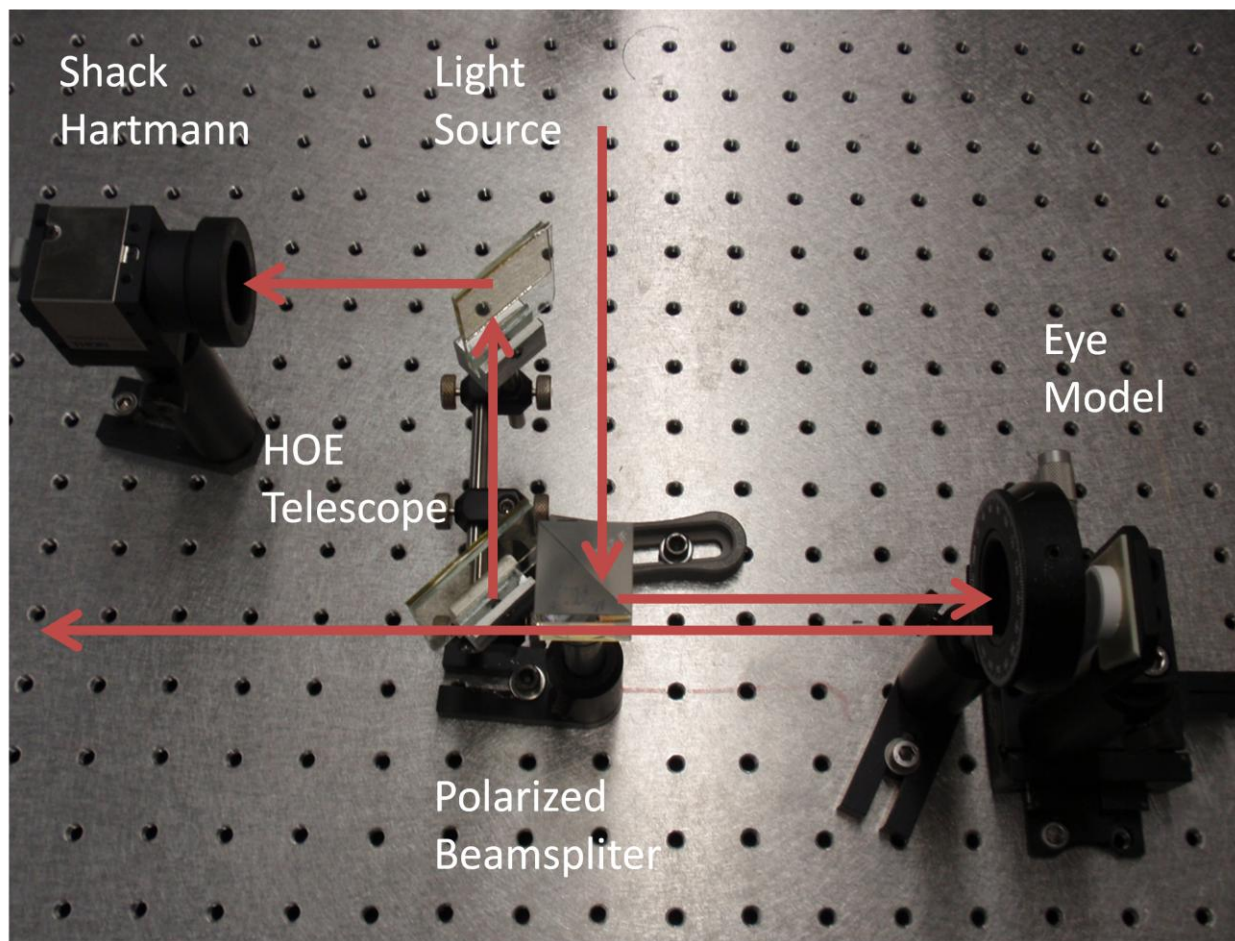


Figure 11-4 **Testing Fluidic Holographic Auto-Phoropter:** The fluidic phoropter is removed as to not induce undesired wave distortion. By adjusting the mirror of the model eye we are replicating power aberration of an eye. We then measure the wavefront power variation of the full optical system with the HOE's and determine the wavefront variation at a given amount of power error from the model eye.

### 11.5 Testing Fluidic Holographic Auto-Phoropter

We are replicating prototype two with our holographic fluidic auto-phoropter. This implies that the shortfalls from prototype two still exist within this holographic auto-phoropter design. We still no longer observe one to one conjugation between the pupil plane and lenslet array. This causes a cropping of the wavefront and magnification effects of the measured slope. There should be a slight slope variation between prototype two and the holographic design as the physical positions and lens powers are replicated with each other. This suggests that the HOE

design will have wavefront measurements in the order of magnitude similar to prototype two rather than the results of prototype one with the 4F imaging design. There is one less beamsplitter in the HOE design and we have taken this into account when positioning the telescope system, model eye, and Shack-Hartmann wavefront sensor. The light loss should be decreased relative to that of prototype two as the quantum efficiency of the HOE's are higher than the 50% loss of light caused by the beamsplitters.

There are a couple of goals to achieve in the comparison of these two systems. The first is to verify that the holographic fluidic auto-phoropter achieves extractable information. If we can correlate a slope to prescriptions then we have verified that the volume holograms can be coupled into a telescopic system that functions actively with the auto-phoropter setup. The second goal is to determine if the HOE lenses produce the exact same results as the traditional lens results. The significance of this second goal is from a scientific standpoint in identifying the affects of change in system design. As long as goal one is achieved, then we have proven that the holographic fluidic auto-phoropter functions. As was stated earlier, the ZEMAX models identified that both prototype two and the holographic design operated from -15 D to +15 D. We adjusted the model eye by 50 microns per measurement and recorded the amount of shift in defocus error that was observed.

Promising results were achieved through the testing of the HOE auto-phoropter. It was found that in fact a slope was measurable as we adjusted the defocus power at the model eye location. The linear change in power was measured with shifts of the mirror position at the eye model location, verifying that our holographic fluidic auto-phoropter can in fact measure a shift in power and can compensate for that power. The results also show that there was a slight variation in the slope of the holographic fluidic auto-phoropter relative to the second prototype.

The HOE telescope in some fashion has diminished the slope variation as measured by the wavefront sensor. As shown in Figure 11-5, the wavefront measurement of the HOE design shows a slightly more gradual slope relative to prototype two. For plus or minus fifteen Diopters of defocus of the model eye, the slope of the HOE prototype is within .1 waves of zero. Whereas, the slope variation of the second prototype is within .4 waves of zero at the plus or minus fifteen Diopters of defocus range of the model eye. This suggests that we can achieve more accurate measurements with the second phoropter design as the slope sensitivity is less. Both systems have gradual slopes relative to our first prototype which was a 4F imaging system.

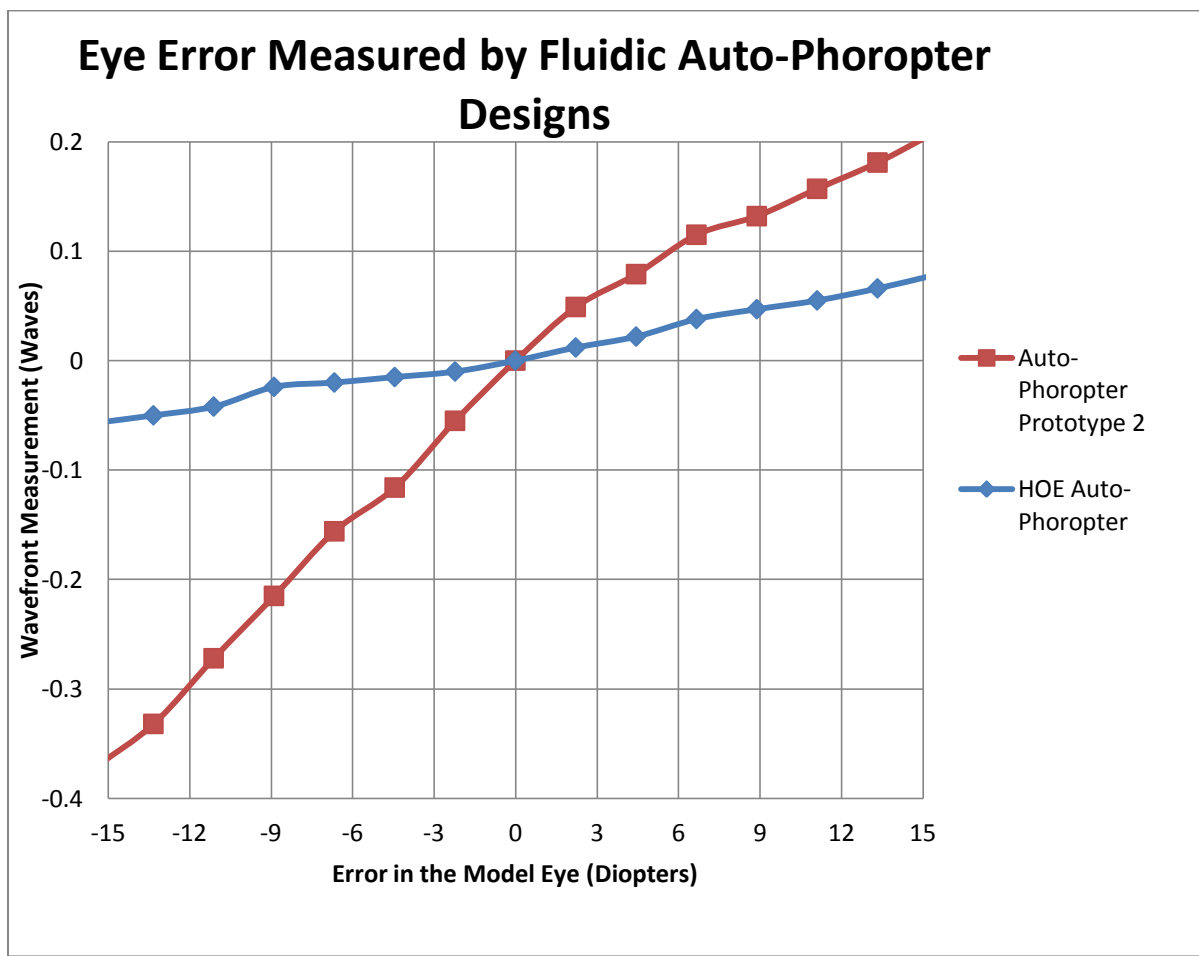


Figure 11-5 Comparing Wavefront Error of Prototypes Two and HOE Designs Relative Defocus Power of the Model Eye: Functionally prototype two will have a better accuracy due to larger slope variation. Both designs offer small slope changes at the same order of magnitude.

Figure 11-6 shows further examination of the wavefront measurement relative to defocus power of the model eye for the holographic prototype. This wavefront measurement shows that there is in fact a slope that is differentiable with the setup of the holographic fluidic phoropter. Although not as steep of a slope as prototype two, we are able to extract model eye measurements and differentiate between various amounts of power at the eye location. As was discussed in Chapter 9, what is necessary is the identification of a linear change in wavefront error relative to the amount of error identified by both the model eye and the fluidic phoropter to compensate for that error for a functional system. Showing that there is a linear variation of the model eye readings in the fluidic phoropter proves that error correction is achievable with this holographic prototype.

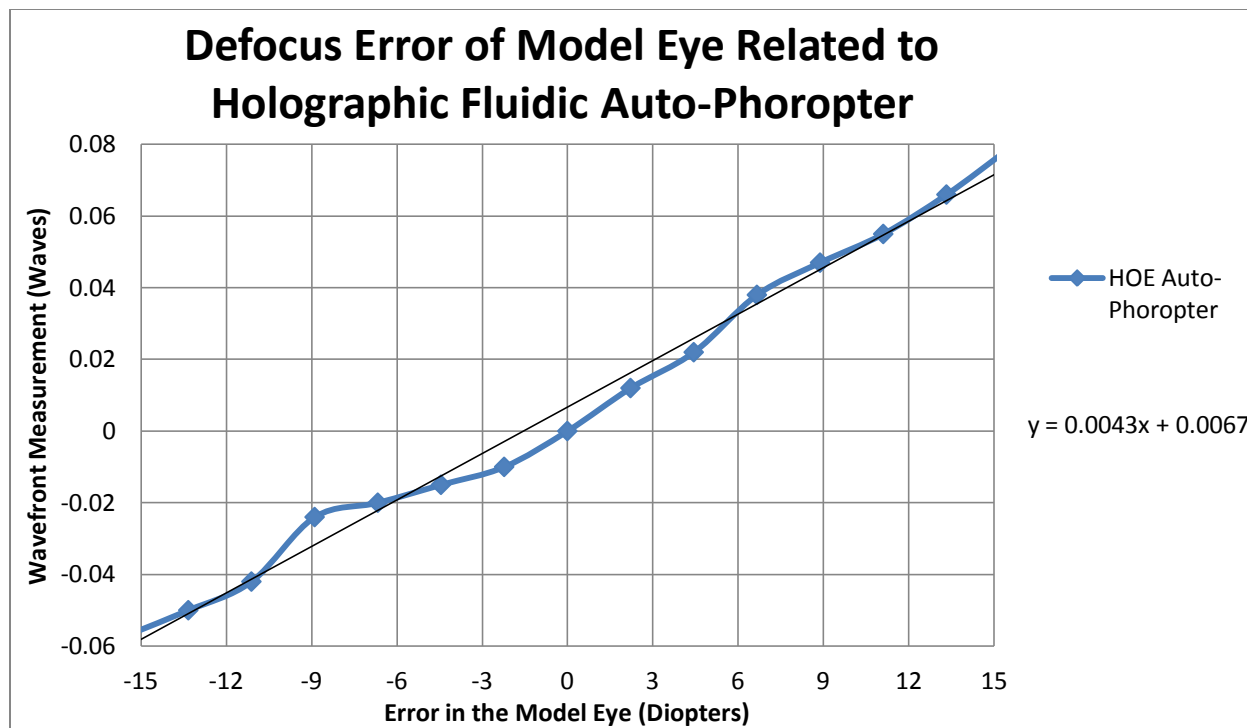


Figure 11-6 **Wavefront Error of Prototype Two Relative to Defocus Power of the Model Eye:** The slope variation of the model eye's defocus measurements proves that holographic fluidic auto-phoropter can functionally measure power variation induced by either the fluidic phoropter or the eye model.

### 11.6 Nulling Error with Fluidic Holographic Auto-Phoropter

In section 11.5 we proved through shifting the mirror position of the model eye that our wavefront sensor is capable of measuring wavefront error variation in the functional holographic prototype. To further verify that our holographic prototype can in fact correct for wavefront error we tested the holographic prototype with our fluidic lens. For both this null test and the model eye test of prototype two we set the auto-phoropter so that it was stopped down to 3 mm. The eye model mirror was shifted relative to the eye model lens so that -15 D of defocus power error was induced and measured in the system with -.057 waves of aberration. We then adjusted the power of the defocus fluidic lens to null this measured error until the wavefront sensor identified zero defocus error. Figure 11-7 shows the setup with both the fluidic defocus lens and

the model eye represented in the setup. Figure 11-8 shows the nulled out wavefront that was outputted by the Shack-Hartmann wavefront sensor.

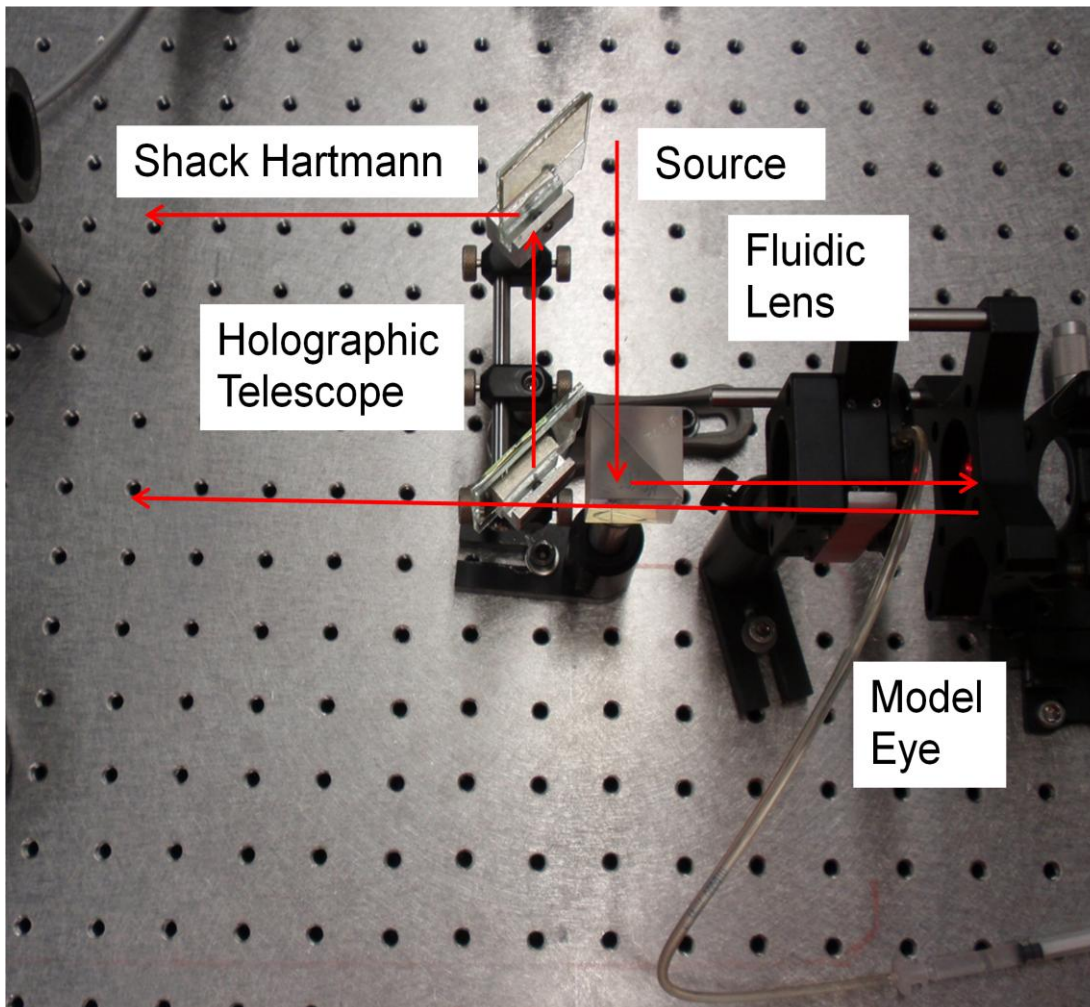


Figure 11-7 **Nulling Power Error with Holographic Fluidic Auto-Phoropter:** The defocus component of the fluidic phoropter was inserted into the system. The eye model is adjusted to -15 D of defocus and nulled out with the fluidic defocus lens in the holographic fluidic auto-phoropter setup.

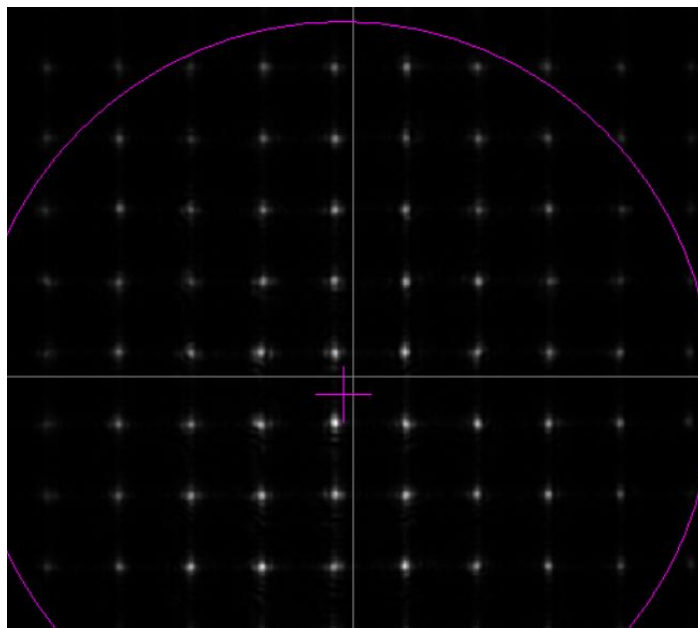


Figure 11-8 **Image Plane of Holographic Fluidic Auto-Phoropter:** The Shack-Hartmann image plane when -15 D of eye model error is nulled by the fluidic phoropter's defocus lens.

### 11.7 Limits of Holographic Optical Design

The first holographic fluidic auto-phoropter was designed with the motivation of proof of concept. We proved that we are capable of replacing the traditional telescope with holographic optical elements designed as a holographic telescope. The next step is to shift the HOE's reading and writing wavelength to the light sources operable wavelength at 785 nm. This will allow for us to achieve full transmission in the visible with our HOE's and test in the NIR without distracting the viewer from the scene in front of them. In the previous chapter we described the shortfalls of the second prototype which were 1) Lack of 4f Imaging and 2) Field of View. We will expand on these two topics as this holographic fluidic phoropter is a replication of that work with a slightly different design in the physical positioning of the optics.

The field of view of the holographic design increased relative to the other auto-phoropter designs. The size of the substrate that the HOE was embedded in was a 2' or 50.8 mm glass

plate. The HOE was set at a  $90^\circ$  angle, giving the lateral width of 36 mm's perpendicular to the optical axis. By replicating prototype two we know that the furthest distance of the HOE is 115 mm along the optical axis, giving a field of view of  $17.3^\circ$  and hence no longer the limiting object in the line of sight. Again, we calculate the field of view with zero power of the fluidic phoropter. The limiting factor of the optical system now becomes the first beamsplitter that brings the system field of view to  $11.8^\circ$ . Remembering in section 9.4, we calculated the maximum field passing through the fluidic lens was  $14^\circ$  relative to the 25 mm eye relief distance between the eye and the flat of the fluidic phoropter. In order to maximize the field of view we must be able to eliminate the second beamsplitter and bring the HOE to a closer distance of the fluidic phoropter. This will cause the fluidic phoropter to become the limitations on the field of view and not the auto-phoropter design.

It is possible to redesign the holographic system so that all beamsplitters are eliminated. This second holographic design takes advantage of polarization in order to eliminate the last remaining beamsplitter. The NIR source will be polarized in the p direction by placing a polarizer in front of the source. The first HOE element will have an embedded layer that function as a mirror for p-pol light at 785 nm, causing the p-pol light at 785 nm to reflect. As an aside, there may be stray p-pol light near 785 nm passing through the first HOE to the second HOE. The second HOE is designed so that p-pol light at 785 nm passes the light through the element in order to eliminate the stray light from the system. Regressing, the 785 nm light that reflects off of the first HOE is in the line of sight of the user. This p-pol light propagates through the fluidic lens to the human eye or the model eye with the scattering screen. The majority of the light exiting the retina upon reflection is no longer polarized. The unpolarized light propagates back to HOE Lens 1. HOE Lens 1 is now a lens to the unpolarized light and becomes part of our

telescopic system. HOE Lens 2 is placed at a proper distance from HOE Lens 1 to produce our telescopic system. The light exiting the second HOE then propagates to the Shack-Hartman wavefront sensor, thus eliminating all beamsplitters from the optical system.

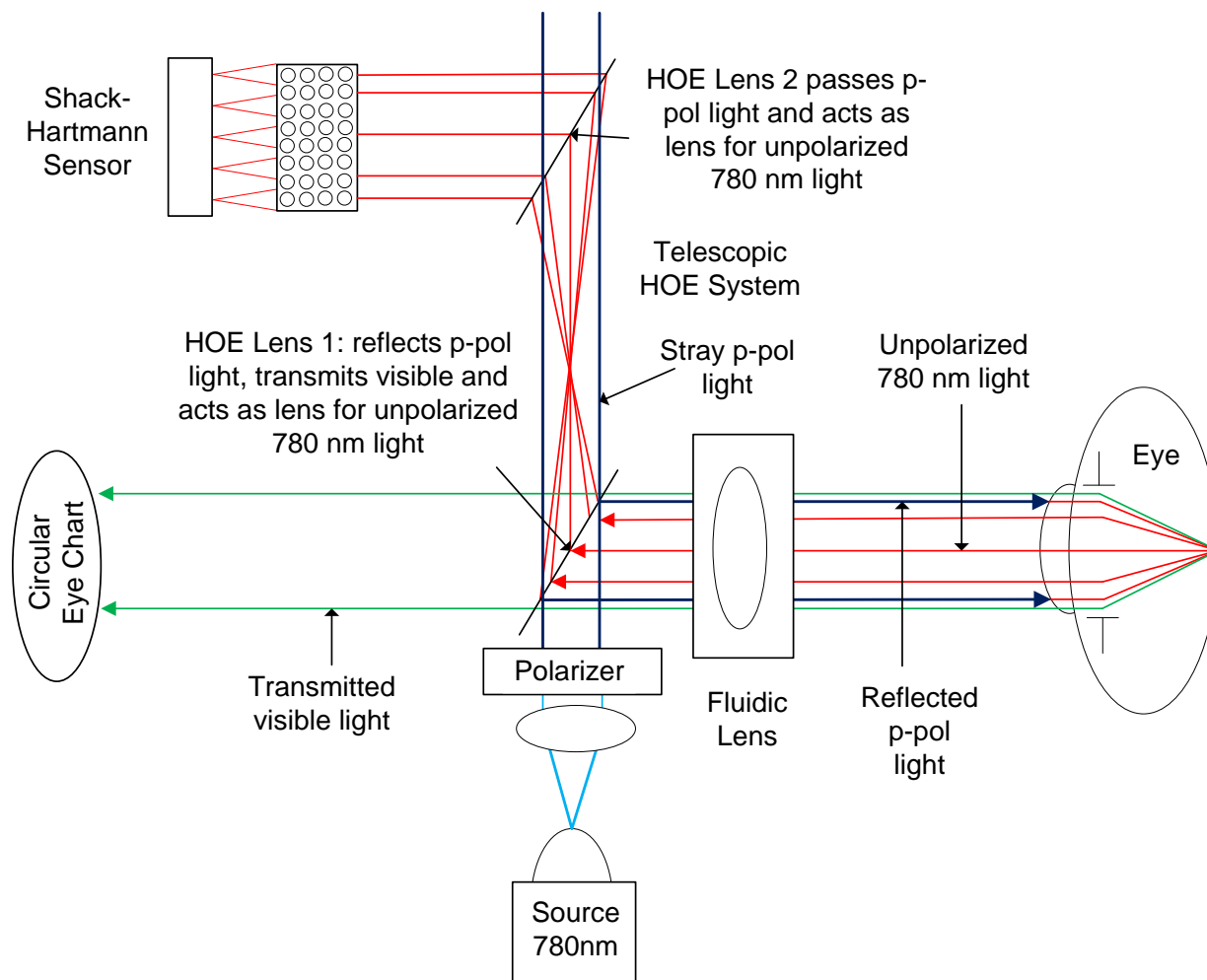


Figure 11-9 **Polarization Controlled Holographic Fluidic Auto-Phoropter Design:** The beamsplitters were eliminated from the first holographic design by the control of polarization.

Again, as the first holographic phoropter was a matching system to the second prototype, it has had the same short falls in  $4f$  imaging. We can expand further with our polarization controlled HOE design in eliminating the shortfall of lacking  $4F$  imaging. The reason we broke the  $4f$  design was to miniaturize the system. If we were to produce a  $4F$  imaging system with the

polarization controlled design we would need space for two elements between HOE lens 1 and the eye for the fluidic phoropter and eye relief. The minimum distance of these two optical elements is approximately 60 mm when we include tolerance. Therefore, the shortest focal length for 4f imaging with HOE's is with the two HOE lenses exhibiting focal lengths of 60 mm and polarization control. The length between the two HOE's would be 120 mm or approximately 4.7 inches. This size would be small enough to fit on a helmet sized fluidic auto-phoropter if desired. If we rotate the optical axis instead so we maximize Bragg efficiency the height in the vertical direction will be less than 4.7 inches, hence making it more suitable for a helmet sized holographic fluidic auto-phoropter design. Therefore, the next step for advancing our holographic designs would be to design a table top setup with two HOE lenses designed with 60 mm focal lengths at a wavelength of 785 nm that have polarization control as described in Figure 11-9.

## 12.0 CONCLUSION AND FUTURE WORK

We have covered throughout the course of this dissertation the fundamental advantages of optofluidic technology. Adaptive optic technology has revolutionized real time correction of wavefront aberrations and optofluidic technology enabled us to produce real time corrective lenses. Fluidic lenses offered superiority relative to their solid lens counterparts in their capabilities of producing tunable optical systems, that when synchronized produced real time variable systems with no moving parts. We have developed optofluidic fluidic lenses for applications of applied optical devices as well as ophthalmic optic devices. This dissertation has covered fluidic based devices for astigmatism and defocus correction. We then produced zoom optical systems with no moving parts by synchronizing these fluidic lenses. The variable power zoom power system incorporates two singlet fluidic lenses that were synchronized. The coupled device has no moving parts and produced a magnification range of 0.1 x to 10 x or a 20 x magnification variation. We further expanded the topics into chromatic aberration correction with the design of our two fluid based variable focal length chromates.

The second half of this dissertation discusses the production of optofluidic technology in ophthalmic applications. We discussed experimental results in the production of a fluidic phoropter which was produced through the combination of a defocus lens with two cylindrical fluidic lenses orientated  $45^\circ$  relative to each other. We then coupled this optofluidic phoropter with relay optics and Shack-Hartmann wavefront sensing technology to produce several designs of fluidic auto-phoropter devices. The auto-phoropter systems combined a designed Shack-Hartmann wavefront sensor with the compact refractive fluidic lens phoropter that was reimaged through various telescope orientations and designs.

As we have covered several different topics there are many directions in which future works can expand on. In the following subsections we will describe future work projects that can advance our research with optofluidic devices. The following suggestions of future work will be sequential with the order that the projects were discussed in this dissertation.

### **12.1 Wavefront Comparison of Freely Supported Edge vs. Clamped Edge Designs**

It would be advantageous to measure the wavefront of the clamped edge design of fluidic defocus lens two and compare the results to the freely supported edge of fluidic defocus lens one. We have built two different designed fluidic defocus lenses. The majority of our systems have applied the freely supported edge design in our optical designs, with the exception of our zoom optical system and the future work of the double fluidic achromat. We analyzed the wavefront measurements of the freely supported edge lens or defocus lens one to identify the outputted wavefront. There was additional astigmatism in addition to defocus as we increased the defocus power of the lens. Through our optimization approach described in Chapter 6 we are able to correct for both astigmatism and defocus by stacking our two astigmatism and one defocus lens together.

There are advantageous in knowing the wavefront of defocus lens two. One, we verify the optical control that is achievable with clamped edge designs. It gives a clearer picture on identifying the optimal clamping mechanism in the creation of our fluidic lenses. Secondly, if the clamped edge design produces less astigmatism than the freely supported edge design, assuming all other aberrations except defocus are negligible, we have decreased the amount of time required for all fluidic auto-phoropter systems to correct for ocular aberrations. The amount of iterations for compensation between the three lenses for astigmatism and defocus will be

decreased, which causes for faster readings. In addition, by creating a larger spread between the defocus and astigmatism wavefront measurements, we can improve on the physical control of the lens and thus improve on the accuracy of our corrections.

## **12.2 Improving Fluidic Zoom with a Redesigned Terrestrial Keplerian Telescope**

The zoom optical system showed a magnification range of 20 x but there are improvements that can be done to the system to increase this range. We found that a loss of throughput as caused by vigneting, reducing the resolvability of the image at larger magnifications. Theoretically, the ranges of the two lens Keplerian system should have had a greater magnification range than 20 x, but the image was unresolvable due to loss of light.

We can alter the traditional Keplerian telescope to a Terrestrial Keplerian telescope, also known as a Relayed Keplerian Telescope, to increase the magnification range of our zoom system. The input of a relay telescope will inverse the orientation of the image but will also increase the amount of throughput through the optical system. This is significant as our system should produce a larger magnification range with only increased throughput. By making the relay lens into a fluidic lens, we now have three fluidic lenses in our new proposed system. Syncing three fluidic lenses will also offer the advantage of increasing the magnification range of the Keplerian Zoom system as we have brought more focal length control to the system. This will most likely cause the system to increase in size but may be worth the tradeoff for the advancement in magnifying power. This Keplerian design still requires the fixed lens to focus the magnified power exiting the Keplerian telescope to the CCD plane.

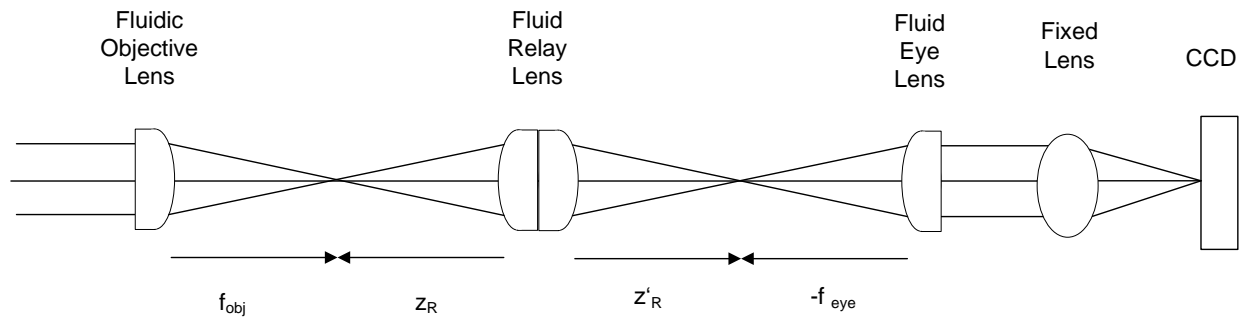


Figure 12-1 **Terrestrial Keplerian Telescope in Zoom System:** The modification to our Zoom system that will improve throughput and magnification range.

### 12.3 Progression of Fluidic Achromat

The two membrane fluidic achromat has been explained in functionality but has not yet been experimented, as not all parts have been completely machined. The next step for the advancement in this project is in the testing of the two synced surfaces synced to produce an achromatic lens. The testing has been explained in Chapter 5 and so we will add one additional suggestion for the fluidic achromat. An even greater advancement for the fluidic achromat would be to create a GUI that interfaces the achromat with the user. If the user can identify the two fluids in a given achromat and the focal length that is desired, then we have in a sense designed a digital achromatic lens. The GUI can cover multiple achromatic lenses and would allow for control of multiple achromatic lenses at the same time. This will assist in the zoom optical system designs as well as any other accommodating optical design one is interested in creating. This will increase the research on producing synced microscopes, telescopes, and other optical devices. An additional test that can be expanded on is to set the fluidic lenses in the vertical direction and verify how gravity affects our membrane suspension with time.

### 12.4 Progression of the Fluidic Auto-Phoropter Systems

There is much advancement that is achievable for the progression of this research. In section 10.4 we discussed the next step in the testing process in verification of the 4f imaging system of prototype three. This should be the next step to identify how the 4f imaging system compares to prototype two. The compensation of the fluidic lenses for a given correction must be compared after full correction is achieved for both systems. If the fluidic lenses are not approximately the same magnitude from both results, then we have identified that we have corrected for the optical systems and not for the users prescription with prototype two. In addition, we will verify the amount of light loss that occurs with the two designs and if we need to maintain 4f imaging. Light loss for a system with less than 15  $\mu\text{W}$  of power may require signal amplification. It is possible to place a signal amplifier between the second beamsplitter and the telescopic system of the off-axis designs. Signal amplification should also be examined as a future direction of the work. Once we established that our off-axis 4F imaging system works, we should perform studies on the fluidic auto-phoropter accuracy to user prescriptions and also the repeatability of the system.

To examine the fluidic auto-phoropter accuracy and repeatability, we must move onto the next phase of testing, which is human testing. Here we will give an example of data collection and what kind of future work can be covered through these examinations. A procedure for testing would be to require two testing sessions per individual with a separation of about 6 months. Each testing session should last for less than 10 minutes. The individual will offer the prescription that was given to them by their eye doctor so that we have reference points for each user. If the individual has 20/20 vision then they will notify us of their 20/20 vision, as a control group is required. The individual then looks into our binocular auto-phoropter systems. We

should test as many systems as possible with each individual to identify variation between optical designs and their relative prescription defined by the doctors. At least four targets at four measured distances should be set so we can identify the accommodation of the user relative to targeted planes. Both eyes should be measured with the device separately and then concurrently.

The sample size and age of the tested population is important in maximizing our test results. The minimum population of subjects to be tested on should be at least 210 and we will continue with this population size for explanation purposes. From these 210 subjects, we should break the grouping down to 7 larger population groups spanning from 18 to 74 years of age with each group spanning a range of 8 years. Each group will have three sub-populations. A sub-population will occur of 10 subjects that offer 20/20 vision, 10 subjects that require corrective eye wear, and 10 subjects with corrective eye surgery for each subgroup. This means that every population will have three sub-populations where there are a total of 21 sub-groups for this research: 1) a group with 20/20 Vision, 2) a group with corrective eye wear, and 3) a group with corrective eye surgery. While we run the experiments, the users in the corrective eye subgroup must not wear contact lenses or other corrective eye wear. Thus, the people excluded from this research are those who are under the age of 18 and over the age of 75 years of age.

Data from this experiment allows for us to extract information from both our system and the human populations. The results measured will be analyzed to determine the quality of the system and the accuracy of our objective vs. subjective eye examinations. Also, the relation of age to the accuracy of the test results is also measured. The purpose of the second test 6 months following the initial testing is to ensure the repeatability of the auto-phoropter. This testing approach enables us to identify the effects of Presbiopia for various populations as we have identified sub-groups at different ages. These subgroups will identify how accurately our system

measures visual performance of age related changes. In addition, we would have data for corrective eye surgery and for healthy eyes. In essence, with at least 210 subjects we can verify accommodation in addition to prescription and their effects for different eye correction groups and healthy groups. The separation of data into 21 sub-groups will allow for information that can test for additional concepts in the future.

In addition, we can develop an approach for the correction of convergence and misalignment of the eye. There are conditions such as Esotropia, Exotropia, Hypertropia and Hypotropia that can be corrected for by designing a fluidic prism. By inserting fluid into the prism, we can adjust the wedge and thus the prism power. This fluidic prism would be a great tool in the correction of individuals with a lack of control for the convergence of their eyes.

### **12.5 Progression of the Fluidic Holographic Auto-Phoropter Systems**

We can further expand on the advancements found in section 11.7 in the discussion of the next steps for the holographic fluidic auto-phoropter project. The next steps are to shift the HOE's so that the system operates at 785 nm and shows a functioning system with low intensity light. After this step is achieved, the following step as described in section 11.7 is to eliminate the beamsplitters in the optical system through the use of polarization control. With the elimination of the beamsplitters we can compress the system further through eliminating space needed for the beamsplitter, but also through the shorter focal length required of the holographic lenses for 4F imaging. The distance between holographic lens 1 and the eye location is reduced to 60 mm for the fluidic lens separation and eye relief. This suggests that with 60 mm focal length holographic lenses, we can produce a 4F based holographic fluidic auto-phoropter. We can further this design with a couple more advancements beyond section

11.7. We can change the lenticular array for the Shack-Hartmann wavefront sensor so that it is replaced with HOE based lenses. It would be interesting to identify how the system compares between a traditional lenslet array and an HOE based lenslet array. A second additional system advancement that can be applied to all of our fluidic auto-phoropter systems would be an off axis pupil imaging device. In the second half of the dissertation we have identified the significance of pupil size to our optical system. By adding an off axis imaging system we can verify the iris size as we test the users prescription, giving us further data about the accommodation of the user as he naturally views various depths. Figure 12-2 shows the combination of the HOE based holographic fluidic auto-phoropter with polarization control combined with an imaging system to measure the pupil size and also a HOE lenslet array for the Shack-Hartmann wavefront sensor. Figure 12-3 further expands the system with the same features as Figure 12-2 except now we have added dimensions to produce the proper geometrical positioning of our optics to produce a 4f imaging system in addition to our desired features. This last holographic fluidic auto-phoropter has the same polarization features for the HOE's as Figure 12-2, geometrically has 4f imaging, applies our fluidic based adaptive optics fluidic technology, offers off axis imaging to identify pupil size, and also proposes an advanced wavefront technology where the Shack-Hartman wavefront sensor takes advantage of holographic optical technology. The 4f advanced holographic fluidic auto-phoropter is also very small in size, with approximately a 3" by 6" area offering us the opportunity to make this device mobile. If the HOE wavefront sensor does not function properly we can revert back to the traditional Shack-Hartmann wavefront sensor.

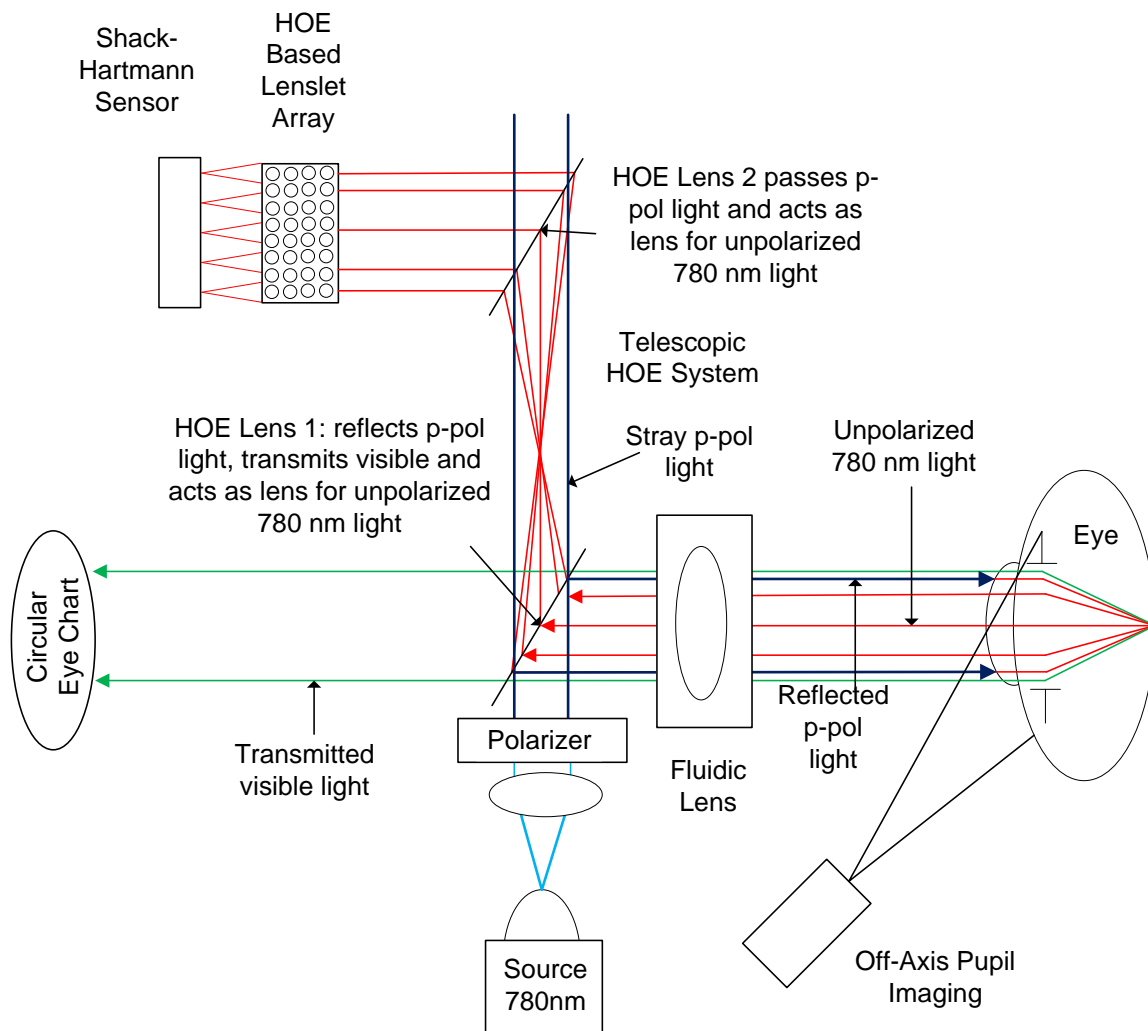


**Figure 12-2 Advanced Holographic Fluidic Auto-Phoropter with Pupil Imaging:** Expansion on system described in Figure 11-8. We have modified the auto-phoropter system in this design so that the lenslet array of the Shack-Hartmann Sensor is designed with holographic optical elements. In addition, we added an off axis imaging system to identify the iris size and thus the pupil size. This system again takes advantage of polarization control and our holographic telescope coupled with our fluidic phoropter.

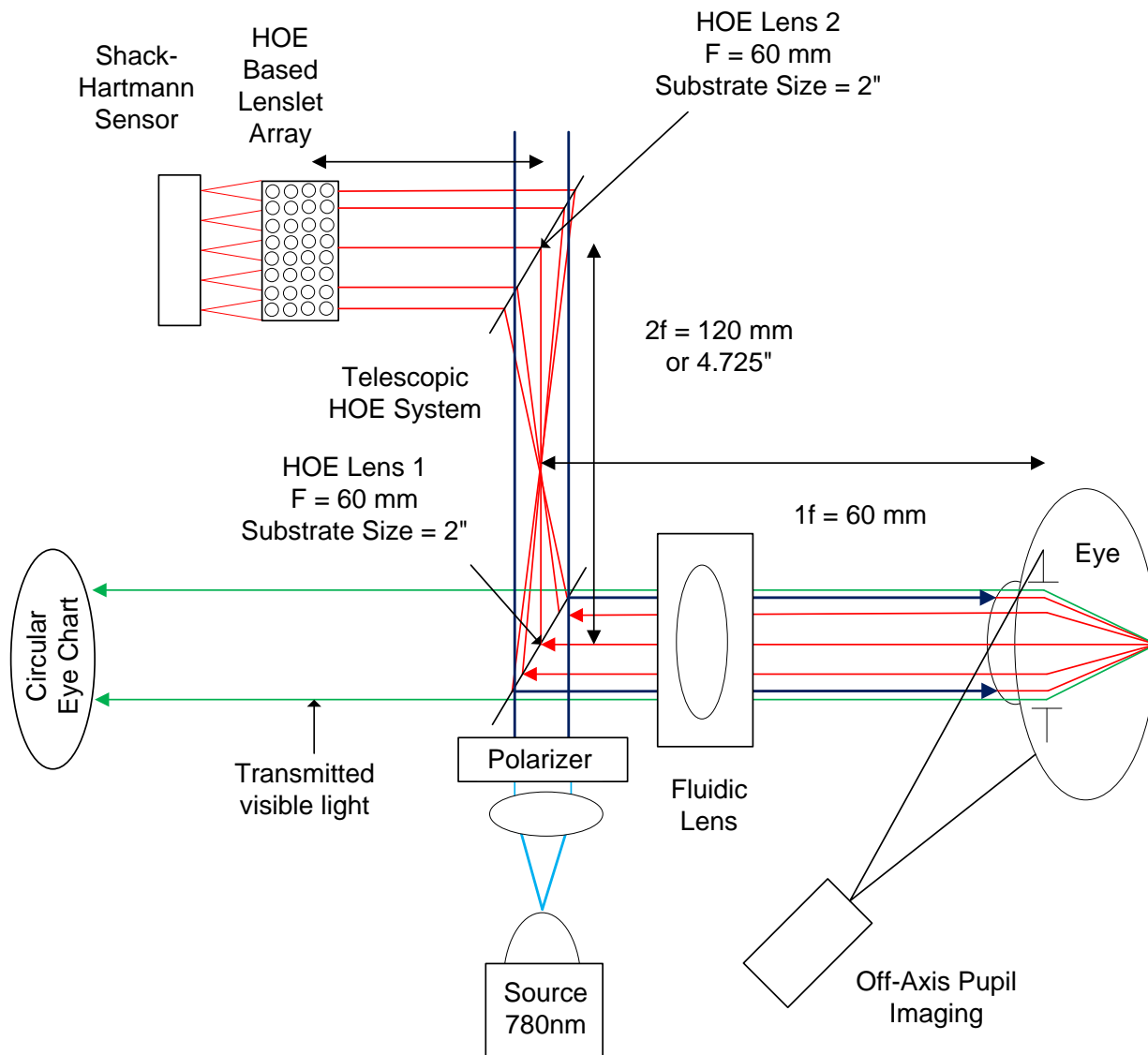


Figure 12-3 **4F Advanced Holographic Fluidic Auto-Phoropter With Pupil Imaging:** With the above defined distances and focal lengths we have designed a 4f imaging system with our fluidic phoropter, pupil imaging system, advance holographic based wavefront technology and a polarization controlled holographic telescope.

## 12.6 Mobile Holographic Fluidic Auto-Phoropter

There are many disadvantaged regions in the world that do not have access to phoropters and eye care. It would be highly advantageous for a phoropter system to become mobile. As is seen in Figure 12-3, the size of our 4F advanced holographic fluidic auto-phoropter can fit within

a helmet. This helmet can hold two of these optical systems next to each other. The next step after testing and verifying that this system functionally measures and corrects for prescriptions is to set the system into a helmet and make it mobile. The following figures show a system without pupil imaging but modifications can be made to add this feature to our binocular system / helmet display. The helmet display was modeled in SolidWorks to identify the coupling of the two holographic auto-phoropters into a single system. The actuators for the fluid pump controls would be inside the periphery of the casing. The inter-pupillary distance is taken into account by adjusting the separation on the helmet with a knob between the two monocular setups. We can make advancements into interfacing with other mobile devices to read out prescriptions and further the advancement of these research projects.

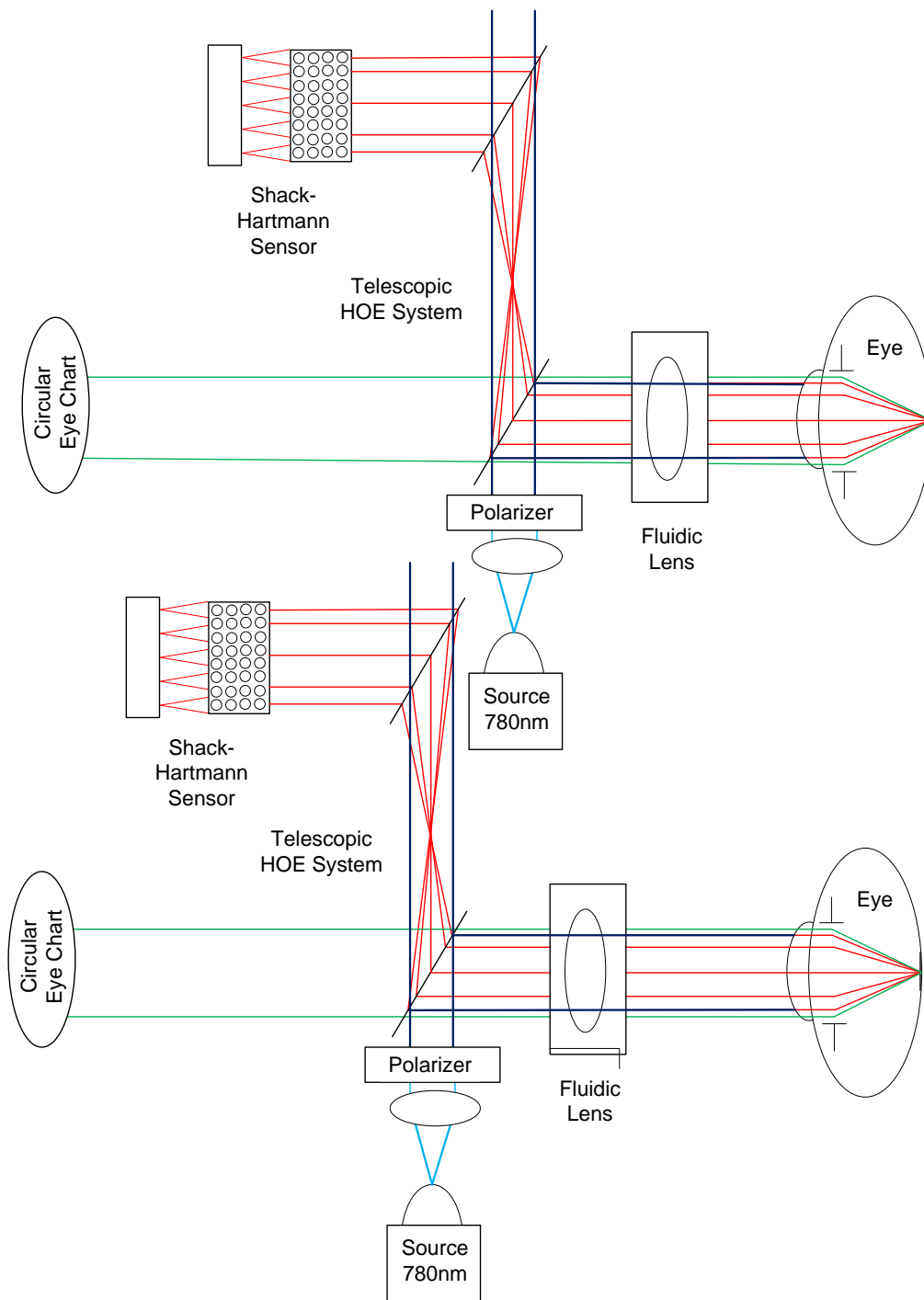


Figure 12-4 **Binocular Advanced 4F Holographic Fluidic Auto-Phoropter Without Pupil Imaging:** This binocular setup is set in sequence next to each other. Both systems are in the north south direction relative or perpendicular to the line of sight of the users. This binocular system fits inside a helmet for a mobile eye exam.

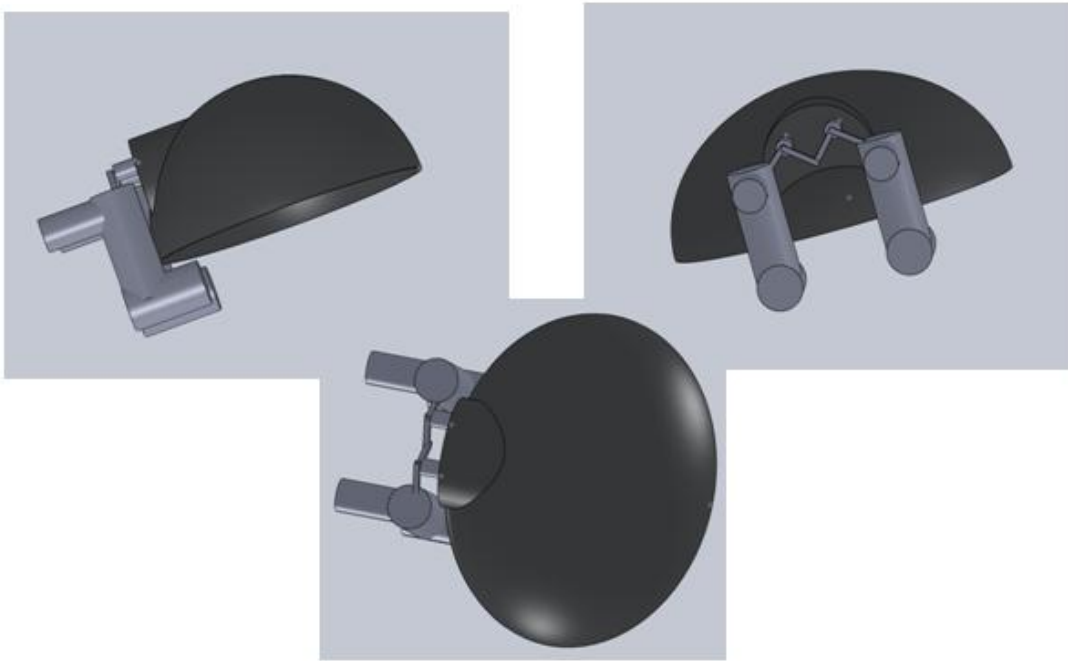


Figure 12-5 **Mobile Binocular Helmet With Two Advanced 4F Holographic Fluidic Auto-Phoropter Designs:** The helmet is applied to combine two monocular setups and account for inter-pupillary separation between the users eyes.

## REFERENCES

1. C. Monat, P. Domachuk, B.J. Eggleton, "Integrated Optofluidics: A new river of light," *Nat. Photonics*, 1,106-114, 2007.
2. D. Psaltis, S.R. Quake, and C. Yang, "Developing optofluidic technology through the fusion of microfluidics and optics," *Nature*, 442, 381-386,2006.
3. Y. Fainman, D. Psaltis, C. Yang, *Optofluidics: Fundamentals, Devices, and Applications*. Adaptive Optofluidic Devices, Chapter 8, McGraw-Hill, 2010.
4. H. C. King, *The History of the Telescope*. pp. 189-191, Charles Griffin & Company Lt., 1955.
5. E. C. Ohmart, "Device for reflecting and refractive radiant energy", United States Patent 504,890 (September 12, 1893).
6. R. L. Gordon, "A Voluntary Association", United States Patent 1,269,422 (June 11, 1918).
7. R. K. Graham, "Optical Instrument", United States Patent 2,269,905 (January 13,1942).
8. E. F. Flint, "Variable Focus Lens", United States Patent 2,300,251 (October 27,1942).
9. B. M. Wright, "Improvements in or relating to variable focus lenses," English Patent 1,209,234 (March 11, 1968).
10. G.C. Knollman, J. L.S. Bellin, and J. L. Weaver, "Variable focus liquid filled hydroacoustic lens" *J. Acoust. Soc. Am.* 49, 253-261, 1970.
11. V. E. Hamilton, A. H. Lanckton, "Stereopsis using a large liquid-filled aspheric field lens stereoscope," *Photogrammetric Eng. And Remote Sensing*, 39,3,294,1973.
12. K. Campbell, Y. Fainman, A. Groisman, "Pneumatically actuated adaptive lenses with millisecond response time," *Appli. Phys. Lett.*, 91 (17), 171111, 2007.
13. H. Mollmann, *Introduction to the Theory of Thin Shells*. John Wiley and Sons, New York, 1981.
14. E. Ventsel, T. Krauthammer, *Thin Plates and Shells-Theory, Analysis and Applications*, Marcel Dekker, New York, 2001.

## REFERENCES - Continued

15. R. Marks, D. L. Mathine, J. Schwiegerling, G. Peyman, and N. Peyghambarian, "Astigmatism and defocus wavefront correction via Zernike modes produced with liquid lenses," *Appl. Opt.*, 49, 19, 3580-3587, 2009.
16. S. Sinzinger, J. Jahns, *Microoptics*. PP. 86-87, Wiley Inc., 1999.
17. R. Marks. *Fluidic Astigmatic and Spherical Lenses for Ophthalmic Applications*. University of Arizona, College of Optical Sciences, Dissertation, 2010.
18. S. P. Timoshenko, J. N. Goodier, *Theory of Elasticity 3<sup>rd</sup>. Ed*, PP. 46-50, McGraw-Hill, 1970.
19. J. Schwiegerling. *Field Guide to Visual and Ophthalmic Optics*. Bellingham, Washington: SPIE PRESS, 2004.
20. J. Grievenkamp. *Field Guide to Geometric Optics*. Bellingham, Washington: SPIE PRESS, 2004.
21. D. A. Atchison, G. Smith. *Optics of the Human Eye*. Reed Educational and Professional Publishing, Chap. 1, 2000.
22. W. J. Smith, *Modern Optical Engineering: The Design of Optical Systems*, Third Edition, McGraw Hill, New York, NY, 2000.
23. V. N. Mahajan, *Aberration Theory Made Simple*. SPIE Optical Engineering Press, 1991.
24. J. Schwiegerling. Class Lecture. Optical Specifications, Fabrication and Testing. University of Arizona, Tucson Arizona. April 12<sup>th</sup>, 2011.
25. L. N. Thibos, R. A. Applegate, J.T. Schwiegerling, R. Webb. "Standards for Reporting the Optical Aberrations of Eyes." *J. Refr. Surg*, September/October 2002; 18:S652-S660.
26. J. Straub. *Design, Validation, and Application of an Ocular Shack-Hartmann Aberrometer*. University of Arizona, College of Optical Sciences, Dissertation, 2003.
27. H. C. Howland, B. Howland. "A Subjective Method for the Measurement of Monochromatic Aberrations of the Eye. *J. Opt. Soc. Am. A*. 1977; 67: 1508-1518.
28. P. Artal, R. Navarro. "Monochromatic Modulation Transfer Function of the Human Eye for Different Pupil Diameters: An Analytical Expression." *J. Opt. Soc. Am. A*. 1994; 11:246-249.

## REFERENCES - Continued

29. H. J. Hofer, P. Artal, B. Singer, et al. "Dynamics of the Eye's Wave Aberration". *J. Opt. Soc. Am. A.* 2001; 18: 497-506.
30. D. R. Williams, P. Artal, R. Navarro, et al. "Off-axis Optical Quality and Retinal Sampling in the Human Eye. *Vision Res.* 1996; 36: 1103-1114.
31. J. C. He, S. A. Burns, S. Marcos. "Monochromatic Aberrations in the Accommodated Human Eye." *Vision Res.* 2000; 40: 41-48.
32. A. Guirao, C. Gonzalez, M. Redondo, et al. "Average Optical Performance of the Human Eye as a Function of Age in a Normal Population. *Invest. Ophthalmol. Vis. Sci.* 1999; 40: 203-213.
33. J. S. McLellan, S Marcos, P. M. Prieto, S. A. Burns. "Imperfect Optics May Be the Eye's Defense Against Chromatic Blur" *Nature.* 2002; 417: 174-176.
34. R. Calver, M. J. Cox, D. B. Elliot. "Effect of Aging on the Monochromatic Aberrations of the Human Eye." *J. Opt. Soc. Am. A.* 1999: 2069-2078.
35. G. Glasser, M. C. W. Campbell. "Presbyopia and the Optical Changes in the Human Crystalline Lens with Age. " *Vision Res.* 1998; 38: 209-229.
36. J. S. McLellan, S. Marcos, S. A. Burns. "Age-Related Changes in Monochromatic Wave Aberrations of the Human Eye." *Invest. Ophthalmol. Vis. Sci.* 2001; 42: 1390-1395.
37. T. Oshika, T. Tokunaga, T. Samejima, K. Miyata, K. Kawana, Y. Kaji. "Relation between Ocular Higher-Order Aberration and Contrast Sensitivity after Laser In Situ Keratomileusis," *Invest. Ophthalmol. Vis. Sci* 2006; 47; 1334-1338.
38. H. S. Ginis, S. Plainis, A. Pallikaris. "Variability of wavefront aberration measurements in small pupil sizes using a clinical Shack-Hartmann aberrometer" *BMC Ophthalmology* 2004, 4:1.
39. T. Kawamorita, K. Uozato. "Changes of natural pupil size and ocular wavefront aberrations under the binocular and the monocular conditions" *Journal of Vision*, 2006, Vol. 6, No. 13, Article 54.
40. J. Schwiegerling, "Scaling Zernike expansion coefficients to different pupil sizes", *J. Opt. Soc. Am. A.*, **19**, 1937-1945, 2002.

**REFERENCES - Continued**

41. D. Malacara. *Optical Shop Testing, 2<sup>nd</sup> Edition*. Chapter 10, D. Malacara (Ed.), John Wiley and Sons, New York, 1992.
42. R. V. Shack, B. C. Platt. "Production and Use of a Lenticular Hartmann Screen. *J. Opt. Soc. Am.*, 1971; 656.
43. R. K. Tyson. *Principles of Adaptive Optics*. Academic Press, New York, 1998.
44. J. M. Geary. *Introduction to Wavefront Sensors*. SPIE Optical Engineering Press, 1995.
45. B. Burge, and J. Peseux, "Variable focal lens controlled by an external voltage: an application of electro-wetting," *J. E. Eur. Phys*, 3, 159-163, 2000.
46. S. Kuiper and B. H. W. Hendriks, "Variable-focus liquid lens for miniature cameras," *Appl. Phys. Lett.*, 85, 1128 (2004)
47. S. Xu, Y. Liu, H. Ren, S-T Wu, "A novel adaptive mechanical-wetting lens for visible and infrared imaging", *Optics Express*, Vol. 18, 12, pp. 12430-12435 (2010).
48. C.A. Lopez, C.C. Lee, and A. H. Hirs, "Electrochemically activated adaptive liquid lens," *Appl. Phys. Lett.*, 87, 2005.
49. C. Dorrer, O. Prucker, and J. Ruhe, "Swellaible surface-attached polymer microlenses with tunable focal length," *Adv. Mater.*, 19 (3), 456, 2007.
50. S. N. Lee, H.W. Tung, W.C. Chen, and W. L. Fang, "Thermal actuated solid tunable lens," *IEEE Photon. Technol. Lett.*, 18, 2191-2193, 2006.
51. H. Yang, Y-H Han, Z-W Zhao, K. Nagai, and Z-Z Gu, "Thermal responsive microlens arrays," *Appl. Phys. Lett.*, 89, 111-121, 2006.
52. A. Casner and J.-P. Delville, "Adaptive lensing driven by the radiation pressure of a continuous-wave laser wave upon a near-critical liquid-liquid interface," *Opt. Lett.* 26, 1418-1420, 2001.
53. R. Kuwano, T. Tokuaga, Y. Otani, and N. Umeda, "Liquid pressure varifocus lens" *Opt. Express*, 15(10), 5931-5936, 2007.
54. H. Ren, S. T. Wu, "Variable-focus liquid lens," *Opt. Express*, 15(10),5931-5936, 2007.
55. D-Y Zhang, V. Lien, Y. Berdichevsky, J. Choi, and Y-H Lo, "Liquid adaptive lens with high focal length tenability," *Appl. Phys. Lett.*, 82,3171,2003.

## REFERENCES - Continued

56. P. Valley, N. Savidis, J. Schwiegerling, M.R. Dodge, G. Peyman, and N. Peyghambarian, "Adjustable hybrid diffractive/refractive achromatic lens" *Opt. Exp.*, 19,8, 7468-7479, 2011.
57. A. Miks and J. Novak, "Analysis of two-element zoom systems based on variable power lenses" *Opt. Exp.*, 18,7, 6797-6810, 2010.
58. A. Miks and J. Novak, "Analysis of three-element zoom lens based on refractive variable-focus lenses," *Opt. Exp.*, 19,24, 23989-23996, 2011.
59. L. Li and Q-H Wang, "Zoom lens design using liquid lenses for achromatic and spherical aberration corrected target," *Opt. Eng.* 51(4), 043001, 2012.
60. J. Draheim, T. Burger, F. Schneider, and U. Wallrabe, "Liquid zoom lens system using two single chamber adaptive lenses with integrated actuation," in *Proceedings of IEEE Conference on MEMS 2011 (IEEE, 2011)*, pp. 692–695.
61. N. Sugiura, and S. Morita, "Variable-focus liquid-filled optical lens", *Applied Optics*, Vol. **32**, 4181-4186 (1993).
62. E. J. Hearn, *Mechanics of Materials 2, 3<sup>rd</sup> ed.*, pp. 200-207 (Butterworth-Heinemann, 1997).
63. W. P. Eaton, F. Bitsie, J. H. Smith, D. W. Plummer, "A New Analytical Solution for Diaphragm Deflection and its Application to a Surface-Micromachined Pressure Sensor", *Technical Proceedings of the 1999 International Conference on Modeling and Simulation of Microsystems*, 640-643 (1999).
64. R. Shellin, G. Hess, W. Kuhel, C. Thielemann, D. Trost, J. Wacker, and R. Steinmann, "Measurements of the mechanical behavior of micromachined silicon and silicon-nitride membranes for microphones, pressure sensors and gas flow meters", *Sensors and Actuators A: Physical*, **41**, 287-292 (1994)
65. H. Ren, D. Fox, P. A. Anderson, B. Wu, S.T. Wu, "Tunable-Focus Liquid Lens Controlled Using a Servo Motor," *Opt. Exp.* , 14, 18, 2006.
66. Sylguard 184 Dow Corning, K.R. Anderson Inc, Phoenix, AZ (2012).
67. R. Marks, D. L. Mathine, G. Peyman, J. Schwiegerling, and N. Peyghambarian, "Adjustable fluidic lenses for ophthalmic corrections," *Opt. Lett.* **34**, 515-517 (2009).

**REFERENCES - Continued**

68. M. Daimon and A. Masumura, "Measurement of the Refractive Index of distilled water from the near-infrared region to the ultraviolet region," *Appl. Opt.* **46**, 3811 (2007).
69. Donald C. O'Shea, Thomas J. Suleski, Alan D. Kathman, Dennis W. Prather, *Diffraction Optics: Design, Fabrication, and Test* (SPIE Press Book, 2004).
70. P. Valley, D. L. Mathine, M. R. Dodge, J. Schwiegerling, G. Peyman, and N. Peyghambarian, "Tunable-focus flat liquid-crystal diffractive lens," *Opt. Lett.* **35**, 336-338 (2010).
71. P. Valley, M. R. Dodge, J. Schwiegerling, G. Peyman, and N. Peyghambarian, "Nonmechanical bifocal zoom telescope," *Opt. Lett.* **35**, 2582-2584 (2010).
72. S. Sato, A. Sugiyama, and R. Sato, "Variable-Focus Liquid-Crystal Fresnel Lens," *Jpn. J. Appl. Phys.* **24** pp. L626-628 (1985).
73. H. Ren, Y. H. Fan, and S. T. Wu, "Tunable Fresnel lens using nanoscale polymer-dispersed liquid crystals," *Appl. Phys. Lett.* **83**, 1515-1517 (2003).
74. B. E. Bagwell, D. V. Wick, R. Batchko, J. D. Mansell, T. Martiez, S. Serati, G. Sharp, and J. Schwiegerling, "Liquid crystal based active optics," *Proc. SPIE* **6289**, 628908 (2006).
75. H. C. Lin and Y. H. Lin, "An electrically tunable focusing liquid crystal lens with a built-in planar polymeric lens," *Appl. Phys. Lett.* **98**, 083503 (2011).
76. O. Pishnyak, S. Sato, and O. D. Lavrentovich, "Electrically tunable lens based on a dual-frequency nematic liquid crystal," *Appl. Opt.* **45**, 4576-4582 (2006).
77. H. Ren, Y. H. Fan, S. Gauza, and S. T. Wu, "Tunable-focus flat liquid crystal spherical lens," *Appl. Phys. Lett.* **84**, 4789-4791 (2004).
78. D. Y. Zhang, N. Justis, and Y. H. Lo, "Integrated fluidic adaptive zoom lens," *Opt. Lett.* **29**, 2855-2857 (2004).
79. H. Ren, D. Fox, P. A. Anderson, B. Wu, and S. T. Wu, "Tunable-focus liquid lens controlled using a servo motor," *Opt. Express* **14**, 8031-8036 (2006)
80. T. Stone and N. George, "Hybrid diffractive-refractive lenses and chromates," *Appl. Opt.* **27**, 2960-2971 (1988)

**REFERENCES - Continued**

81. G. Zhou, H. M. Leung, H. Yu, A. S. Kumar, and F. S. Chau, "Liquid tunable diffractive/refractive hybrid lens," *Opt. Lett.* **34**, 2793-2795 (2009).
82. B. Apter, U. Efron, and E. Bahat-Treidel "On the fringing field effects in liquid-crystal beam-steering devices," *Appl. Opt.* **43**, 11-19 (2004).
83. J. Liang, B. Grimm, S. Goelz, J. F. Bille. "Objective Measurement of Wave Aberrations of the Human Eye with the use of a Hartmann-Shack Wave-front Sensor." *J. Opt. Soc. Am. A.* 1994; 11: 1949-1957.
84. J. Liang, D. R. Williams, and D. T. Miller, "Supernormal vision and high-resolution retinal imaging through adaptive optics" *J. Opt. Soc. Am. A* **14** 2884-2892 (1997)
85. H. Cheng, J. K. Barnett, A. S. Vilupuru, J. D. Marsack, S. Kasthurirangan, R. A. Applegate, A. Roorda, " A population study on changes in wave aberrations with accommodation." *J. Vis.* 4:272-280, 2004.
86. A. Roorda, D. R. Williams, "The arrangement of the Three Cone Classes in the Living Human Eye. *Nature*; 397: 520-522, 1999.
87. G. D. Love, "Wavefront Correction and production of Zernike modes with a liquid-crystal spatial light modulator," *Applied Optics*, **36**, 1517-1524, (1997)
88. J. Porter, H. Queener, J. Lin, K. Thorn, A. Awwal. *Adaptive Optics for Vision Science*, Chapter 18: Design and Testing of a Liquid Crystal Adaptive Optics Phoropter. PP. 506-507, 2006.
89. G. Peyman, "External Lens Adapted to Change Refractive Properties", United States Patent 7,993,399 (August 09, 2011).
90. Varioptic – The Liquid Lens Company, [www.varioptic.com](http://www.varioptic.com).
91. L. Pang, U. Levy, K. Campbell, A. Groisman, and Y. Fainman, "Set of two orthogonal adaptive cylindrical lenses in a monolith elastomer device," *Opt. Express*, 13, 9003-9013, 2005.
92. M. V. Waldkirch, P. Lukowicz, G. Troster, "Oscillating fluid lens in coherent retinal projection displays for extending depth of focus," *Opt. Comm.*, 253 Issue: (4-6), 407-418, 2005.

**REFERENCES - Continued**

93. D. Sliney, M. Wolbarsht. *Safety with Lasers and Other Optical Sources*. Plenum Press, New York and London, 1980.
94. C. Slinger, C. Cameron, M. Stanley. "Computer-Generated Holography as a Generic Display Technology." IEEE Society of Computers. Volume 38, Issue 8, Page(s): 46 – 53, 2005.
95. D. Jurbergs, F-K Bruder, F. Deuber, T. Facke, R. Hagen, D. Honel, T. Rolle, M-S Weiser, A. Volkov. "New Recording Materials for the Holographic Industry." Practical Holography XXIII: Materials and Applications. Proc. Of SPIE Vol. 7233 K 1-10 2009.